
Beamforming and Evaluation of Focal Plane Arrays for Radio Astronomy

By
Douglas Brian HAYMAN B.E.(Hons I) B.Sc.

Supervisors:
Prof. Karu ESSELLE, Prof. Trevor BIRD, Prof. Peter HALL

Conducted at:
The CSIRO Radiophysics Laboratory, Marsfield, NSW
with
The CSIRO Division of Astronomy and Space Science
and
The CSIRO Information and Communication Technologies Centre



Faculty of Science
Department of Physics and Engineering
2011

This thesis is presented for the degree of
Doctor of Philosophy

To Sarah, Peter and Annie

Copyright © Douglas Brian Hayman 2011. All rights reserved.

All persons copying this information are required to adhere to the terms and constraints invoked by the author's copyright.

Company, product and service names used in this thesis are for identification purposes only. All trademarks are the property of their respective owners.

Typeset using L^AT_EX on Monday 7th November, 2011.

The electronic version of this document contains hyperlinks for section numbers, figures, tables, references and URLs. To return to the text after following a hyperlink in both Adobe[®] Reader[®] and SumatraPDF, use *Alt + left arrow*.

Contents

List of Figures	ix
List of Tables	xii
Abstract	xiii
Declaration	xv
Acknowledgements	xvii
Notation, Symbols and Abbreviations	xix
1 Introduction	1
1.1 Thesis Outline	2
1.2 Project Context and Time Frame	3
1.3 Distinct Contributions of this Thesis	3
1.4 Contributions of Others	5
2 Focal Plane Arrays and Radio Astronomy	7
2.1 Radio Astronomy Signals	7
2.1.1 Quasi-Monochromatic Plane Wave Approximation	9
2.1.2 Measures of Source Strength	10
2.1.3 Polarization	11
2.2 Figures of Merit	13
2.2.1 Figures of Merit Related to Gain	14
2.2.2 Figures of Merit Related to G/T	15
2.3 Focal Plane Array Concepts	16
2.3.1 Focal Plane Array Nomenclature	16
2.3.2 Two Views of FPAs	18
2.4 A Brief History of FPA Development	19
2.5 Dense FPAs—Benefits and Challenges	20
2.5.1 Benefits	21
2.5.2 Challenges	23
2.6 FPAs in Radio Astronomy	24

CONTENTS

2.6.1	The SKA and FPAs	26
2.6.2	Wideband Array Elements	27
2.6.3	Prototype FPA Systems	30
2.6.4	Currently Planned Dense FPA Based Radiotelescopes	33
2.6.5	Competitors to FPAs in Radio Astronomy	33
2.7	Summary	34
3	FPA Size and Encircled Power Calculations	37
3.1	Introduction	37
3.2	Focal-Region Fields	38
3.3	Parabolic Reflector Geometry	38
3.4	Element Density	40
3.5	Simple FPA Size Models	42
3.5.1	Ray Tracing	43
3.5.2	Airy Pattern and Beam Deviation Factor	44
3.6	Encircled Power—Theory	47
3.6.1	Tapered Aperture	49
3.7	Encircled Power—Implementation	52
3.8	Encircled Power—Results	53
3.8.1	Focal-Plane Fields—Results	53
3.8.2	Focal-Plane Power-Flux-Density—Results	56
3.8.3	FPA Size—Results	58
3.8.4	Tapered Aperture Results	60
3.9	Encircled Power—Observations and Discussion	63
3.9.1	Independence of Dish Size	63
3.9.2	Feed Blockage	65
3.9.3	Fit of FPA Size to a Closed Form Function	67
3.9.4	Optimum F/D	70
3.9.5	Alternative Focal-Plane Integrations	71
3.9.6	Other Reflector Geometries	71
3.10	Comparison with Measured and Modelled Referenced Data	71
3.11	Summary	74
4	Gain and Noise Model for a Beamformed Array	77
4.1	Detailed FPA Models	78
4.2	Active Antenna Noise Temperature and G/T	80
4.2.1	Reference Plane for a Radiotelescope	84
4.3	Polarization Match of an Antenna	85
4.4	Single Port Antenna Model	86
4.5	Directivity—Single Port Antenna	87
4.5.1	Transmitting Antenna	87
4.5.2	Receiving Antenna	88
4.6	Arbitrarily Polarized Radiation—Single Port Antenna	90

4.7	Noise—Single Port Antenna	91
4.7.1	Receiver Noise—Single Port Antenna	92
4.7.2	Antenna Noise—Single Port Antenna	92
4.8	G/T —Single Port Antenna	94
4.9	Antenna Array Model	95
4.10	Directivity—Array	97
4.11	Arbitrarily Polarized Radiation—Array	99
4.12	Noise—Array	101
4.12.1	Receiver Noise—Array	101
4.12.2	Antenna Noise—Array	101
4.12.3	System Noise—Array	102
4.13	G/T —Array	103
4.14	Summary	103
5	Beamformer Weight Calculation	105
5.1	Survey of Beamforming Approaches	105
5.1.1	Conjugate Field Match	106
5.1.2	Maximum Gain and Maximum G/T	107
5.1.3	Other Considerations	107
5.2	Adaptive Beamforming	110
5.2.1	Measurable Quantities	111
5.2.2	Normalization of the Weight Vector	112
5.2.3	Maximum G/T	113
5.2.4	Maximum Directivity	114
5.2.5	Normalized Conjugate Match	114
5.3	Maximum G/T with Nulls	116
5.4	Scattering Matrix Model and Maximum Gain	118
5.4.1	Scattering Matrix Model Details	118
5.4.2	Conservation of Power	120
5.4.3	One Element at a Time Weighting	121
5.4.4	Maximum Gain Weighting	123
5.4.5	Comparison of Weightings	123
5.5	Summary	125
6	Instrumentation	127
6.1	Introduction	127
6.2	Overview	129
6.3	Reflectors	132
6.4	Focal Plane Array	132
6.4.1	Scattering Parameters	133
6.4.2	Distortion Products	135
6.4.3	Frequency Selection	139
6.4.4	FPA Noise Performance	140
6.4.5	Element Variability	143

CONTENTS

6.4.6	Element Selection	145
6.4.7	Pointing Offsets	145
6.5	Vertex Noise Source	147
6.5.1	Calibration Method	148
6.6	Receiver	149
6.7	Beamformer-Correlator	150
6.8	Instrument Control and Data Collection	152
6.8.1	Antenna Pointing	153
6.8.2	FPA Control and Monitoring	154
6.8.3	Data Processing	154
6.9	System Level Commissioning Tests	165
6.10	Element Gain Stability	166
6.11	Radio Sources	169
6.12	Summary	170
7	Measurement Results	173
7.1	Beamforming Experiments	173
7.2	Beamformer Weight Data Collection	175
7.2.1	Noise Covariance Matrix	175
7.2.2	Point Source Voltage Gain	176
7.3	Weight Calculation	177
7.4	Radiation Patterns	179
7.5	Aperture Field Distribution	179
7.6	Gain and Noise Temperature	181
7.6.1	FPA Losses and the Receiver Noise Temperature	185
7.6.2	Relative G and T Measures	187
7.6.3	Y-Factor From a Known Strength Source	187
7.6.4	Noise Temperature from Absorber Y-Factor	188
7.6.5	Aperture Efficiency	192
7.6.6	Noise Temperature From Extended HI Regions	192
7.7	Summary	196
8	Discussion of Results	197
8.1	Key Antenna Parameters	197
8.2	Radiation Patterns	198
8.2.1	Half-Power Beamwidth	198
8.2.2	Coma Aberration	199
8.2.3	Sidelobe Levels	200
8.3	Aperture Field Distribution	205
8.4	G/T Performance Predictions	206
8.4.1	Subefficiency Estimates	206
8.4.2	Enclosed Power	209
8.5	G/T Measurements	211
8.5.1	Relative Measures	211

8.5.2	On-off Source	212
8.5.3	Absorber Under the Feed	213
8.5.4	Aperture Efficiency	214
8.5.5	System Temperature from Extended HI Regions . . .	215
8.6	Comparison of Beamforming Weightings	215
8.6.1	The Normalized Conjugate Match and Maximum G/T	215
8.6.2	The Normalized Conjugate Match and Maximum Gain	216
8.7	Summary	217
9	Conclusion	221
9.1	Theoretical Treatment of FPAs	221
9.1.1	Enclosed Power Study of FPA Size Requirements . . .	221
9.1.2	FPA Model	222
9.1.3	Beamforming Weighting Algorithms	223
9.2	FPA Prototyping and Evaluation	224
9.2.1	Characterization of Dense FPAs Compared with Sin- gle Feeds and Discrete FPAs	226
9.2.2	Recommendations for FPA Characterization	229
9.3	FPA Systems	230
9.3.1	Calibration	230
9.3.2	Reflector Design	231
9.3.3	FPA Elements	231
9.3.4	Receiver Chains	232
9.4	Summary	233
A	Focal Plane Array Size Results	235
A.1	Focal Plane Power Plots	235
A.2	FPA Size	244
B	Mathematical Relationships	247
B.1	Matrix Formulation of the Overlap Integral	247
B.2	Spectral Decomposition Theorem	248
B.3	Square Root of a Normal Matrix	248
B.4	Hermitian Form Maximum	249
B.5	Rational Hermitian Form Maximum	251
B.6	Hermitian Form Maximum With Null Constraints	253
B.6.1	Gram–Schmidt Process	255
B.6.2	Stabilized Gram–Schmidt Process	255
B.6.3	Rational Hermitian Form with Null Constraints	256
B.6.4	Hermitian Inner Product Equality	257
C	Element Numbering Scheme	259

CONTENTS

D	Pointing for offset beams	261
D.1	Finding the Correct Offset	262
D.2	Mount Setting	262
E	Choice of Radio Sources for Antenna Measurements	265
E.1	Satellites	265
E.2	Moon	267
E.3	Stars and Galaxies	268
E.4	Source Availability	270
E.5	Extended HI Regions	270
E.6	Summary	270
F	Combining Uncertainties	273
G	Pattern Interpolation and Aperture Distribution	275
G.1	Pattern Cut Interpolation	275
G.2	Aperture Distribution from Far Field Pattern Cuts	276
G.3	Further work	277
H	Publications Related to this Thesis	281
H.1	Publications with Content from this Thesis	281
H.2	Supporting FPA Measurements	282
H.3	NTD Interferometer development	283
H.4	CSIRO's FPA work	283
H.5	Tenth Australian Symposium on Antennas, 2007	285
H.6	Workshop on Applications of Radio Science, 2008	291
	References	299

List of Figures

2.1	Discrete and dense FPAs.	16
2.2	Receiving dense FPA beamformer schematic.	16
2.3	Focal plane fields.	18
2.4	Satellite FPA.	20
2.5	Vivaldi array example.	29
2.6	CSIRO's chequerboard array.	30
3.1	Parabolic reflector geometry.	39
3.2	FPA size using ray tracing.	44
3.3	BDF definition.	46
3.4	Focal-plane field calculation.	48
3.5	Poynting theorem cylinder.	48
3.6	Tapered aperture diagram.	51
3.7	Focal-plane fields boresight.	54
3.8	Focal-plane power.	55
3.9	Focal-plane power.	56
3.10	Encircled power sum vs. radius.	57
3.11	FPA radius vs. F/D , 50%.	59
3.12	FPA radius vs. F/D , 79%.	59
3.13	FPA radius vs. scan angle.	60
3.14	Tapered and uniform focal-plane power.	61
3.15	Tapered and uniform integral focal-plane power vs. radius.	62
3.16	FPA radius vs. scan angle—tapered and uniform apertures.	63
3.17	Focal-plane power for two dish sizes	64
3.18	FPA radius vs. dish size.	64
3.19	FPA radius vs. angle—dish size independence.	65
3.20	Efficiency vs. FPA radius—blocked and unblocked aperture.	66
3.21	FPA radius function.	69
4.1	Receive antenna: standard reference plane.	82
4.2	Receiver antenna: reference plane before antenna losses.	82
4.3	Receiver power from uniform scene	83
4.4	Single port receiving antenna model.	86

LIST OF FIGURES

4.5	Receiving array model.	95
5.1	Scattering matrix model of the array	119
6.1	Two-dish prototype radiotelescope located in Sydney.	128
6.2	System diagram of the prototype radiotelescope.	130
6.3	NTD signal flow.	131
6.4	Focal plane array.	133
6.5	Vivaldi array radiation patterns.	134
6.6	THEA S-parameters.	134
6.7	Unmodified FPA spectrum.	136
6.8	Second-order distortion products.	136
6.9	Third-order distortion products.	136
6.10	Distortion products match—unmodified FPA.	137
6.11	FPA modification gain comparison.	137
6.12	FPA modification spectrum comparison.	138
6.13	Distortion products match—modified FPA.	138
6.14	FPA noise uncertainties.	142
6.15	FPA element noise variations.	144
6.16	Array numbering scheme.	146
6.17	Calibration system block diagram.	147
6.18	Maximum ADC levels.	151
6.19	Antenna pointing plot.	156
6.20	Delay between scans.	157
6.21	ADC levels.	157
6.22	ADC histograms.	158
6.23	RFI flagging: frequency vs. frame.	158
6.24	Mean spectrum and flagged frequencies.	159
6.25	Correlator output vs. frame number.	160
6.26	Single frame spectrum.	161
6.27	Single frequency vs. time.	161
6.28	Amplitude vs. frequency for each scan.	162
6.29	Scan amplitude vs. delay.	163
6.30	Scan amplitude vs. delay, expanded.	163
6.31	Delay and fringe rate correction.	164
6.32	Phase vs. frequency for each scan.	165
6.33	Element drifts—correlations.	167
6.34	Element port gain drifts.	168
7.1	FPA correlation matrix.	176
7.2	Element weight amplitudes.	177
7.3	Radiation pattern cuts.	180
7.4	2D Radiation patterns.	181
7.5	2D aperture fields—amplitude.	182

LIST OF FIGURES

7.6	2D aperture fields—phase.	182
7.7	2D aperture fields—phase.	183
7.8	2D aperture fields—phase.	184
7.9	Uncertainty contributions—system temperature on efficiency.	189
7.10	Uncertainty contributions—system temperature.	191
7.11	Uncertainty contributions—aperture efficiency.	193
7.12	Spectra from extended HI region.	194
7.13	Uncertainty contributions—extended HI region.	195
8.1	Aperture blockage.	201
8.2	Blockage far-field patterns.	201
8.3	NTD reflector construction.	204
8.4	Focal plane flux density for the NTD antenna.	209
9.1	Example of a horn feed pattern—Parkes 21 cm multibeam.	226
9.2	Y-factor Measurement of a prototype FPA.	228
A.1	Focal plane power, $D = 70.0$, $F/D = 0.3$ to 0.8 , $\theta_s = 00.00^\circ$	235
A.2	Focal plane power, $D = 70.0$, $F/D = 0.3$ to 0.8 , $\theta_s = 01.00^\circ$	236
A.3	Focal plane power, $D = 70.0$, $F/D = 0.3$ to 0.8 , $\theta_s = 02.00^\circ$	236
A.4	Focal plane power, $D = 70.0$, $F/D = 0.3$ to 0.8 , $\theta_s = 03.00^\circ$	237
A.5	Focal plane power, $D = 70.0$, $F/D = 0.3$ to 0.8 , $\theta_s = 04.00^\circ$	237
A.6	Focal plane power, $D = 70.0$, $F/D = 0.3$ to 0.8 , $\theta_s = 06.00^\circ$	238
A.7	Focal plane power, $D = 70.0$, $F/D = 0.3$ to 0.8 , $\theta_s = 08.00^\circ$	238
A.8	Focal plane power, $D = 70.0$, $F/D = 0.3$ to 0.8 , $\theta_s = 10.00^\circ$	239
A.9	Focal plane power, $D = 70.0$, $F/D = 0.3$ to 0.8 , $\theta_s = 15.00^\circ$	239
A.10	Focal plane power, $D = 70.0$, $F/D = 0.25, 1, 2$, $\theta_s = 00.00^\circ$	240
A.11	Focal plane power, $D = 70.0$, $F/D = 0.25, 1, 2$, $\theta_s = 01.00^\circ$	240
A.12	Focal plane power, $D = 70.0$, $F/D = 0.25, 1, 2$, $\theta_s = 02.00^\circ$	240
A.13	Focal plane power, $D = 70.0$, $F/D = 0.25, 1, 2$, $\theta_s = 03.00^\circ$	241
A.14	Focal plane power, $D = 70.0$, $F/D = 0.25, 1, 2$, $\theta_s = 04.00^\circ$	241
A.15	Focal plane power, $D = 70.0$, $F/D = 0.25, 1, 2$, $\theta_s = 06.00^\circ$	241
A.16	Focal plane power, $D = 70.0$, $F/D = 0.25, 1, 2$, $\theta_s = 08.00^\circ$	242
A.17	Focal plane power, $D = 70.0$, $F/D = 0.25, 1, 2$, $\theta_s = 10.00^\circ$	242
A.18	Focal plane power, $D = 70.0$, $F/D = 0.25, 1, 2$, $\theta_s = 15.00^\circ$	242
A.19	Focal plane power, tapered aperture, $D = 70.0$, $F/D = 0.4$	243
E.1	Spectral flux density of M87.	269
E.2	Radio source availability.	271
G.1	Aperture field generation test.	278

List of Tables

2.1	Radio astronomy FPA prototypes.	31
2.2	Specifications for ASKAP and Apertif.	33
3.1	FPA size parameters.	58
3.2	FPA-size-function coefficients.	68
3.3	FPA-size function—FPA radius and area errors.	68
3.4	Linear FPA-size-function coefficients.	70
3.5	FPA size reference results.	73
6.1	NTD interferometer specifications.	129
6.2	THEA tile scattering parameter data.	135
6.3	FPA parameters for calculating the noise temperature.	140
6.4	THEA tile noise budget and uncertainty contributions.	142
6.5	Receiver noise calculation comparison.	143
6.6	Pointing offsets.	147
6.7	Receiver gains and ADC levels	152
7.1	Observation dates.	174
7.2	Beamformer weights.	178
7.3	Observations from the radiation patterns.	179
7.4	Beamformed performance at 1200 MHz.	186
7.5	Extended HI region T_{sys} measurement.	195
8.1	Dish and FPA physical parameters.	198
8.2	Directivity from HPBW.	199
8.3	FPA Resolution.	205
8.4	Subefficiencies for a model feed.	207
8.5	Enclosed power for NTD FPA.	210
8.6	Limits and measured η_{ap} and $T_{\text{sys}}/\eta_{\text{ap}}$	210
A.1	FPA radii for $D = 70\lambda$	245
A.2	FPA radii—other dish sizes.	246
A.3	FPA size—tapered.	246
E.1	Celestial point sources.	269

LIST OF TABLES

E.2	Extended HI regions.	270
-----	------------------------------	-----

Abstract

Dense focal plane arrays (FPAs) are a key technology for a new generation of radiotelescopes. Their primary benefit is the rapid survey speed facilitated by the wide field-of-view provided by multiple beams. Recent advances have brought dense FPAs within reach of radio astronomy applications and a number of institutions have significant research programs in this field.

The size of the FPA required for a specified field-of-view is an important parameter for preliminary system design. In this thesis, this is examined by calculating the encircled power in the focal plane using physical optics. Design data is provided relating the FPA size, dish size, focal length and field-of-view for prime focus reflectors. A broad minimum in the FPA size for a dish focal length and diameter ratio (F/D) of 0.4 is found and over practical geometries, the FPA size is dependent on only F/D and the scan angle times dish diameter divided by wavelength. The utility of this design data is confirmed by comparing it with current FPA system designs.

In an operational radiotelescope, factors such as electronic gain drift and imperfect modelling result in the beamformer weights being best determined adaptively. Therefore a ‘black-box’ approach is used in this work. The theoretical basis for this approach is detailed; the determination of the gain (G) and system temperature (T) and the calculation of the maximum sensitivity (G/T) weighting are shown.

A prototype interferometer-radiotelescope, built at CSIRO’s Radiophysics Laboratory in Sydney, is used to demonstrate a suite of techniques for FPA beamforming and evaluation for this thesis. The method for calculating the maximum G/T weighting is demonstrated by applying the black-box model to parameters that are readily extracted from an appropriately equipped radiotelescope.

Declaration

I certify that the work in this thesis entitled *Beamforming and Evaluation of Focal Plane Arrays for Radio Astronomy* has not previously been submitted for a degree nor has it been submitted as part of requirements for a degree to any other university or institution other than Macquarie University.

I also certify that the thesis is an original piece of research and it has been written by me. Any help and assistance that I have received in my research work and the preparation of the thesis itself have been appropriately acknowledged.

In addition, I certify that all information sources and literature used are indicated in the thesis.

Signed:

Date: 16 August 2011

Douglas Brian Hayman
Student ID: 40427773

Acknowledgements

It is a pleasure to thank those who have supported me and without whom this thesis would not have been possible. Peter Hall, John Kot, Trevor Bird and Marianna Ivashina were very helpful in establishing the topic. My supervisors have been very helpful and supportive over the somewhat longer than planned course. In particular Trevor Bird has been very patient guiding the project and knocking my writing into shape. Karu Esselle provided excellent support from the university's perspective and Peter Hall from the radio astronomy perspective.

CSIRO generously supported me to undertake this work part time at the Radiophysics Laboratory, where I conducted my work—a place where world class expertise is generously shared. Specific contributions are mentioned in the relevant chapters but I would like to mention John O'Sullivan, Mike Kesteven and in particular Stuart Hay who has been very supportive as my line manager and has always given very precise advice on any technical issues.

CSIRO also provided the prototype radiotelescope used for the experimental component of this work. A large team developed the instrument and I received very responsive support, particularly from Tim Cornwell, Jayasri Joseph, Maxim Voronkov, Mike Kesteven and Chris Cantrall. Wim van Cappellen led the work at ASTRON to modify a THEA tile for use as an FPA. It proved worth the delay to starting the experimental work to have the privilege of exclusive access to this instrument.

My family has been wonderful—Sarah, Peter and Annie have accepted less of my time and have given me plenty of encouragement and moral support. I am greatly indebted to wife, Roz, who has supported me in countless ways and endured through challenges to the health of us both. DJ has kept

Acknowledgements

me company and cheered me on. Thanks also go to my parents, David and Robynne for proof-reading the thesis.

Many open source and free software packages were used during this work and I would like to acknowledge the generosity of the developers. Some of these are \LaTeX , which was used to typeset this thesis, JabRef for reference management, Python for telescope operation and Ticsra's student version of GRASP for antenna modelling. The data storage for the prototype radiotelescope was based on the Common Astronomy Software Applications (CASA) software.

Notation, Symbols and Abbreviations

This section lists many of the mathematical notations, symbols and abbreviations used in this thesis. The sections where the symbols and abbreviations are defined is listed in the table. The lists are not exhaustive, but cover most of the symbols and abbreviations which are used in more than one section or chapter.

Mathematical Notation

- a** : (bold font) column vector, used for signals and weights for the separate elements in the array.
- \vec{a} : row vector giving a position or direction. Usually expressed as in Cartesian (x, y, z) or spherical (θ, ϕ, r) coordinates.
- a_n : n^{th} element of vector **a**.
- $[\mathbf{A}]_{mn}$: m^{th} row and n^{th} column element of matrix **A**.
- \mathbf{A}^T : transpose of a matrix or vector.
- \mathbf{A}^H : conjugate transpose (Hermitian).
- \mathbf{A}^* : conjugate.
- I** : identity matrix.
- $\|\mathbf{a}\|$: Euclidean norm where $\|\mathbf{a}\| = \sqrt{\mathbf{a}^H \mathbf{a}}$.
- $|z|$: absolute value of a complex or real number.
- $\iint_{\Omega} d\Omega$: integral over the sphere (4π sr),

$$\iint_{\Omega} F d\Omega = \int_{2\pi} \int_{\pi} F(\theta, \phi) \sin \theta d\theta d\phi.$$

- \hat{a} : unit direction vector.
- $\langle a \rangle$: expected value of a random variable a .

Symbols

Symbol	Definition	Section
$A_e(\theta, \phi)$: antenna effective area	2.2
B	: radio brightness	2.1.2
$\mathbf{C}_{T_{\text{rx}}}$: covariance matrix of the port receiver temperatures referred to the input	4.12.1
$\mathbf{C}_{T_{\text{scene}}}$: matrix of radiation pattern overlap integrals weighted by the scene temperature	4.12.2
$\mathbf{C}_{T_{\text{sys}}}$: covariance matrix of the port system temperatures	4.12.1
$\mathbf{C}_{T_{\text{sys}},u}$: noise covariance matrix scaled for the weight vector \mathbf{u}	5.2.1
D	: dish diameter or antenna directivity	3.3, 2.2
$D(\theta, \phi)$: antenna directivity	2.2
D_p	: antenna directivity in the \hat{p} polarization	4.19
$\vec{E}(t)$: electric field—complex phasor representation	2.1.2
$\vec{e}(\theta, \phi)$: field radiation pattern	4.5
\vec{e}_i	: field radiation pattern of the i^{th} array element	4.9
F	: focal length	3.3
f	: frequency	
Δf	: bandwidth (Hz)	
$G(\theta, \phi)$: antenna gain	2.2
H	: electronic power gain	4.2
h_i	: electronic voltage gain of the i^{th} array element	4.9
$\vec{H}(t)$: magnetic field—complex phasor representation	2.1.2
k	: wave number $k = 2\pi/\lambda$ ($\text{rad} \cdot \text{m}^{-1}$)	
k_B	: the Boltzmann constant, $1.380\,6504(24) \times 10^{-23} \text{ J} \cdot \text{K}^{-1}$	
P_{rx}	: power at the receiver output	4.2
\mathbb{P}	: spectral power density	2.1.2
\hat{p}'	: polarization unit vector matched to the antenna reception	4.3
\hat{p}	: co-polarization unit vector	2.1.3
\hat{q}'	: cross-polarization unit vector with respect to \hat{p}'	4.3
\hat{q}	: cross-polarization unit vector	2.1.3
R_{Airy}	: FPA radius of an Airy disk	3.5.2
$R_{\text{Airy,BDF0}}$: FPA radius from an Airy disk and beam deviation factor	3.5.2
R_{BDF0}	: FPA radius from beam deviation factor	3.5.2
R_{RT}	: FPA radius from ray tracing model	3.5.1
S	: power flux density	2.1.2
\mathbb{S}	: spectral power flux density	2.1.2

Symbol	Definition	Section
\vec{S}	: Poynting vector	3.6
T_b	: brightness temperature	2.1.2
T_{ant}	: equivalent antenna noise temperature	4.7
T_{rx}	: equivalent receiver noise temperature referred to the radiation port	4.2, 7.6.1
T'_{rx}	: equivalent receiver noise temperature referred to the receiver input	6.4.4, 7.6.1
T_{scene}	: equivalent black body temperature	4.2
T_{sys}	: equivalent system noise temperature	2.2
Y_{abs}	: Y-factor from absorber measurement	7.6.4, 8.5.3
Y_{src}	: Y-factor from measurement of a radio source in the sky	4.8, 7.6.3, 8.5.2
\mathbf{u}	: beamformer weighting vector	4.9, 5.2.1
\mathbf{w}	: beamformer weighting vector incorporating the electronic voltage gains of the elements	4.9, 5.2.1
η_0	: impedance of free space, $\eta_0 = 376.730\,313\,461\,\Omega$ (exact)	
η_{ap}	: aperture efficiency	2.2
η_{blockage}	: blockage efficiency	3.9.2
η_{cr}	: cross polarization efficiency	3.5
η_{enc}	: encircles power efficiency	3.5
η_{ph}	: phase efficiency—due to deviations from a flat phase	3.5
η_{rad}	: radiation efficiency	2.2
η_{sky}	: fraction of the antenna power pattern that is directed toward the sky	7.6.4.
η_{spill}	: feed spillover efficiency	3.5
η_{taper}	: taper efficiency	3.5
θ_c	: paraboloid opening semi-angle	3.3
θ_s	: scan angle	3.3
θ_{HPBW}	: half power beamwidth	3.3
λ	: free space wavelength.	

Abbreviations

Abbreviation	Definition	Section
ADC	: analogue to digital converter	
AIPS++	: Astronomical Image Processing System	6.8
APERTIF	: Aperture Tile in Focus	2.6.3
ASKAP	: Australian Square Kilometre Array Pathfinder	2.6.4
ASTRON	: Netherlands Institute for Radio Astronomy	2.6
ATNF	: Australia Telescope National Facility	E.3
BDF	: beam deviation factor	3.5.2
BYU	: Brigham Young University, Provo, Utah	2.6.3
CASS	: CSIRO (division of) Astronomy and Space Science	6.1
CSIRO	: Commonwealth Scientific and Industrial Research Organisation	
DIGESTIF	: DIGital Early Stage Tile In Focus	2.6.3
DRAO	: Dominion Radio Astrophysical Observatory, Penticton, Canada	2.6.3
FARADAY	: Focal-plane Arrays for Radio Astronomy; Design, Access and Yield	2.6.3
FFT	: fast Fourier transform	6.8.3, G.2
FoV	: field-of-view	3.3
FPA	: focal plane array	2.2, 2.3.1
GPS	: Global Positioning System	E.1
GRASP	: General Reflector Antenna Software Package	3.7
HI	: Hydrogen I line	7.6.6
HPBW	: half power beamwidth	3.3
IEEE	: Institute of Electrical and Electronics Engineers	
LNA	: low noise amplifier	6.4.4
NCM	: normalized conjugate match	5.2.5
NRAO	: National Radio Astronomy Observatory, USA	2.6.3
NTD	: New Technology Demonstrator	6.2
PCB	: printed circuit board	
PHAD	: Phased-Array feed Demonstrator	2.6.3
PO	: Physical optics	3.2
PTF	: Parkes Testbed Facility	2.6.3
RFI	: radio frequency interference	6.4.2
RMS	: root mean squared	
RSS	: root sum of squares	
SKA	: Square Kilometre Array	2.6.1
SLL	: sidelobe level	7.4, 8.2.3
SNR	: signal to noise ratio	
THEA	: Thousand Element Array	6.4
TTL	: transistor-transistor logic	
WSRT	: Westerbork Synthesis Radio Telescope	2.6.4

Chapter 1

Introduction

The exacting requirements of radio astronomy are a major driver of antenna technology. A wide variety of antenna technologies have been used in radiotelescopes over the years, primarily various types of arrays and parabolic dishes [1]. This thesis concerns the development of *dense focal-plane arrays* (FPAs), a reflector feed technology new to radio astronomy.

An FPA replaces a conventional single feed system at the focus of a dish with an array, equivalent to turning a single-pixel camera into a multi-pixel camera. FPAs made up of horn elements have been used in radio astronomy successfully for some time usually as one ‘pixel’ per horn. The resulting image has gaps between the pixels which can be filled by changing the pointing direction of the antenna. The signals from dense FPAs, on the other hand, can be combined to fill these gaps, greatly increasing the total area of sky that can be imaged, the field-of-view (FoV) with one antenna pointing direction only.

A key motivator for FPA development is the Square Kilometre Array (SKA), a proposed radiotelescope that will be orders of magnitude more powerful than the best current instruments. A number of the approaches to building this instrument include dense FPAs and a number of major research projects, including the activity at CSIRO,¹ into this technology are underway.

¹Commonwealth Scientific and Industrial Research Organisation.

1.1 Thesis Outline

The objective of this project is to investigate and demonstrate beamforming of an FPA in the context of radiotelescopes.

In Chapter 2 the signals and figures of merit relevant to radiotelescopes is introduced. The concepts and definitions established here are used in the later chapters. The latter part of the chapter introduces the field of FPAs, their application to radio astronomy and includes a review of current research.

Chapter 3 deals with rules of thumb for FPA design and performance. The element spacing and the size of an FPA required to achieve a given field-of-view is addressed. The data from extensive modelling is reduced to a formula that can be applied to FPA design. This formula is compared with performance data from specific instruments. A selection of results from the modelling is provided in Appendix A.

Chapter 4 establishes a model for analysing FPA performance using a ‘black-box’ approach. This approach is adopted as the measurements in this project are made on an actual radiotelescope consisting of components that had not been fully characterised before it was assembled. Chapter 5 presents the method that was used to combine the signals (i.e. to beamform) from the FPA elements to obtain the maximum sensitivity (gain to equivalent noise temperature ratio). Appendix B provides mathematical details and proofs supporting Chapters 4 and 5.

Chapters 6, 7 and 8 comprise the experimental section. The two dish interferometer that was used in this project is described in Chapter 6. This includes a number of checks that can be made on an FPA system to monitor its performance and operation (‘health’). Chapter 7 presents a selection of the measurement results which are discussed in Chapter 8. The formulation for pointing the antenna for beams that are offset from the antenna axis is shown in Appendix D. The selection of celestial radio sources that were used for the measurements are discussed in Appendix E. The method used for combining measurement uncertainties is given in Appendix F and a technique for analysing the antenna radiation patterns is shown in Appendix G.

Conclusions from the preceding material are drawn in Chapter 9.

1.2 Project Context and Time Frame

The work in this thesis was conducted over a period when research in this field was accelerating. CSIRO, where the author was located, was establishing where it might contribute to new FPA developments. In a wider context CSIRO was also establishing concepts for inclusion in an Australian SKA prototype. As a consequence, the project is aligned ultimately with CSIRO's FPA research program. The FPA size rule-of-thumb work was conducted at a time (2004) when there was interest in estimating FPA system costs for comparison with other potential technologies for the SKA.

When the CSIRO's test-bed for investigating FPA systems the *NTD Interferometer* fortuitously became available, it was used for the experimental aspect of this project. This system had been rapidly deployed and the author invested considerable effort into improving its reliability and repeatability. This resulted in a change of emphasis from investigating beamforming techniques to demonstrating basic beamforming and FPA system evaluation techniques. The completion of the thesis was delayed by various changes of direction, personal and family issues and CSIRO commitments.

1.3 Distinct Contributions of this Thesis

The individual contributions of this thesis are grouped according to their presentation in the thesis. Appendix H lists the author's publications related to this thesis.

Encircled Power

By calculating the encircled power reaching the focal plane for a wide range of scan angles, reflector sizes and focal lengths, the relationship between these parameters and the required focal plane array (FPA) size for a given field-of-view was shown. The results were reduced to a semi-empirical closed form-formula, substantially more accurate than others in use (Chapter 3).

Black-Box Approach to Beamforming Active Receiving Arrays

A theory for array beamforming for an active receiving array where access to internal ports is unavailable is described. It is argued that the appropriate reference plane is the radiation port, i.e. antenna losses are assigned to the

receiver side of the plane as they are indistinguishable from the receiver noise and gain. An important consequence is the antenna gain becomes equivalent to the directivity (Chapter 4). This contribution draws together existing concepts and presents them in a clear way for this application.

Focal Plane Array on a Prototype Radiotelescope

Beamforming and evaluation techniques are demonstrated on a prototype radiotelescope equipped with a focal plane array.

- As one of only six such prototypes known to the author,² the results obtained are considered important to the antenna community [7]. The other test-beds differ sufficiently in approach and design for the demonstration of this instrument to contribute new knowledge to the radio astronomy FPA community. (See Section 2.6.3).
- Comprehensive results from a real-time digital beamforming system are reported, used for the first time in this context. While the initial results for a conjugate match on the instrument were obtained by Tim Cornwell [8], the author developed the techniques for the maximum gain on equivalent noise temperature (G/T) weighting and the *normalized conjugate match weighting*, an approximation to the maximum gain [7].
- The maximum G/T weighting using the noise covariance matrix is demonstrated. A similar approach was published by Jeffs et al. in October 2008 [9] but we published the first results with an interferometer [10] at the same time as Ivashina et al. [11] (Chapters 7, 8).
- An approximation to the maximum gain weighting is demonstrated and the nature of the approximation elucidated (Sections 5.1.2 and 5.1.1).
- The correlation of the signal from a calibration source on the reflector surface against the element signals to compensate for drift in the amplitude and phase of the element gains is demonstrated for the first time. Procedures for its use are developed and demonstrated—proposed in 2008 [12] and demonstrated in 2009 [10] (Section 6.5).

²Fisher et al. at NRAO [2]; FARADAY and APERTIF at ASTRON [3, 4]; Warnick et al. at BYU/NRAO [5]; PHAD at DRAO [6].

- Procedures for generating beamforming weights using only signals typically available from an interferometer radiotelescope are developed and demonstrated (Chapters 5, 7 and 8).
- G/T and noise temperature measurement techniques were demonstrated, some of which required modification from their conventional use with single feed antennas (Chapters 7, 8). Comprehensive uncertainty analyses are shown for these measurements.

1.4 Contributions of Others

Significant contributions to this project by others than the author and supervisors are acknowledged below as well as in the relevant sections of the thesis.

The two dish interferometer system was developed primarily by authors of [12]. The antenna control system was developed by Mike Kesteven. The beamformer-correlator firmware was developed by Jayasri Joseph and the master control and data storage system by Tim Cornwell and Maxim Voronkov. The investigation into the distortion products in the FPA is the author's work. The FPA modifications were designed by Alex Grancea and installed by Chris Cantrall. Carol Wilson assisted in identifying some of the radio frequency interferer (RFI) transmitters (Chapter 6).

The vertex antennas and amplified noise diodes were selected by the author, the control electronics and housing were assembled by Chris Cantrall, the software integration by Maxim Voronkov and it was installed by the Author. The concept of using correlation against a noise source is thought to be due to John Bunton.

The concern over change in radiation patterns due to LNA impedance change was raised by John O'Sullivan (Section 6.5.1).

Jim Caswell provided advice on radio sources (Appendix E).

Mike Kesteven demonstrated the use of using HI regions for system noise calculation with a single element to the author before the author repeated the technique using beamforming (Chapter 7).

Marianna Ivashina and Bert Woestenburg from ASTRON³ assisted in the antenna noise temperature analysis from the *absorber under the feed*

³Netherlands Institute for Radio Astronomy

measurement (Section 7.6.4) and provided data on the FPA, the THEA tile (Section 6.4.4).

Chapter 2

Focal Plane Arrays and Radio Astronomy

In this chapter the field of focal plane arrays (FPAs) for radio astronomy is introduced. Radio astronomy is briefly introduced from the antenna designer's point of view, leading to the relevant figures of merit for radiotelescopes. Focal plane arrays are then introduced including their development in non-radio-astronomy applications. The application of focal plane arrays to radio astronomy is then covered with a discussion of recent developments.

2.1 Radio Astronomy Signals

Astronomy is largely limited by two windows in the atmosphere's opacity—optical and radio. These windows provide complementary views of the objects in the universe [1]. The radio-wave emission from these celestial objects is classified into two main groups—thermal and non-thermal. The information in these *signals* is their intensity and its distribution in space and variation in time. Being generated from a large number of random processes they almost all have the form of Gaussian noise [1, 13]. This is in common with passive imaging and in contrast to most communications signals, although wide band communications signals may have similar statistical behaviour.

Thermal emissions are produced by the random motion of the particles in the object and can be represented by an equivalent temperature. The transparency of the object to radio-waves and its composition can affect

the emission intensity with respect to frequency. For instance ionized gas, neutral gas and solids all behave differently [14].

Non-thermal emission mechanisms can be more efficient and include plasma oscillations and synchrotron emission from relativistic electrons [14]. These emissions are usually at least partially linearly or circularly polarized.

Celestial radio emissions can vary smoothly with frequency referred to as continuum radiation or occur in narrow bands referred to as spectral lines. The sensitivity of continuum depends on the instantaneous bandwidth of the radiotelescope and so benefits from wide bandwidths. The spectral lines relevant to radio emission are due to resonances in molecules and atoms. Although these are narrow band at their origin, they can be Doppler shifted to very different frequencies and so wide bandwidths can be important for spectral-line observations as well.

The polarization of celestial radio emissions reveals important information about the nature of the source. The view of polarization in the astronomy community is quite different from the view in the communications antenna community—this is discussed further in Section 2.1.3.

Another consideration for the antenna engineer is the time variation of astronomical signals. Most sources are stable on periods of at least months if not decades. As a consequence observations are often conducted over periods of many hours and so the stability of radiotelescope performance over these time scales becomes important. Notable exceptions to the relatively static nature of the radio sky include pulsars and *transients*. Pulsars are spinning neutron stars with emission pulsing at periods of a few milliseconds up to eight seconds [15]. Relatively short duration non-periodic emissions are referred to as *transients* in radio astronomy. This is a relatively unexplored but expanding field as most radiotelescope observations attain their sensitivity by using data collected over long periods. Two of the known sources of transients are gamma ray bursts and radio supernovae [16, 17].

A description of typical radio astronomy signals is given here for two purposes: firstly the observation of the intensity and spectra of these signals is the object of the target application of FPAs, and secondly, celestial radio sources are used in the evaluation of radiotelescopes.

2.1.1 Quasi-Monochromatic Plane Wave Approximation

The analysis of radio astronomy signals is simplified by approximating them as quasi-monochromatic plane waves. The quasi-monochromatic assumption holds for the FPA systems under consideration here because they process the signal in sufficiently narrow sub-bands. For instance, they may have a wide tuneable bandwidth of 2:1 or more and a moderate instantaneous bandwidth of 20 to 30% but this is processed into sub-bands that are typically 1% or less of the central frequency, referred to here as the *processing bandwidth*. The great distance between celestial sources and the observer on the earth readily allows the assumption that they are received as uniform plane waves.

In the standard approach, the field of a quasi-monochromatic plane wave is represented by the time varying signal [18]

$$\mathcal{F}(t) = F(t)e^{j(2\pi/\lambda)t} \quad (2.1)$$

where $\mathcal{F}(t)$ is a complex, band-limited, covariance-stationary, ergodic stochastic process. $F(t)$ is the modulation on a carrier sinusoid at wavelength λ .

$F(t)$ is then a phasor representation of the field—electric ($\text{V} \cdot \text{m}^{-1}$) or magnetic ($\text{A} \cdot \text{m}^{-1}$). The narrow band condition leads to $F(t)$ varying far more slowly than the centre frequency. For a strictly monochromatic signal it is constant.

The assumption that the signals are ergodic on the timescales of interest allows the expected value (of random value x denoted $\langle x \rangle$) to be measured using a correlator:

$$\langle x(t) \rangle = \lim_{T \rightarrow \infty} \frac{1}{T} \int_T x(t) dt \approx \frac{1}{\tau} \int_\tau x(t) dt \quad (2.2)$$

where τ is the integration period. It ranges from 1 to 200s in the experimental work that is described in Chapters 6 and 7.

The signal $x(t)$ in a correlator is formed from the product of two signals proportional to voltage $x(t) = v_1^*(t)v_2(t)$. When v_1 and v_2 are the same function v , the mean power in the signal is proportional to

$$\langle |v(t)|^2 \rangle = \langle v^*(t)v(t) \rangle. \quad (2.3)$$

This also applies to the power in an electric field.

Correlation of fields and signals is important for the development of the FPA model in Chapter 4 and beamforming in Chapter 5.

2.1.2 Measures of Source Strength

The description of source strength in radio astronomy falls into two categories: (1) compact sources where the angular extent is a small fraction of the receiving system's beamwidth; and (2) extended sources where the angular extent is at least a few beamwidths across. The beamwidth may be that of a single antenna or of an interferometer depending on the telescope and the same source can be compact for the single antenna and extended for the interferometer.

The IEEE definitions will be used for clarity in the terms used to represent radiation [19]:

power flux density: The time average of the Poynting vector. This is sometimes called the *power density*. The units are $\text{W} \cdot \text{m}^{-2}$. The symbol used here is S .

spectral power density: Power per unit bandwidth at a port or flowing in a transmission line or waveguide. The units are $\text{W} \cdot \text{Hz}^{-1}$. The symbol used here is \mathbb{P} .

spectral power flux density: The power flux density per unit bandwidth. The units are $\text{W} \cdot \text{m}^{-2} \cdot \text{Hz}^{-1}$ or Janskys (Jy) i.e. $10^{-26} \text{W} \cdot \text{m}^{-2} \cdot \text{Hz}^{-1}$. The symbol used here is \mathbb{S} .

When the receiver is in the far field of the source, the magnetic field is perpendicular to the electric field and the *power flux density* is

$$S = \left\langle \left| \vec{E}(t) \times \vec{H}(t) \right| \right\rangle = \frac{\left\langle \vec{E}^*(t) \cdot \vec{E}(t) \right\rangle}{2\eta_0} \quad (\text{W} \cdot \text{m}^{-2}) \quad (2.4)$$

where η_0 is the impedance of free space and $\vec{E}(t)$ is the complex phasor vector representation¹ of the electric field at the antenna and $\vec{H}(t)$ the magnetic field.

¹Two vector notations are used for convenience. Quantities in three dimensional physical space are represented by row vectors and denoted by the over arrow \vec{a} . Signals and weights for the separate elements in the array are represented by column vectors, and are denoted by bold font \mathbf{a} . Similar approaches are used by others, for example Warnick and Jeffs [20].

For sources with bandwidths much less than the processing bandwidth Δf , e.g. a satellite beacon, (2.4) can be used directly.

The power flux density is related to the spectral power flux density \mathbb{S} by

$$S = \int_{\Delta f} \mathbb{S} df \approx \Delta f \mathbb{S} \quad (2.5)$$

where Δf is the processing bandwidth. The spectral power flux density is an appropriate measure of strength for compact sources with spectra broader than the processing bandwidth and is given by

$$\mathbb{S} = \frac{\langle \vec{E}^*(t) \cdot \vec{E}(t) \rangle}{2\eta_0 \Delta f} \quad (\text{W} \cdot \text{m}^{-2} \cdot \text{Hz}^{-1}). \quad (2.6)$$

To evaluate the antenna's response to an extended source, the response to the incident field distribution is integrated over the extent of the source or more generally a sphere. Let $\vec{E}_\Omega(\theta, \phi)d\Omega$ be the 'incident analytic field from sources which subtend a solid angle $d\Omega$ ' [21, p115]. The units of \vec{E}_Ω are $\text{V} \cdot \text{m}^{-1} \cdot \text{sr}^{-1}$.

The power incident from extended sources is best represented by the spectral power flux density per solid angle or *radio brightness* [21, eqn. (4.72)],

$$B(\theta, \phi) = \frac{\langle \vec{E}_\Omega^*(t) \cdot \vec{E}_\Omega(t) \rangle}{2\eta_0 \Delta f} = \frac{\delta \mathbb{S}}{\delta \Omega} \quad (\text{W} \cdot \text{m}^{-2} \cdot \text{Hz}^{-1} \cdot \text{sr}^{-1}). \quad (2.7)$$

Using the Rayleigh–Jeans approximation for black body radiation, the *brightness temperature*, an equivalent black body temperature, can be assigned to the source:

$$T_b = \frac{B\lambda^2}{2k_B} = \frac{\lambda^2}{4k_B\eta_0\Delta f} \langle \vec{E}_\Omega^*(t) \cdot \vec{E}_\Omega(t) \rangle \quad (\text{K}). \quad (2.8)$$

2.1.3 Polarization

As celestial radio emissions are generally produced by the aggregate of many random processes and as in most cases, there is nothing aligning the field, no particular polarization is favoured. That is the emissions are usually *unpolarized*. Non-thermal sources are at least weakly polarized [22], however, and the degree to which a particular polarization, linear or circular, is

favoured reveals information about the source or the medium through which the emissions have passed.

In contrast, communication signals are generally transmitted from an antenna and so are completely polarized as discussed in Section 4.3. The different nature of the signals encountered leads to the astronomy and communications communities having different views of polarization. Astronomers use the Stokes parameters, historically from the optical domain [23], whereas communication antennas engineers commonly use the polarization ellipse or derivations from it [24]. In the field of communication antennas, the figure of merit to be minimized is usually the degree of *cross-polarization* and hence interference from sources other than the desired transmission. In the field of radio astronomy, the figure of merit is referred to as the degree of *instrumental polarization*, indicating degree to which an unpolarized source appears polarized [25]. Consequently for any definition of two orthogonal polarizations, the signals received in those two polarizations are equal in power and uncorrelated.

In this thesis two unit vectors, \hat{p} and \hat{q} , are used to define the polarization of the field. When used to describe the response of an antenna, they are defined as a function of the pointing direction (θ, ϕ) from the antenna bore-sight. Their choice is open as long as they are orthogonal and perpendicular to the radial direction from the antenna. The vectors \hat{p} and \hat{q} are complex for the general case of elliptical polarization. Common definitions are Ludwig's linear definitions where they are real [26] and circular polarization [27, p51]. Linear and circular polarization characterization can then be converted to and from Stokes parameters [13, p97ff], [21, p112].

Let the desired dominant or co-polarized response for a specific port or array weighting be defined by \hat{p} . Design constraints and imperfections in the antenna lead to the orthogonal cross-polarization, \hat{q} , also being received to some degree in general.

The electric field discussed in Section 2.1.2 can be written as the sum of two components defined by the polarization vectors: $E_p(t) = \vec{E}(t) \cdot \hat{p}$ and $E_q(t) = \vec{E}(t) \cdot \hat{q}$ and so

$$\vec{E}(t) = E_p(t) \hat{p} + E_q(t) \hat{q}. \quad (2.9)$$

The total power flux density is then (with the t dependency implicit)

$$\begin{aligned}
 S &= \frac{\langle \vec{E}^* \cdot \vec{E} \rangle}{2\eta_0} \\
 &= \frac{\langle E_p^* E_p \rangle + \langle E_q^* E_q \rangle}{2\eta_0} \\
 &= S_p + S_q.
 \end{aligned} \tag{2.10}$$

The polarization components of the other measures of source strength, spectral power flux density \mathbb{S} , radio brightness B and brightness temperature T_b can be similarly identified.

Unpolarized Radiation

For unpolarized radiation the field components for any choice of \hat{p} and \hat{q} are uncorrelated, that is

$$\langle E_p^* E_q \rangle = \langle E_q^* E_p \rangle = 0 \tag{2.11}$$

and from (2.6) and (2.9)

$$\langle E_p^* E_p \rangle = \langle E_q^* E_q \rangle = \eta_0 \Delta f \mathbb{S}. \tag{2.12}$$

2.2 Figures of Merit

The relevant figures of merit for a radiotelescope are the parameters that affect the quality of the data it produces. These data are most commonly maps of the celestial sphere, either bands of continuum radiation or spectral lines. The parameters identified by Napier [28] are aperture efficiency, pointing accuracy, beam circularity, sidelobe level, polarization purity and noise temperature. While the following discussion focuses on aperture efficiency or gain, G , and the system noise temperature, the figures of merit are all kept in mind and a number of them may be controlled with specific beamforming weightings as discussed in Section 5.1.3.

The equivalent system noise temperature, T_{sys} , is measure of the noise generated by the receiver and antenna. The choice of reference plane for these definitions is discussed in Section 4.2. The sensitivity of a radiotelescope is closely related to the ratio G/T_{sys} , abbreviated to G/T here. The impact of the each antenna's G/T in a synthesis array is addressed in some detail

by Crane and Napier [29] with the conclusion that the image sensitivity is proportional to the G/T . The sensitivity of a total power telescope (e.g. a single dish) similarly is proportional to G/T [1, p233ff].

Many astronomical investigations involve mapping large regions of the sky, known as surveys [16]. The depth or sensitivity of the survey depends on the duration of integration on each pointing and the sensitivity of the telescope. Therefore to map a given region to a given sensitivity, the time required is a function of the field-of-view (FoV) of the telescope and its sensitivity or G/T . Johnston and Gray show that the survey speed (SS) for both single antennas and synthesis arrays is proportional to the FoV and the sensitivity squared [30],

$$SS \propto \text{FoV} (G/T)^2. \quad (2.13)$$

In other applications such as radar, communications and passive sensing, gain and G/T are also key figures of merit.

In addition to the more universal figures of merit discussed below, there have been a number of recent contributions to the literature focussing on figures of merit to enhance the understanding and analysis of low noise arrays and in particular focal plane arrays [20,31–33]. These are particularly valuable in separating sources of noise and losses incurred due to mutual coupling.

2.2.1 Figures of Merit Related to Gain

Common figures of merit for antennas related to the gain, both in a given direction (θ, ϕ) or the direction of maximum gain include (from the IEEE standard [34]):

Effective Area

$$A_e(\theta, \phi) = \frac{\lambda^2}{4\pi} G(\theta, \phi) \quad (\text{m}^2) \quad (2.14)$$

This shows that gain is closely related to the physical dimensions of an aperture antenna and the relationship is independent of frequency.

Aperture efficiency

$$\eta_{\text{ap}} = A_e / A_{\text{aperture}} \quad (2.15)$$

The aperture efficiency is the ratio of effective area and the physical antenna aperture area projected onto the pointing direction A_{aperture} .

For a dish, the aperture area is taken as the area of the dish projected onto the given direction.

Directivity The directivity in transmit is the radiation intensity in a given direction divided by the average radiation intensity over all directions. It is related to the gain by the radiation efficiency:

$$D(\theta, \phi) = \eta_{\text{rad}} G(\theta, \phi) \quad (2.16)$$

In an active antenna, such an array fitted with amplifiers on each element, directivity is more readily defined than gain as discussed in Section 4.2.

2.2.2 Figures of Merit Related to G/T

Astronomers commonly use two figures of merit related to the G/T . The first, the ratio of effective area and system temperature can simplify the comparison of radiotelescopes and the second, the ratio of system temperature and aperture efficiency, can simplify the comparison of feed systems.

Effective Area over System Temperature

$$\frac{A_e}{T_{\text{sys}}} = \frac{\lambda^2}{4\pi} G/T_{\text{sys}} \quad (\text{m}^2 \cdot \text{K}^{-1}) \quad (2.17)$$

This figure of merit removes the frequency dependence from the G/T and so is particularly useful for wide band aperture antennas such as the SKA [35]. It can be related to the weakest detectable source for both single dish total power radiotelescopes and synthesis arrays [1, Ch. 8], [29].

System Temperature over aperture efficiency

$$\frac{T_{\text{sys}}}{\eta_{\text{ap}}} = \frac{4\pi A_{\text{aperture}}}{\lambda^2} \frac{1}{G/T_{\text{sys}}} \quad (\text{K}) \quad (2.18)$$

The use of aperture efficiency makes this figure of merit independent of the reflector size (blockage issues aside) and so is convenient for feed evaluation. The components included in the temperature can be chosen according to what is being considered. With active feeds where there may be no well defined antenna/receiver port the total system temperature is often the most relevant term.

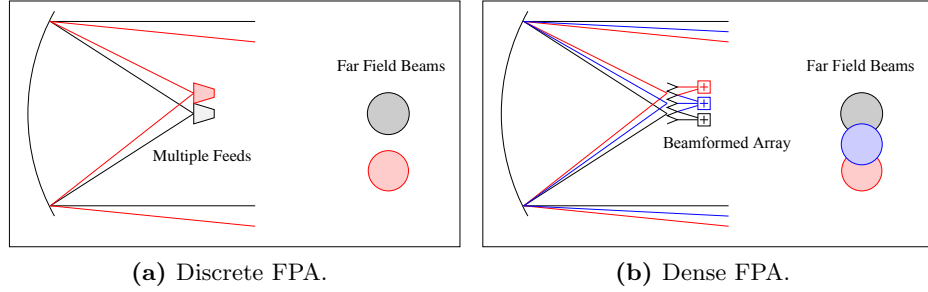


Figure 2.1 – Schematic view of discrete and dense FPAs.

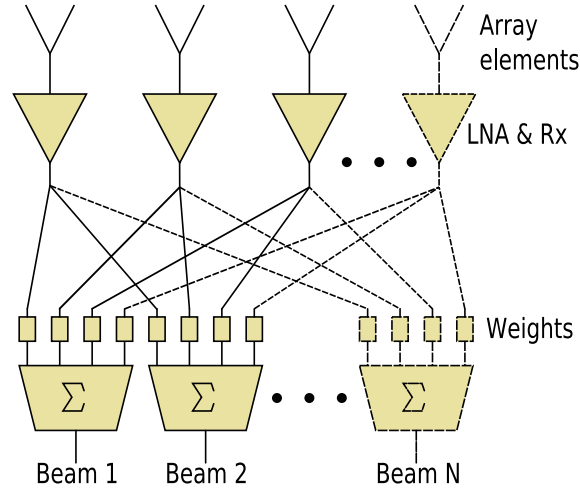


Figure 2.2 – Receiving dense FPA beamformer schematic. The signals from each element can be split to feed a number of beamformers. The beamformers form the weighted sum of the signals. The signal flow and components can be reversed for transmitting arrays.

2.3 Focal Plane Array Concepts

2.3.1 Focal Plane Array Nomenclature

Dense and Discrete Focal Plane Array Nomenclature

This thesis is concerned with focal plane arrays (FPAs) from which beams are formed by combining the signals from a number of the array elements as shown in Figs. 2.1b and 2.2. The expression *focal plane array* also applies to the simpler case where one beam per element is produced and the signals are processed discretely as shown in Fig. 2.1a. In the former case the elements are usually more closely spaced (denser) than the latter. In 2005, to distinguish

easily between these cases in the Square Kilometre Array (SKA) community, the expressions *phased array feed* (PAF) was chosen for the former case and *multi-feed cluster* was chosen for the latter case [36]. The term *phased array feed* has been substantially adopted in the SKA community [37–39] with some competition from *dense focal plane array* [32, 40–43]. In the wider antenna literature, the terms *array feed* [31, 44–46] and *focal plane array* are more commonly used. Fisher and Bradley used *full-sampling focal plane arrays* for the first prototype radio astronomy PAF work [2]. In this work the terms *discrete focal plane array* and *dense focal plane array* are used for the two cases where a distinction is required.

Dense and discrete FPAs can be used with many different focussing systems including lens and multiple-reflector systems. Although this work concentrates on axisymmetric prime-focus reflectors, it can be extended to other focal plane systems such as lenses and offset and multiple reflector systems.

Single-Pixel Feed

In an analogy with optical systems, FPAs have been viewed turning the single feed dish from a single-pixel instrument into a multi-pixel instrument. This is shown for example in Bij de Vaate’s title “Focal plane arrays: Radio astronomy enters the CCD area” for his paper in 2005 [47]. As a consequence of multi-pixel view of FPAs, the expression *single-pixel feed* has been used in a number of situations in the SKA community to contrast it with FPAs [48].

Aperture Array

Another term that is used in the SKA community but less commonly in the wider antenna literature is *aperture array*. This term is used to distinguish directly receiving phased arrays from FPAs.

Number of Elements in a Dual Polarized Array

One may think of a dual-polarized array as having elements with two ports, one for each polarization. However in some array designs the two polarizations are offset with respect to each other and much of the discussion and analysis of FPAs applies equally to single and dual-polarized systems. It is

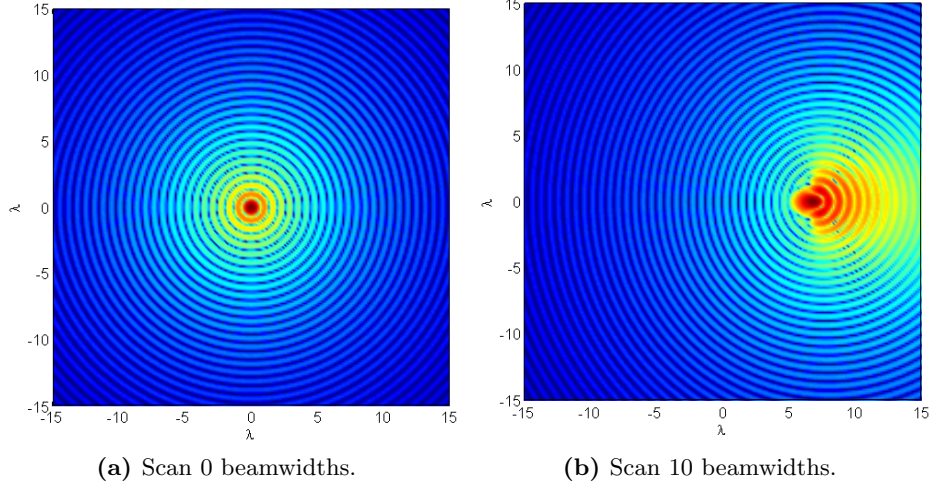


Figure 2.3 – Focal plane fields from an $F/D = 0.5$ paraboloid for incident plane waves on and off axis.

also simplified if separate polarization ports are considered as feeding different elements. Therefore the convention of referring to one *array element* per *polarization port* is adopted in this thesis.

2.3.2 Two Views of FPAs

The fields in focal plane of a paraboloidal reflector for on-axis incidence are close to the two dimensional Fourier transform of the aperture, that is the Airy pattern, as seen in Fig. 2.3a. Feed designs that efficiently receive this field have been refined over many years [46]. The behaviour off axis as shown in Fig. 2.3b, however, introduces aberrations such as astigmatism, coma and defocussing as described in classical optics texts such as Born and Wolf [49]. The nature of focal plane fields is dealt with in more detail in Section 3.2.

Two complementary views can shed light on the design and beamforming of focal plane arrays. If one starts with array elements resembling traditional feeds, such as horns or waveguides, they can, on their own before beamforming, produce reasonable illuminations of the reflector. Beamforming the array forms the weighted sum of the patterns of each element. The amplitude and phase of each element are adjusted to produce the desired feed pattern and hence the desired pattern of the feed-plus-reflector system.

Alternatively, starting with the field in the focal plane received from an incident plane wave, to collect the spatial information present in the

focal plane, the array must sample the field and recombine the samples (beamform) to produce the desired signal. Sampling theory gives the Nyquist spatial frequency limit for the element spacing as discussed in Section 3.4—hence the reference by Fisher and Bradley to *full-sampling focal plane arrays* [2].

Generally, the smaller the elements, the less able they are to efficiently illuminate the reflector on their own but they sample the field more closely to the Nyquist limit. This trade-off brings these two views together and is discussed in Section 3.4.

Another important complication to keep in mind is the interaction between elements known as *mutual coupling*. This disturbs the element patterns and the impedance each element presents on its port. This coupling needs to be carefully considered in any FPA design.

2.4 A Brief History of FPA Development

Placing an array in the focus or near the focus of a reflector or lens has been the subject of study since at least the 1940s. The motivations for doing so include beam scanning, simultaneous generation of multiple beams, improving the efficiency of the reflector, generating a specific beam pattern and correcting deficiencies in the reflector or lens.

In addition to the geometry considered in this thesis, the focal plane of a paraboloid, two related cases of historical significance are worth noting: line sources for spherical reflectors and systems with arrays placed much closer to the reflector than the focus.

Spherical reflectors offer scanning with movement of only the feed but are limited by aberrations with simple feeds. A solution was found using line feeds as early as 1949 [50, 51] with a notable application in the Arecibo radiotelescope [52] in the early 1960s. Similar approaches were used for aberration reduction for scanned beams in paraboloids by Sletten et al. in 1958 [53].

Systems with arrays closer than the focus were introduced to utilize the flexibility of electronic scanning with the gain offered by a reflector. At this location, the amplitude illumination of the array is fairly uniform [54] and the beamforming requires phase shifting and summing only. Studies in this field started as early as 1961 [55] and designs were deployed in operating radar sets by the 1970s [56].

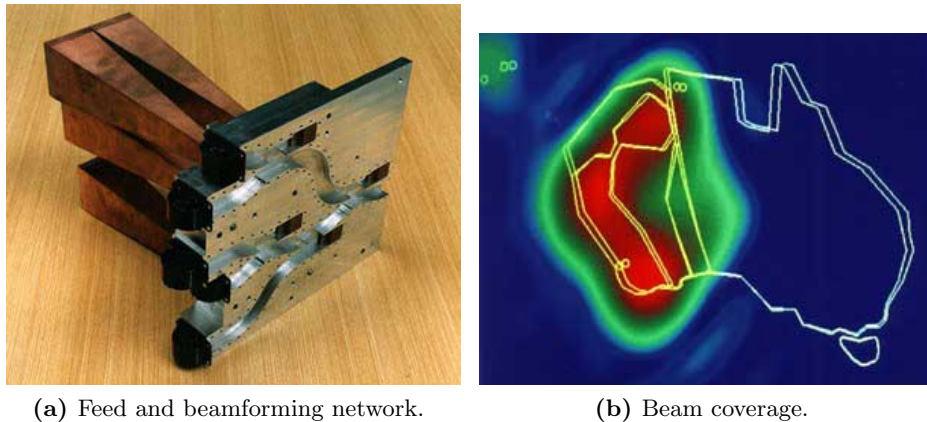


Figure 2.4 – An example of a satellite borne FPA with a bespoke beamforming network designed to cover Western Australia. *Images courtesy CSIRO.*

The correction of scan aberrations was tackled by Loux and Martin with an array of circular waveguides [57] and refined by many others including Blank and Imbriale [44]. Both of these papers also demonstrated compensation for reflector distortions as well as beam scanning. In a similar vein, Rudge and Withers showed scanning up to 15 beamwidths using a butler matrix and phase shifters for a reflector curved in only one plane [58]. Shelton studied the provision of multiple beams with a dense FPA in 1965 [59].

FPA's have been applied in the field of geostationary satellite antennas in the since 1970s. Here the task has been to design an antenna with a pattern illuminating a specific geographical region, often sharing a reflector with other beams [60–66]. Fixed and reconfigurable beamforming networks are used [67, 68] with reconfigurable networks allowing the tasking of the satellite to change whilst in orbit. With stringent pattern requirements, the mutual coupling between array elements becomes important. This subject has been studied in detail for rectangular, circular and coaxial waveguides by Bird [69–73] and others .

2.5 Dense FPA's—Benefits and Challenges

While dense FPA's have been demonstrated in a number of fields, when choosing to investigate them in depth for a given application the potential benefits and challenges must be considered.

2.5.1 Benefits

Dense FPAs offer a number of benefits over single feeds and discrete FPAs. Some of these are well established and some are yet to be demonstrated in operational systems. They include:

Improved Antenna Efficiency: The maximum aperture efficiency of a reflector is achieved when the feed matches the focal plane field generated from an incoming plane wave on the reflector (see Section 5.1.1). Single element feeds are able to match this field to a certain extent as shown by Minnett and Thomas [74, 75]. However the flexibility offered by arrays can provide a better match [58, 76, 77].

Scan Loss Reduction: The asymmetrical aberrations that occur as a feed is moved from the axis of a reflector can be compensated for by dense FPAs. For a sufficiently large FPA, the scan loss can be much less than for a feed designed for the reflector focus. This has been demonstrated with reflectors curved in one dimension by Ricardi et al. [55] in 1961 and Rudge and Withers [58] in 1969. Slotted waveguide line feeds were used for an offset reflector by Sletten in 1958 [53] and a linear array of dipoles was used for the spherical Arecibo reflector [52] a few years later. Two dimensional feed arrays were demonstrated by Loux and Martin in 1964 [57] and many others since.

Scan Aberration Correction: Translating a single feed in the focal plane introduces significant distortion of the radiation pattern with the effect of coma increasing with scan angle. This is evident by increased sidelobe levels. Dense FPA systems have demonstrated that coma can be reduced [44, 53, 57, 58, 78–80] (see Section 8.2).

Vernier pointing: Dense FPAs are capable of minor corrections to the beam direction as proposed by Blank and Imbriale [44]. This may include deformation due to gravity and if the response is fast enough, wind. Alternatively it could apply where the reflector pointing mechanism is too coarse for the precision required.

Field of View (FoV): Discrete FPAs [81, 82] can greatly increase the FoV of an antenna system by placing multiple beams on the sky but the FoV is not contiguous [83] and to fully sample the sky four or more interleaved pointings are required [84]. Dense FPAs however can fill

in these gaps, providing near constant and smoothly varying efficiency [85] and sensitivity across the FoV [11, 86, 87].

Correcting reflector surface defects: A dense FPA can compensate for reflector surface defects [78, 88–90]. These may be constant or change with gravity and the flexibility of the beamformer can adjust as the reflector pointing changes. This compensation is limited by the angular resolution of the FPA pattern which is in turn limited by the size of the FPA (see Section 8.3). Both Loux and Martin [57] and Rudge and Davies [88] demonstrated correcting for reflector surface defects empirically. The ability to compensate for surface defects may allow effective use of lower cost reflectors [88].

Producing specific radiation patterns: FPAs have been employed to produce radiation patterns with specific profiles. This has been exploited extensively in satellite communication satellites where a geostationary satellite is tasked with covering a specific geographic region [61, 63, 64, 66].

Reducing *baseline ripple*: Reflections between the focal plane and the reflector can set up a standing wave. The impedance variation introduces a ripple in the antenna gain and hence the baseline for detecting radio astronomy spectra [91, 92]. Dense FPAs are able to reduce this as shown in the Apertif² program [86].

Interference cancellation: The flexibility that beamforming an FPA allows nulls to be established in directions of an interferer [9, 93–95].

Polarization purity: The flexibility of beamforming a dual-polarized FPA allows the polarization purity to be optimized. A simple approach is to place a null in the cross-polarized response at the centre of the beam [76, 96] (see Section 5.3).

Bandwidth: Discrete FPAs are limited in the bandwidth they can offer [84]. The size of the elements is set by the need to properly illuminate the reflector at the bottom of the band. This results in a large separation in terms of wavelength at the top of the band and hence much greater scan loss and pattern aberration. Dense FPAs can be designed to accommodate these issues.

²‘Aperture tile in focus’. See section 2.6.4 for more details.

Arbitrary polarization and *de-rotating the sky*:

The flexibility in beamforming dense FPAs allows the polarization to be set to any linear angle or either sense of circular polarization. This can be important in astronomical polarization studies with long integration times. With sufficient information and care, a radiotelescope with a non-equatorial mount can follow the rotation of the sky in both pointing and polarization by adjusting the FPA weights.

Reconfigurability: Dense FPAs lend themselves to electronic beamforming and so offer the flexibility to adapt the element weighting to changing demands and environments. This flexibility is necessary for many of the benefits listed above and the weighting can be adjusted to balance them for specific purposes. For example in a radiotelescope a balance may be selected between maximizing sensitivity and pattern control or interference mitigation and pattern control [9].

2.5.2 Challenges

Dense FPAs also present substantial challenges including:

Design complexity: The design complexity is considerably higher for dense FPAs than for arrays of horns for instance. This is because, relative to discrete FPAs,

- the number of elements is higher,
- the mutual coupling can be higher, particularly for the wideband designs for radio astronomy, with implications in efficiency and noise [97, 98],
- it can be more difficult to match the elements to a *standard* impedance such as $50\ \Omega$ [99] and
- the typically large number of beams, flexible beamforming and typically wide bandwidth greatly increases the parameter space that needs to be considered (See Sections 2.6 and 4.1).

Beamforming electronics: Dense receiving FPAs that produce multiple beams will almost always have a separate front-end low-noise amplifier (LNA) for each element for high sensitivity. If analogue beamforming—fixed or electronically steered—is used, separate hardware is required for each beam. Digital beamforming offers superior flexibility but requires a separate receiver chain for each element and has substan-

tial processing requirements. This hardware also requires a substantial amount of power contributing to cooling and running costs.

Beamforming algorithms: Many of the potential benefits of FPAs listed in Section 2.5.1 require specific beamforming algorithms. While the maximum sensitivity weighting is relatively straightforward to achieve, finding the most appropriate weighting for the application is a rich area of research for antenna arrays and will continue to be as high sensitivity radio astronomy systems are refined [9].

Physical size and cooling: The large physical size, particularly the aperture, makes cooling dense FPAs to cryogenic temperatures difficult to achieve [100, 101].

System characterization and calibration:

The increase in element count and electronics and their tight integration requires more effort in system characterization. This effort is compounded as often the beamformer weightings cannot be accurately determined before the array is mounted in the reflector. The parameter space for characterization is also expanded as for the design. Characterization methods and tools are covered in Chapters 6, 7 and 8.

Reliability: The large number of receiver chains and processing electronics demands that close attention is paid to system reliability. It is possible to operate an FPA system with one or more receiver chains having failed as demonstrated in Chapter 7. However it is yet to be seen how a receiver chain failure may affect the demands of high sensitivity synthesis imaging.

Power requirements: The large number of receiver chains and processing electronics can have substantial power requirements.

These challenges are being faced in a number of radiotelescope development programs and the instrument used in this thesis has played a part in this progress.

2.6 FPAs in Radio Astronomy

Much of the science in radio astronomy requires surveys of the sky and using discrete FPAs has greatly increased the survey speed of instruments such as the Parkes 64 m telescope [82]. The even larger fields of view promised by

dense FPAs have led to substantial research efforts in the radio astronomy community and a wide FoV has become a requirement for the SKA [102]. The wide field-of-view potential of FPAs also greatly increases the chance of serendipitous discoveries—for example the proposal to look for transients with ASKAP [17].

Radio astronomy has specific requirements that are not shared with many other FPA applications. This leads to the need for new developments in this technology. The signals the astronomer studies are extraordinarily weak and they are only brought out of the noise through long integration times and highly optimized signal processing techniques. Hence the noise performance of a receiver on a radiotelescope is critical. Combining the efficiency or gain of the system with the noise performance gives the sensitivity. A wide instantaneous bandwidth allows more signal to be collected at any one time and improves the sensitivity. The total tuneable bandwidth is also important as the frequency dependence of emissions of celestial objects is significant. As radiotelescopes are receive-only instruments, there is freedom to explore FPA designs that are not practical where transmission is required as well.

Progress in a number of critical areas over the last 10 to 15 years has facilitated the prototyping and planning of FPA equipped radiotelescopes:

Analogue electronics: Most radiotelescopes use LNAs cooled to cryogenic temperatures. Advances in semiconductor design allow uncooled systems to have sufficiently low noise performance [103, 104]. Other improvements such as integration methods allow the many receiver chains required for digital beamforming to be constructed within practical cost and physical volume limits [86, 105].

Electromagnetic analysis: Progress in electromagnetic modelling of dense FPAs in recent years has been made possible by increased computing speed and memory improvements and the development of more efficient and accurate modelling methods. FPAs being considered for radio astronomy applications are too small for effective use of infinite array techniques due to significant edge effects [106]. They have been too large to be easily optimized using standard techniques and commercial packages [107, 108]. Recent developments in modelling techniques have been applied to FPAs allowing relatively rapid analysis of the structures involved (see Section 4.1).

Digital electronics: Developments in digital electronics and associated software have brought the beamformers required for dense FPAs within reach [109–111].

At the time of writing, the main applications being considered for dense FPAs in radio astronomy were retrofitting existing telescopes such as Arecibo [112] and Westerbork and developments for the Square Kilometre Array (SKA) (see Section 2.6.1). They are also being considered for the Chinese FAST project [113, 114] and are likely to be investigated for other large radiotelescopes as the technology matures.

2.6.1 The SKA and FPAs

The SKA was conceived as ‘the next-generation radio observatory’ with discussions starting in the late 1980s [115] and gathering pace since [35, 116]. It will address a number of fundamental questions in astronomy [117] when it is built. Over time interest grew and specifications were iteratively negotiated between the drivers of astronomical science, engineering capability and the expected funding limits [102].

By 2004 it had become apparent that the astronomical science would be best served with a number of different antenna technologies. At this time a number of concepts had emerged and they are listed here with countries or regions where the technology was being chiefly investigated [118]. These are listed below.

- Adaptive parabolic reflectors with diameters of over 100 m combined with focal plane arrays (Canada: Large Adaptive Reflector, (LAR)) [119, 120] or conventional feeds (China, Five-hundred-meter Aperture Spherical Telescope (FAST)).
- Large cylindrical reflectors with beamformed line feeds (Australia) [121].
- A large number of small diameter (~ 12 m) reflectors (USA [122] and India).
- Luneburg lenses (Australia) [123].
- Aperture phased arrays (Europe) [124–126].

Continued international scientific discussion concluded that the total FoV was more important, at least above 1 GHz, than the main benefit of Luneburg lenses: multiple independent FoVs. Therefore the lens was not

pursued [127] for the SKA even though the lens material was showing promise [123, 128] and its development has continued. The fan beam produced by the cylindrical reflectors was considered to be unsuitable as well and so this work was also discontinued. The Canadian LAR was also discontinued due to the emerging wide FoV requirements. The Chinese FAST development continues but not formally as part of the SKA.

A major factor in design considerations is the processing requirements and these requirements increase approximately as the square of the number of dishes. Calculations showed that reflectors of approximately 12 m diameter fitted FPAs may be able to provide the FoV desired for astronomically revolutionary survey speeds (~ 1 square degree at 1 GHz) cost effectively. This concept was a result of the synthesis of concepts from FPAs for the Canadian LAR, wide-field considerations from the Luneburg lens and cylindrical reflector work, first thoughts from a putative CSIRO-ASTRON project known as MUDDA (multi-use dense digital array) and the US 12 m dish work.

FPA development for the SKA then progressed to the building of pathfinder radiotelescope based on FPAs—ASKAP—and continuing developments at ASTRON and in Canada. Consequently FPAs are a strong contender for the SKA in the 500 to 1400 MHz band [116].

2.6.2 Wideband Array Elements

The specific radio astronomy requirements of wide bandwidth and low noise have led to a number of possible elements for FPAs being studied in detail. The bandwidth requirements are typically about 2:1 in proposed radiotelescopes (Table 2.2) and the array structure should add only a few Kelvin to the noise budget. Two polarizations are also considered essential.

The challenge is to find an element that can be packed sufficiently closely to adequately sample the field at the top of the desired band and at the same time provide a good match to both the incoming field and to the receivers connected to the ports across the band. Rectangular or circular waveguide elements are too large unless they are loaded with dielectric [129] but dielectric-loaded waveguides are difficult to match over wide bandwidths and losses in the dielectric need to be carefully considered in this application. Dielectric rod antennas [130, 131] and coaxial waveguide elements [132]

have been proposed in narrower band applications but it is unlikely their bandwidths can be extended sufficiently.

For single feeds and discrete FPAs, the pattern of each feed, is required to efficiently illuminate the reflector. In an array, these patterns are referred to as the embedded element pattern—reflecting the impact the surrounding elements may have on the pattern. For a dense FPA it is the beamformed pattern that must efficiently illuminate the reflector. The embedded element patterns are important however, as beamforming effort that goes into cleaning up these patterns may detract from other goals such as the sensitivity. This is particularly the case at the top of the frequency band where only a few elements receive almost all the energy. In this situation, there are few degrees of freedom to correct poor element patterns.

The two designs that have received the most attention in the radio astronomy field have been Vivaldi and chequerboard arrays. Wideband dipoles have also been used with very good noise performance but lower bandwidth [133]. In all cases careful matching between the array elements and the connected receivers is required to achieve good sensitivity. This match can be optimized to either a single beam or to the entire FoV [87, 134–136].

Vivaldi Arrays

Vivaldi arrays have been studied in great detail, particularly at the University of Massachusetts [137, 138], and were adopted by ASTRON for both aperture arrays and FPAs. It was considered the best element for this application in 1999 by Schaubert [138] and Weem [139]. Fig. 2.5 shows the Vivaldi array designed by ASTRON and used for the experimental component of this thesis.

Stand-alone Vivaldi antennas boast very high bandwidths but are generally designed to be too large for incorporation in a *dense* wideband array: the flare opening is $\lambda/2$ for the largest wavelength [140] and the spacing requirement of FPAs is about $\lambda/2$ for the shortest wavelength (see Section 3.4 for more details). Therefore the elements must operate in a somewhat different regime than for the single Vivaldi [141]. Care needs to be taken in their design to avoid resonances, particularly from array truncation effects.

Various configurations of the Vivaldi have been investigated and are listed below.

- Standard slot line elements

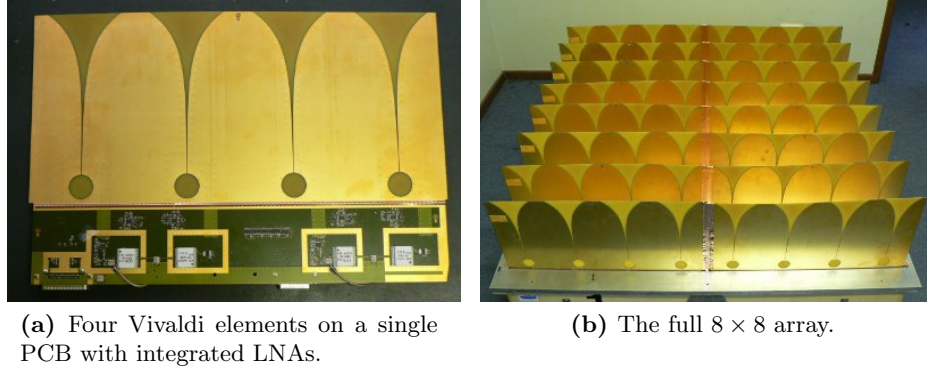


Figure 2.5 – The THEA tile, designed by ASTRON and used for the experimental component of this thesis is a example of a singly polarized dense array.

- Antipodal [142] [143].
- Balanced antipodal Vivaldi [144] [145].
- Dielectric free [146–149].
- Quad element [150, 151].
- Fractal or interleaved elements [152].
- Extension to a three dimensional bullet like conductors [153].

A Vivaldi array has been chosen for the Apertif project (see Section 2.6.4) and used in a number of prototype systems (Table 2.1). They have also been proposed for the Northern Cross cylindrical reflector radiotelescope [154].

Chequerboard Array

The chequerboard array development at CSIRO can be understood as either a self-complementary structure or an array of connected bow-tie antennas. Fig. 2.6 shows a chequerboard array with a 5×4 layout.

Self-complementary antennas have the property of theoretical frequency independent impedance [155, 156]. Their bandwidth is limited by truncation and the need for a ground plane in practical applications [157]. The feeding structures also impinge on the ideal planar behaviour.

The development of the chequerboard array at CSIRO started with connected arrays of dipoles [41, 158] as proposed by Hansen [159]. They were arranged in a grid to provide both polarizations [99, 160, 161]. The chequerboard array may be considered a broadband version of this where the

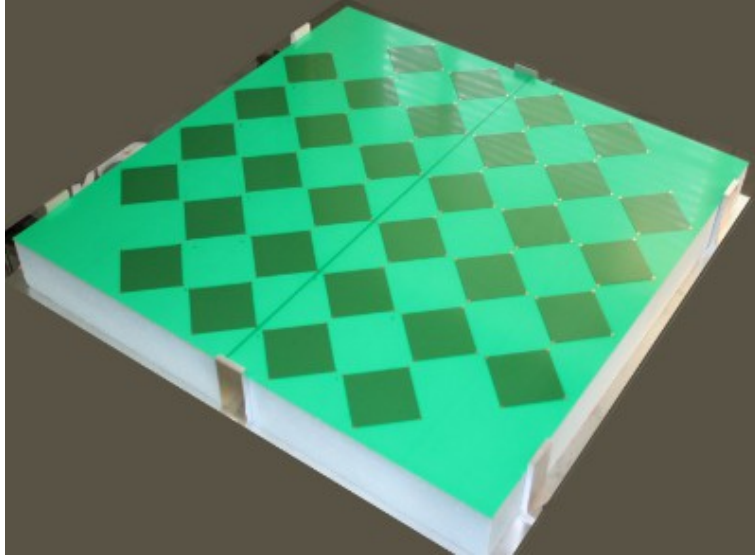


Figure 2.6 – An early prototype from the CSIRO chequerboard array development. There is a twin wire transmission line from corners of the squares on the surface to balanced LNAs placed behind the ground plane. The 5×4 arrangement results in 20 elements per polarization.

connected dipoles are fattened to bow-ties forming the squares of the chequerboard in the same way that bow-tie antennas are broadband versions of dipoles.

2.6.3 Prototype FPA Systems

With the motivation of the SKA and retrofitting existing telescopes, a number of research groups embarked on programs investigating FPAs for radio astronomy. Details of radio astronomy FPA prototypes that have been tested in reflectors are shown in Table 2.1 and a summary of the larger FPA development programs follows.

In 2000, NRAO³ published the results from a prototype of 19 sinuous elements [2]. They demonstrated beamforming by weighting the array with Airy pattern function $\sin(2\pi x)/(2\pi x)$. Their more recent FPA efforts have been largely in collaboration with Brigham Young University (BYU), Provo, Utah.

ASTRON have been pursuing FPA technology for some time with contributions in performance analysis and beamforming [40] and array de-

³National Radio Astronomy Observatory, USA

Table 2.1 – Radio astronomy FPA prototypes.

Project/Org.	NRAO	FARADAY	ASTRON	BYU	NTD	CSIRO	DIGESTIF	ASTRON	PTF	CSIRO	PHAD	DRAO	BYU/NRAO	BYU/Arecibo
First results ^a	2000	2004	2007	2007	2007	2007	2007	2007	2008	2008	2009	2010	2010	2011
Reference	[2]	[162]	[163]	[163]	[8]	[4]	[164]	[135]	[6]	[135]	[133]	[133]	[133]	[133]
F/D	0.43	0.35	0.38	0.38	0.40	0.35	0.50	0.43	0.45	0.43	0.43	0.43	0.43	0.43
D (m)	43	25	3	3	14	25	12	10	10	20	213 × 237 ^f	20	20	213 × 237 ^f
f_{\min} (MHz)	1120	2300	1500	1500	1100	1000	700	1315	1000	1315	1360	1315	1315	1360
f_{\max} (MHz)	1600	5500	2000	2000	1700	1750	1800	1885	2000	1885	1840	1885	1885	1840
Bandwidth ^b	1.4	2.4	1.3	1.3	1.5	1.8	2.6	1.4	2.0	1.4	0.35	1.4	1.4	0.35
Element ^c	S	V	D	D	V	V	C	D	V	C	D	D	D	D
Elt. Pattern	Hex	Square	Hex	Hex	Square	Square	Square	Hex	Square	Square	Square	Hex	Hex	Hex
Rows x cols x pols	19x1	9x8x2	7x1	7x1	8x8x1	8x7x2	5x4x2	11x10x2	11x10x2	11x10x2	19x1	19x1	19x1	19x1
No. Elts.	19	144	7	7	64	112	40	180	180	180	19	19	19	19
Beamformed Elts.	7	9	7	7	21	56 ^d	8 ^e	90 ^d	90 ^d	8 ^e	90 ^d	19	19	19

^a First published results for the FPA performance in a reflector.^b The design bandwidths often have not been fully exploited in measurement programs.^c C: chequerboard; D: dipole; S: sinusoid; V: Vivaldi.^d The number of beamformed elements was not explicitly stated and has been assumed to be one polarization.^e More recent measurements have used all the available elements. ^f The effective diameter of the Gregorian feed system is elliptical [165]

sign in collaboration with others [166, 167]. The notable prototypes they have been involved in developing are FARADAY [162, 168–170], PHAROS [100, 171–173] and DIGESTIF [4, 174]. PHAROS stands out from other prototypes in that it used cryogenically cooled LNAs. ASTRON are progressing in their plans to deploy FPAs on the Westerbork radiotelescope dishes [86, 174–176]. The program is referred to as Apertif and is described in more detail in Section 2.6.4.

BYU, in collaboration with NRAO, have concentrated on interference mitigation [93]. They have demonstrated first a seven [163] and then a 19 element [135, 177] dipole array. They have also demonstrated a 19 element dipole array on the Arecibo radiotelescope [133].

DRAO⁴ have continued FPA development despite of moving on from their large reflector SKA project (LAR) [37]. Results from a 180 element prototype were reported in 2009 [6] and their investigations are continuing [25].

FPAs have also been investigated for the Karoo Array Telescope (KAT), an SKA pathfinder instrument, in South Africa [178].

CSIRO's involvement in the SKA first concentrated on Luneburg lenses [123] with preliminary investigations in FPAs [179]. The prime advantage of the Luneburg lens, being widely independent fields of view, was eventually not considered to warrant the risks involved with the development [123, 127]. Attention then turned to 10 to 20 m dishes fitted with FPAs and plans grew for a radiotelescope now being built in Western Australia: the Australian SKA Pathfinder (ASKAP) [105, 180]. This instrument is designed to not only provide a demonstration of technologies for potential inclusion in the SKA, but also to contribute significantly to the global radio astronomy capabilities [16].

Prototyping for ASKAP commenced with the New Technology Demonstrator (NTD) interferometer, two 14 m dishes at the Radiophysics laboratory [7, 8, 12] and then moved to the Parkes Testbed Facility (PTF) [164, 181], a dedicated 12 m antenna at the Parkes observatory.

⁴Dominion Radio Astrophysical Observatory, Penticton, Canada

Table 2.2 – Specifications and target performance for ASKAP [182] and Apertif [86].

Parameter	ASKAP	Apertif
Number of dishes	36	14
Dish diameter, D (m)	12	25
Focal ratio, F/D^a	0.5	0.35
Maximum baseline (km)	6	2.7
Frequency range (MHz)	700–1800	1000–1750
Tuneable bandwidth	2.6:1	1.75:1
Instantaneous bandwidth (MHz)	300	300
FPA elements ^b	188	112
Instantaneous FoV (deg ²)	30	8
FoV on half power beam area ^c	40	44
Independent beams per dish	30	30–40
Number of Spectral Channels	16384	16384
System temperature (K)	50	50–55
Aperture efficiency (%)		75
$A_{\text{eff}}/T_{\text{sys}}^d$, (m ² K ^{−1})	65	100

^a F/D : focal length on dish diameter.

^b The design at the time of writing is 188 elements, not 192 as reported in [182].

^c $\frac{\text{FoV}}{\pi\theta_{\text{HPBW}}^2/4}$. $\theta_{\text{HPBW}} = 70^\circ \lambda_{\text{min}}/D$ the nominal half power beamwidth for the shortest wavelength in the band is used.

^d Effective area on system temperature. See Section 2.2.

2.6.4 Currently Planned Dense FPA Based Radiotelescopes

There are two radiotelescopes with well developed plans for using dense FPAs: Apertif for the Westerbork Synthesis Radio Telescope (WSRT) and the Australian SKA Pathfinder (ASKAP). The design goals for both are summarized in Table 2.2. Interestingly, the expected survey speeds of both are approximately the same [16, 86].

2.6.5 Competitors to FPAs in Radio Astronomy

While the benefits promised by dense FPA systems for radio astronomy are substantial, they are not a mature technology and alternatives need to be considered.

Discrete FPAs require far less signal processing and as they are more amenable to cooling, can more readily provide superior noise performance. For unshaped reflectors dense FPAs however can provide greater instant-

neous fields of view that are also contiguous. They also can be designed to have much wider bandwidths. A detailed comparison is given by Veidt [84].

Another serious competitor in the SKA field is a wide band single feed, sometimes referred to as a *single pixel feed*. Without the dense packing requirements of FPAs, these can be made with extremely wide bandwidths. The FoV from a synthesis telescope is then determined by the main reflector size with the number of dishes adjusted to provide the required collecting area. With fewer receivers, cryogenic cooling is possible. An example of this technology in use is the Allen Telescope Array [122] and a promising newer design is the ‘Eleven’ feed [183]. A large number of dishes (N) however introduces a large number of baselines (N^2) and pushes up the processing costs. These issues are explored in detail in a number of references including the SKA memo series [35, 102, 184–186].

2.7 Summary

The signals of interest to radio astronomers are most commonly Gaussian noise and the task of the radiotelescope in the main is to map the intensity of these signals. The intensity of compact sources is measured in spectral power flux density and extended sources in radio brightness. As these signals are very weak, the principal figures of merit for radiotelescopes are related to their sensitivity. The précis of radio astronomy signals and figures of merit in this chapter provides background material that will be used for the FPA models presented in Chapters 3 and 4, and the experimental work in Chapters 6, 7 and 8.

Dense FPAs have been studied for at least six decades and been applied chiefly in radar and on-board satellite antennas. The attraction of dense FPAs to radio astronomy is predominantly the expansion of the field of view provided by a reflector and the primary distinguishing features from other applications are the low noise and wide bandwidth requirements. The development of FPAs for radiotelescopes has occurred largely since 2000 with Fisher and Bradley’s demonstration [2], gaining momentum in the mid 2000s with the motivation of wide band arrays for the SKA and enabling technological developments. This thesis describes one of the early prototypes and its characterization (Chapters 6, 7 and 8).

In spite of the competing technologies of extremely wideband single feeds and discrete FPAs, the potential benefits of dense FPAs have driven substantial investment and development efforts by a number of institutions. At the time of writing FPA systems were beginning to realize the performance required for revolutionizing radio astronomy.

Chapter 3

FPA Size and Encircled Power Calculations

3.1 Introduction

The design and construction of complex antenna systems take many man-years of effort and so performance estimates or design guides are used when establishing the design goals for a particular observatory program. When commencing the design process, these design guides assist to reduce the range of possibilities before detailed modelling and prototyping commences. Such guides may be based on previous experience or on calculations that are more general or simple than analysing specific system architectures in depth. There are many design guides for single feed reflector antennas and some for discrete FPAs [187–189] but there are far fewer for dense FPA systems. Studies of scan-loss [190,191] are of some use but they do not show the gain recovery from aberration correction available with FPAs. Design guides that are available such as provided by Mailloux [54] are not directly applicable to the design of dense FPAs for axisymmetric prime focus systems. An exception is [192] which provides an estimate of the bandwidth that can be sustained by one set of beamformer weights. FPA design is also more complex than single feed design, making initial guidance in the design process all the more important. This chapter presents an approach for estimating the size of an FPA required to meet a field of view (FoV) specification.

The size of the FPA is critical to the system cost as it is the dominant factor in the number of elements [193–195]. The element count not

only determines the size and complexity of the array itself but, in low noise multibeam applications, it also determines the number of receiver chains and beamforming complexity. The density or spacing of the elements is also required for estimating the element count. The size and element density for FPAs are discussed and some design rules are established in this chapter.

This chapter expands on the author's 2005 publication [196].

3.2 Focal-Region Fields

A number of studies of focal-region fields are available [75, 187, 197–201] including scanning relationships [44, 187, 202–204] and even the FPA size for a spherical reflector [205]. An understanding of the differences between optical and radio-wave analyses of focal-region fields is provided by [202]. None of the analyses, however, has concentrated on the field-of-view achievable over a wide range of focal ratios for paraboloids as required for SKA costing studies. The scope here has been limited to symmetrical-prime-focus-parabolic dishes but with a little care, the results can be extended to offset and dual reflector designs.

The approach used is to calculate fields in the focal plane generated from a plane wave incident on the dish using physical optics (PO). Power intercepted by a disk representing the FPA is then calculated to find the efficiency. By calculating the encircled power for large number focal ratios, dish diameters and scan angles the relationships between these parameters is explored.

The encircled power approach was used independently by Bunton and Hay¹ in an SKA cost model [193] and also by Granet et al. [206, 207].

3.3 Parabolic Reflector Geometry

The study of FPAs in this chapter concentrates on axially-symmetric prime-focus parabolic reflector antennas. The definitions of key parameters are illustrated in Fig. 3.1. These are:

***D*: dish diameter**

¹Hay undertook this work independently at the same time as the results from this work were being refined.

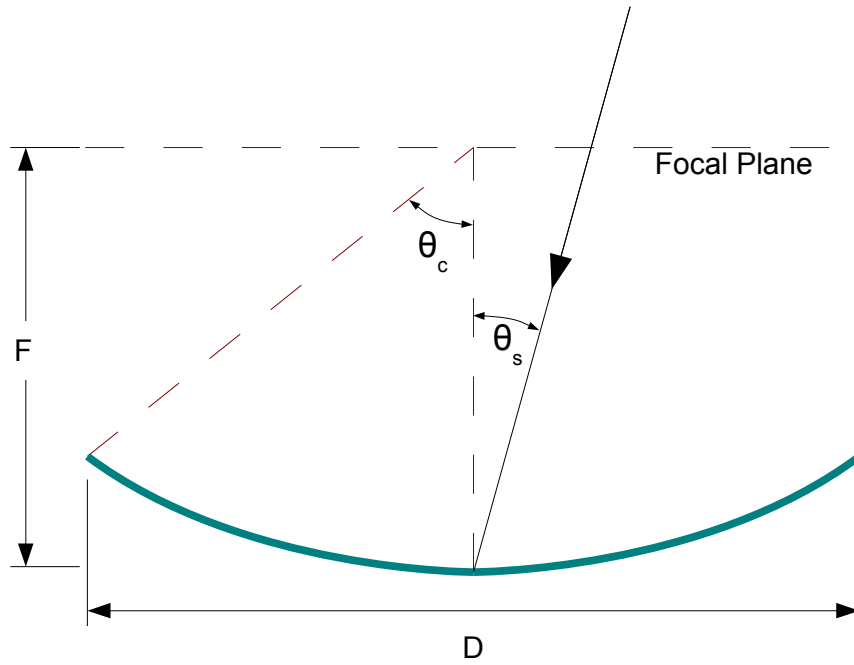


Figure 3.1 – Parabolic reflector geometry. F is the focal length, D is the reflector diameter and θ_c is the angle between the reflector axis and the edge of the reflector. θ_s , the scan angle is the angle between an incoming plane wave and the reflector axis.

θ_{HPBW} : half power beamwidth. The dish diameter D sets a lower limit on the half power beamwidth (HPBW) of $1.02\lambda/D$ radians for an ideal uniform aperture and for more a practical illumination of the dish can be given a nominal value

$$\theta_{\text{HPBW}} \triangleq \frac{k_{\text{BW}}\lambda}{D}. \quad (3.1)$$

where k_{BW} depends on the aperture illumination. The typically value of 70° (1.22 rad) is used here.

F : focal length. The focal ratio is F/D . The ideal feed for a given F/D is relatively independent of the dish size, as in most cases, the dish is in or near the far field of the feed.

θ_c : paraboloid opening semi-angle. The angle at the focus subtended by the apex and the dish rim.

$$\theta_c = 2 \arctan \left(\frac{1}{4F/D} \right). \quad (3.2)$$

θ_s : scan angle. The angle from the dish axis to the direction of incidence of the received signal.

FoV: field of view. The FoV is the solid angle set by the maximum scan angle $FoV = \pi\theta_s^2$.

θ_{BW} : scan angle in beamwidths.

$$\theta_{\text{BW}} \triangleq \frac{\theta_s}{\theta_{\text{HPBW}}} = \frac{\theta_s D}{k_{\text{BW}}\lambda}. \quad (3.3)$$

If $D = 70\lambda$ then $\theta_{\text{BW}} = \theta_s$. This value is used for normalizing scan angle with respect to the dish size. This approach was adopted by many researchers looking at scanning in reflector antennas, for example [202, 208].

3.4 Element Density

A simple rule-of-thumb for element density is to consider the angle of acceptance for the feed, $2\theta_c$. Assuming the feed array needs to scan to the edge of the dish without grating lobes appearing, for a rectangular grid the

maximum feed spacing d in terms of wavelengths is [209]

$$d/\lambda = \frac{1}{1 + \sin \theta_c} \quad (3.4)$$

or expressed in terms of F/D

$$d/\lambda = \frac{1 + (4F/D)^2}{[1 + (4F/D)]^2} \quad (3.5)$$

and for a hexagonal grid

$$d/\lambda = \frac{2}{\sqrt{3}(1 + \sin \theta_c)}. \quad (3.6)$$

In the large F/D limit the focal plane field approaches the Airy pattern (see Section 3.5). Taking the Fourier transform of the Airy pattern gives the highest spatial frequency in the focal plane and a sampling criterion of

$$d/\lambda = \frac{1}{2 \sin \theta_c}. \quad (3.7)$$

Note that (3.4) and (3.7) approach each other for small θ_c , i.e. large F/D —the condition for the focal plane field approaching the Airy pattern.

When considering the sampling criterion, the pattern of the elements needs to be considered outside the opening angle of the reflector. This is because if they have sufficient gain outside this angle, the spillover received in it needs to be minimized. That is, the spatial sampling needs to be close enough to not only receive the signal from the reflector but also minimize the unwanted noise from outside it. A spacing of $\lambda/2$ for a rectangular grid fully samples the field from all directions.

In a study of a particular idealized feed element, hard walled rectangular waveguides, Ivashina et al. [195] found maximum element separations very close to (3.4). They also found efficiency deteriorated significantly as the separations fell below 0.2 to 0.3λ due to mutual coupling losses with optimum spacings around 0.4 to 0.5λ .

In other studies, acceptable performance has been modelled or measured with wider spacing than specified by (3.4) and (3.6). For example both the hexagonal gridded 19 element BYU/NRAO FPA [135] and the square gridded APERTIF FPA [11] have elements that are spaced 14% higher than

the grating lobe conditions, (3.4) and (3.6) respectively. This discrepancy is because the grating lobe condition assumes the elements have sufficient gain perpendicular to the antenna axis to cause a problem. In practice, the embedded-element directivity of the array types being considered for radio astronomy dense focal plane arrays relaxes this requirement.

As seen above the embedded-element patterns are critical in evaluating the minimum spacings. The wider the patterns, the closer they need to be spaced to provide an efficient illumination of the reflector. Elements which on their own, before beamforming, illuminate the reflector reasonably efficiently can be more widely spaced. This has been demonstrated in satellite applications with circular waveguide type feeds [63, 76, 77]. There is, in general, a trade-off between element spacing and embedded element illumination as discussed by Yngvesson et al. [189]. The greater the spacing, the larger the elements and the better the embedded patterns can illuminate the reflector. A counter example is provided by Chantalat et al. [210] where a photonic band-gap resonator is placed over an array of feeds. The elements are both closely spaced and have efficient embedded element patterns. Stein's limit [211] considerations dictate that the mutual coupling of such an array must be high. Nonetheless this example shows the need to consider the specifics of the array elements being considered. Some other references exploring these issues include [83, 212–214].

In summary (3.4) and (3.6) do not provide hard limits for the element spacing but they can be used as a starting point for more detailed modelling.

3.5 Simple FPA Size Models

Two limiting cases are considered here before outlining the PO based design guide for estimating the FPA required to achieve a given scan angle: (1) the high frequency limit and (2) the large F/D and small scan angle limit. These will be compared with the more comprehensive PO based model in Section 3.9.3.

The field in the focal plane extends to infinity and so a decision is needed on where to truncate the FPA, and hence its overall size. The FPA is assumed to be circular and its size is represented by the radius, R . The fractions of 79% and 50% (i.e. -1 dB and -3 dB) of the total on-axis incident power are used here, representing the likely bounds of any design specification. This

fraction is an upper bound on the aperture efficiency and here is referred to as the encircled power efficiency, η_{enc} .

The encircled power efficiency can be expressed in terms of standard subefficiencies as follows. The main subefficiencies of an aperture antenna are given by [27]

$$\eta_{\text{total}} = \eta_{\text{rad}}\eta_{\text{taper}}\eta_{\text{spill}}\eta_{\text{ph}}\eta_{\text{cr}} \quad (3.8)$$

where the sub efficiencies are

- η_{rad} : radiation;
- η_{taper} : taper;
- η_{spill} : feed spillover;
- η_{ph} : phase—due to deviations from a flat phase; and
- η_{cr} : cross polarization.

The encircled power model considers only perfectly absorbing FPAs and so radiation efficiency is unity leaving the encircled power efficiency being an upper bound on the product of the remaining efficiencies. For all but the smallest FPAs, in this model where all the incident field falling on the FPA is received, cross-polarization and phase error losses are expected to be minimal and so

$$\eta_{\text{enc}} \gtrsim \eta_{\text{taper}}\eta_{\text{spill}}. \quad (3.9)$$

3.5.1 Ray Tracing

Considering only the specular reflections and ignoring diffraction, the extreme rays reaching the focal plane come from the edge of the dish (Fig. 3.2). To accommodate a scan angle of θ_s , the array needs to have a radius of

$$R_{\text{RT}} = \frac{D}{2} \left[\frac{\tan(\theta_s + \theta_c)}{\tan \theta_c} - 1 \right]. \quad (3.10)$$

This radius encircles all of power striking the focal plane in the high frequency limit. In order to calculate the FPA size needed to intercept a given fraction of the available power, η_{enc} , a proportionately smaller dish diameter $D = \sqrt{\eta_{\text{enc}}}$ can be used to calculate the size of an FPA needed. R_{RT} is independent of frequency and the ratio of the FPA radius and dish diameter R_{RT}/D is dependent only on the scan angle θ_s .

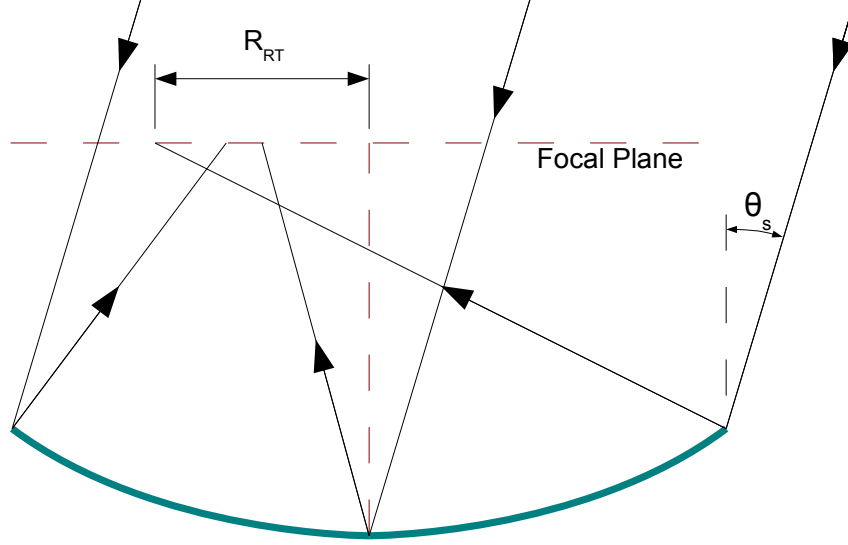


Figure 3.2 – Calculation of FPA size for a given scan angle using ray tracing. R_{RT} shows the extent of the FPA required to collect all the incident energy. An example of power in the focal plane field from a PO calculation is shown for comparison.

Using the identity for $\tan(A + B)$, a small angle approximation for θ_s and (3.3), (3.10) can be written as

$$R_{\text{RT}} = \frac{k_{\text{BW}}\theta_{\text{BW}}\lambda}{2 \tan \theta_c} \left[\frac{1 + \tan^2 \theta_c}{1 - k_{\text{BW}}\theta_{\text{BW}}\lambda \tan \theta_c / D} \right]. \quad (3.11)$$

In the high frequency limit (i.e. $\lambda \rightarrow 0$) the FPA radius in terms of wavelength based on ray tracing is

$$\frac{R_{\text{RT}\infty}}{\lambda} = \frac{k_{\text{BW}}\theta_{\text{BW}}}{2 \tan \theta_c} [1 + \tan^2 \theta_c]. \quad (3.12)$$

3.5.2 Airy Pattern and Beam Deviation Factor

The second limiting case model arises from the fact that, as F/D increases, the focal plane field approaches the Fourier transform of a uniform circular aperture (the Airy pattern). The electric \vec{E} and magnetic \vec{H} fields takes the form

$$\frac{J_1(u)}{u} \quad (3.13)$$

where J_1 is the Bessel function of the first kind and first order [27] and

$$u = 2\pi(\rho/\lambda) \sin \theta_c. \quad (3.14)$$

ρ is distance from the centre of the focal plane. The fraction of the power in the focal plane encircled within given radius R is found by integrating (3.13) to the radius and dividing it by the integral to infinity

$$\eta_{\text{enc}} = \frac{\int_0^R \frac{J_1(u)}{u} 2\pi\rho d\rho}{\int_0^\infty \frac{J_1(u)}{u} 2\pi\rho d\rho} = \frac{1}{2} [1 - J_0^2(u) - J_1^2(u)] \quad (3.15)$$

where J_0 is the Bessel function of the first kind and zeroth order.

Solving for the 50% and 79% efficiency values yields $u_{50\%} = 1.6802$ and $u_{79\%} = 2.771$ respectively. The FPA radii can be determined for the value of θ_c under consideration from (3.14):

$$R_{\text{Airy}} = \frac{u}{2\pi \sin \theta_c} \quad (3.16)$$

where R_{Airy} is in dimensions of wavelength.

As a dish scans, however, the focal spot moves across the focal plane. The location of the peak field in the focal plane can be estimated from the beam deviation factor (BDF) defined as

$$\text{BDF} = \frac{\theta_s}{\theta_f} \quad (3.17)$$

where θ_s is the scan angle of the beam and θ_f is the angle from the vertex to the centre of the feed. In this model the centre of the received Airy pattern is taken as the centre of the feed. A semi-empirical formula has been developed for the BDF and is given by [187, 201, 215]

$$\text{BDF}_0 = \frac{1 + \frac{k}{(4F/D)^2}}{1 + \frac{1}{(4F/D)^2}} \quad (3.18)$$

where k is dependent on the feed pattern taking the value $k = 0.36$ for typical feed patterns [201]. The BDF is weakly dependent on the ratio of the feed displacement and focal length, R_{BDF}/F , and a slightly more accurate

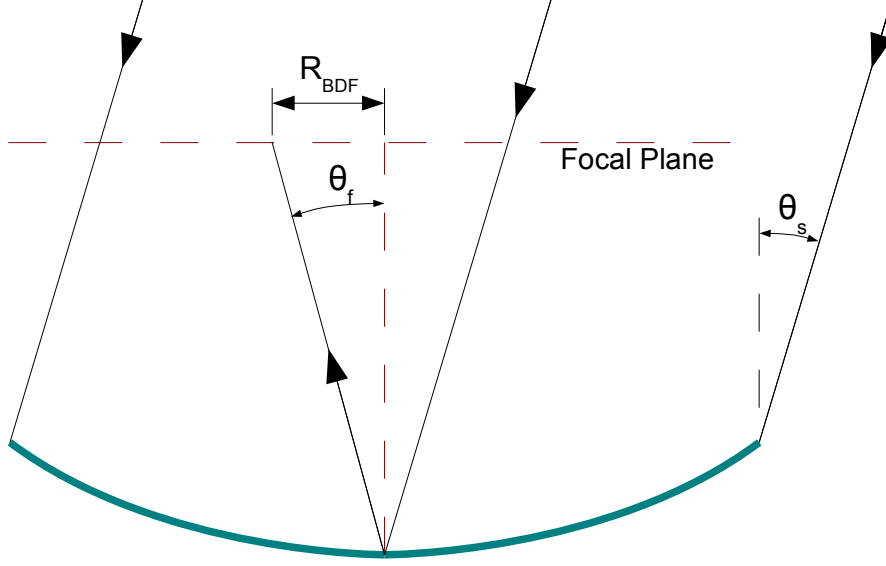


Figure 3.3 – Beam deviation factor (BDF) definition.

version is [201]

$$\text{BDF} = \frac{\arcsin\left(\frac{R_{\text{BDF}}}{2F}\right)}{\arctan\left(\frac{R_{\text{BDF}}}{2F}\right)} \text{BDF}_0. \quad (3.19)$$

Iterative application of (3.19) can be used to find R_{BDF} from θ_s . It converges rapidly.

For the purpose of this work, however, the simpler form (3.18) is adequate. The location of the peak field in the focal plane in terms of wavelengths is then

$$R_{\text{BDF}0} = \frac{F}{\lambda} \arctan \theta_f \quad (3.20)$$

$$= \frac{F}{\lambda} \arctan (\theta_s \text{BDF}_0) \quad (3.21)$$

By means of (3.3), $R_{\text{BDF}0}/\lambda$ is independent of D for small angles as:

$$R_{\text{BDF}0} = \frac{F}{\lambda} \arctan \theta_f \quad (3.22)$$

$$= \frac{F}{\lambda} \arctan \left(\frac{\theta_{\text{BW}} k_{\text{BW}} \lambda \text{BDF}_0}{D} \right) \quad (3.23)$$

$$\approx \frac{F}{D} \theta_{\text{BW}} k_{\text{BW}} \text{BDF}_0. \quad (3.24)$$

By centring the Airy pattern on the peak field location from the BDF the FPA size required to collect 79% and 50% of the total power can be readily estimated as

$$R_{\text{BDF0,Airy}} = R_{\text{BDF0}} + R_{\text{Airy}} \quad (3.25)$$

which is a function of F/D and θ_{BW} only.

These two simple array-size estimates have their limitations but they introduce the focal plane field structure and show the type of field behaviour expected in the more comprehensive PO modelling to follow.

3.6 Encircled Power—Theory

The encircled power approach has been used Minnett and Thomas [198] for the design of corrugated horn feeds and more recently by Ivashina and van't Klooster [216] for FPAs.

The technique uses the plane wave illumination of a paraboloid from which the reflected \vec{E} and \vec{H} fields in the focal plane are calculated using PO. This is shown diagrammatically in Fig. 3.4.

Poynting's theorem is used to calculate the power available to an FPA of a given size. The power flow in an electromagnetic field is given by the Poynting vector,

$$\vec{S} = \frac{1}{2} \vec{E} \times \vec{H}^* \quad (3.26)$$

Consider a cylinder of radius ρ and thickness t enclosing the FPA so the bottom surface is in the focal plane as shown in Fig. 3.5. Poynting's theorem states the power absorbed in the cylinder is given by the dot product of Poynting vector, \vec{S} , and the normal to the surface \vec{ds} ,

$$P = -\text{Re} \oint_{\text{cylinder}} \vec{S} \cdot \vec{ds}. \quad (3.27)$$

Now consider shrinking the thickness t to form an infinitesimally thin closed cylinder and assume the disk absorbs all the incident power from beneath and no power impinges from above. The power absorbed by the disk in the focal plane, with its surface normal in the z direction, is given

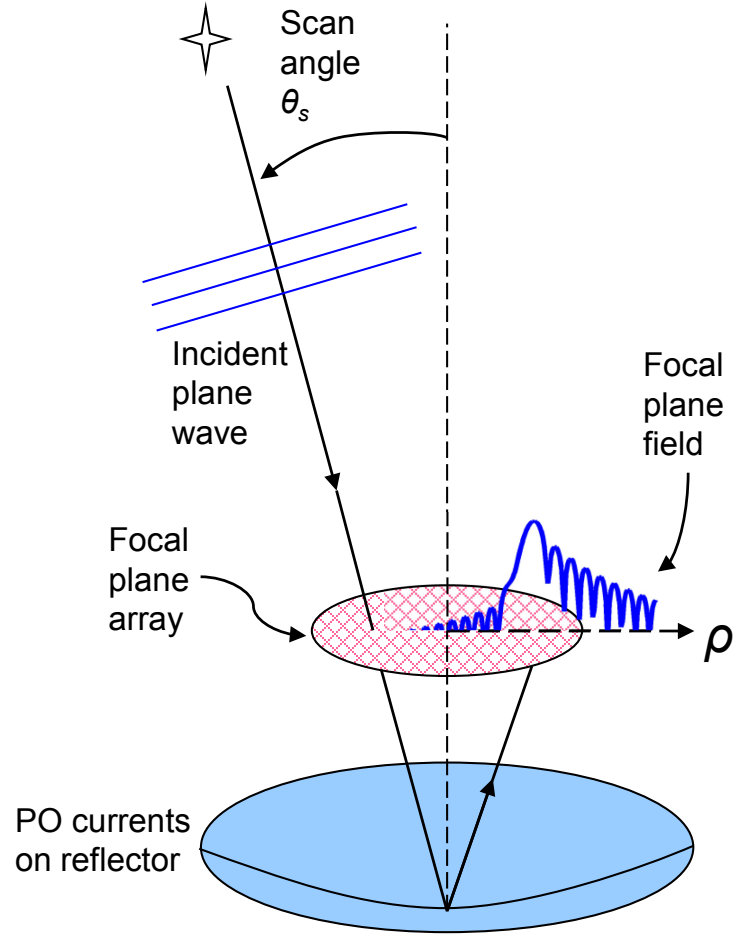


Figure 3.4 – Diagram of the method for calculating the focal plane field.

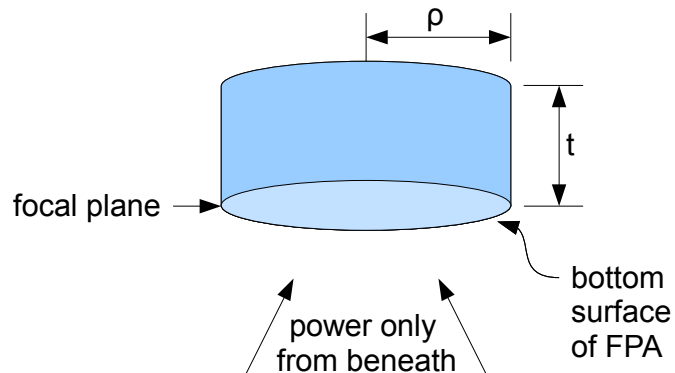


Figure 3.5 – Cylinder enclosing the FPA for the Poynting theorem integration.

by

$$P = \operatorname{Re} \oint_{\text{disk}} S_z ds \quad (3.28)$$

where S_z is the component of the Poynting vector in the \hat{z} direction.

Feed Pattern

In order to understand the putative feed pattern that this encircled power condition would produce, it is helpful to consider the reciprocal transmit case. The total absorption of the incident power corresponds to the conjugate match of the incoming field (see Section 5.1.1 for more detail). In the transmit mode, the ideal FPA of a given radius generates the same fields as the received fields but reverses the direction of travel. An infinite array would reproduce the uniform aperture illumination of the incident wave, truncated sharply at the dish edge. As the array size reduces, the sharp truncation is rounded with some spillover and some reduction of the field at the dish edge. Ultimately the pattern reduces to the pattern of a typical horn feed with a strong edge taper.

Normalization

The power in the focal plane is normalized by dividing it by the maximum available power in the limit of increasing FPA size. That is the power intercepted by the reflector for an on-axis incident plane wave with power flux density S_{incident} .

$$P_{\text{available}} = \oint_{\text{dish}} S_{\text{incident}} ds = 2\pi \int_0^{D/2} S_{\text{incident}} \rho' d\rho' = \frac{\pi D^2 S_{\text{incident}}}{4}. \quad (3.29)$$

A consequence of using the on-axis or boresight power as the reference is that the actual power available to the FPA as the scan angle increases is reduced by $\cos \theta_s$. This normalization was chosen as designers are generally interested in scan loss relative to the on-axis efficiency.

3.6.1 Tapered Aperture

The focal plane calculations described above show the maximum power available from a uniform aperture distribution. This conjugate match condition

however, while maximizing gain, produces higher than desirable spillover for a low-noise radiotelescope. In order to investigate the effect of increasing the taper of the aperture illumination beyond that occurring with the conjugate-field match described above, the amplitude of the incident plane wave is apodized by reducing the field strength of the incident plane wave toward the edge of the dish.

A raised parabolic taper is used with a value at the edge that is 15 dB lower than the centre:

$$\frac{E_{\text{incident}}(\rho')}{E_{0\text{incident}}} = 1 - (1 - C) \left(1 - \left(\frac{\rho'}{D/2} \right)^2 \right) \quad (3.30)$$

where ρ' is the radius from the centre of the dish and

$$C = 10^{-15/20} = 0.178. \quad (3.31)$$

The focal plane fields are then calculated as for the uniform aperture. Fig. 3.6 shows diagrammatically the effect of this tapering on both the focal plane and far field.

Normalization—Tapered Aperture

Careful normalization is required to compare these results with the uniform cases. Apodizing the reflector illumination is equivalent to introducing ohmic losses attenuating the power received. The total power available is less than the uniform case by the factor

$$\eta_{\text{apodized}} = \frac{\oint_{\text{disk}} |E_{\text{incident}}(\rho')|^2 ds}{\oint_{\text{disk}} |E_{0\text{incident}}|^2 ds} = C + \frac{(1 - C)^2}{3} \quad (3.32)$$

Tapering the feed pattern, however, effectively reduces the reception toward the outer edge of the dish but increases the reception toward the centre of the dish without introducing ohmic or scattered loss.

The total power in the focal plane is less than that for the uniform distribution because the directivity is reduced. This factor is given by the

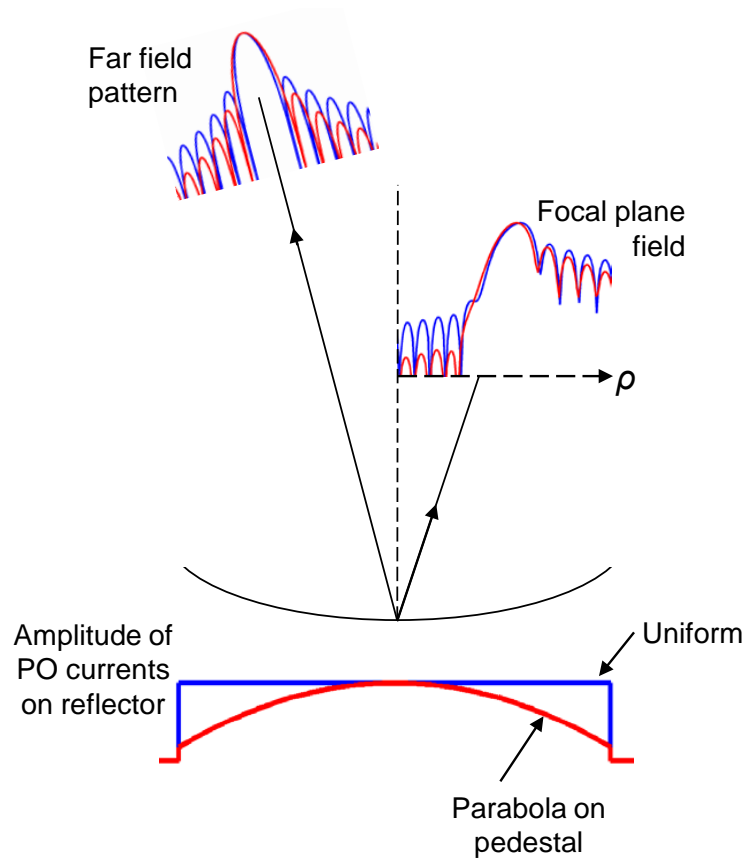


Figure 3.6 – This diagram shows the effect of tapering the aperture on both the focal plane and far field. In both cases the sidelobes are reduced.

taper efficiency for the raised-parabolic distribution [27]

$$\eta_{\text{taper}} = \frac{3(1+C)^2}{4(1+C+C^2)} \quad (3.33)$$

For an infinite FPA, the efficiency for the tapered aperture is η_{taper} and the fraction of encircled power is

$$\eta_{\text{enc}} = \frac{P_{\text{encircled}} \eta_{\text{taper}}}{P_{\text{available}} \eta_{\text{apodized}}}. \quad (3.34)$$

The tapered aperture is modelled to find if it differs markedly from the uniform aperture.

3.7 Encircled Power—Implementation

Computer code was written in MATLAB² to perform the calculations outlined above. With the inclusion of data display routines the number of lines of code came to $\sim 15\,000$.

The fields in the focal plane were calculated by integrating the fields from 8 samples per wavelength in the reflector. Convergence checks show that the focal plane power is within $2 \times 10^{-7}\%$ of the value for 32 samples in the reflector. The density of the points in the focal plane was set at 8 times the sampling criterion in (3.7). The \hat{z} directed focal plane power, S_z was integrated over disks of increasing radii to produce a function of encircled power vs. FPA radius. The radii corresponding to -1 dB and -3 dB (i.e. 79% and 50%) of the total incident power were then calculated using interpolation.

The significant computation time was reduced by using the student edition of a commercial antenna modelling software package, GRASP8-se,³ to perform the E and H field calculations. The tapered aperture calculations were however performed using the author's code as a method of readily apodizing the reflector currents in the GRASP8-se software was not available.

²MATLAB is a registered trademark of The MathWorks Inc., 3 Apple Hill Drive, Natick, MA 01760-2098, USA

³GRASP is a registered trademark of TICRA Engineering Consultants, Læderstræde 34, DK-1201 Copenhagen K, Denmark

Checks on the code included comparing the output with other published results such as [217] and with the output of GRASP8-se. The integrated focal plane power also approached the power intercepted by the reflector as the focal plane size increased.

3.8 Encircled Power—Results

Representative results are presented here for the focal plane fields, focal plane power flux density S_z and the integrated focal plane power. The integrated focal plane power data are then used to show the relationship between required FPA size, dish size, scan angle and F/D .

3.8.1 Focal-Plane Fields—Results

After setting up the reflector geometry and exciting it with a plane wave, the induced currents are used to calculate the electric \vec{E} and magnetic \vec{H} fields in the focal plane. The \hat{x} , \hat{y} and \hat{z} components are plotted for an on-axis and scanned incident wave in Figures 3.7 and 3.8. The plots are normalized to the equivalent power of maximum \hat{z} component of the Poynting vector, S_z . That is the power flux density corresponding to the x directed E field is calculated as

$$S_{E_x} = \frac{1}{S_{z\max}} \frac{1}{2\eta_0} E_x E_x^* \quad (3.35)$$

For the x directed H field the power flux density is calculated as

$$S_{H_x} = \frac{1}{S_{z\max}} \frac{\eta_0}{2} H_x H_x^* \quad (3.36)$$

The subscripts are appropriately substituted for the y and z directed fields.

Under plane wave or far field conditions, E_y , E_z , H_x , H_z are all zero as are S_x and S_y . In the focal plane of a paraboloid, however, there are cross-polarized components of the fields of E_y and H_x as well as the presence of axial components E_z and H_z .

The cross-polar field components peak at 6 and 8% of the peak of S_z for the $\theta_s = 0^\circ$ and $\theta_s = 3^\circ$, $F/D = 0.4$ cases respectively. These can be accommodated by an FPA with two polarizations.

The axial components (\hat{z} directed) are much higher for both the \vec{E} and \vec{H} fields. With the normalization used, it reaches about 20% of the peak of

3. FPA Size and Encircled Power Calculations

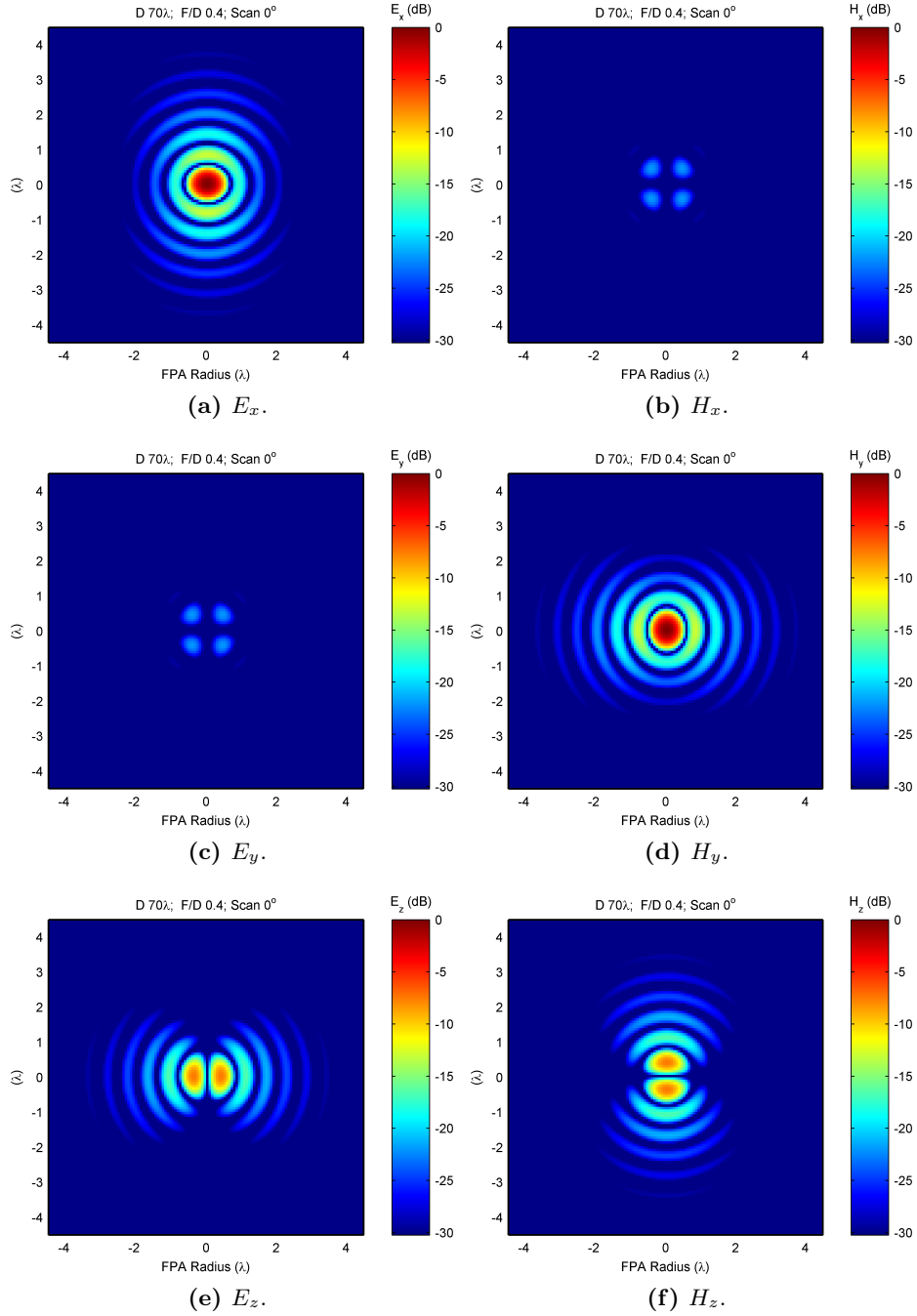


Figure 3.7 – Focal plane electric \vec{E} and magnetic \vec{H} fields for an on-axis plane wave. $F/D = 0.4$, $D = 70\lambda$, $\theta_s = 0^\circ$.

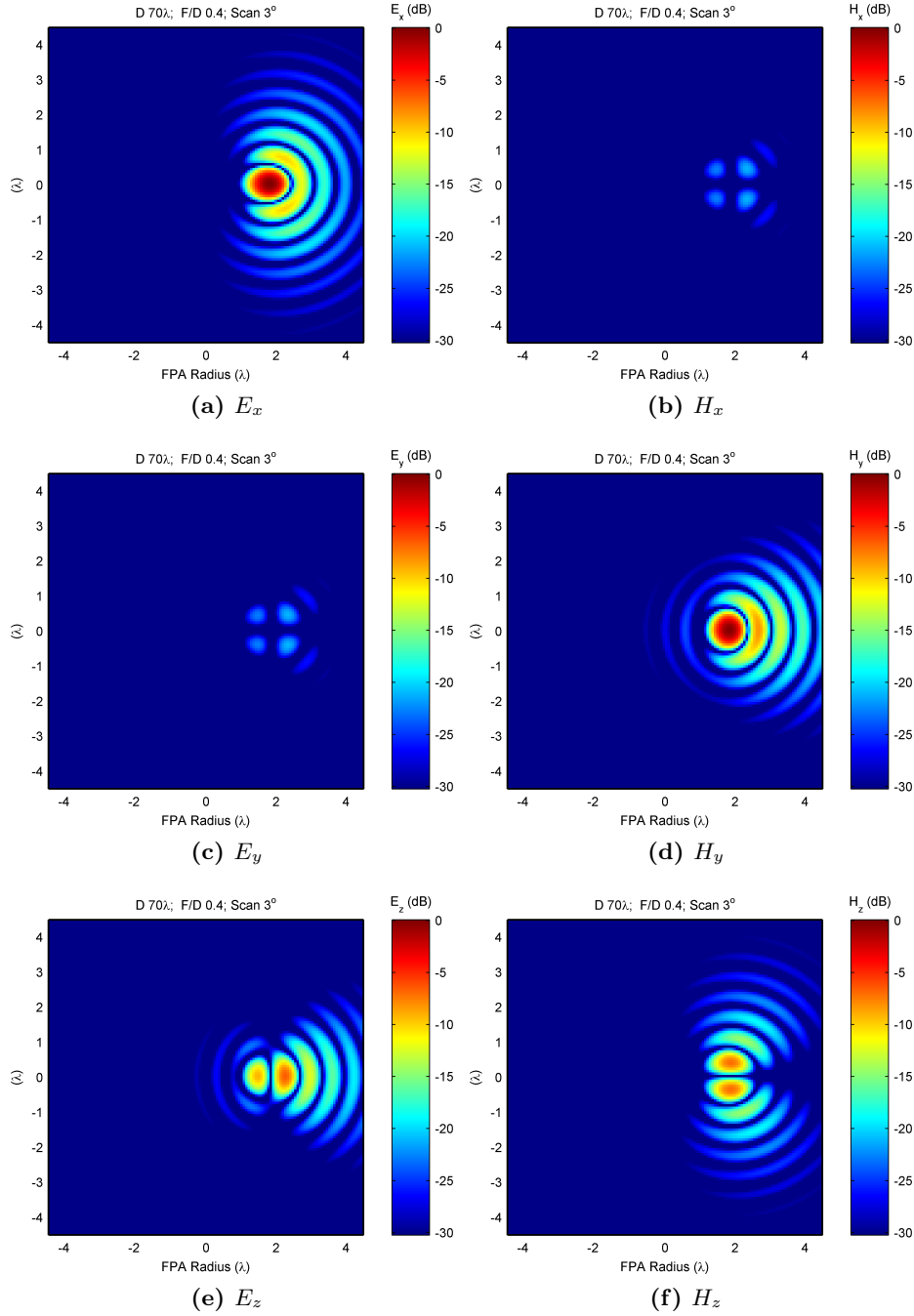


Figure 3.8 – Focal plane electric \vec{E} and magnetic \vec{H} fields for a scanned plane wave. $F/D = 0.4$, $D = 70\lambda$, $\theta_s = 3^\circ$.

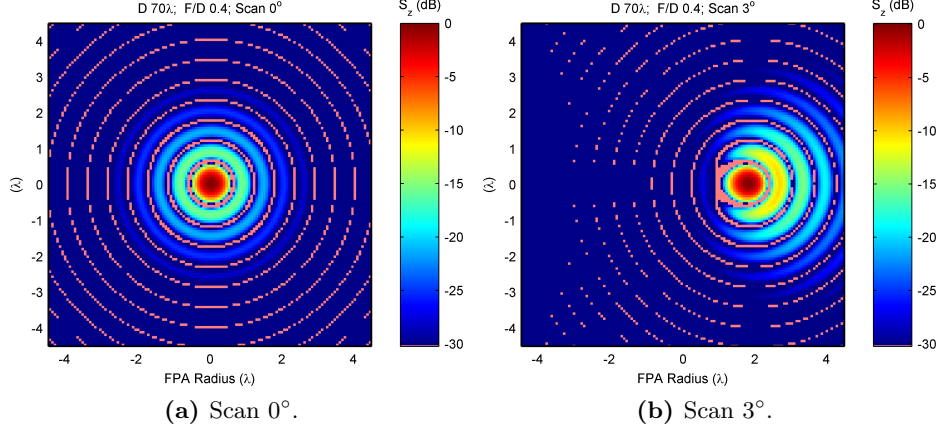


Figure 3.9 – Focal plane Poynting vector— \hat{z} component, S_z . $F/D = 0.4$, $D = 70\lambda$. Negative regions are marked in pink.

S_z for both the E and H field in both the $\theta_s = 0^\circ$ and $\theta_s = 3^\circ$ cases. For $F/D = 0.25$, greater dish curvature provides more \hat{z} directed currents and E_z and H_z are 41% of the peak of S_z . For $F/D = 2$ they are only 0.8% of the peak of S_z .

The axially directed fields can be significant sources of reflection if the FPA does not present an impedance match and therefore absorb them. This is clearly seen in Hay’s investigation [85] of the common and differential mode excitations of the chequerboard array’s feed lines where including of the common or monopole mode increases the efficiency.

The nature of the focal plane fields shows that neither the electric field nor magnetic field alone can be used to adequately evaluate the power present in the focal plane. Hence both are needed to calculate the energy flow, represented by the Poynting vector, \vec{S} , in the focal plane.

3.8.2 Focal-Plane Power-Flux-Density—Results

The focal plane fields are used to compute the \hat{z} component of the Poynting vector S_z (Fig. 3.9). The encircled power, the integral of S_z , is shown in Fig. 3.10 for a number of cases. As F/D is reduced, the nulls in the Airy pattern turn into negative regions (marked in pink in Fig. 3.9 and seen in Fig. 3.10a). Minnett and Thomas [198] discuss this in detail and show the energy flow forms vortices circulating into and out of the focal plane.

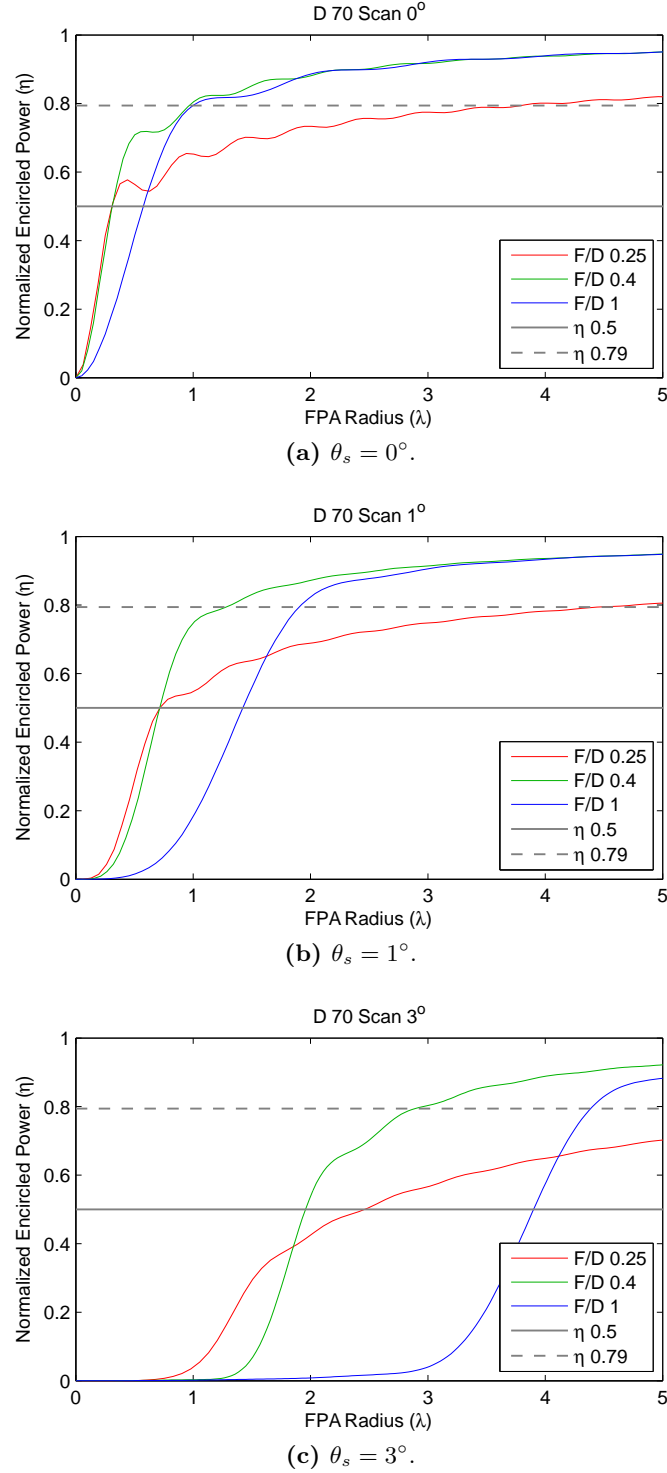


Figure 3.10 – Encircled power focal plane power vs. FPA radius, $D = 70\lambda$.

Table 3.1 – FPA size parameters calculated.

Parameter	Values
D/λ	10, 30, 70, 140, 160
F/D	0.25, 0.3, 0.35, 0.4, 0.5, 0.6, 0.8, 1, 2
θ_s ($^\circ$)	0, 1, 2, 3, 3.57, 4, 6, 8, 10, 15, 20
FoV for θ_s (deg^2)	0, 3, 13, 28, 40, 50, 113, 201, 314, 707, 1257

The negative differential in the integrated power curves (Fig. 3.10a) presents an apparent paradox where making an FPA larger reduces the total power received. A rigorous resolution would require the model to include the interaction between the FPA and the impinging fields and removing the assumption that no power impinges on the top of the array. Our model ignores this interaction, but the negative regions are included as they are required for conservation of energy. This is confirmed by the integrated focal plane power tending asymptotically toward the incident power.

The parameter space of possible FPA system designs was explored by calculating the focal plane fields for a range of dish diameters D , focal ratios F/D and scan angles in beamwidths θ_{BW} . The main values used for each parameter are listed in Table 3.1. Fields were not calculated for every combination and some other combinations are included Appendix A.

The F/D value of 0.35 was chosen to match the value for the Westerbork Synthesis Radio Telescope (WSRT) and the scan angle of 3.57° to match the SKA specification of a 40 deg^2 FoV.

A sample of results is shown in Figs. A.1 to A.18 Appendix A.

3.8.3 FPA Size—Results

The primary aim of calculating the focal plane fields is to understand the relationship between the required FPA size, the FoV or scan angle θ_s and the dish geometry, F/D and D . The FPA size, radius R , for each set of parameters is determined by the point at which the efficiency η_{enc} reaches the nominal levels of 50% and 79%. These results are shown in Tables A.1 and A.2 in Appendix A.

As noted in Section 3.8.2, the η_{enc} vs. R curves are not all monotonic due to the negative regions of S_z (Fig. 3.10). If the $\eta_{\text{enc}} = 50\%$ or 79% intercept occurs in one of these regions, the lowest value of R is used. Even where the

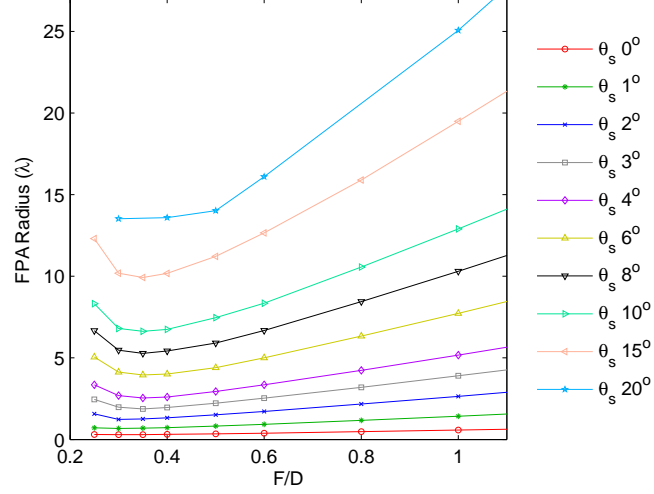


Figure 3.11 – FPA radius vs. F/D , $\eta_{\text{enc}} = 50\%$, $D = 70\lambda$.

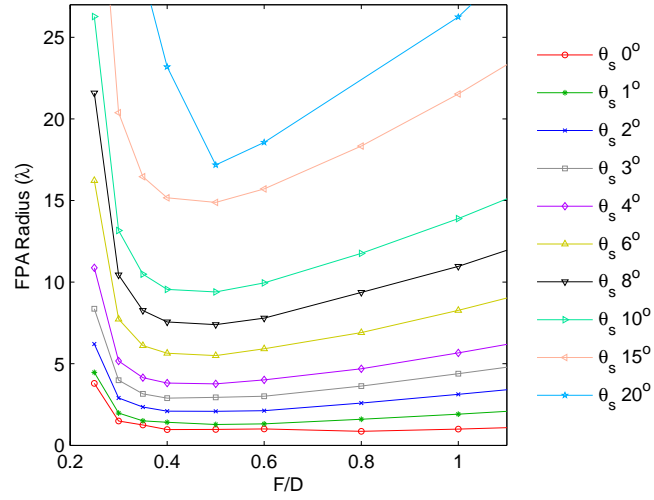


Figure 3.12 – FPA radius vs. F/D , $\eta_{\text{enc}} = 79\%$, $D = 70\lambda$.

curve is monotonic, the step like nature can result in the calculation being ill-conditioned.

The results for the dish diameter D of 70λ are shown graphically. Figs. 3.11 and 3.12 shows FPA radii against F/D and Figs. 3.13a and 3.13b show FPA radii against angle for a selection of the calculated values. The ill-conditioning mentioned above is particularly apparent for on-axis beams and is responsible for the irregular nature of the $\theta = 0^\circ$ curve in Fig. 3.12.

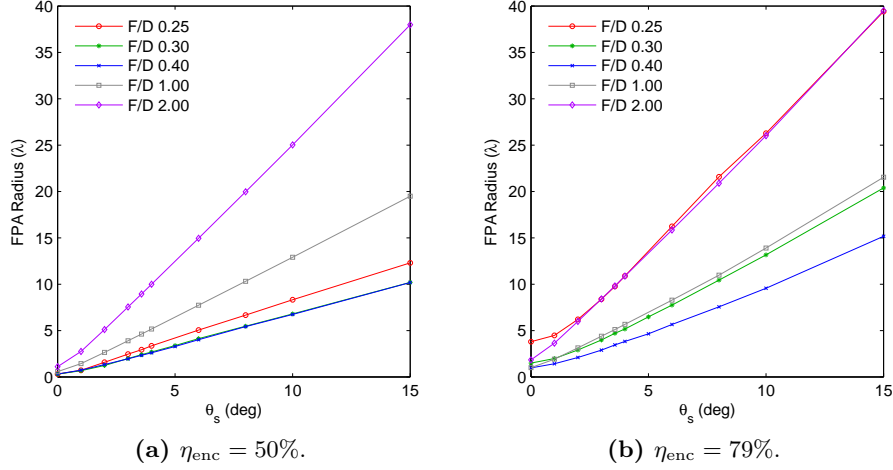


Figure 3.13 – FPA radius vs. scan angle θ_s for $D = 70\lambda$. In (a) the curves for $F/D = 0.3$ and $F/D = 0.4$ almost overlies each other and in (b) the curves for $F/D = 0.25$ and $F/D = 2$ almost overlies each other.

3.8.4 Tapered Aperture Results

The tapered aperture calculations (see Section 3.6.1) were made for an edge taper of 15 dB, $D = 70\lambda$, $F/D = 0.4$ and a range of angles. Fig. 3.14 shows the focal plane power, S_z for uniform and tapered apertures for high (4°) and extreme (10°) scan angles. The patterns are very similar but the tapered aperture pattern is more compact with the sidelobes dropping off faster than the uniform pattern.

The integrated power for three angles is shown with the uniform distribution results in Figs. 3.15a to 3.15c. As the FPA becomes very large, the conjugate-match-feed efficiency tends to unity whereas the tapered feed tends to the value of η_{taper} from (3.33) (0.86 for a 15 dB edge taper).

Note that the integrated power for the taper is greater than for the uniform case in some sections. In this model the total efficiency is the product of the taper efficiency η_{taper} and the spillover efficiency η_{spill} [27]. The tapered aperture case corresponds to a feed with lower η_{taper} and higher η_{spill} than the conjugate match (uniform aperture) case for a given FPA radius. For smaller FPAs, the difference in η_{spill} between the two cases can dominate and results in the overall efficiency of the tapered feed being greater. This is seen in Fig. 3.15. We know, however, that the conjugate-match feed provides the maximum efficiency and so conclude the tapered case is non-physical where

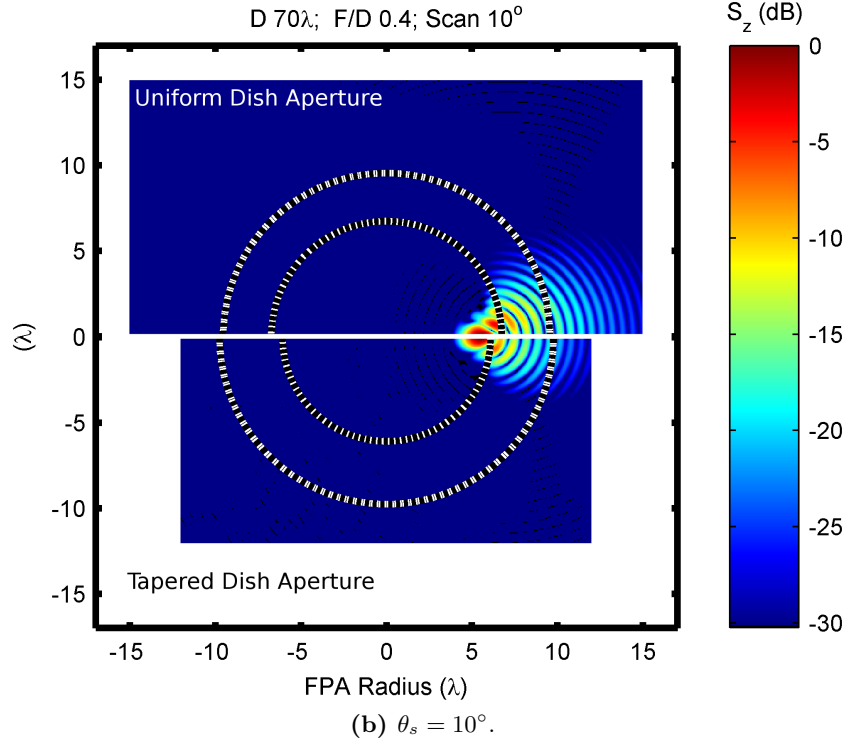
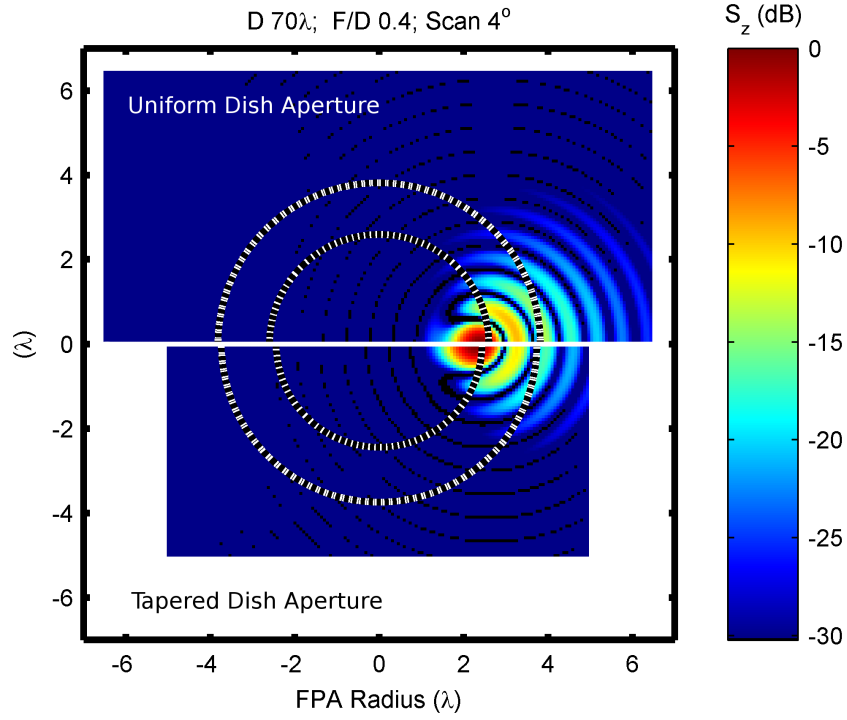
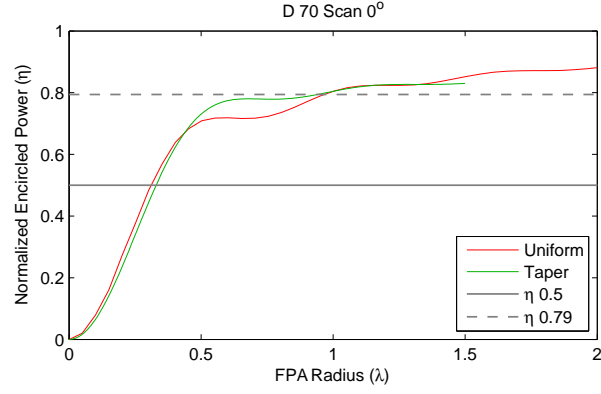
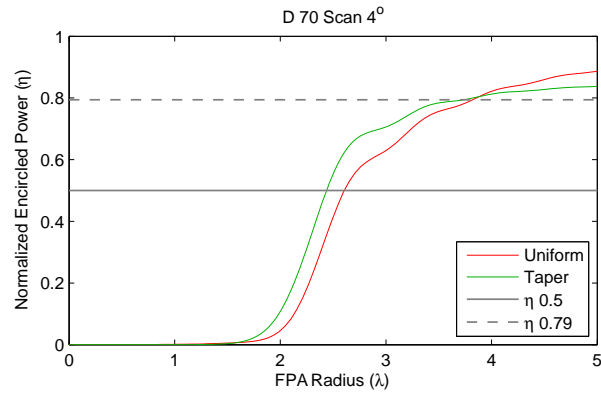


Figure 3.14 – Tapered and uniform S_z . $D = 70\lambda$, $F/D = 0.4$.

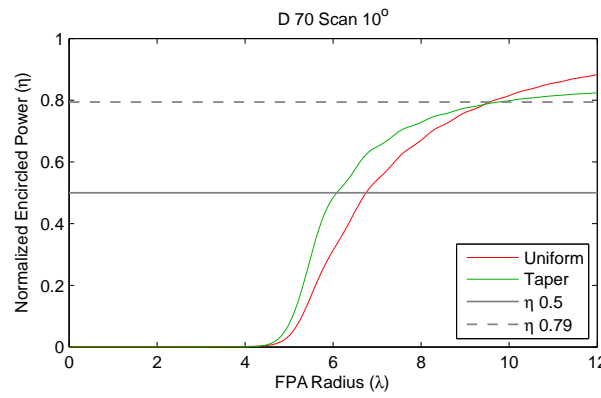
3. FPA Size and Encircled Power Calculations



(a) $\theta_s = 0^\circ$.



(b) $\theta_s = 4^\circ$.



(c) $\theta_s = 10^\circ$.

Figure 3.15 – Tapered and uniform encircled power, $D = 70\lambda$, $F/D = 0.4$.

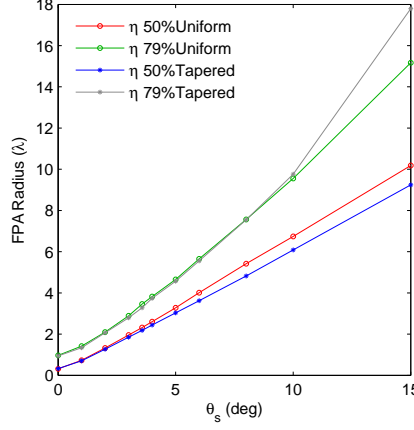


Figure 3.16 – FPA radius vs. scan angle θ_s . $D = 70\lambda$, $F/D = 0.4$ —tapered and uniform apertures.

it provides higher efficiency than the conjugate match case. This may be due to the feed being too small to realize the directivity implied by the taper.

Recalling that the original aim of investigating whether introducing a taper substantially changes the relationship between R , F/D , θ_s and D , the uniform and tapered aperture results are compared in Fig. 3.16. The differences in FPA radius are small however, particularly for $\eta_{\text{enc}} = 79\%$.

3.9 Encircled Power—Observations and Discussion

3.9.1 Independence of Dish Size

In Section 3.5 it was seen that the simple models were independent of dish diameter when θ_{BW} was used for the scan angle. The PO modelling supported this for all but extreme conditions. The distortion of the Airy pattern was more extreme for lower focal ratios F/D and so an investigation was conducted to comparing the dish diameters $D = 30$ and $D = 70$ for the focal length $F/D = 0.3$. Fig. 3.17 shows the similarity between the fields for a scan angle of $\theta_{\text{BW}} = 4$.

Fig. 3.18 shows the FPA radius function tends to a constant as the dish size increases. Fig. 3.19a shows the difference in the FPA radius required for normalized scan angles up to $\theta_{\text{BW}} = 15$. The analysis in this chapter has normalized the efficiency η_{enc} to the total collected power for boresight

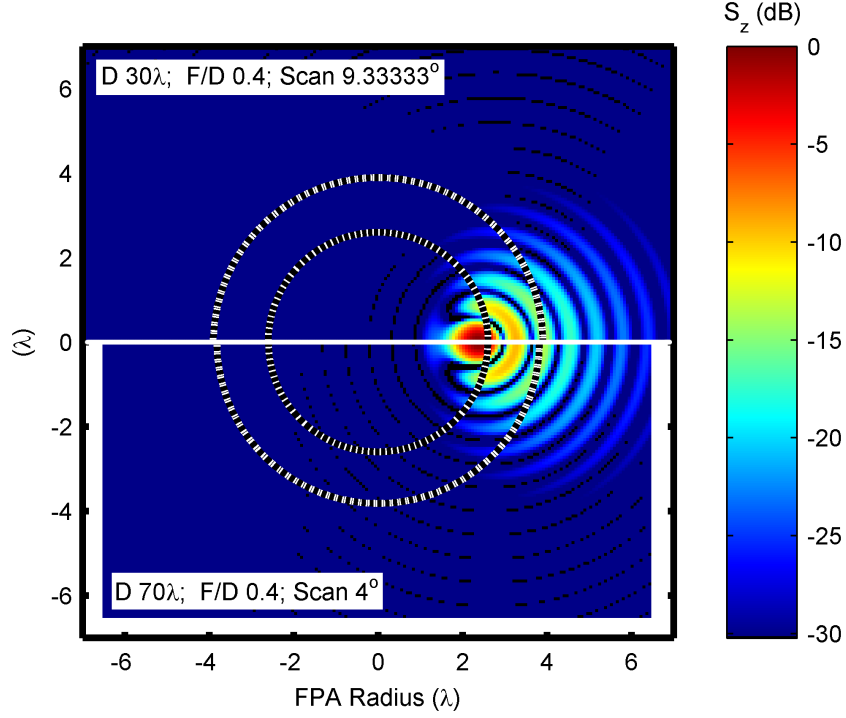


Figure 3.17 – Focal plane power S_z for two dish sizes, $D = 30\lambda$ and 70λ , $F/D = 0.4$. While the different beamwidths, from different dish sizes, result in the different scan angles of 9.3° and 4° as shown, the scan angle divided by beamwidth is the same for the two cases ($\theta_{BW} = 4$).

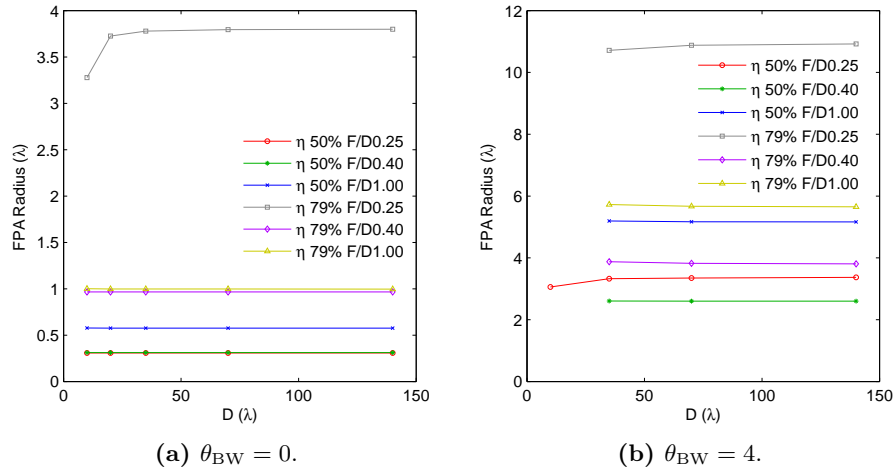


Figure 3.18 – FPA radius vs. dish size D . In (a) the curves for $\eta_{enc} = 50\%$ and $F/D = 0.25$ and $F/D = 0.4$ almost overlie each other and for $\eta_{enc} = 79\%$ and $F/D = 0.4$ and $F/D = 1$ almost overlie each other.

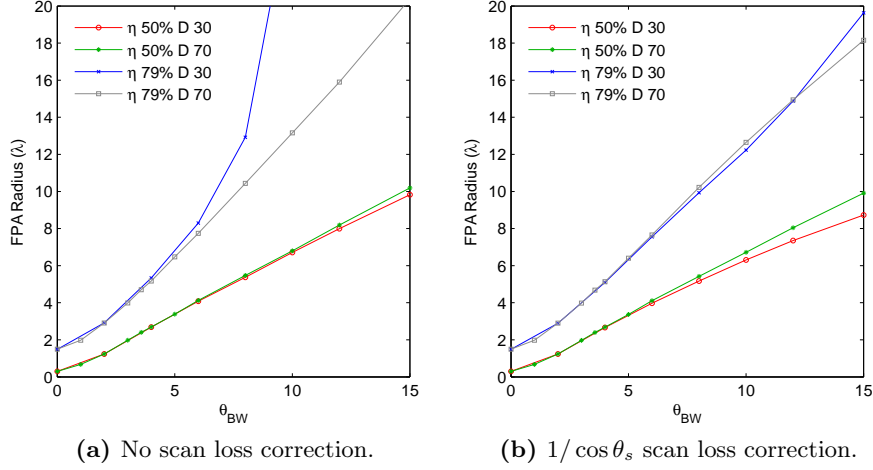


Figure 3.19 – FPA radius vs. θ_{BW} with and without scan loss correction for two dish sizes.

incidence ($\theta_s = 0$) but the total available power for a given scan angle is reduced by a factor of $\cos \theta_s$. For small angles this is small but for this comparison, it becomes significant: for instance for $\theta_{BW} = 15$ and $D = 30$, $\theta_s = 35^\circ$ and $\cos \theta_s = 0.82$. The small gradient of the η_{enc} vs. R curve for $\eta_{enc} = 79\%$ increases the sensitivity of this effect. Fig. 3.19b demonstrates the result when the $\cos \theta_s$ is accounted for.

Considering these results, we conclude the FPA radius is independent of dish size for a given θ_{BW} at least within the following conditions:

- $D \geq 30$,
- $F/D \geq 0.3$,
- $\theta_{BW} \leq 6$ for $\eta_{enc} = 79\%$ and $\theta_{BW} \leq 15$ for $\eta_{enc} = 50\%$ with no scan loss correction and
- $\theta_{BW} \leq 12$ for $\eta_{enc} = 79\%$ and $\theta_{BW} \leq 10$ for $\eta_{enc} = 50\%$ with scan loss correction.

This reduction from three to two independent variables greatly simplifies FPA system parameter space studies.

3.9.2 Feed Blockage

Consideration of blockage produced by the feed has been deferred in the model so far. This has been deliberate as it breaks the dish-size indepen-

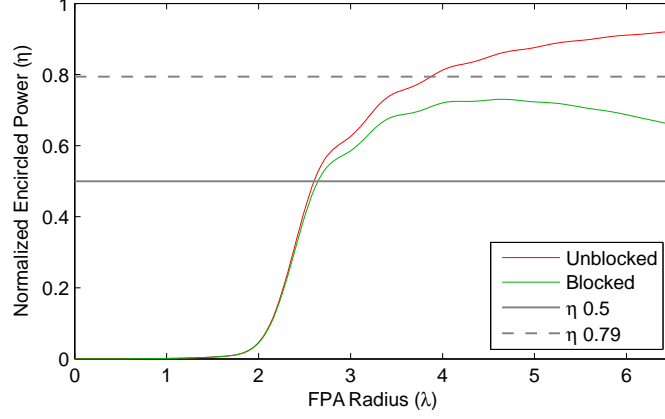


Figure 3.20 – Efficiency vs. FPA radius, $D = 35\lambda$, $F/D = 0.4$, $\theta_s = 8^\circ$ ($\theta_{BW} = 4$)—blocked and unblocked aperture. A typical taper of 12 dB, producing in $\eta_{\text{taper}} = 0.983$ is used (Table 7.1b, [27]).

dence property discussed above. It is an important factor, however, for dishes where the area of the FPA is a significant percentage of the aperture. The impact of blockage on sidelobes is discussed in more detail in Section 8.4.1. Diffraction from the feed package can also be deleterious for the overall performance, both by raising sidelobes and reducing the efficiency. It will not be included in these rule-of-thumb calculations, however, as it is dependent on the specifics of the feed package. In the PO modelling used here, possible approaches include

- reducing integrated power in the focal plane by a factor corresponding to the blockage and
- excising the shadow of the feed from the reflector currents when calculating the focal plane fields.

For the former Stutzman [27] gives the blockage efficiency as

$$\eta_{\text{blockage}} = \left(1 - \frac{1}{\eta_{\text{taper}}} \left(\frac{2\rho}{D} \right)^2 \right)^2 \quad (3.37)$$

where inclusion of η_{taper} , the taper efficiency, compensates for the usual concentration of feed pattern toward centre of the dish. For larger FPAs, however, it is possible for the beamforming to reduce the feed pattern directed toward the blocked area of the dish (see Section 8.3). Nonetheless, the general behaviour can be seen by using (3.37) as shown in Fig. 3.20.

Excising the feed shadow, requires the recalculation of the focal plane fields for each FPA radius and so is computationally intensive and is more useful once the dimensions of a system are close to finality.

Clearly as the FPA size increases relative to the dish size, the blockage eventually becomes a dominant factor and efficiency reduces significantly. An offset design may be more appropriate if a very large FPA is required.

3.9.3 Fit of FPA Size to a Closed Form Function

The FPA radii corresponding to $\eta_{\text{enc}} = 50\%$ and $\eta_{\text{enc}} = 79\%$ for various scan angles and F/D values listed in Appendix A can be used in design processes in a number of ways. As shown above, for most practical parameter limits, θ_s and D can be combined into θ_{BW} leaving the FPA radius R a function of only two rather than three variables. This is why many more cases with $D = 70\lambda$ were evaluated than the other dish sizes.

While the data can be accessed as a lookup table or with or without interpolation, a closed form function is useful for preliminary design calculations. To find a relatively simple closed form function the Airy pattern and BDF were used as the starting point and terms added until a reasonable fit to the data was found. The following approach was used to add terms to the function:

1. Optimize current set of coefficients to find the best fit.
2. Look at the two dimensional error function and propose a term that may improve the fit.
3. Add the term and repeat the first step until the errors are sufficiently small.

As the FPA system cost is very sensitive to the number of elements and hence area of the FPA and the FoV is roughly proportional to the FPA area, the function that was minimized in the optimization was the relative area.

To achieve a reasonable fit it was found necessary to limit the F/D domain to 0.25–1 and split it at $F/D = 0.4$. The scan angle was limited to the θ_{BW} range of 1–5, corresponding to the most likely range of values to be considered in radio astronomy designs. For F/D values below 0.4 a standard polynomial proved more efficient than the ad hoc function (i.e. required fewer coefficients for the same error).

3. FPA Size and Encircled Power Calculations

Table 3.2 – FPA-size-function coefficients.

F/D	η_{enc}	c_1	c_2	c_3	c_4	c_5	c_6
< 0.4	50%	2.63	−1.503	0.21	0.207	0.151	
	79%	20.887	−13.967	−0.843	2.382	0.62	
≥ 0.4	50%	−0.629	0.002	0.202			
	79%	0.601	0.093	−0.162	−0.461	0.106	0.119

Table 3.3 – FPA-size function—FPA radius and area errors.

F/D	η_{enc}	$\max \Delta R$	$\max \Delta \text{Area}$	$\max \frac{\Delta \text{Area}}{\text{Area}}$	$\text{rms} \frac{\Delta \text{Area}}{\text{Area}}$
< 0.4	50%	0.178	3.565	0.162	0.079
	79%	1.204	77.721	0.264	0.139
≥ 0.4	50%	0.442	28.346	0.176	0.061
	79%	0.117	8.004	0.089	0.027

The resulting ad hoc function, using (3.21) and (3.16), is

$$R = R_{\text{BDF0}} + R_{\text{Airy}} (c_1 + c_2 a + c_3 a^2 + c_6 a^3) + \max(0, c_4 + c_5 a b + c_7 a) \quad F/D \geq 0.4 \quad (3.38)$$

and the polynomial is

$$R = c_1 + c_2 a + c_3 b + c_4 a^2 + c_5 a b + c_6 b^2 + \dots \quad (3.39)$$

$$= \sum_{m=1}^M \sum_{n=1}^m c_{[(m-1)m/2+n]} a^{m-n} b^{n-1} \quad F/D < 0.4 \quad (3.40)$$

where $a = 1/(F/D)$ and $b = \theta_{\text{BW}}$. The coefficients c_n are given in Table 3.2 and the errors in Table 3.3.

Fig. 3.21 shows the functions (3.38) and (3.40) compared to the simple FPA size models from Section 3.5. The simple functions generally overestimate the FPA size required, particularly for $0.35 \leq F/D \leq 0.5$. The exception is the beam-deviation factor plus Airy pattern for $\eta = 79\%$. This model underestimates the spreading of the Airy pattern as the focal ratios decreases and as the scan angles increases.

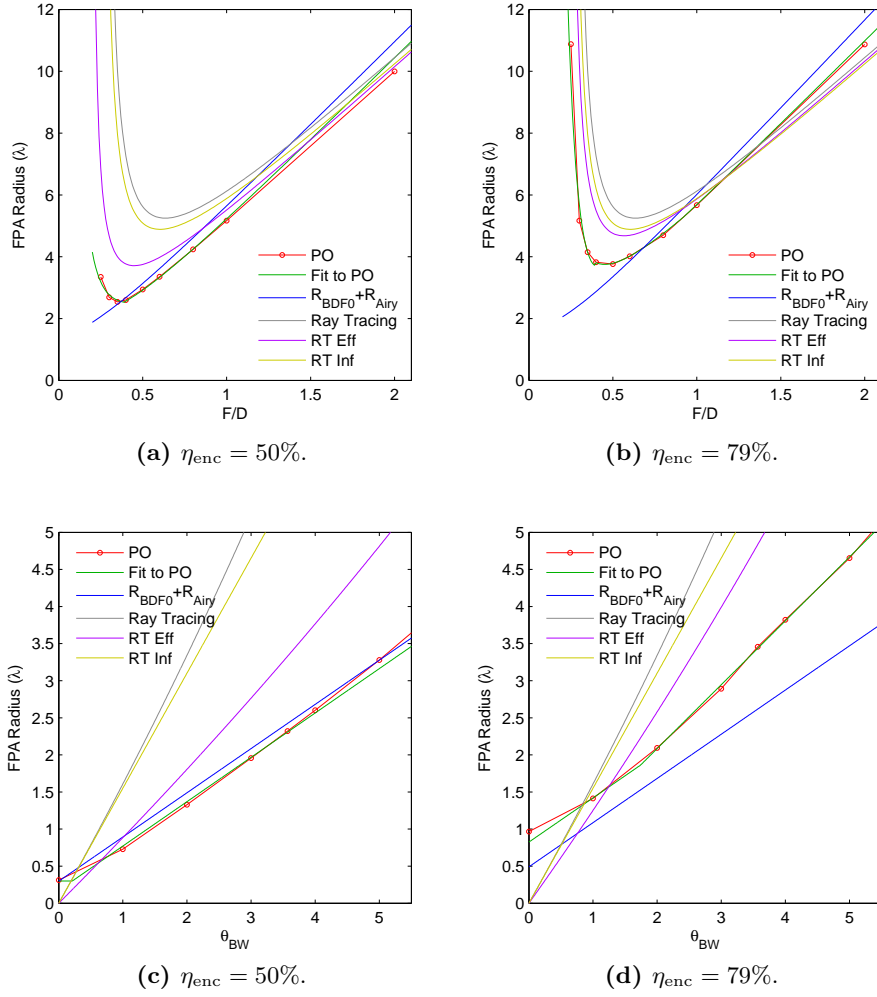


Figure 3.21 – FPA radius required to achieve 50 and 79% aperture efficiency with $D = 70\lambda$. (a) and (b) FPA radius vs. F/D for $\theta_{\text{BW}} = 4$. (c) and (d) FPA radius vs. θ_{BW} for $F/D = 0.4$. The various models discussed in the text are shown. The traces are:

PO: physical optics model,

Fit to PO: the functions in this section, (3.38) and (3.40),

$R_{\text{BDF0}} + R_{\text{Airy}}$: beam deviation factor and Airy pattern, (3.25),

Ray Tracing: ray tracing encompassing 100% of the energy (3.10),

RT Eff: ray tracing with the dish size reduced to match η_{enc} ,

RT Inf: the high frequency limit for ray tracing (3.12).

Table 3.4 – Linear FPA-size-function coefficients.

F/D	η_{enc}	d_1	d_2
0.35	50%	0.026	0.641
0.35	79%	0.426	0.928
0.40	50%	0.174	0.598
0.40	79%	0.363	0.861
0.43	50%	0.148	0.629
0.43	79%	0.269	0.873
0.45	50%	0.135	0.650
0.45	79%	0.221	0.883
0.50	50%	0.109	0.703
0.50	79%	0.140	0.913

Using (3.24), the linear approximation to R_{BDF0} , for a given F/D value, (3.38) and (3.40) reduce to linear equations in θ_{BW} :

$$R = d_1 + d_2\theta_{\text{BW}}. \quad (3.41)$$

The coefficients for this equation, d_1 and d_2 , are listed in Table 3.4. The F/D values match the prototype FPAs from Table 2.1.

3.9.4 Optimum F/D

The required FPA radius against F/D generally follows a J-shaped curve (Figs. 3.11 and 3.12). The increases at either end of this curve are due to:

Low F/D The distortion of the Airy pattern increases, spreading it away from the centre of the focal plane (Fig. A.5a).

High F/D The Airy pattern moves further from the centre for a given scan angle due to the longer focal length (Fig. A.14b).

The focal field also distorts as the scan angle increases with the focal plane power decreasing inside the peak value and increasing beyond it [198] (compare Figs. A.2c and A.4c).

The 50% encircled power plots (Fig. 3.11) shows a broad minimum in FPA radius at $F/D = 0.35$ and the $\eta_{\text{enc}} = 79\%$ plots (Fig. 3.12) show a broad minimum at $F/D = 0.5$. These values hold for scan angles at least up to $\theta_{\text{BW}} = 20^\circ$.

3.9.5 Alternative Focal-Plane Integrations

Square vs. Circular FPA

If the proposed FPA design is square, the power integral in the focal plane can be done over a square rather than a circle. The general behaviour is very similar. Another shape used for FPAs is the hexagon but in this case the circle is likely to be a sufficiently close match.

Number of Elements Needed for Each Beam

Beamforming on a subset of the FPA elements can reduce the beamformer costs significantly. A modification of the approach used here has been used to determine the number of elements needed to form such a beam. The approach is to find the power enclosed in circles (or squares) centred to maximize their efficiency. A small study for this purpose for $F/D = 0.5$ showed centring circles on the peak predicted by the BDF was very close to the optimum, moving by only 0.2λ for θ_{BW} up to 10.

3.9.6 Other Reflector Geometries

The most comprehensive approach to deal with geometries other than the prime-focus axisymmetric antenna analysed here is to repeat the approach and recalculate the focal plane fields as done by [218]. Alternatively the equivalent focal ratio and scan angle can be calculated. Lee and Rahmat-Samii [187] provide relevant formulas for offset prime focus antennas. The equivalence formulae for Cassegrain and Gregorian systems can be found in many places including Hannan [219] and Granet [220] and offset Cassegrain systems in Wong [221].

3.10 Comparison with Measured and Modelled Referenced Data

Recently a number of FPA systems have been designed in detail and some have been tested. This section compares published results for these against predictions from the encircled power work presented here. The predicted scan angles from the PO calculations in this chapter are compared with the published measured or modelled results for these systems. The published

data includes effects that are not included in the PO calculations and so generating valid comparisons involves a number of steps as outlined below.

The approach for predicting the performance from the PO calculations is as follows:

1. Using the published dimensions of the FPA, estimate the radius of an equivalent circular FPA corresponding to the actual FPA shape. This was taken as a circle inscribed or circumscribed on the geometry of the published FPA. A value of half an element spacing was added to the radius to account for reception of fields beyond the centre of edge element.
2. Calculate the normalized scan angles, θ_{BW} , corresponding to $\eta_{enc} = 50\%$ and $\eta_{enc} = 79\%$ from the PO encircled power calculations. This was achieved by inverting the function (3.38) or (3.40) using a numerical search. An equivalent approach could be used to find a closed form approximation of scan angle as a function of FPA radius and F/D .

The approach for finding an equivalent scan angle from the published results is as follows:

1. Estimate the on-axis efficiency corresponding to the FPA radius using the PO calculations, $\eta_{enc,\theta=0}$.
2. From the publication, find the calculated or measured on-axis efficiency $\eta_{pub,\theta=0}$.
3. Scale η_{enc} by the ratio of published and calculated on-axis efficiencies to find the corresponding efficiency at the edge of the FoV scan angle

$$\eta_{pub,\theta_s} = \eta_{enc} \frac{\eta_{pub,\theta=0}}{\eta_{enc,\theta=0}} \quad (3.42)$$

4. Find the angle corresponding to $\eta_{enc} = 50\%$ and $\eta_{enc} = 79\%$ from the publication.

The data from this procedure is shown in Table 3.5.

For the BYU cases, the efficiency has significant dips in the FoV, possibly due to the element spacing undersampling the focal plane. With the superposition of this ripple on top of the scan loss, calculating a scan angle for $\eta_{enc} = 79\%$ proved too difficult. The scan angle for $\eta_{enc} = 50\%$ is much better conditioned with a sharp falloff in efficiency. Explicit efficiency values were not available and so the sensitivity result—proportional to η_{ap}/noise —was used with the noise assumed to be constant with scan angle.

Table 3.5 – FPA size reference results.

System	Apertif ^a			BYU ^b		ASKAP ^c	
Data type	Model	Model	Model	Model	Meas.	Model	Model
Equiv. disk ^d	Ins.	Ins.	Ins.	Circ.	Circ.	Ins.	Circ.
F/D	0.35	0.35	0.35	0.43	0.43	0.5	0.5
D (m)	25	25	25	20	20	12	12
Freq (MHz)	1200	1420	1600	1600	1600	1250	1250
R_{FPA} (m)	0.40	0.40	0.40	0.28	0.28	0.45	0.57
R/λ	1.60	1.89	2.13	1.50	1.50	1.88	2.36
θ_{HPBW} ($^\circ$) ^e	0.70	0.59	0.52	0.66	0.66	1.40	1.40
η_{enc} EP ^f on-axis	0.84	0.85	0.87	0.83	0.83	0.85	0.90
θ_{BW} Ref. $\eta = 50\%$				2.34	2.46	2.50	3.44
θ_{BW} EP ^g $\eta = 50\%$	2.46	2.91	3.29	2.15	2.15	2.52	3.23
Rel. error $\eta = 50\%$				9%	14%	−1%	6%
θ_{BW} Ref. $\eta = 79\%$	1.43	1.69	1.91			1.57	2.12
θ_{BW} EP ^g $\eta = 79\%$	1.27	1.58	1.84	1.23	1.23	1.82	2.45
Rel. error $\eta = 79\%$	13%	7%	4%			−14%	−13%

^a Data taken from Figs. 3a, 4a and 4b in [11].

^b Data taken from Fig. 6b in [135].

^c Data taken from Fig. 8b in [85]. As a two dimensional FoV is provided, the inscribed case uses an inscribed circular FoV from the Fig. 8b and the circumscribed case uses a circumscribed circular FoV.

^d Inscribed or circumscribed.

^e Nominal half power beamwidth (3.1)

^f Encircled Power—On-axis efficiency determined from Table A.1.

^g Encircled Power—Scan angle calculated by inverting (3.38) and (3.40).

The reference efficiency vs. angle curves for Apertif also showed some, albeit smaller, ripple in the FoV. The model also shows a flattening or increase in efficiency beyond about 1.5° which prevented angles being extracted for $\eta = 50\%$.

The ASKAP paper shows a very flat FoV followed by a sharp fall off at the edge. The $\eta = 79\%$ angle is in this flat region and is very sensitive to matching the on-axis efficiencies accurately. The steep falloff yields a much less sensitive $\eta = 50\%$ angle. The choice of radius for circumscribed case cuts off the outer diagonal element based on the assumption that too much of the focal spot would be lost past the edges in the corner.

The relative error in Table 3.5 shows the encircled power calculations presented here matches the more comprehensive modelling and measurements for the calculation of scan angle to within 14%. An error in the FPA radius transfers roughly linearly to the scan angle (see Fig. 3.13) and a difference of 14% in scan angle corresponds to a difference of only 0.2λ to 0.4λ in R . This is comparable to the uncertainty in selecting the equivalent FPA radius for the FPAs used here.

3.11 Summary

By calculating the encircled power reaching the focal plane for a wide range of scan angles, reflector sizes and focal lengths it was shown how these parameters related to the required FPA size. This method is relatively insensitive to different aperture tapers resulting from different beamforming weights.

By scaling the scan angle to nominal half-power beamwidths, the FPA size function can be reduced to a function of only two variables: scan angle in beamwidths and focal ratio F/D . A closed form function was fitted to the calculations over a range of scan angles and focal ratios covering most radio-astronomy applications. The numerical results have been compared with modelled and measured references with fair agreement showing the utility of the approach. The formula is limited to symmetric prime focus paraboloids but other geometries can be accommodated either by repeating the modelling exercise or by using focal length equivalence formulae.

The reduction of the data to a formula provides a readily calculable approximation to the FPA size over a practical design domain. The results

showed that simpler rules of thumb differed substantially from the encircled power calculations. This has implications for FPA system cost estimations and can be incorporated into cost optimization formulae.

Other avenues of investigation along these lines include investigating other geometries such as spherical [80] and cylindrical reflectors. Non-planar FPAs may provide superior performance, particularly for low F/D reflectors and high fields of view as suggested by some studies [222] and implementations [62, 208, 223]. Offsetting the array from the focal plane could also be investigated although others have found the focal plane is very close to optimal [224, 225].

Chapter 4

Gain and Noise Model for a Beamformed Array

This chapter starts with a brief review of the modelling used for designing FPAs before presenting the model that is used for the beamforming theory in the following chapter. The model is applicable to active receiving arrays where it is assumed there is no access to internal ports—only to setting the beamformer weights and the beamformed output. First a suitable reference plane, dividing antenna and electronic gain is established. There are a number of possibilities here and it is important that it is clearly defined as Van Cappellen points out [226]. Then a model for a single antenna is developed where the standard figures of merit, gain G , noise temperature T and their ratio G/T are expressed in terms of the embedded-element radiation patterns and the surrounding noise scene.

The single antenna development is used to introduce a number of standard antenna concepts in the terms of the chosen reference plane before introducing the complexity of an array. The figures of merit are then expressed for the array with the weighting vector as a parameter.

The focus is on a model suitable for the performance of an assembled low-noise receiving array but the results are general. This emphasis is to establish a foundation for the FPA evaluation in Chapters 6, 7 and 8.

4.1 Detailed FPA Models

Accurate modelling of FPAs challenge the limits of current electromagnetic modelling capabilities and this section provides a brief review. An FPA system can be divided into three main areas: (1) the concentrator (reflector or lens), (2) the FPA antenna structure and (3) the electronics attached to the FPA.

A reflector, including the feed support struts, may typically be modelled using physical optics [227] and the geometric theory of diffraction [228], such as that provided in commercial software, e.g. GRASP [229].

Practical FPAs are expected to have 50–200 elements and the fine detail required to model the array elements combined with the total size makes modelling computationally intensive. Infinite array models have been found to be of limited value due to the different excitations required and edge effects, a problem also encountered in conventional phased arrays. The most promising progress has been made with the characteristic basis function method [85, 99, 161, 230–233] which exploits the repetitive nature of the structure whilst retaining the ability to deal with the finite nature of the array.

The close proximity of the elements in a dense FPA leads to mutual coupling being a major factor [97, 98, 234]. The requirement for wide band FPAs for radio astronomy compounds this issue: the maximum element separation at the top of the band is limited to about $\lambda/2$ (see Section 3.4) and so at the bottom of the band the elements are typically only $\lambda/4$ apart.

FPAs in radio astronomy applications are required to have very low noise performance, a feature that differentiates them from many other applications. To achieve this, low noise amplifiers (LNAs) are attached directly to the FPA terminals with beamforming carried out in subsequent processing, either in the analogue or digital domain. This avoids the noise contribution from any beamforming network and allows the signals to be split and reused to form different beams whilst having no effect on each other. It also isolates the impedances seen by the elements from the beamforming weighting. The LNAs and receiver chains need to be included in the analysis as they contribute to the reflected signal and noise. Noise is transmitted in the desired direction of the signal flow and also back into the array [98, 235] and coupled into other array elements.

The signals from each element are then combined in the beamformer. In an analogue beamformer the accuracy and stability of the weighting electronics has limitations. In a digital beamformer, issues such as the resolution of the analogue to digital converter arise. For both analogue and digital beamformers, linearity, cross talk and the resolution of the weights may affect the system performance.

The reflector, FPA and receiver electronics interact with each other. Multiple reflections will be present between the reflector and the FPA and, although a secondary consideration, they can have an impact on the frequency response of the system, causing *baseline ripple* [236–238]. With relatively large FPAs in moderately small dishes (i.e. $\sim 50\text{--}200\lambda$), such as in the ASKAP design, these effects will be greater than in applications such as fitting an FPA to large reflectors such as the 64-m Parkes Telescope and the 100-m Green Bank Telescope where the blockage is a much smaller fraction of the total aperture. Results from a prototype FPA system suggest FPAs may reduce this effect [86] although the mechanisms may require further study [239].

The interactions between the LNAs and FPA have been found to be critical to the performance of closely coupled arrays [20, 149, 240–243]. These interactions can be modelled using network theory with scattering, admittance or impedance matrices. The LNAs usually provide sufficient isolation between their outputs and inputs for the following circuitry to be considered separately. An important consequence is the impedance seen by the LNA inputs,¹ which is important for their noise performance, is not affected by the beamformer weighting. If, in contrast, an analogue beamformer is placed before the LNA, the weighting can affect the impedance seen by the LNA.

Recent work on FPA modelling has proceeded at Brigham Young University [242, 244–246] and ASTRON [32, 231, 247, 248] with detailed network modelling. In FPA development at CSIRO the required performance has been made possible through a joint design optimization between the LNA and FPA design [41, 85, 99].

In this work, a detailed theoretical model of the components and their interactions is not pursued. The objective is to describe a model that utilizes

¹This impedance is different from the *active impedance* which does change with weighting. The former entails noise waves generated by the LNA and latter involves the signal excitation. These two are uncorrelated.

only readily measured data from an operational radiotelescope. The model assumes a linear system with sufficiently narrow band processing to allow quasi-monochromatic analysis (see Section 2.1.1).

4.2 Active Antenna Noise Temperature and G/T

The standard definitions of antenna gain (used by the IEEE [34]) and noise temperature assume the ability to separate the antenna from the receiving electronics and it is common practice to do so [249]. This becomes a problem with *active antennas* where separating the electronics and the antenna is very difficult or impossible. Even when there is a convenient port for measurements, if either component is not well matched, care must be taken to account for mismatch loss and for any change in the receiver's noise performance when presented with a different source load. The problem becomes more acute when the antenna has an array with amplifiers before the signals are combined. These are referred to as *signal-processing antennas* by Ksien-ski [250] and Jacobs [251] or more commonly as *active arrays* [31, 252, 253].

Waldman and Wooley [252] described a theory for noise temperature for an active receiving array which converts the active array to an equivalent passive array and combiner with a single port and a two port receiver with gain and noise performance equivalent to the active system. Their proposed measurement techniques however require access to or modelling of the individual receiver paths.

Jacobs [251] proposed using a reference antenna with an identical receiver to those in the array to evaluate the performance of the array. This requires producing a receiver that is identical to those in the array, a condition that may be impossible where the coupling between the elements of the array is strong. It also will not apply if the elements in the array are not all very similar. This is a likely scenario given edge effects in an array. Nonetheless from a point of view of understanding the performance, this approach will often aid in the array development, particularly in gaining confidence in measurement techniques.

Lee [253] approached G/T in the field of active aperture array radars considering amplitude weighting of identical elements. In [20] Warnick provides insight into the various contributors to the sensitivity of an array. The formulation, however, requires knowledge of a number of parameters in the

array. In [33] Warnick et al. have brought together different figure of merit definitions and related them to the conventional definitions.

All of the approaches referred to above require modelled or measured knowledge of parameters internal to the active antenna. These are important for designing the system and identifying ways of improving the system. It is valuable however to have a way of finding the figures of merit for an active antenna without this knowledge.

The approach used here was informed from measurements made on low noise block down converters used in the satellite subscription television industry [254]. This in turn was based on standard practice in evaluating radiotelescopes and their feeds. While it is an extension of the approaches in Ashkenazy et al. [255] and Pozar and Kaufman [256], the author is unaware of this being proposed elsewhere as a general approach for defining noise temperature and G/T for active antennas.

The issue facing characterization of active receiving antennas where there is no access to internal ports is inseparability of the antenna losses and the electronic gain. The conventional location of the reference plane² for G/T definitions, between the antenna and the receiver, is inaccessible in an active antenna or active array and so the performance is more readily expressed with a different reference plane.

The definition of G/T in the relevant IEEE standard [257] states that any reference plane can be used as long as both the gain and the noise temperature are referred to the same plane. Care needs to be taken to account for the match presented in both directions. Noise that comes from before that plane is attenuated by any loss it incurs as does any signal and so the ratio signal to noise ratio (SNR) remains constant as does its equivalent, G/T .

Taking the reference plane on the radiation side, that is the *radiation port*, of the antenna losses allows us to treat the antenna as a ‘black-box’ where the relevant parameters are (1) the radiation pattern, (2) the response at the receiver output to a point source of known strength and (3) the noise at the receiver output. Two important consequences are:

1. the antenna gain and directivity are equivalent, and

²The boundary used for signal analysis in a waveguide or transmission line is usually a plane but when the boundary is in a region where the fields are unguided, such as surrounding an antenna, it is usually a closed surface. It is common however to use the expression *reference plane* for these surfaces as well.

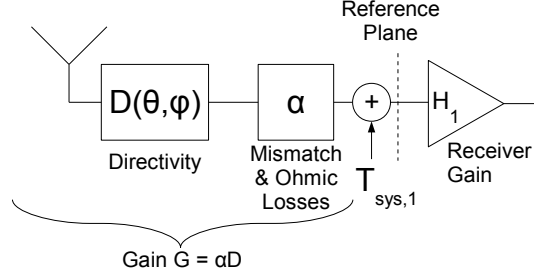


Figure 4.1 – Model for a receive antenna with the reference plane between the antenna and the receiver. The ohmic losses in the antenna contribute to T_{sys} according to the temperature of the structure.

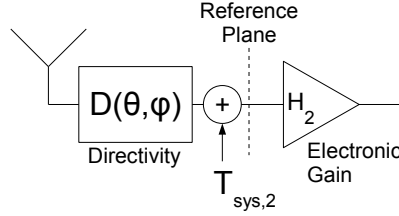


Figure 4.2 – Model for a receive antenna with shows the reference plane moved to before the losses in the antenna.

2. antenna losses are incorporated in the *electronic gain*.

Fig. 4.1 shows a model for a receive antenna with the reference plane between the antenna and the receiver and Fig. 4.2 shows the reference plane placed before the losses in the antenna. For the first case,

$$G/T = \frac{\alpha D}{T_{\text{sys},1}} \quad (4.1)$$

where D is the directivity and $T_{\text{sys},1}$ is the system temperature referred to the plane shown in Fig. 4.1. For the second case,

$$G/T = \frac{D}{T_{\text{sys},2}}. \quad (4.2)$$

The values of G/T for (4.1) and (4.2) are the same as $T_{\text{sys},2} = T_{\text{sys},1}/\alpha$. Note also that $H_2 = \alpha H_1$.

Consider the immersion of the antenna in a scene of uniform radiation characterized by a black body temperature, T_{scene} . The power at the output

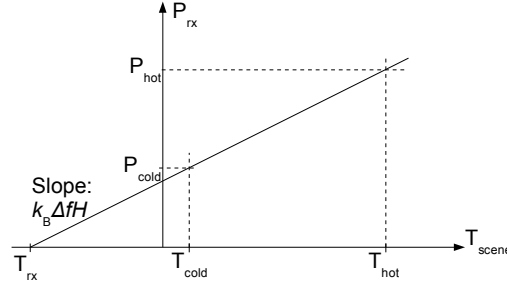


Figure 4.3 – Power at receiver port from uniform temperature noise scene.

of the receiver is then

$$P_{rx} = k_B \Delta f H (T_{scene} + T_{rx}) \quad (4.3)$$

where k_B is the Boltzmann constant, Δf is the bandwidth and H is the electronic power gain (or loss). T_{rx} is an equivalent noise temperature that includes the receiver noise and losses in the antenna. The noise contribution of the scene is important in the analysis of the antenna performance and is incorporated as an independent term. An example is the feed spillover in prime focus reflector antennas.

By taking measurements at two values of T_{scene} , T_{hot} and T_{cold} , resulting in P_{hot} and P_{cold} , T_{rx} and $\Delta f H$ can be determined from (4.5) as follows:

$$Y_{hot/cold} = \frac{P_{hot}}{P_{cold}} = \frac{k_B \Delta f H (T_{hot} + T_{rx})}{k_B \Delta f H (T_{cold} + T_{rx})}. \quad (4.4)$$

Rearranging gives

$$T_{rx} = \frac{Y_{hot/cold} T_{cold} - T_{hot}}{1 - Y_{hot/cold}}. \quad (4.5)$$

Using data from either measurement,

$$\Delta f H = \frac{P_{rx}}{k_B (T_{scene} + T_{rx})}. \quad (4.6)$$

If Δf is known, H can be determined. Fig. 4.3 shows these relationships graphically.

The directivity is then the response to a plane wave of known power flux density, S ($\text{W} \cdot \text{m}^{-2}$) for the selected direction referred to the same plane:

$$P_{rx} = S A_e H \quad (4.7)$$

where A_e is the effective area in terms of directivity, $D(\theta, \phi)$:

$$A_e = \frac{\lambda^2}{4\pi} D(\theta, \phi). \quad (4.8)$$

Therefore

$$D(\theta, \phi) = \frac{P_{\text{rx}}}{H} \frac{4\pi}{\lambda^2 S}. \quad (4.9)$$

If the source is noise like, the spectral power flux density $\mathbb{S} = S/\Delta f$ ($\text{W} \cdot \text{m}^{-2} \cdot \text{Hz}^{-1}$) is often known rather than the power flux density so:

$$D(\theta, \phi) = \frac{P_{\text{rx}}}{\Delta f H} \frac{4\pi}{\lambda^2 \mathbb{S}}. \quad (4.10)$$

In a similar fashion, the electronic gain can be defined for a transmitting antenna such that it incorporates losses in the antenna so the measured gain is the electronic gain times the directivity.

In this section it has been argued that the most convenient way to consider the G/T of an active receiving antenna is to take the reference plane as the radiation port (i.e. the gain reference is directivity). In principle, doing so allows a series of measurements to yield the system temperature and directivity without separating the antenna from the receiving system.

4.2.1 Reference Plane for a Radiotelescope

As discussed in Section 2.2, the key figure of merit for a radiotelescope is sensitivity or G/T , and for most ground based radiotelescopes, radiation from the surrounding scene, particularly the ground, contributes a significant portion of the system noise. This leads to a dilemma if the preceding approach to the reference plane is strictly adhered to. Consider two cases for a reflector antenna: (1) a sphere enclosing just the reflector and feed, and (2) a plane parallel with the ground, just above the antenna. The former excludes the scene radiation. The latter includes the major component of the scene radiation (the ground) but results in the directivity being the usual antenna directivity divided by the fraction of the antenna power pattern that is directed toward the sky, η_{sky} (see Section 7.6.4). An approach that includes the radiation from the ground and uses a standard definition of directivity is preferred.

The common practice is to use a reference plane at the port connecting the feed system to the receiver and then add the scene radiation as a separate component to system temperature. The scene radiation component in this case needs to be referred to this port. The sum of this scene radiation and any noise coming from losses in the antenna is referred to as the antenna temperature T_{ant} . With active antennas such as FPA systems, this port is inaccessible and the reference plane is moved to a sphere enclosing the reflector and feed. Antenna losses are included in the receiver temperature and T_{ant} is the integral over all angles of $T_{\text{scene}}(\theta, \phi)$ weighted by the directivity (4.41). The system temperature is then taken as the sum of the receive and antenna temperatures (see Section 4.7).

Note that the signals of interest to radio astronomy are strictly part of T_{ant} . For discussions of system noise, however, it is convenient to use a background level of T_{ant} as measured when the antenna is directed away from all strong sources.

The system temperature, T_{sys} , is usually considered to include the contribution from a typical or actual noise scene surrounding the antenna. This component adds to the receiver temperature (see Section 4.7).

4.3 Polarization Match of an Antenna

The far field generated by single port transmitting antenna or array fed with a single or coherent source is always fully polarized. That is, for each direction from the antenna (θ, ϕ) (see Section 2.1.3), the polarization state of the field can be described by a polarization ellipse. By reciprocity, receiving antennas are sensitive to only one polarization for each incoming direction per port. That is, we can again find a polarization ellipse for each direction that will receive the maximum signal. Fields in the orthogonal polarization will not be received by that antenna port [22]. There can be exceptions to this in antennas that are not phase sensitive such as bolometers. Let the complex unit vector function $\hat{p}'(\theta, \phi)$ represent this perfectly matched polarization, and consequently any field in the orthogonal polarization $\hat{q}'(\theta, \phi)$ is not received. In ideal theoretical examples of antennas, the matched polarization \hat{p}' may be purely linear or circular and follow a desired polarization definition but in practice it will be elliptical to some degree at least in some directions and diverge from the desired polarization.

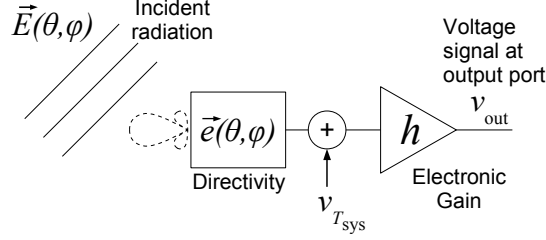


Figure 4.4 – Single port receiving antenna model.

4.4 Single Port Antenna Model

The description in the following sections establishes concepts and notation for a single port antenna before extending them to the more complex beamformed array. Particular attention is given to the voltages at the receiver port as they are the terms added in the beamformer for the array.

The model used is the single-port voltage parallel to the power model described in Section 4.2 (Fig. 4.2). The voltage rather than power gain is used as both amplitude and phase are needed for beamforming (Fig. 4.4). The expressions *signal voltage* and *noise voltage* will be used to refer to the values that are equal in magnitude to the square root of power.³ These voltages may not actually be realised anywhere, particularly in the case of a digital beamformer. The voltage signal at the output port in the presence of a desired plane wave field $E_p(t)$ and including the system noise is given by

$$v_{\text{out}}(t) = \left(\frac{\lambda}{\sqrt{2\eta_0}} E_p(t) e_p + v_{T_{\text{sys}}}(t) \right) h. \quad (4.11)$$

where λ is the free space wavelength, η_0 is the impedance of free space, e_p is the co-polarization field pattern, $v_{T_{\text{sys}}}$ is the noise from all sources referred to the input and h is the *electronic gain*, including ohmic losses in the antenna and receiver circuitry and gains of amplifiers. The derivation of the factor $\lambda/\sqrt{2\eta_0}$ is shown below in (4.22).

³These are the forward travelling voltages scaled to a unit impedance, and are the scattering matrix waves if the characteristic impedance is chosen appropriately, but to use the expression *wave* would be more confusing.

4.5 Directivity—Single Port Antenna

In this section a lossless transmitting antenna is used to establish an expression for directivity and reciprocity is used to consider an active receiving antenna. The receiving antenna expressions are then used to find the voltage signal response to an incident polarized wave and then extended to an arbitrarily polarized wave.

4.5.1 Transmitting Antenna

Consider an antenna radiating a total power of P_{radiated} . Let $\vec{E}(\theta, \phi, r)$ be the complex phasor representation of the resultant electric field. Let us define a complex vector quantity proportional to the electric field in the Fraunhofer region (far field), normalized so that its square has units of $\text{W} \cdot \text{sr}^{-1}$, i.e.:

$$\vec{E}_{\text{far field}}(\theta, \phi) = \lim_{r \rightarrow \infty} \frac{\vec{E}(\theta, \phi, r)}{\sqrt{2\eta_0}} r e^{-jkr} \quad (\text{W}^{1/2} \cdot \text{rad}^{-1}) \quad (4.12)$$

where θ , ϕ and r are spherical coordinates centred on a reference point of the antenna. It is convenient to normalize $\vec{E}_{\text{far field}}(\theta, \phi)$ so it is independent of the power driving the antenna, i.e.

$$\vec{e}(\theta, \phi) = \frac{\vec{E}_{\text{far field}}(\theta, \phi)}{\sqrt{P_{\text{radiated}}}} \quad (\text{rad}^{-1}). \quad (4.13)$$

This *field radiation pattern* of the antenna, $\vec{e}(\theta, \phi)$, is constrained to be perpendicular to the direction of propagation due to the far-field condition (i.e. $\vec{e} \cdot \vec{r} = 0$).

Summarizing the definitions from Sections 2.1.3 and 4.3, the following notation is used:

$\hat{p}(\theta, \phi)$: desired polarization, referred to as co-polarization.

$\hat{q}(\theta, \phi)$: unwanted polarization, referred to as cross-polarization.

$\hat{p}'(\theta, \phi)$: polarization transmitted by the antenna or matched to a receiving antenna.

$\hat{q}'(\theta, \phi)$: polarization orthogonal to $\hat{p}'(\theta, \phi)$. For a transmitting antenna, no power is transmitted with this polarization and for a receiving antenna it is rejected (reflected or absorbed in losses).

Consequently, the matched cross-polarization response by definition is zero ($e_{q'} = 0$) for all angles (θ, ϕ) . The voltage response of the antenna to incident radiation is then by definition

$$\vec{e}(\theta, \phi) = e_{p'}(\theta, \phi) \hat{p}' = e_p(\theta, \phi) \hat{p} + e_q(\theta, \phi) \hat{q} \quad (4.14)$$

where $e_p(\theta, \phi) = \vec{e}(\theta, \phi) \cdot \hat{p}$ and $e_q(\theta, \phi) = \vec{e}(\theta, \phi) \cdot \hat{q}$.

Leaving out the (θ, ϕ) dependency notation, the radiation intensity is (p38 [27]):

$$\begin{aligned} U &= P_{\text{radiated}} \vec{e}^* \cdot \vec{e} \\ &= P_{\text{radiated}} e_{p'}^* e_{p'} \quad (\text{W} \cdot \text{sr}^{-1}) \\ &= P_{\text{radiated}} (e_p^* e_p + e_q^* e_q). \end{aligned} \quad (4.15)$$

The total power radiated is the integral of U over the entire sphere, so

$$\frac{1}{P_{\text{radiated}}} \iint_{\Omega} U d\Omega = \iint_{\Omega} \vec{e}^* \cdot \vec{e} d\Omega = \iint_{\Omega} (e_p^* e_p + e_q^* e_q) d\Omega = 1 \quad (4.16)$$

where

$$\iint_{\Omega} d\Omega = \int_{2\pi} \int_{\pi} \sin \theta d\theta d\phi$$

denotes the integral over a sphere.

The directivity follows as $D = 4\pi U / P_{\text{radiated}}$ (p40 [27]) so we have

$$\begin{aligned} D &= 4\pi \vec{e}^* \cdot \vec{e} \\ &= 4\pi (e_p^* e_p + e_q^* e_q) \\ &= D_p + D_q \end{aligned} \quad (4.17)$$

where $D_p = 4\pi e_p^* e_p$ and $D_q = 4\pi e_q^* e_q$ are the partial directivities. Note that for the matched polarization \hat{p}' , $D = D_{p'}$ and $D_{q'} = 0$.

4.5.2 Receiving Antenna

We now use reciprocity to adapt this definition from a transmitting antenna to an active receiving antenna. Let the complex electronic voltage signal gain be h and $h^* h = H$ (Fig. 4.4). The phase of h will be defined below. Note that H includes any ohmic losses in the antenna. Using the effective area $A_{e,p} = D_p \lambda^2 / (4\pi)$, the power at the receiver output port in response

to a \hat{p} polarized wave with power flux density S_p is

$$\begin{aligned} P_{S_p} &= S_p A_{e,p} H \\ &= \frac{\lambda^2 S_p H}{4\pi} D_p. \end{aligned} \quad (4.18)$$

Rearranging (4.18) gives an expression for the directivity that will be used later:

$$D_p = \frac{4\pi}{\lambda^2 S_p H} P_{S_p}. \quad (4.19)$$

Using (2.10) and (4.18),

$$P_{S_p} = \frac{\langle E_p^*(t) E_p(t) \rangle}{2\eta_0} e_p^* e_p \lambda^2 h^* h. \quad (4.20)$$

where η_0 is the free space wave impedance.

Equation (4.20) is now used to find an expression for the voltage signal $v_p(t)$ at the receiver output port in response to a \hat{p} polarized wave with power flux density S_p .

Using the condition that $v_{\text{out}} = \sqrt{P_{\text{out}}}$, the amplitude of $v_p(t)$ is constrained by

$$P_{S_p} = \langle v_p^*(t) v_p(t) \rangle. \quad (4.21)$$

and

$$v_p(t) = \frac{\lambda}{\sqrt{2\eta_0}} E_p(t) e_p h \quad (4.22)$$

satisfies both (4.20) and (4.21). The phase of $v_p(t)$ is only important with respect to voltage signals from other antennas.

Rearranging (4.22) gives the co-polarized field pattern

$$e_p = \frac{\sqrt{2\eta_0}}{\lambda h} \frac{v_p(t)}{E_p(t)}. \quad (4.23)$$

Equation (4.13) gave the field pattern for a transmitting antenna. The equivalent for a receiving antenna can be found from (4.23) by referring the voltage signal response to the radiation port ($v_{p,\text{RadPort}} = v_p/h$). It is equal to the voltage response $v_{p,\text{RadPort}}$ to a plane wave with a power flux density of one watt per square wavelength, ($S_p = 1/\lambda^2$ ($\text{W} \cdot \text{m}^{-2}$)) or equivalently a field strength of $E_p = \sqrt{2\eta_0}/\lambda$ ($\text{V} \cdot \text{m}^{-1}$).

The field pattern for the orthogonal polarization e_q can be similarly defined. This definition is similar to Sinclair's *complex effective length vector* \mathbf{h} [258] (also Collin and Zucker [21, p. 105]): the two differences being (1) the effective length yields an open circuit voltage in response to the plane wave and the field pattern yields the normalized voltage into a load matched to the antenna port and (2) the effective length includes losses in the antenna whereas the field pattern, being based on directivity, rather than gain, includes no losses.

4.6 Arbitrarily Polarized Radiation—Single Port Antenna

An arbitrarily polarized field can be resolved into two orthogonal field components. The voltage signal at the receiver port is the sum of the responses to the two components, i.e.:

$$\begin{aligned} v(t) &= \frac{\lambda h}{\sqrt{2\eta_0}} \vec{E}(t) \cdot \vec{e} \\ &= \frac{\lambda h}{\sqrt{2\eta_0}} (E_p(t)e_p + E_q(t)e_q). \end{aligned} \quad (4.24)$$

The power from an arbitrarily polarized wave of S_{arb} is then (leaving out the (t) dependency notation):⁴

$$\begin{aligned} P_{S_{\text{arb}}} &= \langle v^* v \rangle \\ &= \frac{\lambda^2 H}{2\eta_0} [\langle E_p^* E_p \rangle e_p^* e_p + \langle E_q^* E_q \rangle e_q^* e_q \\ &\quad + \langle E_p^* E_q \rangle e_p^* e_q + \langle E_q^* E_p \rangle e_q^* e_p] \\ &= \lambda^2 H [S_p D_p + S_q D_q + 2\Re(S_{pq} e_p^* e_q)] \end{aligned} \quad (4.25)$$

where $S_{pq} = \langle E_p^* E_q \rangle / (2\eta_0)$ is the covariance of the fields and $D_{pq} = 4\pi e_p^* e_q$.

The received spectral power density is then

$$\mathbb{P}_{S_{\text{arb}}} = \frac{P_{S_{\text{arb}}}}{\Delta f} = \frac{\lambda^2 H}{4\pi} [\mathbb{S}_p D_p + \mathbb{S}_q D_q + 2\Re(\mathbb{S}_{pq} D_{pq})] \quad (\text{W} \cdot \text{Hz}^{-1}). \quad (4.26)$$

⁴Equation (4.25) is closely related to [21, eqn. (4.50)].

Using the matched polarization directivities, $D_{q'} = D_{p'q'} = 0$ and (4.26) becomes

$$\mathbb{P}_{\text{Sarab}} = \frac{\lambda^2 H}{4\pi} \mathbb{S}_{p'} D_{p'}. \quad (4.27)$$

If the radiation is unpolarized, the incident spectral power flux density is equally shared between any two orthogonal polarizations and so $\mathbb{S}_{p'} = \mathbb{S}_{q'} = \mathbb{S}/2$. From (2.11) and (2.12)

$$\mathbb{P}_{\text{unpolarized}} = \frac{\lambda^2 H \mathbb{S}}{4\pi} \frac{1}{2} D_{p'}. \quad (4.28)$$

This expression is used in finding sensitivity using a compact source of known flux (see Section 4.8). The peak of the main beam the directivities for the matched and desired polarizations are almost equal ($D_{p'} \approx D_p$) and so D_p is usually used in place of $D_{p'}$ in calculations.

To determine the received spectral power density from extended radio sources and the noise temperature scene surrounding an antenna, the spectral power flux density is integrated over the extent of the source or the entire sphere respectively. The spectral power flux density per unit solid angle is used in this case and using (2.7) and (2.8), is given by

$$\frac{\delta \mathbb{P}_{\text{Sarab}}}{\delta \Omega} = \frac{\lambda^2 H}{4\pi} [B_p D_p + B_q D_q + 2\Re(B_{pq} D_{pq})] \quad (4.29)$$

$$= \frac{k_B H}{2\pi} [T_p D_p + T_q D_q + 2\Re(T_{pq} D_{pq})] \quad (\text{W} \cdot \text{Hz}^{-1} \cdot \text{sr}^{-1}). \quad (4.30)$$

4.7 Noise—Single Port Antenna

In the field of radio astronomy, the major contributors to the noise received by the system are the black body radiation from sources around the antenna and the noise from the receiver. Section 4.2 shows how the external antenna noise, T_{ant} , and the receiver noise, T_{rx} , can be identified in an active antenna.

The noise that the receiver adds to the system is uncorrelated with the thermal noise from the scene and so we can simply add it to obtain an equivalent system temperature:

$$T_{\text{sys}} = T_{\text{rx}} + T_{\text{ant}}. \quad (4.31)$$

The spectral power density is then

$$\begin{aligned}\mathbb{P}_{T_{\text{sys}}} &= Hk_{\text{B}}T_{\text{sys}} \\ &= Hk_{\text{B}}T_{\text{rx}} + Hk_{\text{B}}T_{\text{ant}} \\ &= \mathbb{P}_{T_{\text{rx}}} + \mathbb{P}_{T_{\text{ant}}}.\end{aligned}\tag{4.32}$$

4.7.1 Receiver Noise—Single Port Antenna

The receiver noise contribution T_{rx} can be measured using two different uniform noise scenes as outlined in Section 4.2. It can be modelled with knowledge of the antenna port match, losses in the antenna, the receiver input port match and the noise parameters of the receiver. This contribution is usually heavily influenced by the antenna match, an issue that substantially complicates the analysis in the array environment.

4.7.2 Antenna Noise—Single Port Antenna

The usual method of calculating the contribution of the surrounding noise scene to the system temperature is outlined by Stutzman and Thiele [27] and Cortés-Medellín [259]. This section expands on the usual method with the voltage signal response at the receiver port in preparation for the array model.

Using the definition of \vec{E}_{Ω} in Section 2.1.2, the voltage signal at the receiver's output port is

$$v(t) = \frac{h\lambda}{\sqrt{2\eta_0}} \iint_{\Omega} \vec{E}_{\Omega} \cdot \vec{e} d\Omega.\tag{4.33}$$

The total spectral power density is

$$\mathbb{P}_{T_{\text{scene}}} = \frac{\langle v^*(t)v(t) \rangle}{\Delta f} = \frac{H\lambda^2}{2\eta_0\Delta f} \left\langle \iint_{\Omega} \vec{E}_{\Omega}^* \cdot \vec{e}^* d\Omega \iint_{\Omega} \vec{E}_{\Omega} \cdot \vec{e} d\Omega \right\rangle.\tag{4.34}$$

The general case of partially coherent sources is addressed by Collin and Zucker [21, p118] and Thompson et al. [13] but they conclude that radiation from the ground and most radio astronomy sources can be assumed to be spatially incoherent. This allows the power from each direction Ω to be added

linearly:

$$\mathbb{P}_{T_{\text{scene}}} = \frac{H\lambda^2}{2\eta_0\Delta f} \iint_{\Omega} \langle \vec{E}_{\Omega}^* \cdot \vec{e}^* \vec{E}_{\Omega} \cdot \vec{e} \rangle d\Omega \quad (4.35)$$

$$\begin{aligned} &= \frac{H\lambda^2}{2\eta_0\Delta f} \iint_{\Omega} \langle E_{\Omega,p}^* E_{\Omega,p} \rangle e_p^* e_p + \langle E_{\Omega,q}^* E_{\Omega,q} \rangle e_q^* e_q + \\ &\quad \langle E_{\Omega,p}^* E_{\Omega,q} \rangle e_p^* e_q + \langle E_{\Omega,q}^* E_{\Omega,p} \rangle e_q^* e_p d\Omega. \end{aligned} \quad (4.36)$$

Expressing this response in terms of an antenna temperature, referred to the antenna output port (rather than the receiver output port) and noticing the last two terms are conjugates of each other,

$$\begin{aligned} T_{\text{ant}} &= \frac{\mathbb{P}_{T_{\text{scene}}}}{Hk_B} \\ &= \iint_{\Omega} T_p e_p^* e_p + T_q e_q^* e_q + 2\Re(T_{pq} e_p^* e_q) d\Omega \end{aligned} \quad (4.37)$$

where using (2.7) and (2.8), T_p and T_q are the polarization components of the brightness temperatures:

$$T_p = \frac{\lambda^2}{4k_B\eta_0\Delta f} \langle E_{\Omega,p}^* E_{\Omega,p} \rangle \quad \text{and} \quad T_q = \frac{\lambda^2}{4k_B\eta_0\Delta f} \langle E_{\Omega,q}^* E_{\Omega,q} \rangle \quad (4.38)$$

and T_{pq} is the covariance of the fields,

$$T_{pq} = \frac{\lambda^2}{4k_B\eta_0\Delta f} \langle E_{\Omega,p}^* E_{\Omega,q} \rangle. \quad (4.39)$$

There are two important special cases of (4.37). The first is where the matched polarization definition \hat{p}' is used. Then $e_{q'}(\theta, \phi) = 0$ for all angles (θ, ϕ) and

$$\begin{aligned} T_{\text{ant}} &= \iint_{\Omega} T_{p'} e_{p'}^* e_{p'} d\Omega \\ &= \frac{1}{4\pi} \iint_{\Omega} T_{p'}(\theta, \phi) D(\theta, \phi) d\Omega. \end{aligned} \quad (4.40)$$

The second special case is where the noise scene is unpolarized so $T_p = T_q = T_{\text{scene}}$ and $T_{pq} = 0$. The formulation reduces to the usual method for calculating the noise scene contribution as this is the case with thermal black

body radiators:

$$T_{\text{ant}} = \frac{1}{4\pi} \iint_{\Omega} T_{\text{scene}}(\theta, \phi) D(\theta, \phi) d\Omega. \quad (4.41)$$

If the scene temperature is uniform, $T_{\text{ant}} = T_{\text{scene}}$, as used in Section 4.2.

The noise scene for a radiotelescope or satellite earth station reflector antenna is often broken down into the spillover (radiation from the ground reaching the feed directly), atmospheric and cosmic background radiation. In this case, the integral in (4.41) is evaluated by splitting it into corresponding sections of the enclosing sphere.

4.8 G/T —Single Port Antenna

The G/T for polarization \hat{p} can be found from the field patterns, the noise scene temperature and the receiver noise temperature. Recall that we have selected a reference plane that makes gain and directivity equivalent $G/T \equiv D/T$ (4.2). Using (4.17), (4.31) and (4.37), the gain over system temperature for a \hat{p} polarized plane wave is

$$G_p/T = \frac{D_p(\theta, \phi)}{T_{\text{sys}}} = \frac{4\pi e_p^* e_p}{T_{\text{rx}} + \iint_{\Omega} T_p e_p^* e_p + T_q e_q^* e_q + 2\Re(T_{pq} e_p^* e_q) d\Omega}. \quad (4.42)$$

Using (4.19) and (4.32) the G/T can be obtained from two measurements at the receiver port; namely the power P_{S_p} from a plane wave of known flux density S_p and the spectral power density from the noise scene and receiver noise $\mathbb{P}_{T_{\text{sys}}}$. Thus

$$\begin{aligned} G_p/T &= \frac{(4\pi P_{S_p})/(\lambda^2 S_p H)}{\mathbb{P}_{T_{\text{sys}}}/(k_B H)} \\ &= \frac{4\pi k_B}{\lambda^2} \frac{P_{S_p}}{S_p \mathbb{P}_{T_{\text{sys}}}}. \end{aligned} \quad (4.43)$$

Equation (4.43) is best used for high SNR situations such as observing a satellite. When using continuum sources for antenna evaluation, a Y-factor approach is used: the power is measured pointing at the source, P_{on} and then pointing to a region of sky nearby that is clear of strong sources, P_{off} .

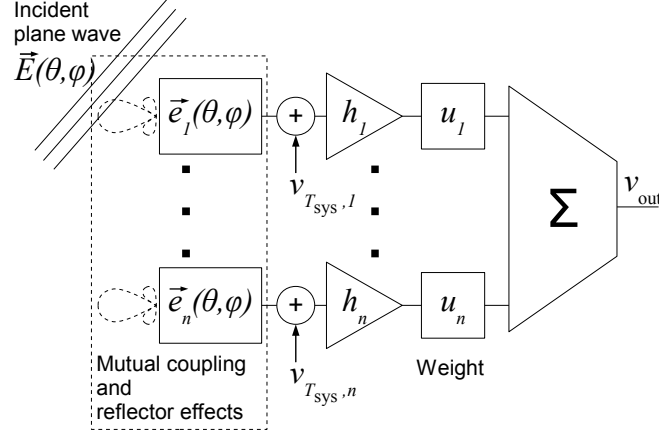


Figure 4.5 – Receiving array model.

Using (4.28) and (4.32), the Y-factor is

$$Y_{\text{src}} = \frac{P_{\text{on}}}{P_{\text{off}}} = \frac{\frac{\lambda^2 H}{4\pi} \frac{\mathbb{S}}{2} D_{p'} + H k_B T_{\text{sys}}}{H k_B T_{\text{sys}}}. \quad (4.44)$$

Rearranging gives

$$G_p/T = D_p/T = 4\pi \frac{2k_B(Y_{\text{src}} - 1)}{\lambda^2 \mathbb{S}} \quad (4.45)$$

Chapter 7 shows how these measurements are used to evaluate the performance of a prototype radiotelescope.

4.9 Antenna Array Model

In this section the previous development for a single receiving antenna is extended to incorporate an array of beamformed antenna elements and receivers. The array model is shown in Fig. 4.5. This model can be thought of as an array of single-port active antenna and the array output is the weighted sum of their voltage signal outputs.

As mentioned in Section 4.1 there will be significant mutual coupling between FPA elements and so their field patterns $\vec{e}_i(\theta, \phi)$ will be modified by the surrounding elements. To accommodate this in our model we use the *embedded* field patterns for each element, i.e. the field patterns with the other elements present and terminated in their receiver electronics. The \vec{e}_i are normalized as with the single antenna model (4.16) to integrate to unity

over the sphere:

$$\iint_{\Omega} \vec{e}_i^* \cdot \vec{e}_i d\Omega = 1. \quad (4.46)$$

The polarization components are denoted $e_{p,i}$ and $e_{q,i}$ such that

$$\vec{e}_i(\theta, \phi) = e_{p,i} \hat{p} + e_{q,i} \hat{q} \quad (4.47)$$

The receiver (or electronic) voltage gains h_i incorporate contributions from a number of sources including the losses from scattering by the antenna, dissipative losses in the antenna, mutual coupling losses and mismatch effects as well as the electronic gains.

With the black-box approach taken here we can measure the response v_{out} to the incident radiation $\vec{E}(\theta, \phi)$. The beamformer weighting vector \mathbf{u} can also be controlled.⁵ The embedded-element field patterns $\vec{e}_i(\theta, \phi)$ can be determined by setting the weighting to select the i^{th} element (i.e. $u_i = 1$ and $u_j = 0, \forall j \neq i$) and measuring the response v_{out} to plane waves from different directions. For smaller antennas this can be done in an antenna test range [158]. For larger antennas satellites or celestial sources can be used [14, 260] (Chapter 7 and Appendix E).

The receiver (or electronic) voltage gains h_i are initially identified separately from the weights u_i to highlight its role in an active antenna and to give a means for calibrating out variations in the electronic gains between elements as well as drift in gains with time. The model and further analysis is, however, simplified by combining the electronic voltage gain and weight in a combined complex column vector \mathbf{w} of weights. The i^{th} component of the vector is

$$w_i = h_i u_i. \quad (4.48)$$

We return to this subject when considering measurable quantities in Section 5.2.1.

An important consideration in array analysis is the effect of the beamformer state on the coupling between the elements and noise performance. For instance the impedance presented by an analogue beamformer may change with the beamformer weighting. If there is no isolation between antenna elements and the beamformer, this can affect the embedded ele-

⁵Another notational convention, common in the signal processing field, uses the conjugate of the beamformer weights.

ment field patterns and noise performance of each element. In the model being considered here (Fig. 4.5), however, the receiver is assumed to prevent reverse transmission of signals, isolating the antenna elements from the beamformer. This isolation of the reverse path is a feature of good receiver design. With digital beamforming, the analogue to digital converter adds to the isolation and beamforming in the digital domain removes the mechanism for the beamformer weights to affect the analogue electronics. Note that there will be some coupling after the antenna elements with front end amplifiers in close proximity and sharing power supplies and co-located down-converters. In this model, however, this coupling is indistinguishable from the array-element mutual coupling and accommodated by the model used here.

The isolation of the array from the beamformer state allows the voltage signal of the beamformed output to be equal to the weighted sum of the elements taken one at a time. Therefore the voltage signal at the output port in the presence of a desired plane wave field $E_p(t)$ and including the system noise is given by (cf. (4.11))

$$v_{\text{out}}(t) = \sum_{i=1}^n \left(\frac{\lambda}{\sqrt{2}\eta_0} E_p(t) e_{p,i} + v_{T_{\text{sys}},i}(t) \right) w_i. \quad (4.49)$$

To establish directivity and noise temperature expressions the development of the single port antenna model is paralleled, this time using expressions incorporating the weights of a beamformed array. Once the weights are fixed, the array can be considered an active single port antenna and the development of the G/T definition (see Section 4.2) and the single port antenna model (see Section 4.4) apply.

4.10 Directivity—Array

Superposition (implicit in (4.49)) is used to find the expression of the field pattern for an array to within a constant h_{array} . The normalization of the field patterns (4.16) is then used to find the amplitude of h_{array} . The following directivity expressions apply to both transmitting and receiving arrays.

The field pattern for the array with weight vector \mathbf{w} is

$$\begin{aligned}\vec{e}_{\text{array}} &= \frac{\sum_{i=1}^n e_{p,i} w_i \hat{p} + e_{q,i} w_i \hat{q}}{h_{\text{array}}} \\ &= \frac{\mathbf{e}_p^T \mathbf{w} \hat{p} + \mathbf{e}_q^T \mathbf{w} \hat{q}}{h_{\text{array}}} \\ &= \frac{\mathbf{e}_{p'}^T \mathbf{w} \hat{p}'}{h_{\text{array}}}\end{aligned}\tag{4.50}$$

where $\mathbf{e}_p = [\dots e_{p,i} \dots]^T$ is the vector of the co-polarized (\hat{p}) field pattern of each element taken one at a time with unity weighting, similarly \mathbf{e}_q is the vector of responses for the cross polarization \hat{q} . h_{array} is a constant (to be determined) that permits the directivity to be

$$D = 4\pi \vec{e}_{\text{array}}^* \cdot \vec{e}_{\text{array}}\tag{4.51}$$

as in (4.17).

As discussed in Section 4.3, the response of the antenna follows the matched polarization \hat{p}' , i.e. $\vec{e}_{\text{array}} = e_{\text{array},p'} \hat{p}'$. The response to the orthogonal polarization is zero, i.e. $e_{\text{array},q'} = 0$ for all angles (θ, ϕ) . As the field pattern is dependent on the weighting \mathbf{w} , \hat{p}' and \hat{q}' may change with this weighting. Note also that in general the individual element field patterns may respond to \hat{q}' polarized radiation, i.e. $\mathbf{e}_q^T \mathbf{w} = 0$ does not imply $e_{q',i} = 0$ for each i . That is, \hat{p}' and \hat{q}' are the weighted array polarizations, not the individual element polarizations.

From the identity (4.16) and (4.50)

$$\begin{aligned}1 &= \iint_{\Omega} \vec{e}_{\text{array}}^* \cdot \vec{e}_{\text{array}} d\Omega \\ &= \frac{1}{H_{\text{array}}} \iint_{\Omega} [(\mathbf{e}_p^T \mathbf{w})^* (\mathbf{e}_p^T \mathbf{w}) + (\mathbf{e}_q^T \mathbf{w})^* (\mathbf{e}_q^T \mathbf{w})] d\Omega \\ &= \frac{1}{H_{\text{array}}} \iint_{\Omega} \mathbf{w}^H (\mathbf{e}_p^* \mathbf{e}_p^T + \mathbf{e}_q^* \mathbf{e}_q^T) \mathbf{w} d\Omega\end{aligned}\tag{4.52}$$

where $H_{\text{array}} = h_{\text{array}}^* h_{\text{array}}$. Rearranging (4.52) and using (B.1) gives

$$\begin{aligned}H_{\text{array}} &= \iint_{\Omega} \mathbf{w}^H (\mathbf{e}_p^* \mathbf{e}_p^T + \mathbf{e}_q^* \mathbf{e}_q^T) \mathbf{w} d\Omega \\ &= \mathbf{w}^H \mathbf{C}_e \mathbf{w}\end{aligned}\tag{4.53}$$

where the elements of \mathbf{C}_e are the overlap integrals (found using (B.2))

$$[\mathbf{C}_e]_{ij} = \iint_{\Omega} e_{p,i}^* e_{p,j} + e_{q,i}^* e_{q,j} d\Omega \quad (4.54)$$

$$= \iint_{\Omega} e_{p',i}^* e_{p',j} d\Omega. \quad (4.55)$$

These overlap integrals incorporate the way in which closely spaced antennas share the incident fields. This can be thought of as their effective areas overlapping. In a transmit model the effect is seen in the mutual coupling.

The directivity of the array can be expressed as

$$D = 4\pi \frac{\mathbf{w}^H (\mathbf{e}_p^* \mathbf{e}_p^T + \mathbf{e}_q^* \mathbf{e}_q^T) \mathbf{w}}{\mathbf{w}^H \mathbf{C}_e \mathbf{w}}. \quad (4.56)$$

D_p and D_q can be identified as in (4.17). This expression is used in the derivation of the maximum directivity weighting in Section 5.2.4. Noting from the definition of \vec{e}_i and (4.16), $[\mathbf{C}_e]_{ii} = 1$, the directivity for the case of a single element selected ($\mathbf{w} : w_i = 1$ and $w_j = 0 \quad \forall j \neq i$) is

$$D_{p,i} = 4\pi e_{p,i}^* e_{p,i}. \quad (4.57)$$

This expression will be used in Section 5.4.3 where a relationship is found between the maximum gain weighting and an approximation to it, referred to in this thesis as the normalized conjugate match.

4.11 Arbitrarily Polarized Radiation—Array

To deal with arbitrarily, partially and unpolarized radiation, we find the receiver voltage signal at the beamformer output port $v(t)$ as a function of the field $\vec{E}(t)$ with components $E_p(t)$ and $E_q(t)$

$$v(t) = \frac{\lambda}{\sqrt{2\eta_0}} (E_p(t) \mathbf{e}_p^T \mathbf{w} + E_q(t) \mathbf{e}_q^T \mathbf{w}) \quad (4.58)$$

$$= v_p(t) + v_q(t). \quad (4.59)$$

For polarization matched to the antenna, defined by \hat{p}' (see Section 4.3),

$$v(t) = \frac{\lambda}{\sqrt{2\eta_0}} E_{p'}(t) \mathbf{e}_{p'}^T \mathbf{w}. \quad (4.60)$$

The power at the receiver port due to a \hat{p} polarized plane wave of power flux density S_p from (4.58) and (2.4) is then

$$P_{S_p} = \langle v_p^*(t) v_p(t) \rangle \quad (4.61)$$

$$= \frac{\lambda^2}{2\eta_0} \langle E_p^*(t) \mathbf{e}_p^H \mathbf{w}^* E_p(t) \mathbf{e}_p^T \mathbf{w} \rangle \quad (4.62)$$

$$= \frac{\lambda^2}{2\eta_0} \langle E_p^*(t) E_p(t) \rangle \mathbf{w}^H \mathbf{e}_p^* \mathbf{e}_p^T \mathbf{w} \quad (4.63)$$

$$= \lambda^2 S_p \mathbf{w}^H \mathbf{e}_p^* \mathbf{e}_p^T \mathbf{w}. \quad (4.64)$$

The array version of (4.26) gives the receiver power at the beamformer output port due to an arbitrarily polarized plane wave:

$$\begin{aligned} \mathbb{P}_{S_{\text{arb}}} &= \frac{\langle v^* v \rangle}{\Delta f} \\ &= \frac{\lambda^2}{2\eta_0 \Delta f} \langle \mathbf{w}^H (E_p \mathbf{e}_p + E_q \mathbf{e}_q)^* (E_p \mathbf{e}_p + E_q \mathbf{e}_q)^T \mathbf{w} \rangle \\ &= \mathbf{w}^H \mathbf{C}_{Ee} \mathbf{w} \end{aligned} \quad (4.65)$$

where the matrix \mathbf{C}_{Ee} has elements

$$\begin{aligned} [\mathbf{C}_{Ee}]_{ij} &= \frac{\lambda^2}{2\eta_0 \Delta f} \langle (E_p e_{p,i} + E_q e_{q,i})^* (E_p e_{p,j} + E_q e_{q,j}) \rangle \\ &= \frac{\lambda^2}{2\eta_0 \Delta f} \left(\langle E_p^* E_p \rangle e_{p,i}^* e_{p,j} + \langle E_q^* E_q \rangle e_{q,i}^* e_{q,j} + \right. \\ &\quad \left. \langle E_p^* E_q \rangle e_{p,i}^* e_{q,j} + \langle E_q^* E_p \rangle e_{q,i}^* e_{p,j} \right). \end{aligned} \quad (4.66)$$

Thompson et al. [13] and Cotton [22, 261] use an equivalent expression based on Stokes parameters for calibration of synthesis arrays. Hay [160] presents a similar expression but assumes the last two terms are conjugates of each other as was the single port case (4.36) but they are not for elements with different embedded radiation patterns.

For unpolarized radiation with spectral power flux density \mathbb{S} (considered for noise scene calculations and celestial sources) from (2.11) the last two terms of (4.66) are zero and from (2.12)

$$[\mathbf{C}_{Ee}]_{ij} = \frac{\lambda^2 \mathbb{S}}{2} [e_{p,i}^* e_{p,j} + e_{q,i}^* e_{q,j}]. \quad (4.67)$$

4.12 Noise—Array

4.12.1 Receiver Noise—Array

The voltage signal at the beamformer output due to the receiver noise is $v(t) = \mathbf{v}_{T_{\text{rx}}}^T \mathbf{w}$ where $\mathbf{v}_{T_{\text{rx}}}(t) = [\dots, v_{T_{\text{rx}},i}(t), \dots]^T$ is the voltage signal due to receiver noise from each element, that is the signal that would be measured at the beamformer output port with the weighting ($\mathbf{w} : w_i = 1, w_{j \neq i} = 0$).

The spectral power density at the beamformer output port is then

$$\begin{aligned} \mathbb{P}_{T_{\text{rx}}} &= \frac{\langle v^* v \rangle}{\Delta f} \\ &= k_B \mathbf{w}^H \mathbf{C}_{T_{\text{rx}}} \mathbf{w} \end{aligned} \quad (4.68)$$

where $\mathbf{C}_{T_{\text{rx}}}$ is the covariance matrix,

$$[\mathbf{C}_{T_{\text{rx}}}]_{ij} = \Delta f k_B \langle v_{T_{\text{rx}},i}^*(t) v_{T_{\text{rx}},j}(t) \rangle. \quad (4.69)$$

The scaling for $\mathbf{C}_{T_{\text{rx}}}$ has been chosen so the equivalent receiver noise temperature is

$$T_{\text{rx}} = \frac{\mathbb{P}_{T_{\text{rx}}}}{H_{\text{array}} k_B} = \frac{\mathbf{w}^H \mathbf{C}_{T_{\text{rx}}} \mathbf{w}}{\mathbf{w}^H \mathbf{C}_e \mathbf{w}}. \quad (4.70)$$

4.12.2 Antenna Noise—Array

The spectral power density at the beamformer output due to the noise scene, described most generally by $E_{\Omega,p}(t, \theta, \phi)$ and $E_{\Omega,q}(t, \theta, \phi)$, from (4.35) and (4.43) is:

$$\begin{aligned} \mathbb{P}_{T_{\text{scene}}} &= \frac{H \lambda^2}{2 \eta_0 \Delta f} \iint_{\Omega} \langle |\vec{E}_{\Omega} \cdot \vec{e}|^2 \rangle d\Omega \\ &= \frac{\lambda^2}{2 \eta_0 \Delta f} \iint_{\Omega} \left\langle \left| \sum_i E_{\Omega,p} e_{p,i} u_i + E_{\Omega,q} e_{q,i} u_i \right|^2 \right\rangle d\Omega. \end{aligned}$$

Using (B.1) and reversing the order of expected value and multiplication by the weights,

$$\mathbb{P}_{T_{\text{scene}}} = k_B \mathbf{w}^H \mathbf{C}_{T_{\text{scene}}} \mathbf{w} \quad (4.71)$$

where $\mathbf{C}_{T_{\text{scene}}}$ is matrix of radiation pattern overlap integrals weighted by the scene temperature, using (4.38) and (4.39)

$$\begin{aligned} [\mathbf{C}_{T_{\text{scene}}}]_{ij} &= \frac{\lambda^2}{4k_B\eta_0\Delta f} \iint_{\Omega} \langle (E_{\Omega,p}e_{p,i} + E_{\Omega,q}e_{q,i})^* (E_{\Omega,p}e_{p,j} + E_{\Omega,q}e_{q,j}) \rangle d\Omega \\ &= \iint_{\Omega} T_p e_{p,i}^* e_{p,j} + T_q e_{q,i}^* e_{q,j} + T_{pq} e_{p,i}^* e_{q,j} + T_{pq}^* e_{q,i}^* e_{p,j} d\Omega. \end{aligned} \quad (4.72)$$

The scaling was chosen to give $\mathbf{C}_{T_{\text{scene}}}$ units of Kelvin. A corresponding result is developed in terms of Stokes parameters for an interferometer in [13]. For an unpolarized noise scene where $T_p = T_q = T_{\text{scene}}$ and $T_{pq} = 0$ (see Section 4.7.2) (4.72) simplifies to

$$[\mathbf{C}_{T_{\text{scene}}}]_{ij} = \iint_{\Omega} T_{\text{scene}}(\theta, \phi) (e_{p,i}^* e_{p,j} + e_{q,i}^* e_{q,j}) d\Omega. \quad (4.73)$$

For a spatially-uniform noise scene (4.73) simplifies further using (4.54) to

$$\mathbf{C}_{T_{\text{scene}}} = T_{\text{scene}} \mathbf{C}_e. \quad (4.74)$$

The antenna temperature for the array (cf. (4.37)) is then

$$\begin{aligned} T_{\text{ant}} &= \frac{\mathbb{P}_{T_{\text{scene}}}}{H_{\text{array}} k_B} \\ &= \frac{\mathbf{w}^H \mathbf{C}_{T_{\text{scene}}} \mathbf{w}}{\mathbf{w}^H \mathbf{C}_e \mathbf{w}}. \end{aligned} \quad (4.75)$$

4.12.3 System Noise—Array

The noise from the array is found using the noise covariance matrix $\mathbf{C}_{T_{\text{sys}}}$. It includes the receiver noise and radiation from the surrounding scene:

$$\mathbf{C}_{T_{\text{sys}}} = \mathbf{C}_{T_{\text{rx}}} + \mathbf{C}_{T_{\text{scene}}}. \quad (4.76)$$

The elements of $\mathbf{C}_{T_{\text{sys}}}$ are shown here for use in the calculation of beamforming in Chapter 5:

$$[\mathbf{C}_{T_{\text{sys}}}]_{ij} = \Delta f k_B \langle v_{T_{\text{sys}},i}^*(t) v_{T_{\text{sys}},j}(t) \rangle \quad (4.77)$$

$$= \frac{\Delta f k_B}{h_i^* h_j} \langle v_{\text{out } T_{\text{sys}},i}^*(t) v_{\text{out } T_{\text{sys}},j}(t) \rangle. \quad (4.78)$$

where $v_{\text{out}T_{\text{sys},i}}(t)$ is the noise measured at the output port with only the i^{th} element given unity weighting ($\mathbf{u} : u_i = 1$ and $u_j = 0 \quad \forall j \neq i$). The total equivalent noise temperature is then

$$T_{\text{sys}} = \frac{\mathbf{w}^H \mathbf{C}_{T_{\text{sys}}} \mathbf{w}}{\mathbf{w}^H \mathbf{C}_e \mathbf{w}}. \quad (4.79)$$

4.13 G/T —Array

In a similar manner to the single port antenna, the G/T for polarization \hat{p} can be found from the embedded element field patterns, the noise scene temperature and the receiver noise temperature. From the expressions for the directivity (4.56) and the noise temperature (4.79) for the array, the array version of (4.42) is

$$G_p/T = \frac{D_p(\theta, \phi)}{T_{\text{sys}}} = 4\pi \frac{\mathbf{w}^H \mathbf{e}_p^* \mathbf{e}_p^T \mathbf{w}}{\mathbf{w}^H \mathbf{C}_{T_{\text{sys}}} \mathbf{w}}. \quad (4.80)$$

Note that the term $H_{\text{array}} = \mathbf{w}^H \mathbf{C}_e \mathbf{w}$ cancels.

Equation (4.80) is used to find the weights that provide the maximum G/T in Chapter 5.

4.14 Summary

A model of active receiving arrays has been developed in this chapter for calculating the salient figures of merit: directivity, system temperature and G/T . These can be calculated from the embedded element field patterns, the surrounding noise scene, the receiver noise covariance matrix and the weighting vector. It is simplified by the isolation provided by the receiver between the array elements and beamformer.

In developing the model it became clear that because antenna losses are indistinguishable from receiver gain and noise contributions, the reference plane for gain and noise is most appropriately placed at the radiation port (i.e. directivity is taken as the gain measure and antenna losses are on the receiver side of the reference plane).

The general approach taken allows the model to be applied to almost any receiving array, not just FPAs. Although the model treats the antenna array as a black-box with access only to the external ports (the radiation

port and the beamformed output) and manipulation of the weighting vector, it is consistent with analyses based on the internal details of an array.

This model will be used in Chapter 5 for the investigation of beamforming methods and in Chapter 7 it is used in the measurement of FPA performance.

Chapter 5

Beamformer Weight Calculation

This chapter covers the beamforming approaches used in the prototype system presented in Chapters 6, 7 and 8. The emphasis is on low-noise active receiving arrays and in particular focal plane arrays (FPAs) but the results are general.

A brief survey of beamforming techniques is followed by optimization approaches applied to the receiving array model developed in Chapter 4. The optimization formulae are presented in terms of two sets of parameters: one is more amenable to the theoretical treatment and the other to measurement. The maximum sensitivity weighting is shown first and maximum directivity is derived as a special case. A weighting referred to as the *normalized conjugate match* (NCM) here was used in the measurements before the calculation of the covariance matrix was available and so it is also discussed.

As an adjunct to the beamforming weighting used in measurement, the formulation for the optimal weightings with multiple nulls is presented.

The chapter concludes by using the equivalence of a scattering matrix model of an array with the ‘black-box’ model from Chapter 4 to show that the NCM is close to the maximum gain condition.

5.1 Survey of Beamforming Approaches

The field of beamforming antenna arrays with various goals has been the subject of extensive research and application in a diverse range of fields

including radar, sonar, communications, geophysical, biomedical and radio astronomy [262].

Beamforming strategies for FPAs can draw on many insights developed for aperture arrays, even though an FPA requires very different weights. Of particular interest are analyses of finite arrays where the assumption of identical element patterns has been dropped and where the noise component is considered. The close proximity of elements in FPAs also demands the inclusion of mutual coupling. Much of the early work in this field was in defence research, particularly for radar [263]. The recent history of beamforming for radiotelescope FPAs is discussed in Section 2.6 where the distinction from radar applications is the focus on low-noise receive-only arrays.

One approach to beamforming is to characterize the system through modelling or measurement so that the weights can be determined and fixed before the system is deployed. Another approach, often referred to as the field of *adaptive arrays*, is to use the signals coming into the array to dynamically recalculate the weights continually or periodically [263]. The approach taken here falls into the adaptive array category, with the ability to adjust to changes in both the environment and the radiotelescope itself. The motivation for delineating this ‘black box’ approach is that neither adequate measurements nor modelling of the FPA used in the experimental work were available and there was concern over changes to gain and phase in the receiver chains.

5.1.1 Conjugate Field Match

For an antenna to collect the maximum signal available, it needs to provide a perfect absorptive match to the incoming signal fields. By reciprocity this is equivalent to the antenna in transmit producing the conjugate of the incoming field on a surface surrounding it. This can be seen by considering reversing time so that the transmitted field reproduces the incoming field with the direction of propagation reversed. This translates to

$$\mathbf{E}_a = \mathbf{E}_f^* \quad \text{and} \quad \mathbf{H}_a = -\mathbf{H}_f^* \quad (5.1)$$

where \mathbf{E}_a and \mathbf{H}_a are the feed aperture electric and magnetic fields (in transmit) and \mathbf{E}_f and \mathbf{H}_f^* are the focal plane electric and magnetic fields from the reflector (in receive) [264]. It can be shown that for an FPA to efficiently col-

lect the available signal power, it must come close to this conjugate match condition both in the design of the elements and the way they are combined [77]. This is the condition assumed in the encircled power calculations in Chapter 3.

The conjugate field match was used in horn feed design by Minnett, Thomas, Rumsey and Bao [74, 75, 198, 199, 265]. It was applied to beam-forming FPAs by Loux [57] and Bird [77] and is referred to in texts such as Howell [266]. Ivashina et al. [168, 267] at ASTRON applied this by calculating the field at the focal plane due to a distant point source and matching the weighting of the array elements to match that field. Respectable aperture efficiencies were obtained and the potential of FPAs in the field of radio astronomy was clearly demonstrated.

The use of this approach is however limited by the assumption that the array elements are point field samplers, or at least have identical patterns with no mutual coupling (Lam et al. [191] find the maximum directivity solution is superior, particularly for more closely spaced FPAs.). The conjugate field match also does not directly address noise but only gain.

5.1.2 Maximum Gain and Maximum G/T

The maximum gain condition for an arbitrary array was described by Cheng and Tseng [268]. Lam et al. [191] explores the maximum directivity for an FPA, comparing it with the conjugate field match. The maximum G/T was shown by Bryn [269] for three dimensional acoustic arrays. Applebaum [270] applied it to antenna arrays. Bach and Hansen apply it to uniformly spaced arrays [271]. It was applied to FPAs by Bird and Hayman [96], Briskin and Craeye [272, 273] and has been studied in depth in the collaboration of Brigham Young University (BYU) and NRAO [9, 20, 31, 93, 163, 234, 242]. The form used in this thesis is discussed in Section 5.2.3.

5.1.3 Other Considerations

Considerations other than G/T need to be taken into account in a radiotelescope design even though any array weighting is likely to be close to the maximum G/T case. Some of these are listed in this section with the most important secondary considerations for a synthesis array expected to be radiation pattern stability and shape.

Radiation pattern stability and shape

In a synthesis radiotelescope the image is derived from a significant portion of the main beam. The subject of the ideal beamforming strategy for FPA equipped synthesis radiotelescopes is the subject of ongoing research [274, 275]. The main beam also needs to be stable over the observation time, often many hours or less satisfactorily, variations need to be identified and removed by calibration [276, 277]. The sidelobe level and stability are also important because they determine the susceptibility to strong sources, both interferers and astronomical, corrupting the image. There are many publications in the field of optimizing array performance with constraints on the radiation pattern, for example Applebaum and Chapman [278] and Bird [77].

Solution stability

A concern in beamforming is the sensitivity of a solution to small changes in the element gains. For instance Lam et al. [191] found the maximum directivity solution for an FPA resulted in “an oscillatory cluster excitation” and supergain. Lo et al. [279] address this problem by constraining the “Q-factor” of the array. This is also discussed in the focal plane array context by Briskin [280] and Hansen et al. [93].

The conjugate match weighting involves no matrix inversion, is unlikely to achieve a supergain result and is expected to be well conditioned. The maximum G/T weighting (5.11) involves the inversion of the noise covariance matrix. If the receiver noise is high, this will have the effect of increasing the diagonal terms of the noise covariance matrix, regularizing the result and making it more stable. For high sensitivity FPAs, on the other hand, the receiver noise will be low relative to the spillover noise and an ill-conditioned case may result. This issue should be the subject of further investigation but it is expected to be tractable as similar problems have been addressed in beamforming and signal processing.

Interference Mitigation

An interferometer filters out interference that is out of its field-of-view naturally to a much greater extent than a single dish and so this is of greater importance in a single dish telescope. There is also a trade-off between pattern stability and interference mitigation [9].

The use of an auxiliary antenna, for instance pointed toward a known interferer, has also been investigated [281, 282]. This could be incorporated into the beamformer weight calculation with an FPA system as the beamforming infrastructure is readily available rather than being dealt with as a separate process (cf. sidelobe cancellation for a dish with a broad beam auxiliary antenna [263]).

Reflector Deformation and Vernier Beam Steering

Using an FPA to compensate for reflector deformation with gravity or wind and for vernier beam steering have also been considered by Blank and Imbriale [44]. To some extent these can “come for free” with the adaptive beamforming approaches outlined below. This is because the weighting is based on the actual signals received and takes into account any changes to the system at the time including deformations.

Decoupling Networks

Orthogonalizing the field patterns using a decoupling network before the first amplification stage is discussed in the antenna array and FPA literature [245, 283]. This has the potential to improve the signal to noise ratio but the noise contribution from the losses in the network needs to be considered. It may be applicable where the noise is less dominant in interference limited systems or those with high environmental noise as may be encountered in the MIMO¹ field [244]. It may also be appropriate in a radiotelescope with cryogenically cooled electronics, such as in the PHAROS project [167], where the decoupling network may contribute very little noise (or no noise if superconducting). However many systems currently being considered for FPAs are uncooled and the losses in the decoupling network would contribute too much noise. Placing the network after the amplifiers may be appropriate to simplify the processing, particularly if the number of ports can be reduced and the amplifiers are well matched. In ASKAP and similar applications with a wide bandwidth digital beamforming system, such a network is unlikely to be practical.

¹Multiple Input Multiple Output

Polarimetry

FPA systems allow polarization purity to be optimized not just on-axis as proposed in Bird and Hayman [96] but also over the entire field-of-view. The expressions in Section 4.11 show a level of complexity on top of that for a synthesis array with single feeds. Work in this area has been recently presented by Veidt [284] and Warnick et al. [285]. The formulation for introducing nulls in the beam in Section 5.3 shows one approach.

Beamforming for Specific Observations

There is a rich area of research in finding the best beamforming strategy for specific purposes. For instance while synthesized image clarity with its need for a very stable radiation pattern, will be most important for many observations, in spectral line and pulsar work, the sensitivity or G/T may be most important. The beamforming for specific purposes is explored by Ivashina et al. [286] for wide field surveys and Gunaratne et al. [95] for pulsar observations.

5.2 Adaptive Beamforming

In this section we concentrate on beamforming using the model developed in Chapter 4. The approach uses input parameters that are readily available from an operational radiotelescope. The expected mode of operation is to periodically determine the input parameters and fix the weights between these data collections. This is referred to by Jeffs et al. as ‘fixed-adaptive beamforming’ [9].

The motivation for using an adaptive approach is the application of beamforming to a completed system. Even if the details of the internal structure have been accurately modelled and component variability measured, the component performance is likely to drift with temperature for instance. With a mechanically steerable antenna, the pointing direction changes the alignment of the radiation pattern with the surrounding noise scene (4.41) and changing the array weighting can improve the resulting sensitivity.

5.2.1 Measurable Quantities

In the black-box model developed in Chapter 4 the embedded element response has been based on the directivity. A consequence is the h_i terms include contributions from a number of sources including the losses from scattering by the antenna, dissipative losses in the antenna, mutual coupling losses, mismatch effects and the electronic gain (see Section 4.9).

The absolute and relative values of these contributions are unknown in this model and the weight vector $\mathbf{u} : u_i = w_i/h_i$ (see Section 4.9) is used to represent the weights that are actually set in the beamformer. The *active embedded-element responses* are represented by $\acute{e}_{p,i} = h_i e_{p,i}$ and $\acute{\mathbf{e}} = [\acute{e}_1 \dots \acute{e}_n]^T$.

The voltage signal at the beamformer output port is then (cf. (4.49))

$$v_{\text{out}}(t) = \sum_{i=1}^n \left(\frac{\lambda}{\sqrt{2}\eta_0} E_p(t) \acute{e}_{p,i} + \acute{v}_{T_{\text{sys}},i}(t) \right) u_i \quad (5.2)$$

$$= \frac{\lambda}{\sqrt{2}\eta_0} E_p(t) \acute{\mathbf{e}}_p^T \mathbf{u} + \sum_{i=1}^n \acute{v}_{T_{\text{sys}},i}(t) u_i \quad (5.3)$$

where $\acute{v}_{T_{\text{sys}},i} = h_i v_{T_{\text{sys}},i}$ is the noise voltage for unity weighting for the i^{th} element ($u_i = 1$).

The relative amplitudes and phases of the \acute{e}_i are determined from the correlation product from the interferometer pointed at a point source.

The directivity of the array in terms of \mathbf{u} and $\acute{\mathbf{e}}$ is then (cf. (4.56))

$$D_p = 4\pi \frac{\mathbf{u}^H \acute{\mathbf{e}}_p^* \acute{\mathbf{e}}_p^T \mathbf{u}}{\mathbf{u}^H \mathbf{C}_{\acute{\mathbf{e}}} \mathbf{u}} \quad (5.4)$$

where (cf. (4.54))

$$[\mathbf{C}_{\acute{\mathbf{e}}}]_{ij} = \iint_{\Omega} \acute{e}_{p,i}^* \acute{e}_{p,j} + \acute{e}_{q,i}^* \acute{e}_{q,j} d\Omega \quad (5.5)$$

The noise covariance matrix scaled for the weight vector \mathbf{u} is

$$[\mathbf{C}_{T_{\text{sys}},u}]_{ij} = \left\langle \acute{v}_{T_{\text{sys}},i}^*(t) \acute{v}_{T_{\text{sys}},j}(t) \right\rangle = h_i^* h_j [\mathbf{C}_{T_{\text{sys}}}]_{ij} \quad (5.6)$$

These terms can be measured by correlating element pairs with the antenna pointed off-source (away from all strong sources).

The system temperature is then

$$T_{\text{sys}} = \frac{\mathbf{u}^H \mathbf{C}_{T_{\text{sys}},u} \mathbf{u}}{\mathbf{u}^H \mathbf{C}_{\dot{\epsilon}} \mathbf{u}}. \quad (5.7)$$

The G/T , equivalent to (4.80), is given by

$$G_p/T = \frac{D_p}{T_{\text{sys}}} = 4\pi \frac{\mathbf{u}^H \dot{\epsilon}_p^* \dot{\epsilon}_p^T \mathbf{u}}{\mathbf{u}^H \mathbf{C}_{T_{\text{sys}},u} \mathbf{u}}. \quad (5.8)$$

The relative amplitudes and phases of the $\dot{\epsilon}_i$ can be obtained from single dish measurements. Jeffs et al. [9] and Veidt et al. [6] used the difference between the on-source and off-source covariance matrices. The dominant eigenvector of this difference matrix is $\dot{\epsilon}_i$. O’Sullivan et al. [164] used an iterative approach to reconstruct the amplitude and phases of $\dot{\epsilon}_i$ from a passing GPS satellite. These single dish methods are less direct and less sensitive than using an interferometer. They have been used with very bright astronomical sources, a satellite source and they may also be suitable for very large reflectors, such as the Parkes 64 m telescope or the Green Bank 100 m telescope.

The noise covariance matrix, $\mathbf{C}_{T_{\text{sys}},u}$, makes use of only one dish by recording the cross correlations of the FPA elements with the dish steered away from strong sources. Therefore there is no benefit in having an interferometer.

5.2.2 Normalization of the Weight Vector

In these results the excitation (or weight) vector is presented un-normalized for convenience. In practice this is usually normalized to suit the beamformer, often to have a unit length, that is

$$\hat{\mathbf{u}} = \frac{\mathbf{u}}{\|\mathbf{u}\|} \quad \text{and} \quad \hat{\mathbf{w}} = \frac{\mathbf{w}}{\|\mathbf{w}\|} \quad (5.9)$$

Note also that an arbitrary phase multiplier can be applied to the weight vector and the results below still apply. Physically this is akin to adding or subtracting equal lengths of transmission line to or from the ports of the array or changing the line length after beamforming.

5.2.3 Maximum G/T

The maximum G/T weighting can be found by analysing the expression (4.80). The formulation requires $\mathbf{C}_{T_{\text{sys}}}$ to be a positive-definite Hermitian matrix. The Hermitian condition is clear from (4.78). As the antenna temperature from any set of weights \mathbf{w} will be positive or zero, $\mathbf{C}_{T_{\text{sys}}}$ is a positive-semidefinite matrix. The zero case is one where no radiation is received by the antenna and corresponds to a weighting that is “blind” in all the directions that the noise distribution is not zero, a condition that will not occur for a real FPA. The development below requires the matrix $\mathbf{C}_{T_{\text{sys}}}$ to be positive-definite, that is the denominator of (5.7) positive for any non-zero weighting or the noise is always finite. This is certainly the case for any practical antenna array.

Applying the result from Corollary 4 in Appendix B.5 to (4.80),

$$G_p/T = 4\pi \frac{\mathbf{w}^H \mathbf{e}_p^* \mathbf{e}_p^T \mathbf{w}}{\mathbf{w}^H \mathbf{C}_{T_{\text{sys}}} \mathbf{w}}. \quad (5.10)$$

is maximized with

$$\mathbf{w} = \mathbf{C}_{T_{\text{sys}}}^{-1} \mathbf{e}_p^* \quad (5.11)$$

and substituting (5.11) into (4.80) and (4.56) we obtain

$$G_p/T = 4\pi \frac{\mathbf{e}_p^T (\mathbf{C}_{T_{\text{sys}}}^{-1})^H \mathbf{e}_p^* \mathbf{e}_p^T \mathbf{C}_{T_{\text{sys}}}^{-1} \mathbf{e}_p^*}{\mathbf{e}_p^T (\mathbf{C}_{T_{\text{sys}}}^{-1})^H \mathbf{C}_{T_{\text{sys}}} \mathbf{C}_{T_{\text{sys}}}^{-1} \mathbf{e}_p^*} \quad (5.12)$$

$$= 4\pi \mathbf{e}_p^T \mathbf{C}_{T_{\text{sys}}}^{-1} \mathbf{e}_p^* \quad (5.13)$$

For the weighting vector used in practice \mathbf{u} , this condition is

$$\mathbf{u} = \mathbf{C}_{T_{\text{sys},u}}^{-1} \mathbf{e}_p^* \quad (5.14)$$

and is equivalent to (5.11).

5.2.4 Maximum Directivity

The condition for the maximum directivity can be found by applying the method used for maximum G/T to (4.56). The weightings are then

$$\mathbf{w} = \mathbf{C}_e^{-1} \mathbf{e}_p^* \quad (5.15)$$

or equivalently from (5.4)

$$\mathbf{u} = \mathbf{C}_\epsilon^{-1} \mathbf{e}_p^*. \quad (5.16)$$

In principle this \mathbf{C}_ϵ can be measured using two uniform scene temperatures. The noise covariance matrix $\mathbf{C}_{T_{\text{sys}},u}$ is measured for both temperatures $T_{\text{scene},a}$ and $T_{\text{scene},b}$. The scene contribution from (4.74) is $T_{\text{scene}} \mathbf{C}_\epsilon$, giving

$$\mathbf{C}_{T_{\text{sys}},ua} = \mathbf{C}_{T_{\text{rx}},u} + T_{\text{scene},a} \mathbf{C}_\epsilon \quad (5.17)$$

$$\mathbf{C}_{T_{\text{sys}},ub} = \mathbf{C}_{T_{\text{rx}},u} + T_{\text{scene},b} \mathbf{C}_\epsilon. \quad (5.18)$$

Solving these equations for \mathbf{C}_ϵ gives

$$\mathbf{C}_\epsilon = \frac{\mathbf{C}_{T_{\text{sys}},ua} - \mathbf{C}_{T_{\text{sys}},ub}}{T_{\text{scene},a} - T_{\text{scene},b}} \quad (5.19)$$

Clearly the larger the difference between the two temperatures $T_{\text{scene},a}$ and $T_{\text{scene},b}$ the more accurate the measurement will be. The measurement could be done with the feed on the ground using absorber as the hot load and the sky or absorber cooled with liquid nitrogen as the cold load. This would not take into account the secondary interaction between the reflector and the feed, but in most cases, this should be a minor effect. If such a measurement of \mathbf{C}_ϵ is used, care is needed to track gain and phase changes between the elements with temperature changes and drift over time.

5.2.5 Normalized Conjugate Match

An alternative beamforming approach that is simpler to implement than the maximum G/T but yields similar results is attractive in some practical situations. For instance the covariance matrix may not be available early in a system deployment, as was the case for this project. Weightings based

on conjugate match were used in the early development of the NTD Interferometer. They were used later for comparison with the maximum G/T weighting.

The simplest approach would be to use the conjugate match to the active embedded-element responses

$$\mathbf{u} = \hat{\mathbf{e}}_p^* \quad (5.20)$$

This maximizes the signal but, recalling that $\hat{e}_{p,i} = h_i e_{p,i}$ (see Section 5.2.1), if the electronic gains h_i are not equal in magnitude the antenna directivity is not directly maximized. Such variability is common in high gain front ends and in the experimental FPA system used in this thesis it was minimized by adjusting the receiver gains (see Section 6.4.5).

To lessen this effect, the conjugate match was scaled by the noise from each element. The relationship of this weighting and the maximum gain or directivity weighting is discussed in Section 5.4.5.

The weighting vector is given by

$$\mathbf{u} = \left[\cdots \hat{e}_{p,i}^* / [\mathbf{C}_{T_{\text{sys},u}}]_{ii} \cdots \right]^T \quad (5.21)$$

The weights in terms of the field patterns and noise covariance matrix referred to the radiation port are

$$\mathbf{w} = \left[\cdots e_{p,i}^* / [\mathbf{C}_{T_{\text{sys}}}]_{ii} \cdots \right]^T \quad (5.22)$$

Both (5.21) and (5.22) give a result where the weight vector element amplitudes are proportional to the square root of the signal to noise ratio for those elements.

It is readily seen that the NCM maximizes *directivity* if the overlap integrals of element pairs are zero and the noise from each element is identical (see (4.56) and (4.54)). The NCM and the maximum G/T weightings are equivalent if the noise from each element is uncorrelated, i.e. $\mathbf{C}_{T_{\text{sys}}}$ and $\mathbf{C}_{T_{\text{sys},u}}$ are diagonal. The similarity between this NCM and the maximum gain is given in Section 5.4. Where there are amplifiers on each element, the absorption of power reflected from the array can lead to significant differences between the gain and directivity. In general, more information than the element responses and the noise covariance matrix (black-box model) is required to find the maximum directivity and maximum gain weightings.

In this project the results from maximum G/T and NCM weightings were very similar. For a lower noise FPA there is expected to be less similarity. It is also shown that this NCM weighting is very close to the maximum gain weighting for the prototype system. Thus comparing this and the maximum G/T weightings provided insight into the system performance (see Section 8.6).

5.3 Maximum G/T with Nulls

This section shows how nulls in the radiation patterns can be inserted in a relatively simple manner. Applications include interference mitigation and minimizing the cross-polarized response of the antenna. There are more sophisticated approaches being considered particularly for interference mitigation [9] but the formulation presented here demonstrates how one or more nulls can be incorporated in the beamformer in a relatively straight forward manner.

A null in a particular direction and polarization \hat{q} corresponds to (cf. (4.50))

$$e_{q,\text{array}} h_{\text{array}} = \mathbf{e}_q^T \mathbf{w} = 0 \quad (5.23)$$

This is equivalent to requiring \mathbf{w} to be orthogonal² to \mathbf{e}_q^* . We can apply Theorem 5 in Appendix B.6 where each $\{\mathbf{b}_1 \dots \mathbf{b}_M\}$ is set to the conjugate match of the field responses $\{\mathbf{e}_1 \dots \mathbf{e}_M\}$ in the null directions (θ_i, ϕ_i) . The polarization for each of these directions can be specified separately. If a null is required in both polarizations from one direction, two sets of responses $\mathbf{e}_i = \mathbf{e}_p$ and $\mathbf{e}_j = \mathbf{e}_q$ can be included for that direction.

Note that even if the interference comes via multiple paths due to reflections, if we can find the weighting that maximizes the interferer, we can use its conjugate match to null out the interferer even though there may not be absolute nulls in all the directions it is coming from.

Having established the weightings for the null directions, we seek the maximum of (4.80)

$$G_p/T = \frac{D_p(\theta, \phi)}{T_{\text{sys}}} = 4\pi \frac{\mathbf{w}^H \mathbf{e}_p^* \mathbf{e}_p^T \mathbf{w}}{\mathbf{w}^H \mathbf{C}_{T_{\text{sys}}} \mathbf{w}}. \quad (5.24)$$

²The inner product definition $\langle \mathbf{u}, \mathbf{v} \rangle = \mathbf{u}^H \mathbf{v}$ is used so \mathbf{u} and \mathbf{v} are orthogonal if $\mathbf{u}^H \mathbf{v} = 0$.

with nulls in the directions corresponding to the weightings $\{\mathbf{e}_1^* \dots \mathbf{e}_M^*\}$. Define $\mathbf{C}_{T_{\text{sys},u}}^{1/2}$ such that $\mathbf{C}_{T_{\text{sys},u}}^{1/2} \mathbf{C}_{T_{\text{sys},u}}^{1/2} = \mathbf{C}_{T_{\text{sys},u}}$ (see Appendix B.3) and

$$\mathbf{P} = \mathbf{I} - \sum_{l=1}^L \mathbf{c}_l \mathbf{c}_l^H \quad (5.25)$$

where $\{\mathbf{c}_1 \dots \mathbf{c}_L\}$ is an orthonormal basis spanning the same subspace as $\{\mathbf{C}_{T_{\text{sys},u}}^{-1/2} \mathbf{e}_1^* \dots \mathbf{C}_{T_{\text{sys},u}}^{-1/2} \mathbf{e}_M^*\}$. The \mathbf{c}_l are generated using the Gram-Schmidt process described in Section B.6.2. Using Theorem 6 from Section B.6.3, the Hermitian nature of $\mathbf{C}_{T_{\text{sys},u}}^{1/2}$ and \mathbf{P} , and the idempotent nature of \mathbf{P} , we have

$$\mathbf{w} = \mathbf{C}_{T_{\text{sys},u}}^{-1/2} \mathbf{P} \mathbf{C}_{T_{\text{sys},u}}^{-1/2} \mathbf{e}_p^* \quad (5.26)$$

$$\frac{G_p}{T_A} = 4\pi \mathbf{e}_p^T \mathbf{C}_{T_{\text{sys},u}}^{-1/2} \mathbf{P} \mathbf{C}_{T_{\text{sys},u}}^{-1/2} \mathbf{e}_p^* \quad (5.27)$$

$$= 4\pi \|\mathbf{P} \mathbf{C}_{T_{\text{sys},u}}^{-1/2} \mathbf{e}_p^*\|^2 \quad (5.28)$$

These results reduce to those in Section 5.2.3 when there are no nulls, that is $\mathbf{P} = \mathbf{I}$.

For a single null, from (B.16) and (B.17) (as developed by Bird [77,96]),

$$\mathbf{w} = \mathbf{C}_{T_{\text{sys},u}}^{-1} \left(\mathbf{I} - \frac{\mathbf{c}_1^* \mathbf{c}_1^T \mathbf{C}_{T_{\text{sys},u}}^{-1}}{\mathbf{c}_1^T \mathbf{C}_{T_{\text{sys},u}}^{-1} \mathbf{c}_1^*} \right) \mathbf{e}_p^* \quad (5.29)$$

$$= \mathbf{C}_{T_{\text{sys},u}}^{-1} \left(\mathbf{e}_p^* - \frac{\mathbf{c}_1^T \mathbf{C}_{T_{\text{sys},u}}^{-1} \mathbf{e}_p^*}{\mathbf{c}_1^T \mathbf{C}_{T_{\text{sys},u}}^{-1} \mathbf{c}_1^*} \mathbf{c}_1^* \right). \quad (5.30)$$

The extension to other beamforming cases can be found by replacing $\mathbf{C}_{T_{\text{sys},u}}$ with the appropriate matrix when defining the null subspace. For instance the diagonal of $\mathbf{C}_{T_{\text{sys},u}}$ is used for the NCM and replacing $\mathbf{C}_{T_{\text{sys},u}}$ with the identity matrix yields the conjugate match with nulls.

5.4 Scattering Matrix Model and Maximum Gain

5.4.1 Scattering Matrix Model Details

The purpose of presenting a scattering matrix model of the array is to demonstrate the conditions under which the NCM weighting is equivalent to the maximum gain weighting.

The scattering matrix is chosen over its cousins, the impedance and admittance matrix forms, as conservation of power³ and consequently antenna gain is expressed more directly. Scattering matrix analyses of arrays is well covered in the literature in a range of different forms (e.g. [287]), but some details are outlined here to ensure clarity in the choice of form and reference plane, which are essential for the conclusions that are drawn.

The receiver electronics (with the LNA having the major effect) is included in the model by splitting each receiver into a passive-reciprocal two-port, \mathbf{S}_i , representing the match presented to the array port and an isolating-matched amplifier representing the electronic gain (Fig. 5.1a). The weighting terms a_i are included in this second component. The $g_{p,i}(\theta, \phi)$ are embedded-element field-patterns for the \hat{p} polarization. It is assumed there is no cross coupling of the signals after the receiver inputs other than that represented by the weighting and the summation in the beamformer. If there were, it might be possible to include the effects in the array matrix (this is implicit in the black-box model). The voltage signal response to a \hat{p} polarized plane wave E_p in terms of the scattering matrix model is (cf. (5.3))

$$v_{\text{out}}(t) = \frac{\lambda}{\sqrt{2\eta_0}} E_p(t) \mathbf{g}_p^T \mathbf{a}. \quad (5.31)$$

where \mathbf{a} and \mathbf{g} are the weight and field-pattern column vectors.

The choice of reference plane is in contrast to the more common choice where the receiver match is included in the beamformer scattering matrix [241] and has been made to simplify the inclusion of receiver mismatch and results in any pattern distortion due to these mismatches being accounted for. Therefore the field patterns from the two models can be related by

³The systems are assumed to be in a steady state and so the conservation of power is an extension of the conservation of energy.

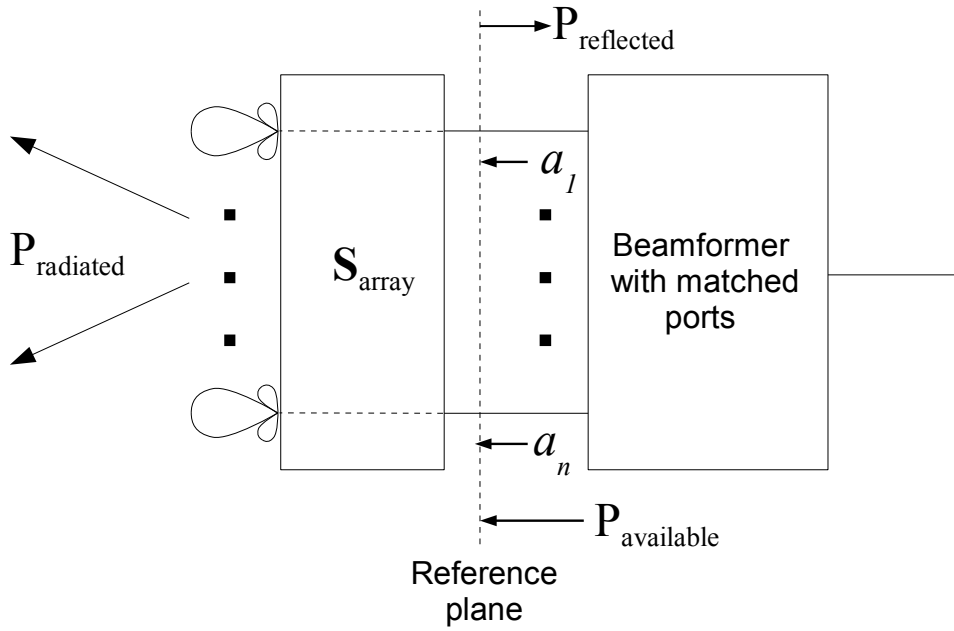
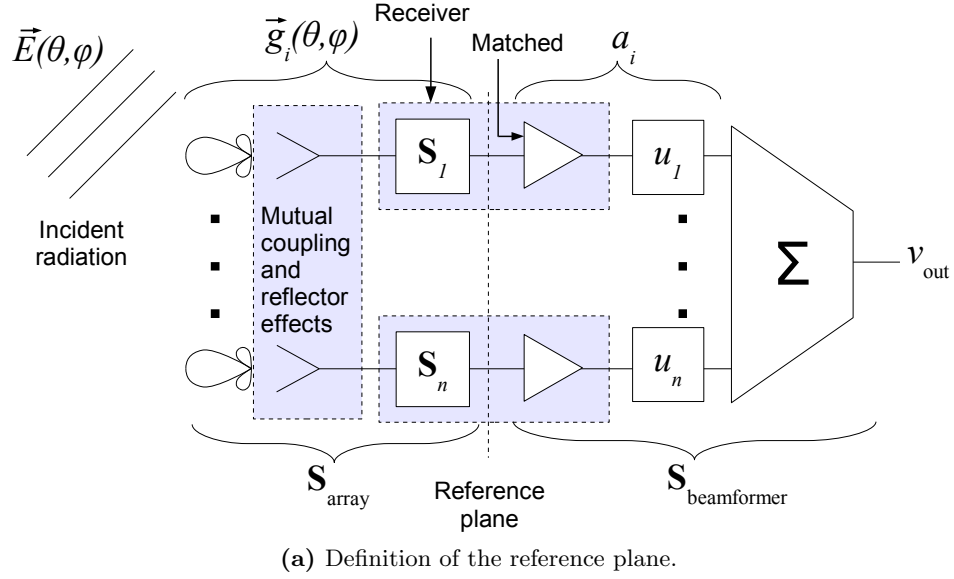


Figure 5.1 – Scattering matrix model of the array

complex terms that are constant over the sphere:

$$\mathbf{g}_p(\theta, \phi) = \mathbf{A}\mathbf{e}_p(\theta, \phi) \quad (5.32)$$

where \mathbf{A} is diagonal.

Unless the receivers are very well matched, the interaction between the receiver and the array can have a significant impact on the array patterns [99, 242].

The weightings for the black-box and scattering matrix models will be equivalent if the voltage out of the array is the same for the same incident field E_p . From (4.49) and (5.31):

$$\begin{aligned} v_{\text{out}}(t) &= \frac{\lambda}{\sqrt{2\eta_0}} E_p(t) \mathbf{e}_p^T \mathbf{w} \\ &= \frac{\lambda}{\sqrt{2\eta_0}} E_p(t) \mathbf{g}_p^T \mathbf{a}. \end{aligned} \quad (5.33)$$

Rearranging (5.33), the condition for equivalence can be expressed as

$$\mathbf{e}_p^T \mathbf{w} = \mathbf{g}_p^T \mathbf{a}. \quad (5.34)$$

Using (5.32), the relationship between the weightings is then

$$\mathbf{w} = \mathbf{A}\mathbf{a} \quad (5.35)$$

Conservation of power is used to find first, an expression for \mathbf{A} in terms of the scattering matrix model, and then the conditions for equivalence between the maximum gain and NCM weightings.

5.4.2 Conservation of Power

Conservation of power has been used to deduce a number of properties of arrays including relationships between the radiation patterns and scattering matrices [211, 213, 288]. The expressions are repeated here in our notation for reference.

In transmit, the total power available to the array is the sum of the radiated power, reflected power and dissipated power in the antenna structure—

the $\mathbf{S}_{\text{array}}$ block of Fig 5.1b:

$$P_{\text{available}} = P_{\text{radiated}} + P_{\text{reflected}} + P_{\text{dissipated}}. \quad (5.36)$$

From scattering matrix theory, $P_{\text{available}} = \mathbf{a}^H \mathbf{a}$. $P_{\text{radiated}} = \mathbf{a}^H \mathbf{C}_g \mathbf{a}$ where \mathbf{C}_g is the overlap integral of the field patterns (the black-box parallel is (4.54))

$$[\mathbf{C}_g]_{ij} = \iint_{\Omega} g_{p,i}^* g_{p,j} + g_{q,i}^* g_{q,j} d\Omega \quad (5.37)$$

$P_{\text{reflected}} = \mathbf{a}^H \mathbf{S}_{\text{array}}^H \mathbf{S}_{\text{array}} \mathbf{a}$ where $\mathbf{S}_{\text{array}}$ is the scattering matrix for the array concatenated with the receiver matches. The conservation of power can then be expressed in scattering matrix terms as

$$\mathbf{a}^H \mathbf{a} = \mathbf{a}^H \mathbf{C}_g \mathbf{a} + \mathbf{a}^H \mathbf{S}_{\text{array}}^H \mathbf{S}_{\text{array}} \mathbf{a} + P_{\text{dissipated}}. \quad (5.38)$$

Power dissipated in the array structure itself, $P_{\text{dissipated}}$, is often referred to as ohmic loss as it results from resistivity in the conductors and dielectrics. In receive, this appears as an attenuation of the fields impinging on the array and more importantly in our application, increases the system noise temperature. It is difficult to determine $P_{\text{dissipated}}$ both experimentally and in models because it is usually a small effect in well designed arrays.

The reflected or scattered loss $P_{\text{reflected}}$, in transmit, is power scattered back into the ports of the array and can be determined from the scattering matrix if the ports to the array are accessible. In receive mode, this appears as energy from the impinging field scattered or re-radiated from the array structure.

The ratio of radiated and available power is the radiation efficiency [34]:

$$\eta_{\text{rad}} = \frac{P_{\text{radiated}}}{P_{\text{available}}} = \frac{\mathbf{a}^H \mathbf{C}_g \mathbf{a}}{\mathbf{a}^H \mathbf{a}} = 1 - \frac{\mathbf{a}^H \mathbf{S}_{\text{array}}^H \mathbf{S}_{\text{array}} \mathbf{a}}{\mathbf{a}^H \mathbf{a}} - \eta_{\text{dissipated}}. \quad (5.39)$$

5.4.3 One Element at a Time Weighting

The scattering matrix model has been defined so that if only one element is excited or selected, the radiation pattern for the i^{th} element $g_{p,i}(\theta, \phi)$ will be the same as that for the black-box model with only one element selected $e_{p,i}(\theta, \phi)$ to within a complex constant (see (5.32)). Therefore we can equate

their directivities:

$$D_{p,i} = 4\pi \frac{e_{p,i}^* e_{p,i}}{\iint_{\Omega} e_{p,i}^* e_{p,i} + e_{q,i}^* e_{q,i} d\Omega} \quad (5.40)$$

$$= 4\pi \frac{g_{p,i}^* g_{p,i}}{\iint_{\Omega} g_{p,i}^* g_{p,i} + g_{q,i}^* g_{q,i} d\Omega}. \quad (5.41)$$

The denominator of (5.40) is unity from the definition of the $e_{p,i}$ (4.57). Consider (5.41) in terms of the scattering matrix model in transmit. The denominator of (5.41) is the radiation efficiency for the weighting $\mathbf{a} : \{a_i = 1 \text{ and } a_j = 0 \forall j \neq i\}$:

$$\iint_{\Omega} g_{p,i}^* g_{p,i} + g_{q,i}^* g_{q,i} d\Omega = [\mathbf{C}_g]_{ii} = \frac{\mathbf{a}^H \mathbf{C}_g \mathbf{a}}{\mathbf{a}^H \mathbf{a}} = \eta_{\text{rad}} \quad (5.42)$$

where (5.39) was used.

Inserting the denominators into (5.40) and (5.41),

$$D_{p,i} = 4\pi e_{p,i}^* e_{p,i} = 4\pi \frac{g_{p,i}^* g_{p,i}}{\eta_{\text{rad}}}. \quad (5.43)$$

This gives the relationship between the $g_{p,i}$ and $e_{p,i}$ as

$$g_{p,i}(\theta, \phi) = \sqrt{\eta_{\text{rad},i}} \exp(j\Psi_i) e_{p,i}(\theta, \phi) \quad (5.44)$$

The relationship between the w_i and a_i from (5.35) is then

$$w_i = \sqrt{\eta_{\text{rad},i}} \exp(j\Psi_i) a_i. \quad (5.45)$$

where Ψ_i is an (undetermined) phase difference. This thought experiment uses specific weightings. However, it can be extended to all weightings using superposition and so the diagonal matrix \mathbf{A} has elements

$$[\mathbf{A}]_{ii} = \sqrt{\eta_{\text{rad},i}} \exp(j\Psi_i). \quad (5.46)$$

5.4.4 Maximum Gain Weighting

Equation (5.31) results in the gain for the array being⁴

$$G_{p,\text{array}} = 4\pi \frac{\mathbf{a}^H \mathbf{g}_p^* \mathbf{g}_p^T \mathbf{a}}{\mathbf{a}^H \mathbf{a}}. \quad (5.47)$$

The antenna gain is maximized by the conjugate match $\mathbf{a} = \mathbf{g}^*$. This condition can be understood in both receive and transmit as with a passive beamforming network (Beamformer in Fig. 5.1b):

Receive: The weight vector \mathbf{a} is chosen such that all the available power at the reference plane from a point source excitation is delivered to the beamformer output.

Transmit: For a given excitation power $\mathbf{a}^H \mathbf{a}$ the transmitted field in a given direction is maximized.

This thought experiment requires the existence of a beamforming network that is passive, matched to all ports and lossless—the losses are accounted for in $\mathbf{S}_{\text{array}}$. Such a network could be synthesized, for instance, from hybrid couplers with the required power ratios to combine the signals and varying line-lengths to adjust the phases between them.⁵

Inserting the maximum gain condition $\mathbf{a} = \mathbf{g}^*$ and (5.44) into (5.45),

$$\begin{aligned} w_i &= \sqrt{\eta_{\text{rad},i}} \exp(j\Psi_i) \sqrt{\eta_{\text{rad},i}} \exp(-j\Psi_i) c_{p,i}^* \\ &= \eta_{\text{rad},i} c_{p,i}^*. \end{aligned} \quad (5.48)$$

5.4.5 Comparison of Weightings

The purpose of introducing the scattering matrix model is to show the relationship between the NCM (5.22) and the maximum gain weighting (5.48). These two cases are equivalent if their weights are the same, that is

$$w_i \Big|_{\text{Norm Conj}} = k_w w_i \Big|_{\text{Max Gain}} \quad \forall i \quad (5.49)$$

⁴*Realized partial gain* as it accounts for mismatch and polarization match (IEEE Standard Definitions of Terms for Antennas [34]).

⁵This only applies to a given excitation. If the excitation changes it may become lossy or unmatched and in many cases it is impossible to realize matched-lossless-multiport networks for arbitrary excitations [289].

where k_w is an arbitrary complex constant. Using (5.22) and (5.48) this implies

$$\eta_{\text{rad},i} = k_w / [\mathbf{C}_{T_{\text{sys}}}]_{ii} \quad \forall i. \quad (5.50)$$

That is the radiation efficiency is inversely proportional to the noise power for each element.

It is difficult to conceive of a physical condition that would result in this relationship but a stronger case may be approximately true under certain circumstances: this stronger condition is that all the noise powers are equal

$$[\mathbf{C}_{T_{\text{sys}}}]_{ii} = [\mathbf{C}_{T_{\text{sys}}}]_{jj} \quad \forall i \text{ and } j \quad (5.51)$$

and all the radiation efficiencies are equal

$$\eta_{\text{rad},i} = \eta_{\text{rad},j} \quad \forall i \text{ and } j. \quad (5.52)$$

The noise powers for FPAs are dominated by the spillover noise and the receiver noise. The former depends on the radiation pattern and will be roughly similar for each element of an FPA. The latter depends on losses in the array, the receiver noise temperature and noise coupled into it from other elements. For an FPA it is also expected to be fairly similar for each element. In the experimental work, the maximum difference between the receiver temperatures for this project was found to be 2.7 dB and the RMS 1.5 dB (see Section 6.4.5).

The conditions for the radiation efficiencies (when being excited one-at-a-time) being the same for each element can be illuminated by considering conservation of power again. For the i^{th} element only excited in the scattering matrix model, (5.36) becomes

$$P_{\text{available},i} = P_{\text{radiated},i} + P_{\text{reflected},i} + P_{\text{dissipated},i}. \quad (5.53)$$

Dividing by the right $P_{\text{available},i}$ and rearranging, the radiation efficiency is (for $a_i = 1$ and $a_j = 0, \forall j \neq i$)

$$\eta_{\text{rad},i} = 1 - \eta_{\text{reflected},i} - \eta_{\text{dissipated},i} \quad (5.54)$$

$$= 1 - \sum_j S_{ji}^* S_{ji} - \eta_{\text{dissipated},i} \quad (5.55)$$

where the $S_{ji} = [\mathbf{S}_{\text{array}}]_{ji}$ are the scattering matrix elements. The $\eta_{\text{reflected},i}$ terms will be similar where the power lost from the reflection coefficient (S_{ii}) and mutual coupling (S_{ji} , $j \neq i$) terms are similar for each element. This occurs in the centre of a large uniform array or in the special cases of a uniform circular array [211] and an array of two identical elements [213]. Therefore beamforming an FPA with central elements dominating (having the highest weights) will tend toward this condition. Dissipation in the array (not in the terminations), $\eta_{\text{dissipated},i}$, will be relatively low for an FPA with sufficiently low noise for practical radiotelescopes.

In the case of the FPA system used for this project the difference between the gain for NCM and the maximum achievable is of the order of 0.3 dB (see Section 8.6.2).

5.5 Summary

In this chapter a brief review of beamformer strategies was followed by the formulation of the weightings used in the experimental side of this project. The emphasis is on weightings that can be calculated using signals available from an operational radiotelescope. The ‘black-box’ array model from Chapter 4 was developed for this purpose and the weightings are expressed using the model’s parameters.

The beamforming weightings used in this project are the maximum G/T and the NCM. Radio astronomy puts a premium on sensitivity above other figures of merit and so while other factors are important, the beamforming weighting used in an operational telescope will, in most cases, be very close to the maximum G/T weighting. The NCM provides a weighting that can be convenient in the evaluation and commissioning of a radiotelescope. Both weightings require a point source reference and measurement representing the noise on the array ports with the former needing the full covariance matrix and the latter only the auto-correlations (diagonal) and not the cross correlations (off-diagonal) terms.

A scattering matrix model was developed to demonstrate the relationship between the maximum gain and the NCM weightings. It was shown that the NCM is similar to the maximum gain weighting if the equivalent noise temperatures and mutual coupling elements is similar for each element. This is the case with the instrument used in this project and will be for arrays

with similar elements seeing similar noise scene environments. In general, however, there is insufficient information from the black-box model to determine or maximize the antenna gain where losses in the array are taken into account. The maximum directivity weighting can be found, however, if the noise covariance matrix can be measured in two different uniform noise scenes.

The algorithm for finding weightings with multiple nulls at arbitrary locations was also developed. This can be used to minimize cross-polarization or interference.

There are more sophisticated beamforming approaches and finding the optimum for different applications will be a rich field of research as ASKAP, Apertif and other radiotelescopes are deployed [286, 290, 291]. Some of the considerations are optimization for polarimetry, interference mitigation, pattern stability, compensation for reflector deformation with gravity and Vernier beam steering.

Further work on the developments in this chapter could include an investigation of relationships between the maximum directivity and maximum gain conditions. There may also be more relationships between the scattering matrix and ‘black-box’ models that can improve marrying array models and measurements. Mutual coupling effects have been implicit in this work and studying them more explicitly may bring further insights.

This chapter brought together existing theory and presented it in terms of the black-box model. The contribution is considered to be the clarity of the presentation for applications where the internals of an array are inaccessible such as evaluating an assembled system. The author is unaware of the relationship between the maximum gain and NCM being expressed elsewhere.

Chapter 6

Instrumentation

6.1 Introduction

A two-dish interferometer was built at the CSIRO Radiophysics Laboratory in metropolitan Sydney to study the use of FPAs in radio astronomy. This location is the headquarters of both the CSIRO ICT Centre¹ and CASS.² The system is known as the *New Technology Demonstrator (NTD) Interferometer* and was suitable for demonstrating beamforming and investigating FPA evaluation techniques and so it was used for the empirical work in this thesis (Fig. 6.1).

The content of the three chapters dealing with the experimental component of this thesis is as follows:

Chapter 6 Instrumentation. FPA system description and debugging and verification of the system performance.

Chapter 7 Measurement Results. Measurements to evaluate the performance of the FPA itself—gain, noise performance and radiation patterns.

Chapter 8 Discussion of Results. Discussion of the FPA evaluation measurements. The results are compared with predictions based on the dish structure and the FPA.

The NTD Interferometer is described in detail in [12]. This chapter emphasises the author’s contribution to the system and its commissioning. The level of detail is higher than required to follow the measurements described

¹Information and Communication Technologies Centre

²CSIRO Astronomy and Space Sciences



Figure 6.1 – The two-dish prototype radiotelescope located in Sydney; the east antenna in the foreground is fitted with the FPA and the west antenna in the background with a single horn.

Table 6.1 – NTD interferometer specifications.

Dish Diameter ^a	14.174 m
Dish F/D ^b	0.399
Frequency range ^c	1.1–1.8 GHz
Instantaneous bandwidth	24 MHz
Mount	Equatorial

^a Earlier project documents and some publications [12] had erroneously stated the diameter as 13.7 m.

^b F/D : focal length on dish diameter.

^c Initially the range was 0.7–1.8 GHz.

in Chapter 7 but it is provided in the hope that it may be of assistance in other FPA projects.³

6.2 Overview

The NTD Interferometer was built during 2005 and 2006 with improvements to the system, mainly in the operating software and beamformer firmware, continuing during the life of the instrument. In January 2009 there was a major equipment failure in the system. This failure was not repaired as CSIRO’s FPA technology development focus had moved to a new test bed built adjacent to the Parkes 64 m radiotelescope and sufficient data had been gathered on the NTD Interferometer.

The primary specifications for the NTD instrument are shown in Table 6.1. A block diagram of the system is shown in Fig. 6.2 and a more detailed signal flow diagram in Fig. 6.3.

The system was developed by the project team that is listed in [12] (reprinted in Appendix H.6). The author took prime responsibility for the system after initial investigations were completed [8]. Although basic beamforming was demonstrated at this time, a methodical approach to understanding, optimizing and stabilizing the system was undertaken by the author. This provided more consistent results and facilitated demonstrating the maximum G/T beamforming weighting. The following list clarifies the attributions for the NTD Interferometer project:

6.3 Reflectors. This work was performed by Mike Kesteven, external con-

³Lessons from the NTD project have certainly been applied the ASKAP FPA measurements.

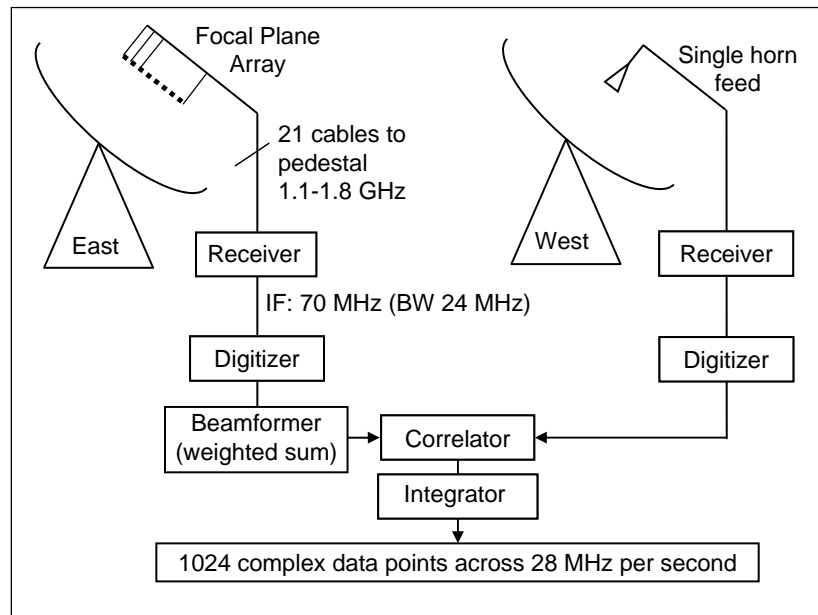


Figure 6.2 – System diagram of the prototype radiotelescope. Twenty one signals are brought down from the FPA through the receiver to the digitizer. Autocorrelations and cross-correlations between any two FPA inputs were also possible.

tractors and other CSIRO staff.

6.4 Focal Plane Array. This section is the author’s work with the exception of the design and supply of the FPA (ASTRON) and the design and installation of the filter circuit—Alex Grancea and Chris Cantrall respectively (Section 6.4.2). The author provided the initial identification of the presence of distortion products, performed the measurements and provided the analysis.

6.5 Vertex Noise Source. The design of the system was the author’s. The noise source hardware was built by Chris Cantrall and the software driver was written by Maxim Voronkov. The higher level software control and calibration method was the author’s work.

6.6 Receiver. The receivers were designed by Alex Grancea. Establishing the ideal gain settings was the author’s work.

6.7 Beamformer-Correlator. The beamformer correlator was designed and built by others at CSIRO including Joseph Pathikulangara, Jayasri Joseph and John Bunton.

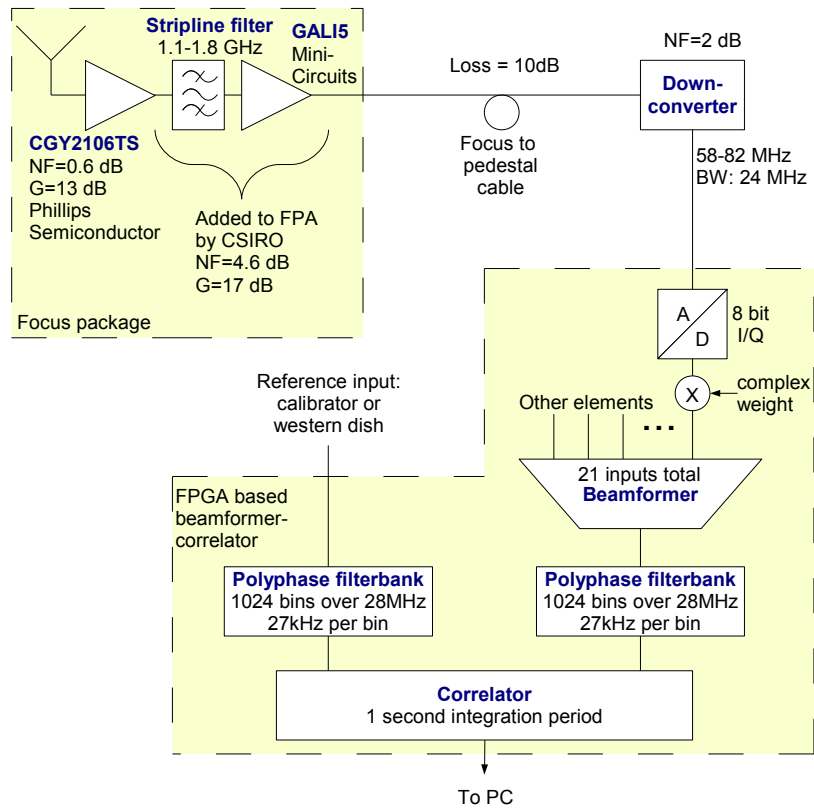


Figure 6.3 – Signal flow diagram for the NTD Interferometer indicating the key components.

6.8 Instrument Control and Data Collection. The basic system control functionality including the data processing was augmented by the author as described in this section.

6.9 System Level Commissioning Tests. This was the author's work.

6.10 Element Gain Stability. This was the author's work.

6.11 Radio Sources. Suitable radio sources for this work were identified by Tim Cornwell, Maxim Voronkov and the author.

6.3 Reflectors

The two reflectors were recovered from the University of Sydney Fleurs Synthesis Telescope, an instrument that was in use in the 1970s and 1980s [292]. The reflectors, quadripods and mounts with gearboxes were refurbished and the original surface was replaced with a 6 mm mesh.

A survey reported a 3 mm RMS deviation from the paraboloid. This corresponds to 0.012λ at 1200 MHz. The effect of the mesh transparency and surface errors to the efficiency is addressed in Section 8.4.1.

The equatorial mount allows the reflectors to follow the rotation of the sky with respect to the ground with the declination axis fixed and only the hour angle axis moving. The sky coverage was $\pm 3\text{h}44'(\pm 56^\circ)$ in hour angle and $-83^\circ, +16^\circ$ in declination.

6.4 Focal Plane Array

The array used was designed as a prototype for wideband-directly-receiving arrays for the SKA. This array was developed under the *Thousand Element Array* (THEA) project [293, 294] and was one of a number of *THEA tiles* built by ASTRON. The fortuitous availability of this hardware assisted CSIRO to rapidly assemble their prototype FPA system.

The THEA tile is an 8×8 single polarization array of Vivaldi or tapered slot line elements. They nominally cover the band of 600–1700 MHz. The array spacing is 127.5 mm (half wavelength at 1.176 GHz) with the array occupying a $1\text{ m} \times 1\text{ m}$ area (Fig. 6.4). The focus package 30 dB of gain to compensate for losses in the cable run from the focus to the receivers in the pedestal.

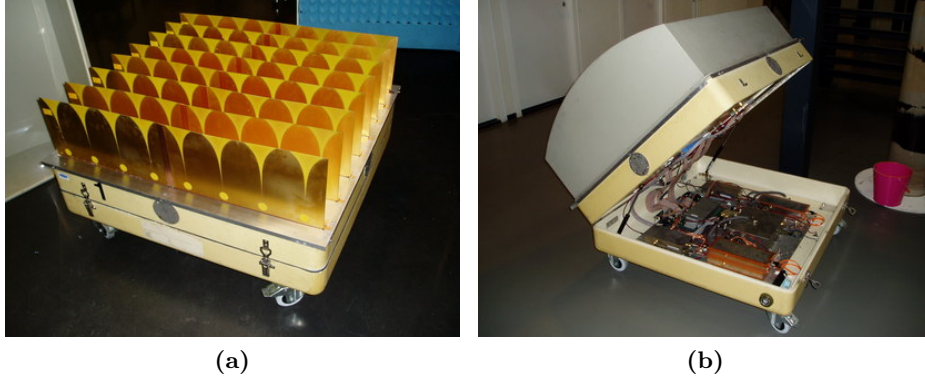


Figure 6.4 – Focal plane array with (a) the cover removed showing the Vivaldi elements and (b) the top opened to reveal control electronics and power supplies.

The embedded element radiation patterns were neither measured nor accurately modelled by ASTRON or CSIRO.⁴ Simulated radiation patterns from an array, designed under the FARADAY project, with similar Vivaldi elements are shown in Fig. 6.5 [295]. This is an 8×9 element array with two polarizations in an *egg-crate* configuration [169, 267]. The element spacing for the frequency analysed is 0.45λ rather than the 0.51λ in this work. With these differences, these patterns can be taken only as a rough guide to the THEA patterns. The feed taper at the edge of the dish $\theta_{\text{edge}} = 64^\circ$ would be about 6 dB. With the spherical spreading loss of 2.9 dB this implies an aperture edge taper of about 9 dB. Integrating the pattern over the sphere for the antenna at zenith, the spillover efficiency, $\eta_{\text{spill}} = 81\%$ and the sky efficiency, as defined in (7.8), $\eta_{\text{sky}} = 86\%$. Using a ground temperature of 300 K and sky temperature of 6 K, the antenna temperature from this pattern would be 46 K. These figures will be used for comparison with the measurements made on the NTD antenna in Chapter 8.

6.4.1 Scattering Parameters

Scattering parameter data for one of the THEA tiles was measured by ASTRON [296] and provided to the author. This data was for element 1 of the central subarray (see Fig. 6.16a) with respect to all other elements. Fig.

⁴ASTRON did measure the beamformed pattern of the array as this was more relevant to their program. At CSIRO the priority at that time was to obtain FPA system experience rather than the in-depth analysis of this particular array.

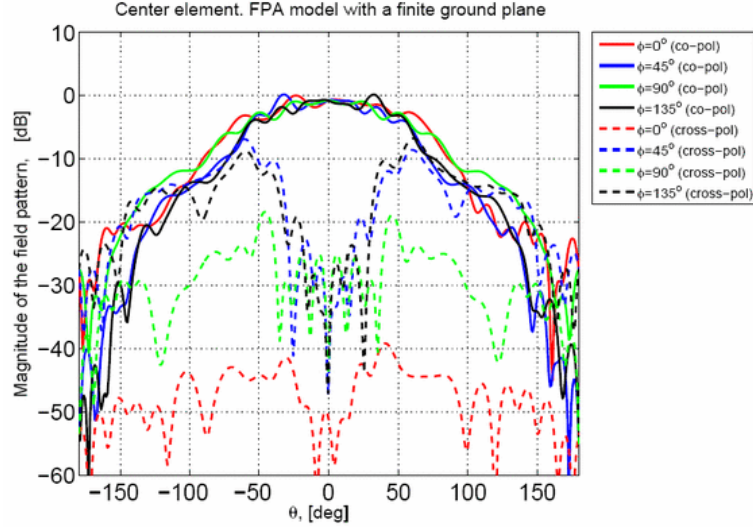


Figure 6.5 – Central element radiation patterns for the FARADAY array, a Vivaldi array similar to the THEA tile. Graph courtesy of ASTRON.

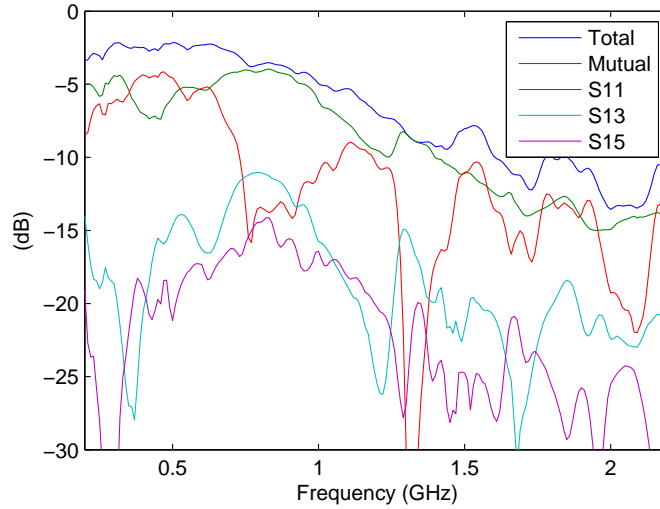


Figure 6.6 – Scattering parameters of a THEA tile. The *Total* trace is the total coupling loss coefficient including the reflection coefficient. The *Mutual* trace is the sum of the fraction power coupled into other elements. The element numbering is for the central subarray (Fig. 6.16a).

6.6 shows the total scattering loss coefficient, total mutual coupling loss coefficient, and representative scattering parameters.

The scattering and coupling losses for element 1 at 1200 MHz are shown in Table 6.2.

Table 6.2 – THEA tile scattering parameter data.

Total scattering loss	7.0 dB	19.9%
Mutual coupling loss	9.5 dB	11.2%
Return loss	10.6 dB	8.8%

The mutual coupling losses can be recovered to some extent by beam-forming. The coupling does however conduct noise emitted from surrounding LNAs into a given element’s input. The return loss impacts the noise match of the LNA as well as the overall antenna’s radiation efficiency.

6.4.2 Distortion Products

Tests on the FPA, prior to mounting it in the dish, showed it was picking up significant interference from local transmitters (Fig. 6.7) and distortion products in the intended band of operation were (600–1700 MHz) suspected. Convolution of the spectrum was used to identify which peaks in the desired band were real in-band transmissions and which were distortion products from out-of-band transmissions. The method described below was done with both the power spectrum and its square-root, representing voltage. While the levels of the peaks in the resulting spectra differed, the conclusions to be drawn from them were the same for both power and voltage spectra convolution. The figures shown here are for the power convolution.

The 0–1 GHz band was convolved with itself to indicate the spectrum of the second order products (Fig. 6.8). This spectrum was then convolved with the original 0–1 GHz spectrum to indicate the third order products (Fig. 6.9). The levels of these spectra were shifted to match peaks in the original spectrum (Fig. 6.10).

To reduce this distortion, the FPA was modified by adding 1150–1750 MHz filters between the first and second amplifiers on all 64 elements. The original second amplifier was replaced with one incorporated into the new filter PCB.⁵ The array was illuminated with a small log-periodic antenna and the frequency response recorded before and after the modification as seen in Fig. 6.11 where the difference between the traces is the relevant feature.

The interference spectrum was measured under the same conditions as for the unmodified FPA and the distortion-product spectra matched in level

⁵Printed Circuit Board

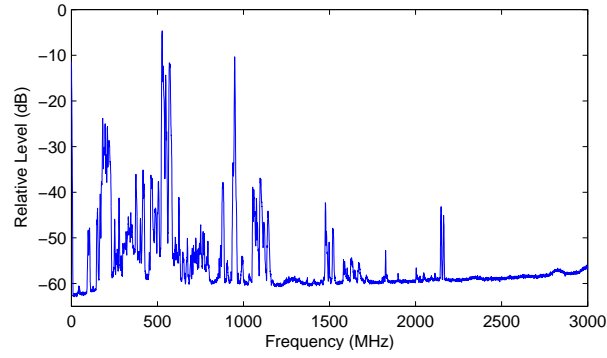


Figure 6.7 – Unmodified FPA spectrum measured whilst the focus package was on the ground near the eastern dish.

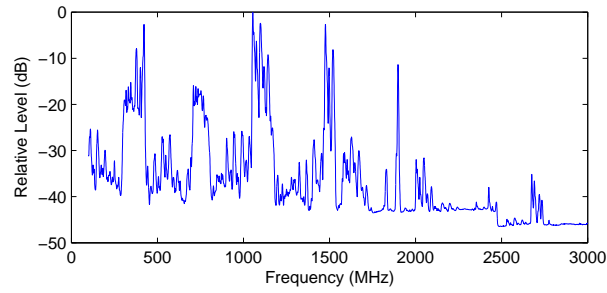


Figure 6.8 – Second-order distortion products.

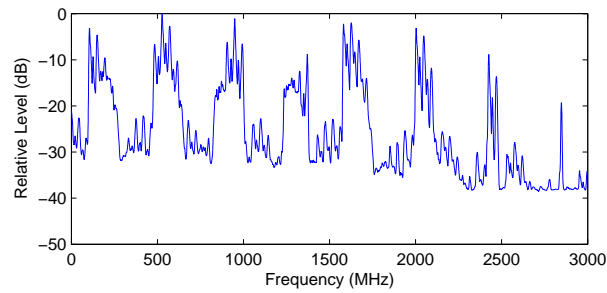


Figure 6.9 – Third-order distortion products.

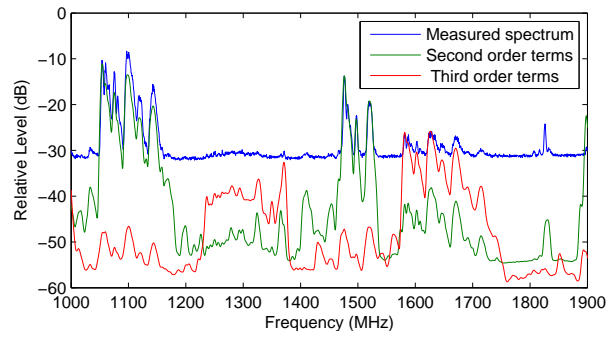


Figure 6.10 – Distortion products with levels matched to the original spectrum peaks for the unmodified FPA.

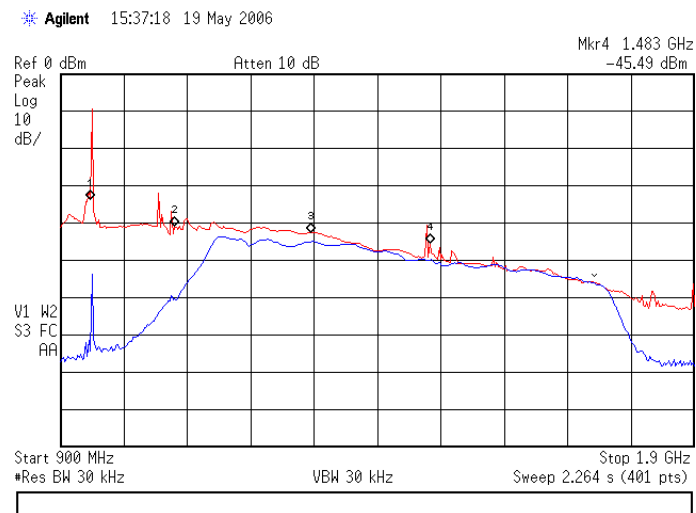


Figure 6.11 – The response of the FPA before and after the filter modification was added. The array was illuminated by a small log-periodic antenna.

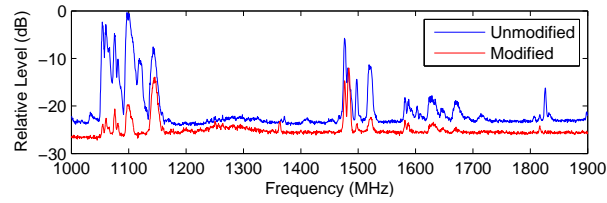


Figure 6.12 – FPA modification spectrum comparison showing marked reduction in the presence of distortion products.

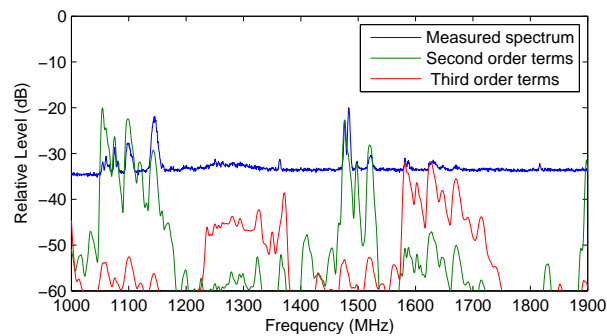


Figure 6.13 – Distortion products with levels matched to the original spectrum peaks for the modified FPA. Note that in the modified channel the bandwidth was limited to 1.15–1.75 GHz so distortion products outside this range are not present.

as before. A signal at 1484 MHz (identified as an in-band transmission and not a distortion product) was used to align the levels of the pre- and post-modification spectra (Fig. 6.12).⁶ The addition of the filter resulted in a reduction of the distortion products by 10–20 dB in the new operational band of 1150–1750 MHz. The second and third order distortion-product spectra were matched in level as with the unmodified case (Fig. 6.13).

This convolution approach provides only a coarse estimate of the distortion levels: measuring and or modelling the electronics would provide more detailed information regarding the traditional intermodulation-distortion measures. Nonetheless, this method evaluates an active antenna in its operating radio frequency interference (RFI) environment and rapidly identifies major sources of intermodulation.

⁶A subsequent search for a possible transmitter at this frequency on the Australian spectrum regulator’s database yielded no match in NSW [297] and a search of the internet showed that 1.5 GHz CPUs often run at around 1484 MHz. A nearby CPU clock is the most likely candidate therefore with some other possibilities being other nearby equipment, and the second or third harmonic of a lower frequency transmission.

Another benefit of this analysis is the prediction of the presence of distortion products below the noise floor. This is important for interferometry because, as most of the noise in each of the two inputs to the correlator is uncorrelated, its impact reduces with integration time. Distortion products such as these, however, could be present in both inputs and not reduce with integration time. Both the power and voltage based convolutions shown in Fig. 6.13 display the same bands as the best for observations, albeit with different predicted noise floors. These bands are in the regions of 1200, 1400 and 1560 MHz.

In the case of the NTD Interferometer, the western dish feed does not suffer from these distortion products as it has very high rejection of signals below the cut-off frequency of 1.06 GHz of the circular waveguide in the throat of the horn.

6.4.3 Frequency Selection

The considerations for the selection of a frequency for measurements are listed below.

- The band needs to be largely clear of interferers and distortion products.
- A lower frequency is preferred to keep the element spacing in terms of wavelength low. Wider spacing results in the efficiency of the FPA falling and/or the central element dominating, reducing the effect of beamforming—the subject of this work. Grating lobes can also reduce the effectiveness of reducing the noise contribution of radiation from the ground (see Section 3.4).

The frequency band chosen for the measurements was 1188–1212 MHz (24 MHz centred on 1200 MHz) with the corresponding element spacing in terms of wavelength of 0.51λ . This is the lowest frequency band available for the system that was mostly clear of RFI. This band lies within an *aeronautical radionavigation* band as designated by the Australian Communications and Media Authority [298] and interference was encountered above 1207 MHz on days when the Sydney airport landing approach was routed overhead. The interference was managed by reducing the frequency range to 1188–1207 MHz on these days and accepting the slightly lower sensitivity.

Table 6.3 – FPA parameters for calculating the noise temperature.

Parameter	Low	Typ.	High
Noise from surrounding elements ^a (K)	6.	11.	16.
Dissipative loss in antenna ^a (dB)	0.4	0.5	0.7
LNA noise figure ^b (dB)	0.5	0.6	0.8
Gain of LNA ^b (dB)	11.7	12.6	13.5
Filter and second amp. Noise Figure ^c (dB)	4.2	4.6	5.0
Gain of filter and second amp. ^c (dB)	15.0	17.0	19.0
Focus to receiver cable loss ^d (dB)	11.5	10.0	8.5
Receiver Noise Figure ^c (dB)	1.8	2.0	4.0

Source of data: ^a Woestenburg [299] ^b Data sheet [300] ^c Grancea [301]
^d Measured

Input parameters used for the calculation of the THEA tile receiver temperature, T'_{rx} , with specified or estimated uncertainties. The uncertainties represent the 95% confidence interval.

6.4.4 FPA Noise Performance

In this section an estimate of the noise performance of the THEA tile array is presented. The parameter of interest here is the receiver temperature T_{rx} , including losses in the antenna but not radiation from the surrounding scene, such as spillover (see Section 4.2). The noise performance was not measured directly and so an estimate based on the following analysis of the tile is used here. The reference plane we are using for active antennas requires this receiver noise to be referred to the radiation port. Here the noise performance is calculated at the input to a single antenna and does not include the reduction in efficiency due to losses in other elements nor scattering from the element in question. These effects are addressed in Section 7.6.1. To denote this difference, the receiver temperature calculated here will be denoted T'_{rx} .

The parameters for the calculation are presented in Table 6.3. The typical or best estimate values are taken from a number of sources as indicated in the table. Approximate uncertainties are assigned to each parameter, based on background engineering knowledge of similar systems.

The equivalent noise temperature for an n stage cascade of amplifiers is given by

$$T'_{\text{rx}} = T_{\text{e},1} + \sum_{i=1}^{n-1} \left(T_{\text{e},i+1} / \prod_{j=1}^i G_j \right) \quad (6.1)$$

where $T_{e,i}$ is the equivalent noise temperature referred to the input of the i_{th} stage and G_i is the power gain of the i_{th} stage.

The equivalent noise temperature can be found from the noise figure using

$$T_e = T_0 (F - 1) \quad (6.2)$$

where $T_0 = 290$ (K) and F is the noise figure as power ratio.

The noise coupled in from the surrounding elements can be considered a stage with unity gain. The contribution from loss $L = 1/G$ in the antenna and the cables results in an equivalent noise temperature of

$$T_e = T_{\text{phys}} (L - 1) \quad (6.3)$$

where T_{phys} is the physical temperature of the lossy element in Kelvin. This is 40°C and 30°C for the antenna loss and the cable loss respectively. The physical antenna temperature is taken as a typical temperature as reported by the temperature sensor inside the tile. It was typically 10°C above the ambient temperature. The cable temperature is for a typical day during the measurement period. The final receiver noise is relatively insensitive to these physical temperatures within the range of actual temperatures experienced.

The uncertainties are combined (see Appendix F for the details) and the contributions to the total uncertainty are presented in Table 6.4. The dissipation in the array and loss in the focus to receiver cable, contribute both noise and loss in the equivalent noise temperature calculation. Only the noise contribution is counted in the total uncertainty as in both cases the loss is a linear function of the noise contribution and so the uncertainty should only be counted once.

The major contributors to the noise are the dissipative losses in the antenna, the LNA noise and the filter and second stage. The uncertainty is dominated by the loss in the antenna and the LNA noise figure.

In this analysis it is assumed the dominant noise sources are uncorrelated from element to element and so the beamformed receiver noise temperature will be similar to that for a single element. Noise coupled from other elements will be correlated but this is a small contribution [302]. A potential contributor that has not been included is the switch-mode power supply used to convert the 48V supplied from the ground to the local supply voltages.

Table 6.4 – THEA tile noise budget and uncertainty contributions.

Parameter	Contrib. to T'_{rx} (K)	$\Delta T'_{\text{rx}}$ (K)		Fig. 6.14
		Low	High	
Noise from surrounding elements	11	−5	5	T Elts
Dissipative loss in antenna	38	−10	20	L Ant
Gain of LNA		−7	9	G LNA
Noise from LNA	48	−9	18	T LNA
Gain of filter and second amp.		−2.0	3.2	G Fltr
Noise from filter and second amp.	34	−5	5	T Fltr
Focus to receiver cable loss	3	−1.7	2.4	L Cbl
Noise from receiver/downconverter	2	−0.3	3.3	T Rx
Total	137	−17	30	

The Low and High columns show the uncertainty contributions in the negative and positive directions for each of the input parameters. The last column shows the designations given in Figure 6.14.

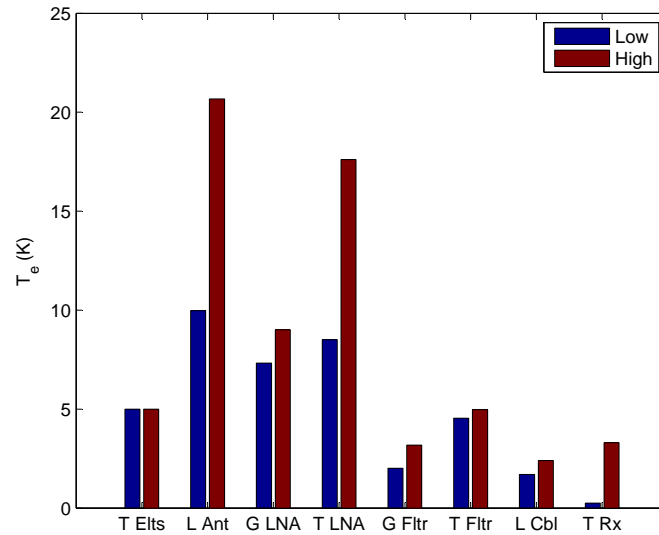


Figure 6.14 – Contributions to the uncertainty in the FPA noise estimate. Contributions to the lower bound are marked *Low* and the upper bound are marked *high*.

Table 6.5 – Receiver noise calculation comparison.

	T'_{rx} (K)		
	Low	Typ.	High
Woestenburger [299]		146	
Grancea [301]	100		130
This work	120	137	166

Analyses conducted by Bert Woestenburger of ASTRON [299, 302] and Alex Grancea of CSIRO [301] arrived at similar conclusions (Table 6.5). One of the THEA tiles was measured by ASTRON [303] arriving at a figure of about 180 K at 1200 MHz. The conditions of the ASTRON measurement differ from the NTD application, as radiation from the ground from behind the array and their beamformer were included in their noise temperature. The tile was also subsequently modified by CSIRO, inserting a filter and using a different second amplifier.

6.4.5 Element Variability

The separate receiver chains for each element have differing electronic gain and noise parameters due to component and layout differences. The complex gain differences are compensated for by adjusting the down-converter attenuators and in the beamforming. The noise variability is also compensated for in the maximum signal to noise beamformer weighting. The degree of similarity is significant in the interpretation of the beamforming weighting (see Sections 5.4.5 and 8.6.2).

A direct measurement of the noise performance of each element was not readily available and so two indirect measurements were combined. The first is the power received from each element with the reference noise source turned off and the antenna looking at cold sky. This measure is proportional to the equivalent noise temperature of each element and to the electronic gain.

$$P_{\text{sky},i} = k_{\text{B}} T_{e,i} B H_i \quad (6.4)$$

where k_{B} is the Boltzmann constant, $T_{e,i}$ is the equivalent noise temperature of the element, B is the bandwidth and H_i is electronic gain of the element.

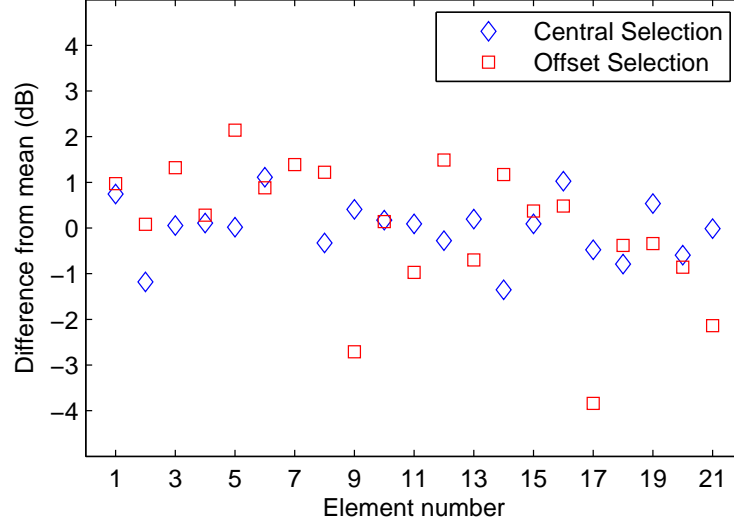


Figure 6.15 – Relative differences between the response to the vertex noise source and the cold sky element noise temperature. The mean difference was subtracted from the data.

The second measure is the correlated element response (amplitude squared) to noise radiated from the dish surface:

$$R_{\text{NS},i} = k_{\text{corr}} S_i A_{\text{NSE},i} B H_i \quad (6.5)$$

where k_{corr} is a constant dependant noise source level coupled into the reference arm of the correlator, S_i is the spectral flux density from the surface noise source at the i^{th} element, $A_{\text{NSE},i}$ effective area of the i^{th} element in the direction of the noise source. The noise source antenna has a half power beamwidth of order 100° so S_i is almost the same for all elements. The ratio of the cold sky power and the noise source power gives the noise temperature of each element to within a constant and an assumed small perturbation due to the difference in the element effective areas:

$$\frac{P_{\text{sky},i}}{R_{\text{NS},i}} = \frac{k_B}{k_{\text{corr}} S_i A_{\text{NSE},i}} T_{e,i}. \quad (6.6)$$

This ratio, divided by the geometric mean, is plotted in Fig. 6.15. The failed element, number 7, from the central subarray is not plotted and was omitted from the geometric mean calculation. The level from element 17 from the offset subarray was typically low and fluctuated intermittently with a

difference of 3.8 dB from the mean. The maximum difference from the mean, excluding these elements, is 2.7 dB. The RMS variation is 0.6 and 1.5 dB for the central and offset subarrays respectively.

The dominant contributor to the noise is thought to be the first LNA transistor. While measurements of the equivalent noise temperature of these devices are not available, the specification sheet provides an indication with a variation of 15 K between the typical and maximum noise figures (0.5–0.7 dB) [300]. Using the receiver temperature estimate of 137 K, this corresponds to 11% (0.5 dB) of the equivalent noise temperature. Other sources of difference include spillover differences and other component and layout variations.

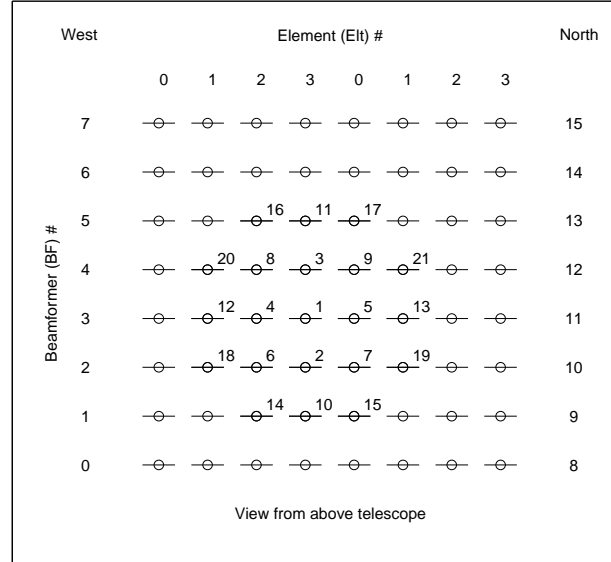
6.4.6 Element Selection

The receiver and beamformer have 24 signal channels. One channel was used for the western antenna and one each for the two calibration noise sources. This left 21 channels for beamforming. This conveniently allowed a symmetrical pattern of elements comprising a 5×5 square with the corners removed. The element numbering scheme is described in Appendix C.

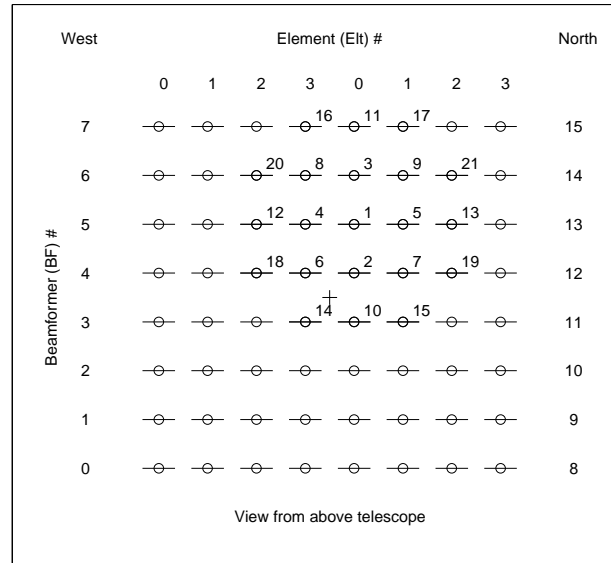
A subarray of elements close to the centre of the 8×8 THEA tile was selected initially (Fig. 6.16a). Element failures occurred during the measurement campaign. For the measurements reported in this work, element 7 of the central subarray showed very low gain indicating it had failed. When element 20 of the central subarray failed, an offset subarray was connected to the focus-to-pedestal cables for the remainder of the measurement campaign (Fig. 6.16b). Element 17 of the offset subarray also failed soon after the change in subarray but it was decided to accept the reduced performance, particularly as this element was at the edge of the subarray.

6.4.7 Pointing Offsets

The central element from both subarrays was used as the reference for beamforming. Consequently both the single central element patterns and the beamformed patterns had peaks in the same location. The offset from the boresight of the dish can be estimated using the geometry of the structure and the beam-deviation factor [201]. The calculated and measured values are presented in Table 6.6. The measured values varied by up to $\pm 0.5^\circ$ from



(a) Central Subarray.

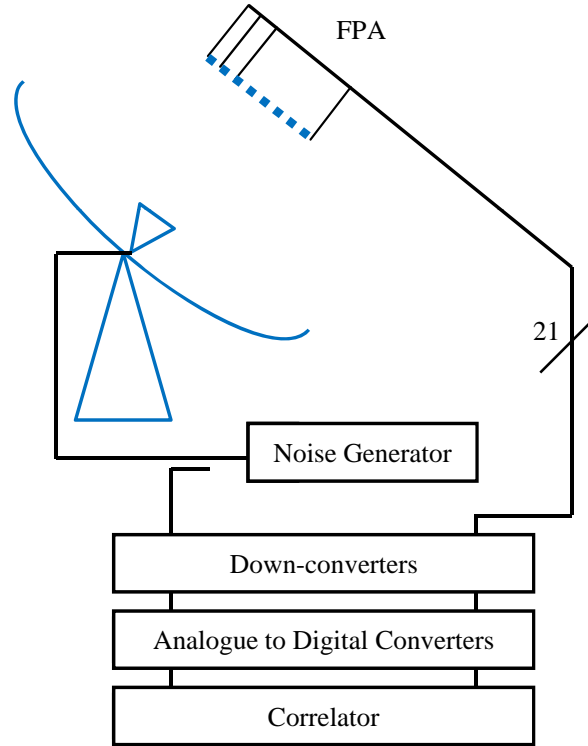


(b) Offset Subarray.

Figure 6.16 – Array numbering scheme viewed from above. The electric field is horizontal. Radiation pattern cuts in declination (north–south) correspond to the 45° plane and cuts in hour angle (east–west) correspond to the 135° plane with respect to the E-field.

Table 6.6 – Pointing offsets for central and offset subarrays.

Subarray	Focal Plane Offsets		Polar Coords.		Equatorial Coords.		Measured	
	x (mm)	y (mm)	θ ($^{\circ}$)	ϕ ($^{\circ}$)	Ha ($^{\circ}$)	Dec ($^{\circ}$)	Ha ($^{\circ}$)	Dec ($^{\circ}$)
Central	-64	-64	0.75	180.00	0.00	0.75	-0.45	0.53
Offset	64	191	1.67	26.57	-0.75	-1.50	-0.35	-1.95

**Figure 6.17** – Calibration system block diagram.

the means shown due to an error in the pointing solution. To avoid this problem, the peak of the beam was found before each measurement set.

6.5 Vertex Noise Source

Drift in the amplitude and phase responses of FPA elements need to be compensated to maintain good beamformed performance. Amplitude changes in radiotelescope horn feeds are often monitored using noise injected in the

throat of the feed. With dense FPAs, the large number of elements and close spacing makes a similar approach difficult. The FPA used in the NTD Interferometer had only basic temperature stabilization, allowing the operating temperature to vary significantly with a corresponding expected variation in element gains.

The approach taken to monitor the element gains (amplitude and phase) was to place a small antenna connected to a noise source at the vertex of the reflector and radiate this at the FPA. A directional coupler was used to provide a sample of the noise signal to the beamformer-correlator allowing amplitude and phase comparisons.

The noise source was a commercially available amplified noise diode with a TTL switch to turn it on and off.⁷ It was assumed the device would be maintained in a “hot” standby mode whilst in the off state with little turn on drift but it was found to take ~ 15 minutes for the level to stabilize after the TTL “on” signal. This precluded using noise source as a quick amplitude calibrator and care should be taken to avoid this warm-up issue in future systems [276].

In this implementation, the antenna placed at the vertex was a log-periodic with the required bandwidth. Other antennas may be more appropriate and dual polarization may also be useful for a dual polarized FPA. Further consideration should also be given to the location of the radiator to reduce any cavity effect formed between the FPA and the dish.

6.5.1 Calibration Method

The objective was to use the signal source located on the dish surface to compensate for amplitude and phase drifts of the FPA elements periodically during an observation. Of primary concern were drifts of the elements relative to each other as this perturbs the beamforming. Changes that are common to all the elements can be removed by standard calibration techniques used in interferometry, for instance employing a strong radio source [304].

Referring to Section 4.9, it is the electronic gains, h_i , that are assumed to require compensation. The weights, u_i , are adjusted to compensate for the drift in electronic gains.

⁷Noisewave NW3G-M

Two data collection phases are used in the observation cycles. Firstly the data for the calculation of weights is collected. The weights are calculated according to the formulation described in Chapter 5. In the second phase, the weights are applied and data is taken on the source.

During the weight-data-collection phase, calibration data (the response to the vertex radiator) is recorded periodically. The complex electronic gains at the completion of this phase are taken as the reference values as this is the point at which the weights are calculated. Linear interpolation is used to compensate for drift during the weight-data-collection phase. In the second phase, when the weights are applied, values of electronic gains are determined from the most recently obtained calibration data.

The application of weights is made irreversible by the summation in the beamformer. This is in contrast to the post processing application of calibration that can be applied to antenna gains in *single pixel* synthesis-imaging arrays [304]. In an investigative stage of FPA system development, the uncorrelated data from each element may be stored allowing different weights to be applied in post processing [86, 180, 209]. In an operational system, however, the volume of data would, in most cases, prevent this approach.

Change in the dish patterns or directivities from each element, $e_i(\theta, \phi)$, may have an impact on the imaging from high sensitivity instruments such as ASKAP and the SKA. Possible mechanisms are

- distortion of the dish due to gravity as it tilts,
- distortion of the dish due to thermal changes, and
- changes in LNA impedance due to thermal changes. The work of Qiao and Shaw in [276] showed that the impact on the radiation pattern may be minimal. Nonetheless, this issue is being investigated further.

This is an area of current research for ASKAP and the use of multiple radiators on the dish surface is being considered to monitor any changes [276].

6.6 Receiver

The receiver used dual frequency conversion to translate the received signal (i.e. sky frequency or RF) to the 70 MHz intermediate frequency (IF). Twenty one of the 24 channels were used for FPA elements and channel 22

was used as a reference containing a sample of the calibration signal. Another two-channel receiver was used in the western dish pedestal for the feed and a noise source in the same fashion as the eastern dish.

The gain of the receivers could be programmed over a range of 32 dB in 1 dB steps. The objective in selecting the gain setting for each receiver, was to ensure the analogue-to-digital converter (ADC) was supplied with a signal that maximizes the dynamic range. It was also important to ensure the calibration signal did not saturate the system. The firmware in the beamformer-correlator was modified to provide the maximum ADC level for each channel over the integration time (1 s). Subsequent designs at CSIRO have incorporated a histogram of the ADC level as this gives a more accurate indication of the range of levels encountered.

Table 6.7 shows the gain setting chosen and the corresponding median of the maximum ADC levels (over 1 s) for each receiver. The maximum ADC levels for all receivers are shown as a function of time in Figs. 6.18a and 6.18c for the reference source off and on respectively and as histograms in Figs. 6.18b and 6.18d. These are for 50 samples and the range is 0–127 corresponding to the (signed) eight bit resolution of the ADC. With the reference radiator signal off, the mean of maxima is 50, corresponding to 8 dB below compression and with the reference on, the mean is 103, corresponding to 2 dB of below compression. The headroom for the reference-signal-off condition allows for RFI to be filtered in the frequency domain after the visibility data is recorded.

6.7 Beamformer-Correlator

The beamformer-correlator digitized the signals from the receiver, produced a weighted sum (beamformed signal) and correlated this against the reference signal, or for autocorrelations, against itself. The correlation product was integrated over 1 s and sent to the control computer every 1.2 s as 1024 complex numbers, each representing a 27 kHz frequency bin. The band covered was 28 MHz.

This system took two frame cycles (2.4 s) to purge data from the previous state after a change in its settings. This dead time substantially increased the duration of operations where the system needed to run through a series of state changes. The most critical of these were the calibration against

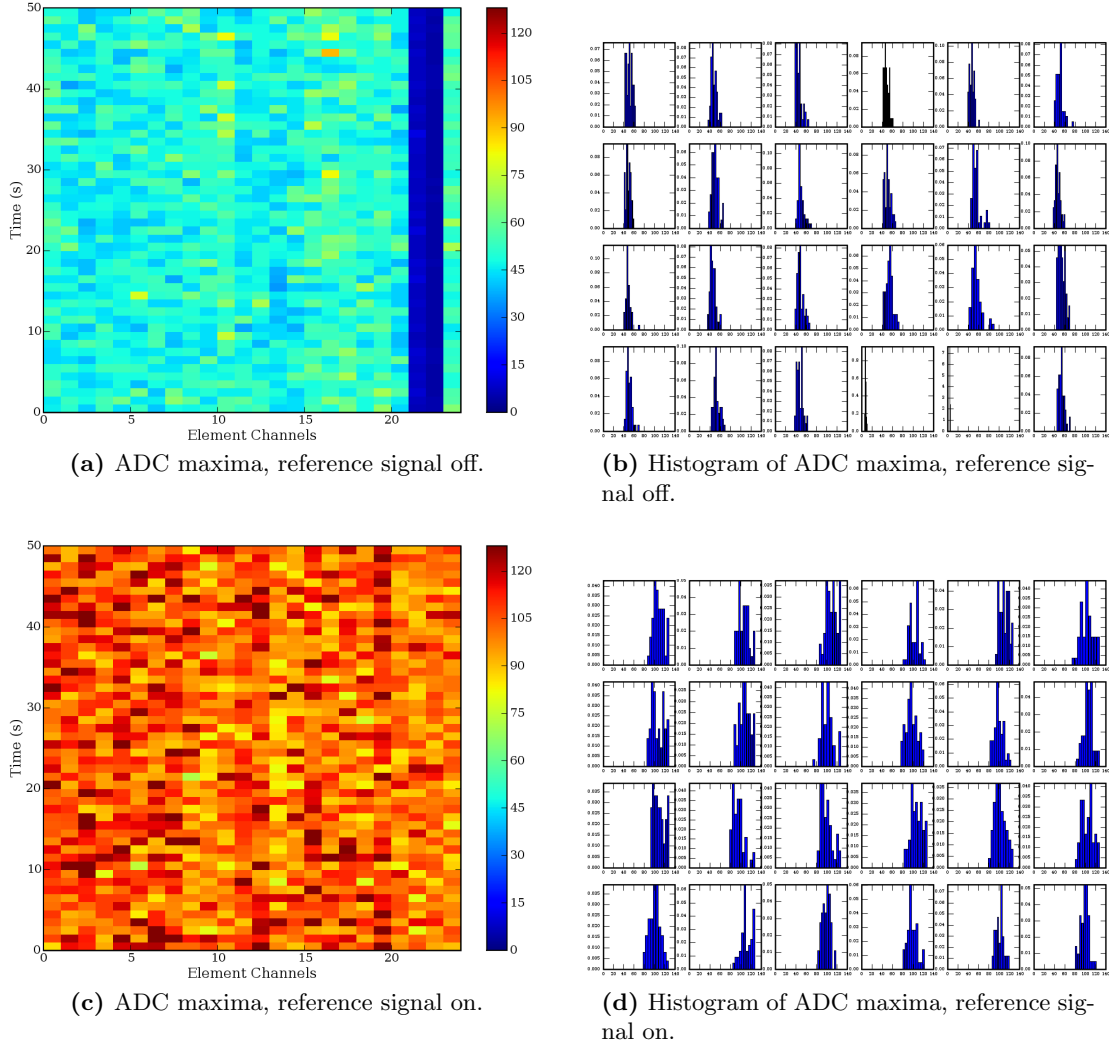


Figure 6.18 – Maximum ADC levels over the 1 s integration period for 50 periods. The histogram horizontal scales range from 0–128 and the vertical range is scaled to the maximum of each data set.

Table 6.7 – Receiver gains and ADC levels

Element	1	2	3	4	5	5	7	8
Gain setting	31	30	28	29	29	30	29	29
ADC Ref. off	51	47	46	48	47	51	48	49
ADC Ref. on	105	105	110	103	110	105	105	108
Element	9	10	11	12	13	14	15	16
Gain setting	29	27	29	27	28	28	28	30
ADC Ref. off	48	51	54	46	48	45	47	54
ADC Ref. on	101	96	98	106	107	93	97	106
Element	17	18	19	20	21	ER ^a	WR ^b	WF ^c
Gain setting	27	31	30	30	28	25	26	27
ADC Ref. off	54	54	49	52	47	7	4	53
ADC Ref. on	99	104	100	109	99	97	101	98

^a ER: eastern dish reference sample^b WR: western dish reference sample^c WF: western dish feed

The ADC levels range from 0–127.

the vertex radiator taking 7 minutes and the measurement of the covariance matrix (correlation of each FPA element against every other element) taking 28 minutes.

6.8 Instrument Control and Data Collection

The control and data collection system comprise three computers that provide [12]:

- antenna pointing control,
- beamformer control and data reception, and
- master control, data repository and data processing.

The system is controlled through running scripts written in the Python computer language and the standard AIPS++⁸ measurement set is used for data storage [305]. When the author took over prime responsibility for the system, basic functionality was available but there were a large number of parameters that needed to be set and sometimes changed during an observation run. The existing ~4000 lines of original control code were augmented by ~8670 lines of code written by the author. This additional software sim-

⁸Astronomical Image Processing System

plified the setting of operational parameters, automated the operation and processed the data collected.

The operation was broken down into a hierarchy of four levels, starting at the shortest time frame as described below:

1. **Frame:** ~ 1.2 s: the integration time of the correlator. The complex correlator products for the 1024 frequency bins (across 28 MHz) were stored for each frame.
2. **Scan:** Typically 10 to 20 frames: during this period the setting of the system, and in particular the beamformer-correlator, remained constant. The correlator products were averaged over this period after fringe rate and delay compensation (see Section 6.8.3).
3. **Observation Cycle:** a schedule of scans and processing steps was defined. The system state such as antenna pointing and beamformer-correlator settings was set and the scans were performed with state changes between them. The data from the scans was then processed to provide a complex response value for each scan.
4. **Meta-Observation Cycle:** in a number of operations, data from one observation cycle was required in a following cycle, for instance calibration data was used to adjust the weight settings. To enable this, the facility was developed to concatenate a number of observation cycles and access the processed data from the previous cycles.

It was also found very useful in system development and testing to run the control system with any of the major hardware components disabled. This allowed testing and development to continue on the software and hardware systems while part of the system was out of commission for repair or independent development.

Processing the data immediately upon completion of an observation cycle allows the observer to decide on the next course of action. If the result is unsatisfactory, the operation can be immediately repeated, often with a minor change in parameters. Attention was paid the speed of the processing so that it comprised only a fraction of the overall time required for an observation cycle.

6.8.1 Antenna Pointing

The primary pointing system was based on the optical axis of the reflectors and pointing solutions were established using single horn feeds prior to the

author's involvement. The beam centres for the FPA work were chosen to be centred on the central element of the selected 21 elements.

Pattern cuts showed the pointing for celestial sources drifted by fractions of a degree over time. The error was enough to degrade pattern measurements significantly and reduce the accuracy of gain measurements. Initially small angle approximations were used and it was thought these may be contributing to the drift. To ensure that this was not the case, a thorough investigation of the transforms was conducted. Three coordinate frames were considered: 1) The mount frame attached to the earth, 2) the pointing direction and orientation of the reflector determined by the equatorial mount and 3) the offset of the beam centre from the reflector reference. The latter is necessary—as with any multibeam system—to accommodate the offset from the boresight of the reflector. The details are outlined in Appendix D.

When the full angle correction was implemented, the pointing drift was still present, and therefore the drift was thought to be in the primary antenna motion control and tracking system. Ultimately the drift was managed by correcting the pointing regularly by finding the peak of short pattern cuts on the source.

6.8.2 FPA Control and Monitoring

A command line facility was available to turn on and off the LNAs in the FPA individually using the control system provided by ASTRON. This proved useful to confirm the mapping from the input through to data processing. The temperature of the FPA could also be interrogated, and this function was used to verify that the FPA was not overheating during high external ambient temperatures.

6.8.3 Data Processing

An important aspect of the processing was to provide rapid quality control information regarding the observation. The identification of hardware faults, interference and incorrect system settings allows the observation to be repeated rapidly and prevents time being wasted on collecting corrupted data. The information is presented in graphical form or tabular form. A typical series of images is displayed in Figs. 6.19 to 6.31. These have been taken from one observation cycle with the exception of the figures showing

antenna movement (Fig. 6.19) and RFI flagging (Figs. 6.23 and 6.24). These data were taken from other cases as they better illustrate the value of the data presentation.

The pointing parameters of the antennas were displayed upon conclusion of the observation. This was done in three coordinate systems, each with different uses (see Fig. 6.19):

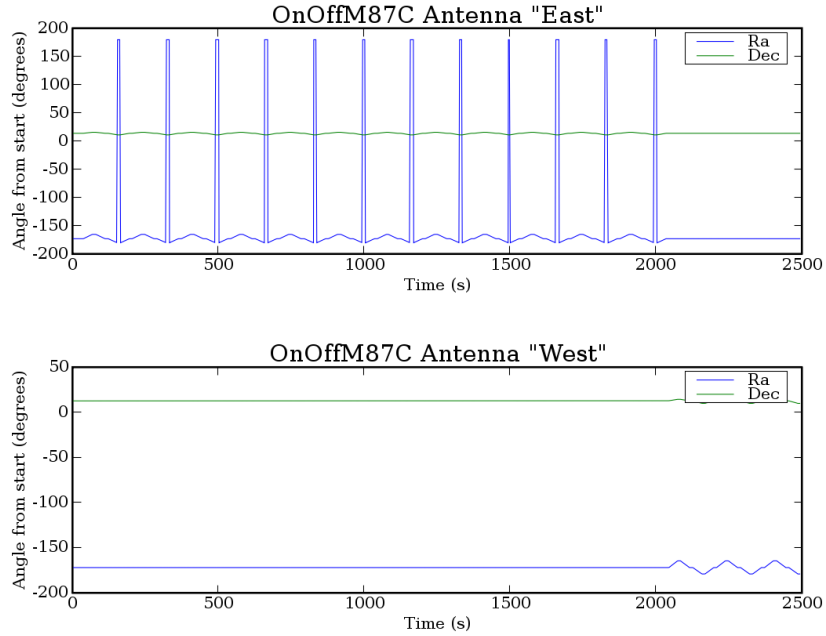
- azimuth and elevation—spillover will change with elevation,
- hour angle and declination—the natural system for the equatorial mount, and
- right ascension and declination—reveals motion relative to astronomical sources.

A plot of the time of each scan is shown in 6.20. The integration period of ~ 1.2 s is progressively subtracted from the plot so only the additional delays are displayed. These plots are useful in identifying ways to reduce unnecessary time losses in the system and instabilities such as “retries” in communication between subsystems.

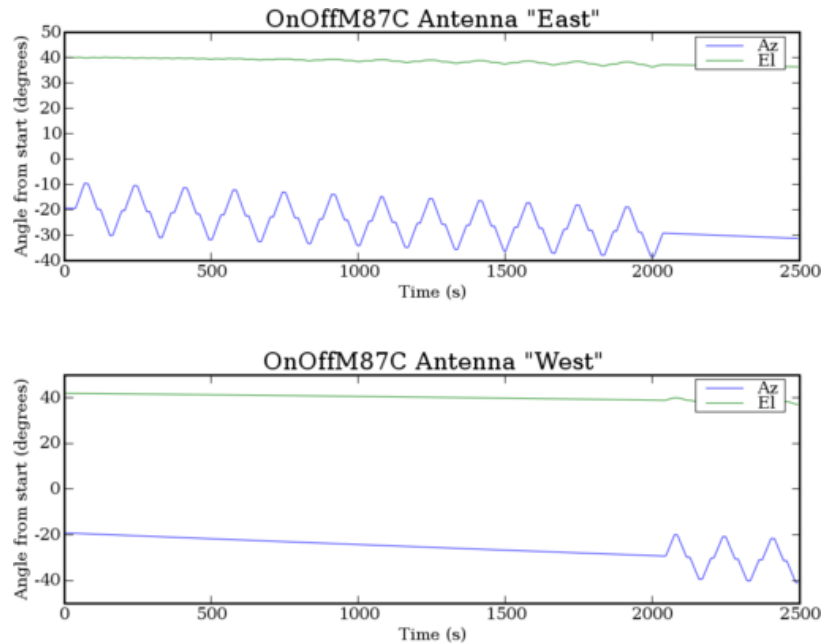
Fig. 6.21 shows the maximum ADC levels against time. Short term radio frequency interference (RFI) could often be seen in these plots and the variation of levels with different system configurations can also be seen. For instance, scanning through strong celestial sources and the vertex calibrators are clearly visible. Combining this view with a presentation of the same data as a histogram (Fig. 6.22) allowed the receiver gain levels to be set to optimize the dynamic range of the system.

In order to mitigate the effect of RFI, a method was sought to automatically excise easily identifiable narrow band RFI. Peaks in the frequency response were assumed to be RFI and flagged using a median filter. If RFI was identified in a frequency bin in one frame, that bin was excised in all the frames for that observation. The system also had provision to excise or protect sections of the frequency bands during processing. This protection was required when observing the HI spectral line for instance. Fig. 6.23 shows the amplitude data before and after flagging and the frequency bins that were flagged.

Fig. 6.24 shows the mean received spectrum over an observation with the flagged sections excised. This display allows the performance of the median filter to be checked and demonstrates how even short term frequency spikes, such as the one at 1199 MHz, are detected and cause that bin to be excised



(a) Right ascension and declination vs. time.



(b) Azimuth and Elevation vs. time.

Figure 6.19 – Antenna pointing plot. The observation run cycled eastern antenna on and off radio source and then did the same for the western antenna. The angular distance from the source can be seen in (a) and the minimal change in elevation can be seen in (b).

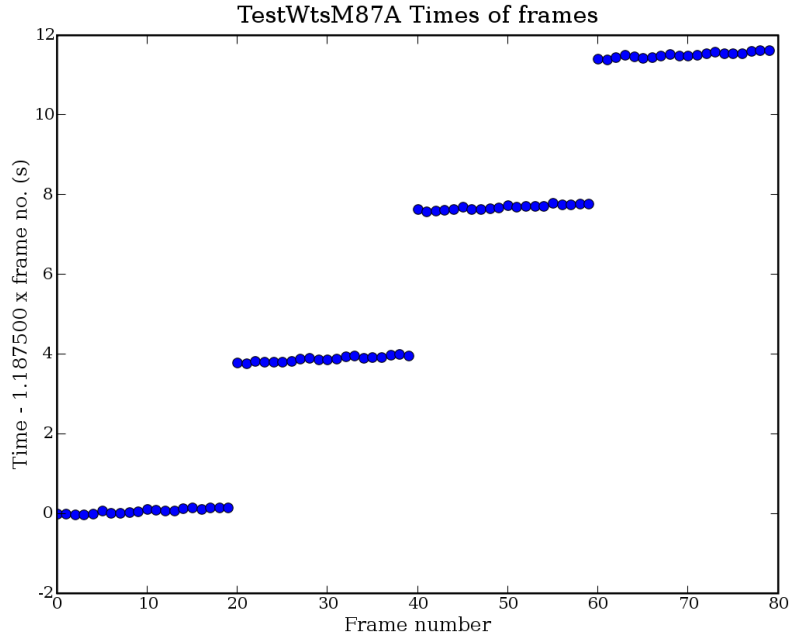


Figure 6.20 – Delay between scans. Each frame takes about 1.2s. This plot shows how long it takes to change the system settings between scans. Unusually long delays can indicate problems in the system operation.

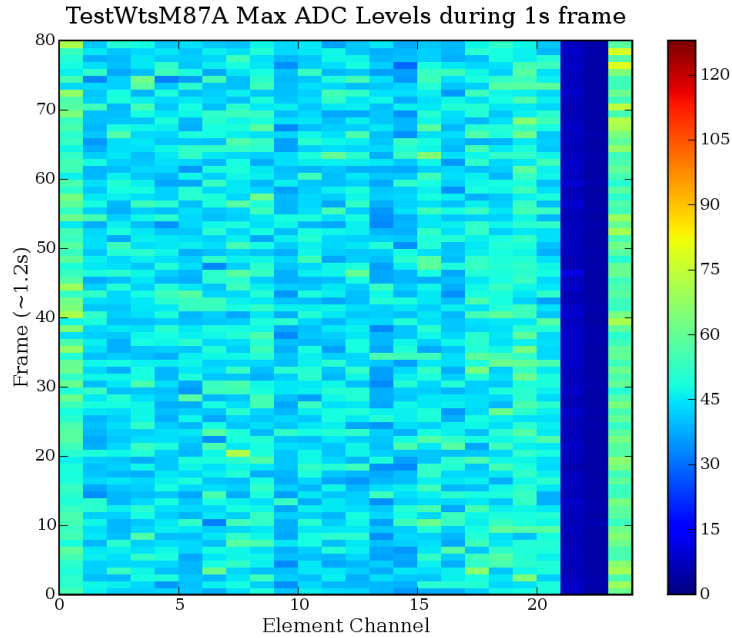


Figure 6.21 – ADC levels vs. time.

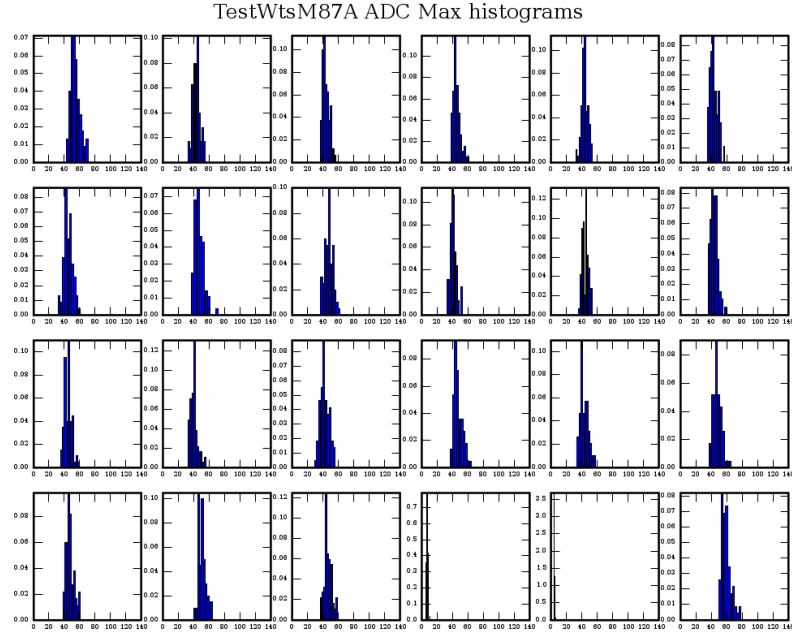


Figure 6.22 – ADC histograms, one per channel.

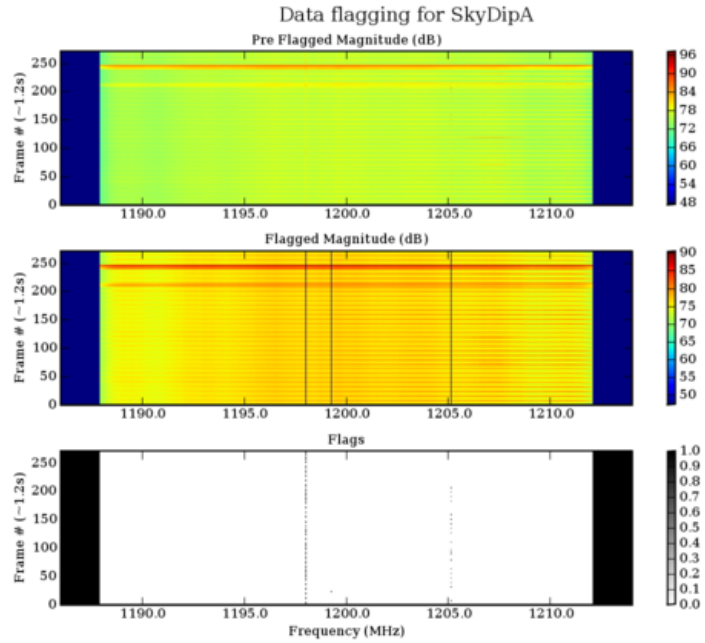


Figure 6.23 – RFI flagging: frequency vs. frame number. The first plot is before RFI excision, the second after RFI excision and the last shows the frequencies identified as RFI by the median filter code.

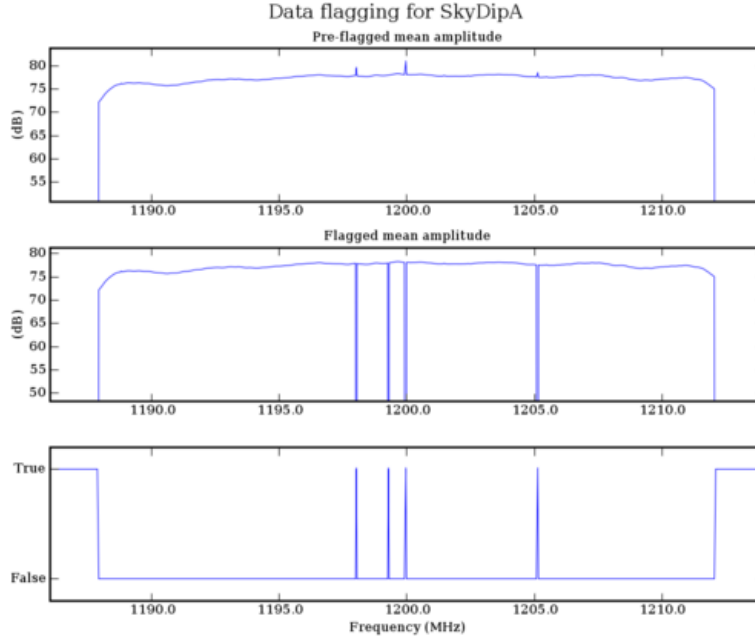


Figure 6.24 – Mean received spectrum over the observation. RFI identified by the median filter is shown excised. The bottom plot shows the flagged frequency bins.

for the entire cycle. Note the edges of the data are flagged, as they are beyond the analogue filters in the system, leaving the central 24 MHz of the 28 MHz of the digital system to be evaluated in post processing.

Fig. 6.25 shows the correlator output against frame number. This data is averaged over the scan period, in this case 20 frames (24s), and used to determine the system response with various beamforming weightings and in response to various stimuli. In Fig. 6.25 the response to the radio source M87 of four element weightings is being measured. The faint diagonal striping in the amplitude (top) plot is evidence of an artefact beating with the radio source signal. More details on this artefact are given below. The strong diagonal striping in the phase (bottom) plot shows linear variations in frequency and time:

Frequency The frequency variation is due to a residual delay between the correlated signals (a coarse delay correction is set in the beamformer-correlator before correlation).

Time The time (or frame number) variation is due to movement of the source in the sky (the fringe rate).

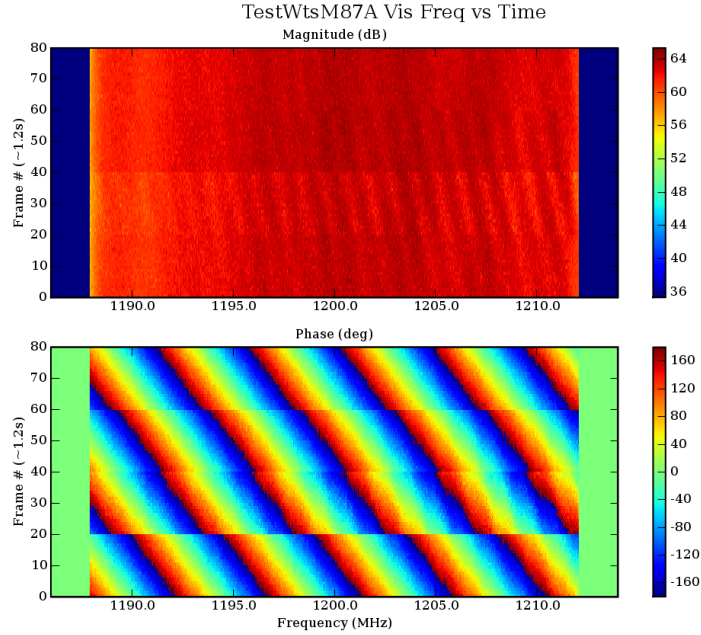


Figure 6.25 – Correlator output vs. frame number. This example shows the response of four weightings on the radio source M87.

The compensation for fringe rate and residual delay is described below. The discontinuities in the phase at 20, 40 and 60 frames are due to an arbitrary phase shift on the application of each new set of weights.

Fig. 6.26 and Fig. 6.27 present a single frame and a single frequency channel. The utility of these plots was chiefly in processing debugging, providing a quick check on the raw and processed values.

Having collected the correlator products, the data were processed to provide an average value for each scan. The process was as follows:

1. The delay and fringe rate for the geometric movement of the source was compensated for by applying a phase adjustment in frequency and time respectively. For auto-correlations this was not required as the delay and fringe rate are both zero. The mean amplitude vs. frequency is displayed in Fig. 6.28.
2. For each frame a zero padded fast Fourier transform (FFT) was applied to obtain level vs. delay data (Figs. 6.29 and 6.30).
3. An FFT was then applied to each delay bin of the central 600 ns of the level vs. delay frames in a scan resulting in level vs. fringe rate data for each delay.

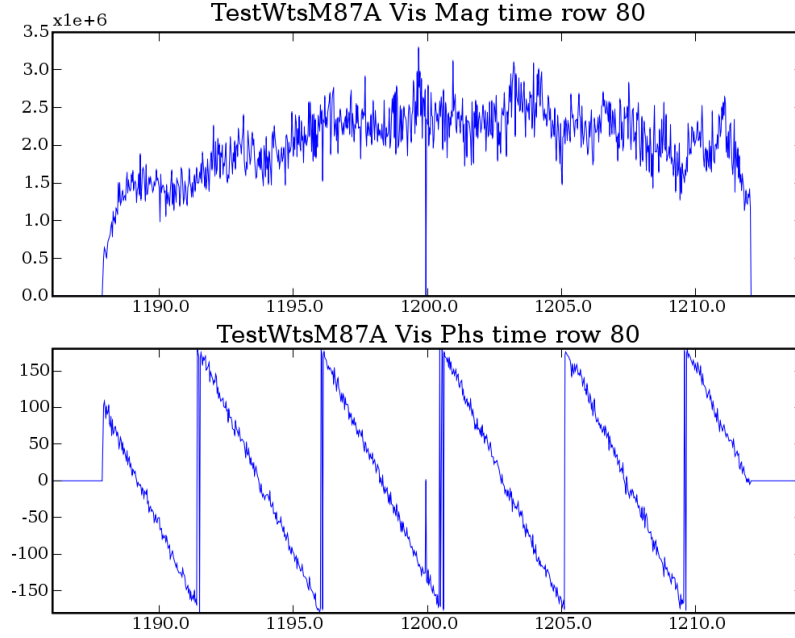


Figure 6.26 – Single Frame Spectrum.

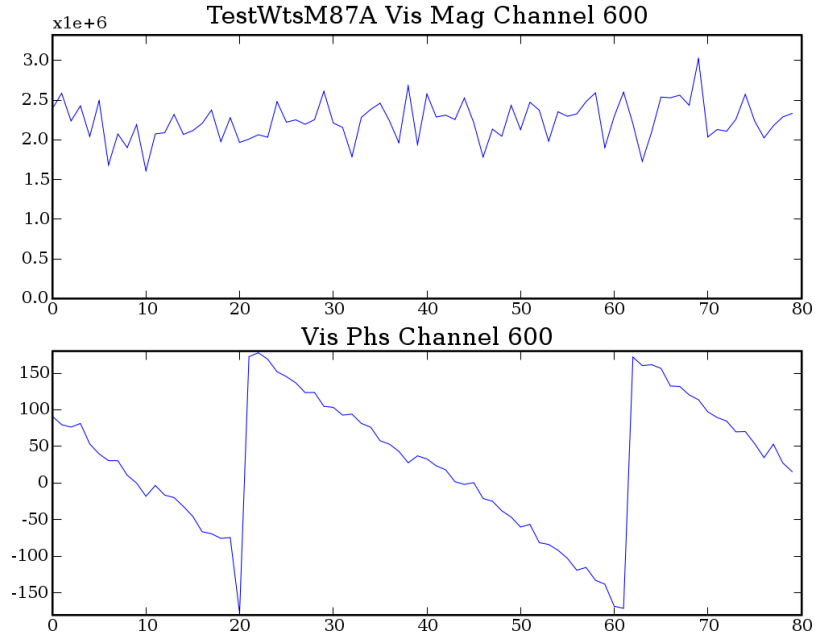


Figure 6.27 – Single frequency channel vs. frame number.

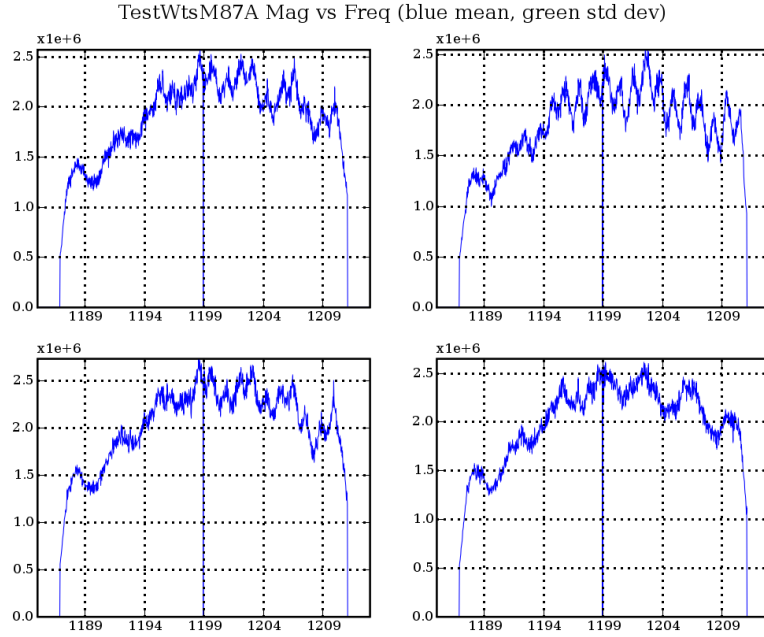


Figure 6.28 – Amplitude vs. frequency for each scan. The mean and standard deviation over the scan are shown. In this example the standard deviation is so small it is obscured by the zero line.

4. The data were reassembled so that the complex correlation was transformed from a time vs. frequency-matrix to a fringe-rate vs. delay-matrix (Fig. 6.31).⁹
5. The peak of the two dimensional data was found and a parabolic fit on each axis was used to refine the location of the peak. The errors in the delay and fringe rate correction result from imperfect knowledge of the locations of the antennas and drift in the electrical path lengths from the two antennas to the correlator. Fig. 6.31 shows the amplitude and phase of a scan on a strong source corresponding to the top left plots in Figs. 6.28, 6.29 and 6.30.
6. The residual fringe rate and delay corrections were then applied to the data and the complex mean value calculated. Fig. 6.32 demonstrates the phase correction from the residual delay value.

Other parameters that are calculated for quality control are listed here.

⁹The process could have been accomplished with a single two-dimensional Fourier transform. With the zero padding, however, this was beyond the memory capabilities of the computer being used. Therefore the two step process was used.

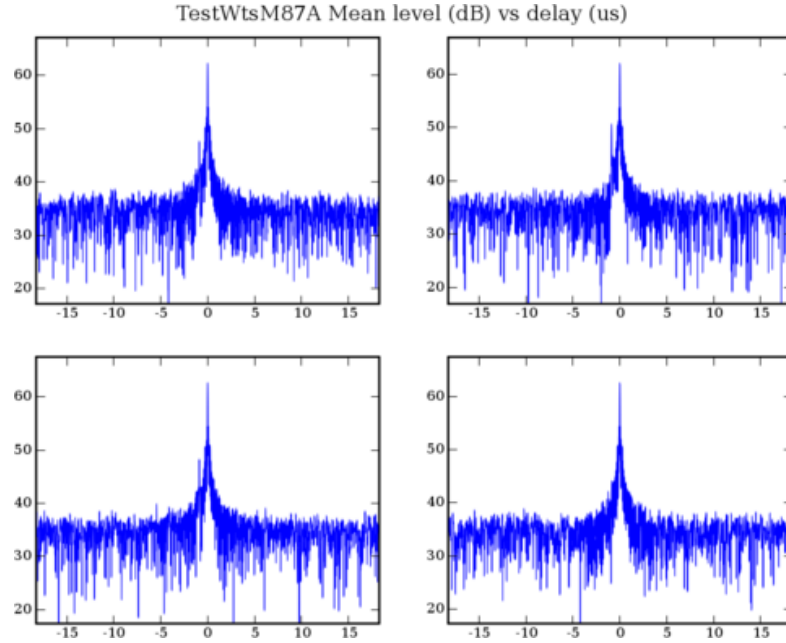


Figure 6.29 – Mean scan amplitude vs. delay. Each plot is for a different scan.

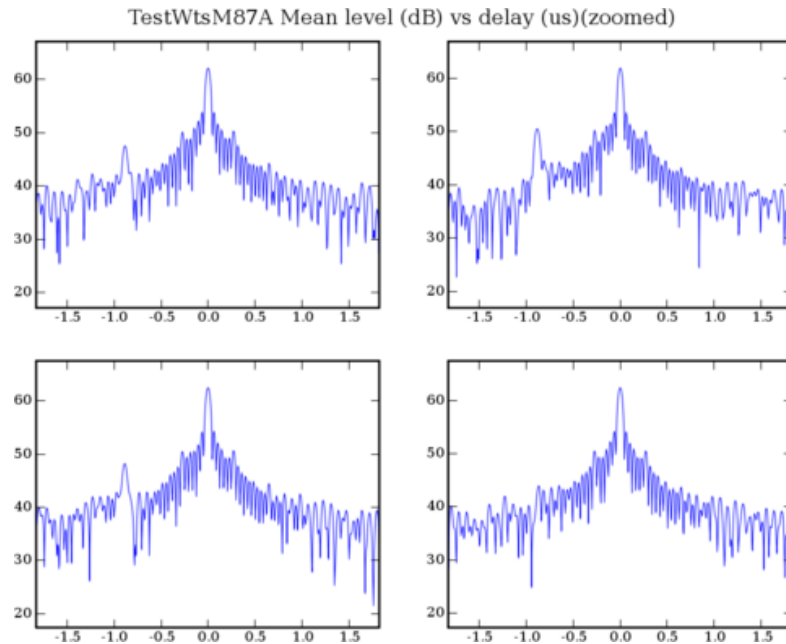


Figure 6.30 – Mean scan amplitude vs. delay, expanded. Each plot is for a different scan. A crosstalk artefact is clearly visible at $-0.9\mu s$ in the first three scans. The reason for its absence in the bottom right plot is unknown.

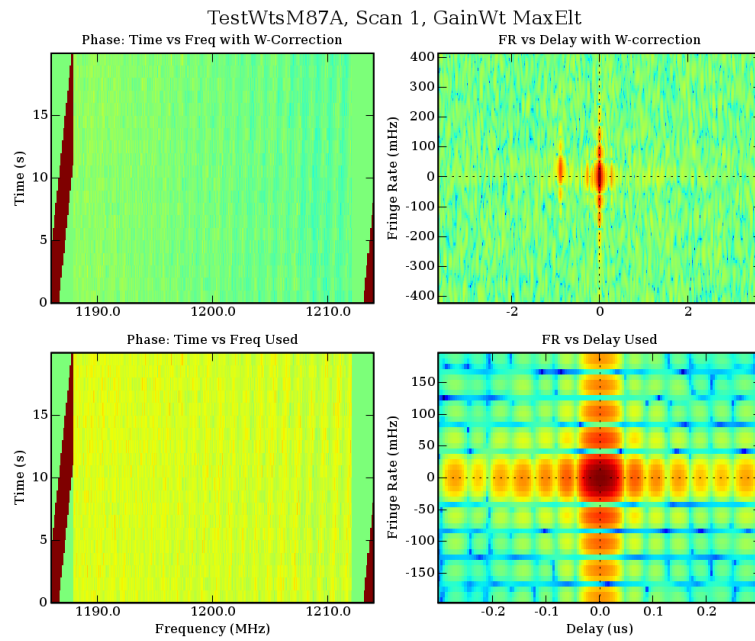


Figure 6.31 – Delay and fringe rate correction. The residual correction is small in this example. The cross-talk artefact is clearly visible in the amplitude fringe-rate vs. delay plots as a second peak offset in fringe rate. It is also seen as ripple in the phase time vs. frequency plots. Windowing could have been used in the Fourier transforms to reduce the sidelobes and hence contamination from interference but the chosen point source was sufficiently dominant to avoid the need for this with its inherent reduction in resolution.

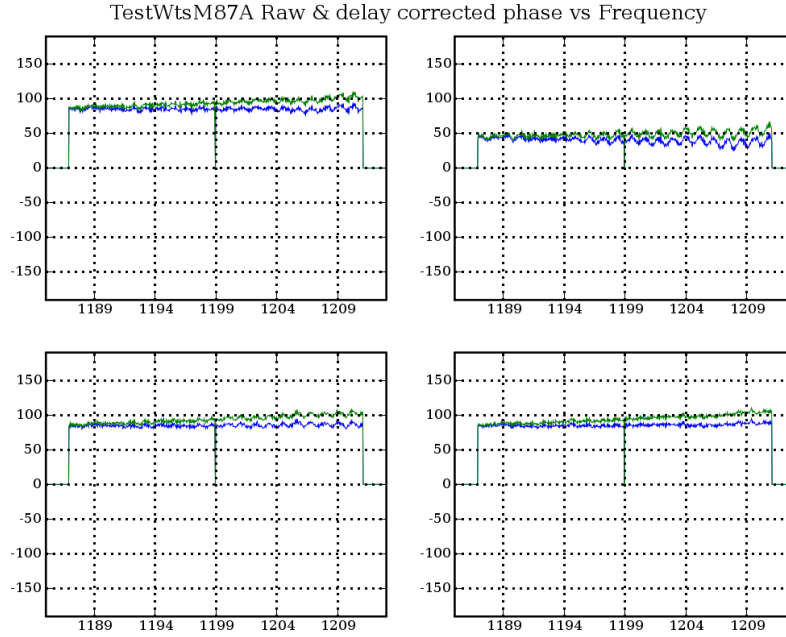


Figure 6.32 – Phase vs. frequency for each scan showing the result before (green) and after (blue) correction with the residual delay. The cross talk is quite visible, particularly in the top right plot.

- The mean of the amplitude is compared with the final value. A large difference indicates the measured signal is weaker than the noise, interference or system artefacts.
- The standard deviation is calculated as the root-mean-square (RMS) of the difference between each data point and the mean with fringe de-rotation. This provides an estimate of the noise level of the scan.

6.9 System Level Commissioning Tests

The following examples of system level tests are useful in ensuring correct operation on initial commissioning, identifying failures and as ‘self tests’ to ensure the system is operating correctly after modifications.

A correction to the frequency mapping of the system was made after testing the response of the system to test signals. A signal generator was set up transmitting a low level signal toward the feed. The frequency was checked against the response registered by the recording system and it was found that incorrect assumptions had been made regarding the interface between the beamformer-correlator and the data taking software.

The element responses were tested periodically by recording the response to the vertex noise-source. A test of interferometer operation was also done by correlating the reference (western) antenna response with the vertex noise-source in the eastern dish. This also allowed a delay comparison.

Tests were also performed to check the programmable receiver gain control and beamformer-correlator delay control. The data from these tests were used to produce a mapping of the control parameters with the gain and delay time respectively.

6.10 Element Gain Stability

The stability of the element gains was measured by correlating against the vertex noise source over a period of time. This measurement was done on 11 May 2008 between 11:34 hrs and 13:17 hrs (103 min). The vertex noise source was turned on at the start and system cycled 30 times through a series of measurements. These were (the numbering refers to Figs. 6.33 and 6.34):

- the 21 FPA elements correlated against the eastern dish vertex noise source (Nos. 0–20),
- the autocorrelation of the eastern dish vertex noise source (No. 21),
- the autocorrelation of the western dish vertex noise source (No. 22), and
- the western dish feed correlated against the western dish vertex noise source (No. 23).

The results are shown in Fig. 6.33. There was a marked drop in the amplitude response over the first 700 s for the eastern (FPA) dish (numbered 0–20) but not in the western (horn feed) dish. Further investigation identified this as drift due to the noise source warming up after it was switched on.

To provide a better representation of the channel amplitude drifts, the cross-correlation data was divided by the noise source amplitude (the square root of the vertex noise source auto-correlations). These data are presented in Fig. 6.34. The element to element drift was within about 0.1 dB in amplitude and 2° in phase relative to the mean over the 100 min test period. The absolute drift was 0.4 dB in amplitude and 6° in phase—with the exception of the western dish (horn feed) which showed 12° phase drift.

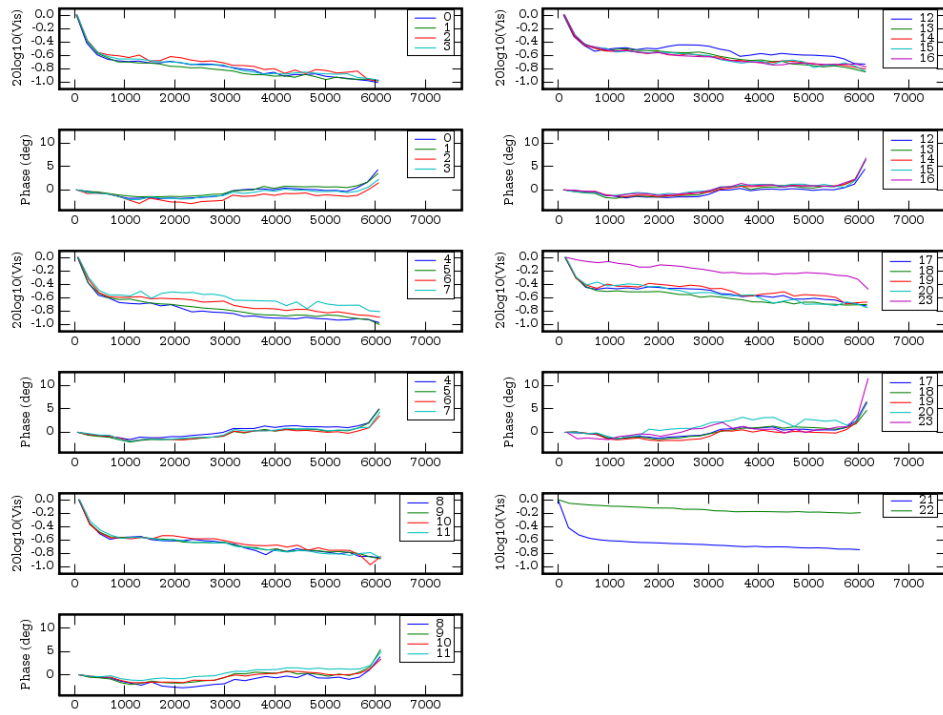


Figure 6.33 – Correlation of elements against the vertex sources. The horizontal axis is time (s) and the vertical axes are amplitude (dB) and phase ($^{\circ}$) normalized to the first data point. The cross-correlation amplitudes are displayed as $20 \log_{10}$ because the reference signal is constant and the auto-correlations (Channels 21 and 22) are displayed as $10 \log_{10}$.

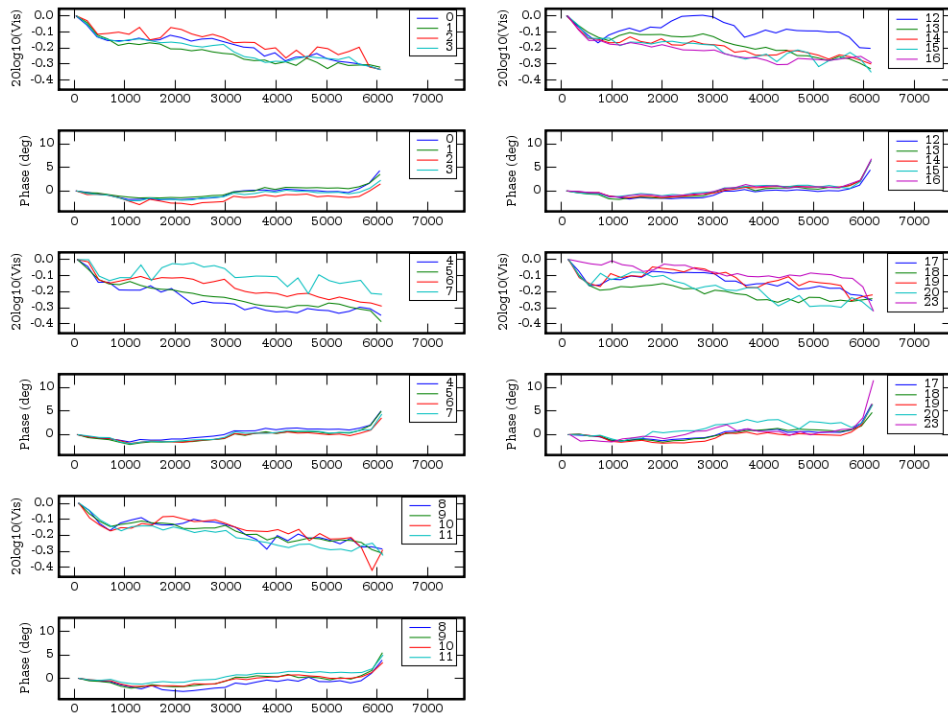


Figure 6.34 – Element port gain drifts. The horizontal axis is time (s) and the vertical axes are amplitude (dB) and phase ($^{\circ}$) normalized to the first data point.

The temperature stabilization in the FPA consists of a simple control of the internal fan speed. The temperature of the FPA can be interrogated and when the ambient temperature is below about 20°C, the FPA is maintained within a few degrees of 30°C. Above 20°C, the FPA temperature tracks about 10°C above ambient.¹⁰ The ambient temperature for the day of these drift measurements was 18°C so the FPA temperature was maintained within a few degrees Celsius.

In addition to the drift when switching on, it has also been found that amplified noise diodes can drift when the impedance presented to the output is significantly changed. Therefore, in future designs [276] it is recommended to:

- keep the noise source powered (preferably temperature stabilized), and
- switch the output between the dish-surface radiator and a matched load.

As time precluded a redesign of the noise sources, the autocorrelation of each element was used to provide the amplitude measure for calibration. This is less accurate as it is susceptible to RFI, changes in spillover and changes in the noise performance of the elements. The noise source continued to be used for phase calibration as this is independent of the amplitude of the source. The test period of 100 min was approximately the length of time between calibrations in the system and therefore these drift data can be used as an estimate of the expected drift in the overall system.

6.11 Radio Sources

Radio sources are required for making measurements on the prototype radiotelescope. The choice of frequency band for measurements (see Section 6.4.3) precluded the use of the only convenient geostationary satellite transponder: Optus MobileSat at 1550 MHz.

The measurements made on a source with a single dish were for gain or G/T determination. The parameter of interest is the peak gain response to a compact source and so a source substantially smaller than the beamwidth of the single dish ($\sim 1^\circ$) is the simplest to use. Extended sources need a correction to deconvolve the source and the antenna beam adding a layer of complexity and uncertainty. The galaxy M87 (Virgo A) was used for most

¹⁰The THEA tile was designed to operate in a much cooler climate in the Netherlands.

of the single dish measurements due to it being sufficiently compact and strong.

In interferometer mode, the primary operations were to determine relative gain of the beamformed dish and to generate radiation patterns. In this case, if the source is extended relative to the synthesized beamwidth that is produced by the baseline (90 m giving 0.16° at 1200 MHz) the level received after correlation is reduced. This is referred to as the source being ‘resolved’. This behaviour was observed. The radiation patterns from such extended sources were the same shape as those from more compact sources as they were still a fraction of the single dish beamwidth. M87 was also used for most of the interferometer measurements.

6.12 Summary

This chapter augments the description of the instrument used in this project that is given in [12] with an emphasis on the author’s contributions. The system setup was evaluated and methods were described for the diagnosis and optimization of the instrument.

The noise performance of the FPA was analysed along with the uncertainties involved. Results on this FPA element variability were presented and a calibration algorithm was developed. A number of system level commissioning tests were described and a comprehensive set of plots provide rapid diagnostic tools for faults and imperfections in observations.

The instrument described in this chapter, at the time of the experimental work, was one of only five such prototypes known to the author world-wide.¹¹ The other testbeds used different approaches and different equipment and so the demonstration of this instrument has contributed new knowledge to the FPA community.

The calibration signal radiated from the surface reduced the impact of gain drift, allowing weights calculated at one time to be used in subsequent days and weeks. Further research is underway on the best location of the source, the recalibration period and the most suitable signal to use for this type of system [276, 277]. This system also provided a very convenient self-

¹¹Fisher et al. at NRAO [2]; FARADAY and APERTIF at ASTRON [3, 4]; Warnick et al. at BYU/NRAO [5]; PHAD at DRAO [6].

test facility that was used to verify there were no major changes in the signal paths from day to day and after maintenance on the system.

The author's key contributions are considered to be the uncertainty analysis of the FPA noise, the calibration algorithm using the dish surface radiator (the author understands that he was the first to use this calibration method with an FPA), and the development of a wide range of diagnostic tools for assessing the system performance during any observation.

Future work in the calibration area should include an investigation into whether the element patterns do change significantly (with implications in high sensitivity synthesis imaging), an analysis of the calibration requirements and development of suitable hardware solutions. The methods shown in this chapter can be used for directing future FPA system development and evaluation.

Chapter 7

Measurement Results

The primary objective in using the NTD Interferometer in this work was to demonstrate beamforming and evaluation techniques for FPAs in a prototype radiotelescope. The previous chapter introduced the instrumentation and the methods used for collecting and processing data. The purpose of this chapter is to present the key measurement results from applying the beamforming weightings described in Chapter 5. These results are discussed in Chapter 8 where they are compared with predictions based on the dish structure.

Unless otherwise stated the uncertainties quoted represent the 95% confidence interval and are calculated as shown in Appendix F.

7.1 Beamforming Experiments

Through the life of the NTD Interferometer, a large number of data sets was recorded for various experiments as the system was developed. The most representative results of the system performance are listed in Table 7.1.

The data for calculating the weights was collected, the weights calculated and then various weightings were compared using a series of evaluation techniques. The initial data collection was time consuming. Therefore, using the vertex noise source to recalibrate the system periodically (see Section 6.7), weights calculated on one day were used on subsequent occasions.

The 21 elements were taken from two regions of the 8×8 array, central and offset, as described in Section 6.4.6. The element that was central to the

Table 7.1 – Observation dates.

Subarray	Date	Test Weights					Pattern Cuts			On-Off M87				On-Off M17				Absorber ^a		
		Collect ^b	Single elt.	Max. G/T	Norm. conj.	Max G/T	Single elt.	Max. G/T	Norm. conj.	Max G/T	Single elt.	Max. G/T	Norm. conj.	Max G/T	Single elt.	Max. G/T	Norm. conj.	Max G/T	Single elt.	Max. G/T
No. elts.		21	1	5	21	21	1	5	21	21	1	5	21	21	1	5	21	21	1	5
Central ^c	2006-11-21																		x	
Central ^c	2007-09-20	x	7.2a		7.2b		7.3a		7.3b		x		x							
	2008-10-25	x	7.2c		7.2e	7.2f					x		x	x	x	x				
	2008-12-15												x	x	x	x				
Offset	2008-12-16																	x	x	x
	2009-01-06			7.2d							x	x	x	x						
	2009-01-07							7.3d												
	2009-01-08						7.3c		7.3e	7.3f										

^a System temperature determined from a power level comparison of the dish looking at the cold sky and ambient temperature absorber under the feed.

^b Collection of data for calculating weights.

^c The vertex noise source was not available for calibrating these experiments. Figure numbers have been shown where relevant.

21 element pattern (labelled element 1 in both cases) was used as a reference for comparison with beamformer weightings. This provided a convenient pointing reference (particularly for correcting a small pointing error that was present in the system) as well as a performance reference. For comparison with the 21-element-beamforming subarray, measurements were also made for a 5-element subarray.

7.2 Beamformer Weight Data Collection

Two sets of data are required to calculate the beamformer weights (see Section 5.2): (1) The *noise covariance matrix* that is formed from the correlations between the elements with the antenna pointed at a region of sky with no significant radio sources and (2) the *complex voltage responses* of each element of the array to a point source.

7.2.1 Noise Covariance Matrix

The noise covariance matrix, $\mathbf{C}_{T_{\text{sys}}}$, is the sum of two components: the receiver noise, $\mathbf{C}_{T_{\text{rx}}}$, and noise from the surrounding scene, $\mathbf{C}_{T_{\text{scene}}}$ (see Section 4.12.2). $\mathbf{C}_{T_{\text{rx}}}$ includes noise coupled from one element into another and antenna losses. It is used to adjust the beamformer weights to minimize the system noise (see Section 5.2.3). The scene component, $\mathbf{C}_{T_{\text{scene}}}$, is dominated by noise from the ground (spillover) at approximately 300 K with the sky presenting about 6 K in the band of operation [306]. Therefore $\mathbf{C}_{T_{\text{rx}}}$ will change as the pointing direction changes and so, ideally, the covariance matrix should be remeasured for different pointing angles. This aspect was not investigated due to the time the covariance matrix took to obtain (approximately 1 hour). The time taken to measure the covariance matrix is a limitation of the beamformer and more recent developments, for instance for the Parkes Testbed Facility [164], allow for the rapid acquisition of this matrix.

For evaluation and display purposes (Fig. 7.1), the *correlation* matrix \mathbf{R} was calculated from the *covariance* matrix $\mathbf{C}_{T_{\text{sys},u}}$. The elements of \mathbf{R} are the correlation coefficients given by:

$$[\mathbf{R}]_{ij} = \frac{[\mathbf{C}_{T_{\text{sys},u}}]_{ij}}{\sqrt{[\mathbf{C}_{T_{\text{sys},u}}]_{ii}[\mathbf{C}_{T_{\text{sys},u}}]_{jj}}} \quad (7.1)$$

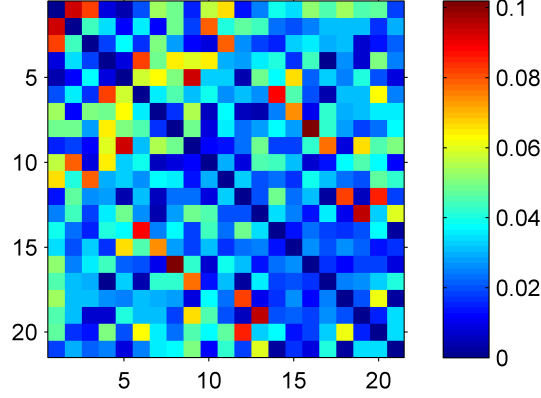


Figure 7.1 – Amplitude of the correlation matrix at 1200 MHz, linear scale. The diagonal elements, with unity value, have been displayed as zero to increase the displayed dynamic range.

where $\mathbf{C}_{T_{\text{sys},u}}$ is the covariance matrix from (5.6). The normalization results in unity diagonal elements, i.e. the autocorrelations. The amplitude is plotted in Fig. 7.1. The condition number is 1.8, making inversion quite stable—a result of the low off diagonal terms (i.e. cross-correlation). These are 0.1 or lower. The highest terms are from elements pairs adjacent in the H-plane (e.g. elements 5 and 8, Fig. 6.16) with correlations between 0.06 and 0.1. Pairs adjacent in the E-plane have much lower values. This pattern of coupling is compatible with electric source dominated elements [307] but differs from scattering parameter measurements made on the FPA at ASTRON [296]. However no pattern was apparent in the phases in this matrix. This is not surprising as the path lengths of the cabling for each element were not equalized.

7.2.2 Point Source Voltage Gain

With both dishes of the interferometer pointed at M87, the correlation of an array element against the reference (western) antenna yields the relative complex voltage response of that element, denoted \hat{e}_i in Section 5.2.1. Data was collected for 24s on each element, filtered and integrated to obtain the gains for each element as described in Section 6.8.3. These values were then normalized by the calibration data collected immediately before and after the point source response data.

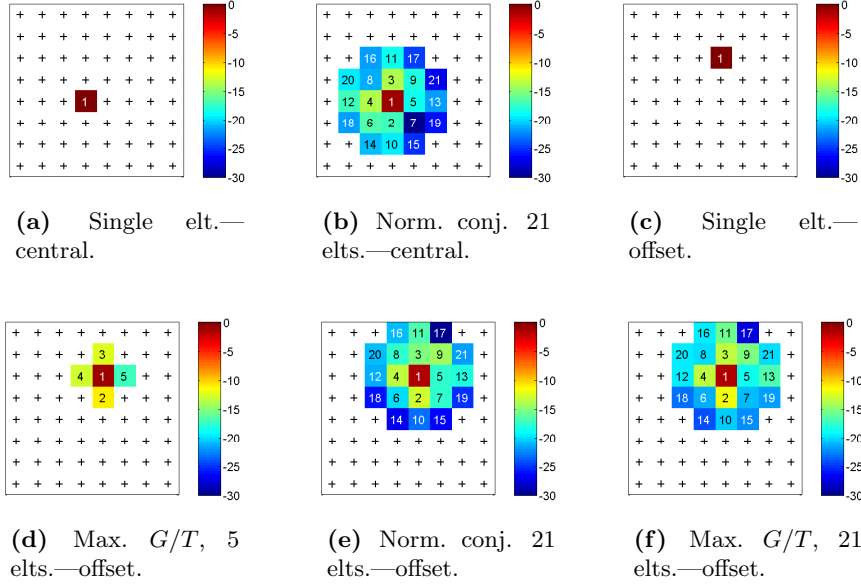


Figure 7.2 – Amplitude of array element weights in decibels at 1200 MHz for the weighting cases applied, showing the central and offset subarrays. The E field polarization of the array is horizontal with respect to these diagrams.

7.3 Weight Calculation

The data collected was then used to calculate the weights as per Section 5.2 and the G/T performance and radiation patterns were evaluated. The amplitude and phase of the weights are shown in Table 7.2 and the amplitudes are illustrated Fig. 7.2. In both the central and offset subarrays, there was an element with a failure in the electronics. The failed elements exhibited very low gain and so had very little of the wanted signal \hat{e}_i . The beamforming algorithm (5.14), therefore, applies a very low weight u_i to them. To avoid corruption from intermittent behaviour the weights of these elements was set to zero: element 7 in the central subarray and 17 in the NCM weight for the offset subarray. This was overlooked for the maximum G/T weighting but the effect is small due to the low weighting—0.2% of the total power. The automatic suppression of signals from a failed element shows the power of this beamforming weighting approach.

The calibration method described in Section 6.5.1 is applied to update the weights at the start of each observation cycle.

Table 7.2 – Beamformer weights.

Element	Central Sel.		Offset Subarray					
	Norm. Conj.		Max. G/T		Norm. Conj.		Max. G/T	
	amp	phs	amp	phs	amp	phs	amp	phs
1	0.862	−71.7	0.887	47.4	0.834	46.2	0.807	47.8
2	0.138	117.1	0.289	−3.4	0.223	7.1	0.256	−1.9
3	0.208	85.0	0.242	−115.1	0.173	−111.2	0.211	−116
4	0.200	−78.4	0.226	−140.7	0.215	−139.5	0.210	−140.5
5	0.119	106.5	0.142	−96.2	0.130	−97.2	0.119	−97.7
6	0.146	−155.7			0.100	153.6	0.087	136.5
7	0.000	0.0			0.129	123.7	0.092	124.2
8	0.088	57.6			0.133	−157.2	0.103	−155
9	0.123	55.6			0.189	80.2	0.172	79.7
10	0.105	72.3			0.070	113.2	0.094	97.8
11	0.117	85.7			0.145	31.9	0.160	30.0
12	0.141	−127.2			0.088	−52.4	0.108	−58.7
13	0.081	−68.4			0.124	−97.3	0.146	−90.5
14	0.093	−60.4			0.044	75.6	0.061	59.3
15	0.056	−136.1			0.048	−139.4	0.075	−149.1
16	0.083	110.9			0.089	−16.5	0.109	−17.8
17	0.058	−14.1			0.000	0.0	0.042	78.0
18	0.081	51.0			0.050	41.6	0.070	26.5
19	0.049	−138.6			0.057	133.7	0.082	128.9
20	0.106	−177.9			0.090	25.7	0.109	26.4
21	0.046	−163.7			0.083	−91.5	0.099	−86.6

Table 7.3 – Observations from the radiation patterns.

Subarray	Weighting	Num. elts.	HPBW (°)	Maximum SLL ^a (dB)
central	single	1	1.16	−16.3
central	norm. conj.	21	1.18	−13.7
offset	single	1	1.17	−14.0
offset	maximum G/T	5	1.27	−14.9
offset	norm. conj.	21	1.22	−14.9
offset	maximum G/T	21	1.24	−15.1

^a Maximum sidelobe level relative to the main beam peak.

7.4 Radiation Patterns

Radiation patterns were obtained in the interferometer mode. The central subarray used M87 and the offset subarray SGRA* as the point source. Cuts were made in the E, H, 45° and 135° planes. The spacing of the data points is 0.2° over 8° spans for the central subarray of elements and 0.25° over 10° spans for the offset subarray. Fig. 7.3 shows this data interpolated using the method described in Appendix G.

Table 7.3 lists the maximum sidelobe level and the mean half-power beamwidth (HPBW) for each weighting case.

The H-plane cuts for the single (Fig. 7.3a) and beamformed central subarray (Fig. 7.3b) suffered contamination. A possible cause is a faulty connection in the system, for instance in the distribution of the local oscillators.

7.5 Aperture Field Distribution

The nature of the beamformed feed pattern is important for understanding the result of the weight calculation. Direct measurements of these patterns were not available and so the aperture field distribution of the dish for the various weightings was used. The aperture field is usually found by transformation of the far field measured on a two dimensional grid. The aperture field reveals the combination of the feed and dish surface along with obstructions such as struts and feed blockage. It is often used to determine imperfections in the reflector surface [308]. In the present case the reflector is well characterized (see Section 6.3) and so the aperture distribution can be used to determine the feed response.

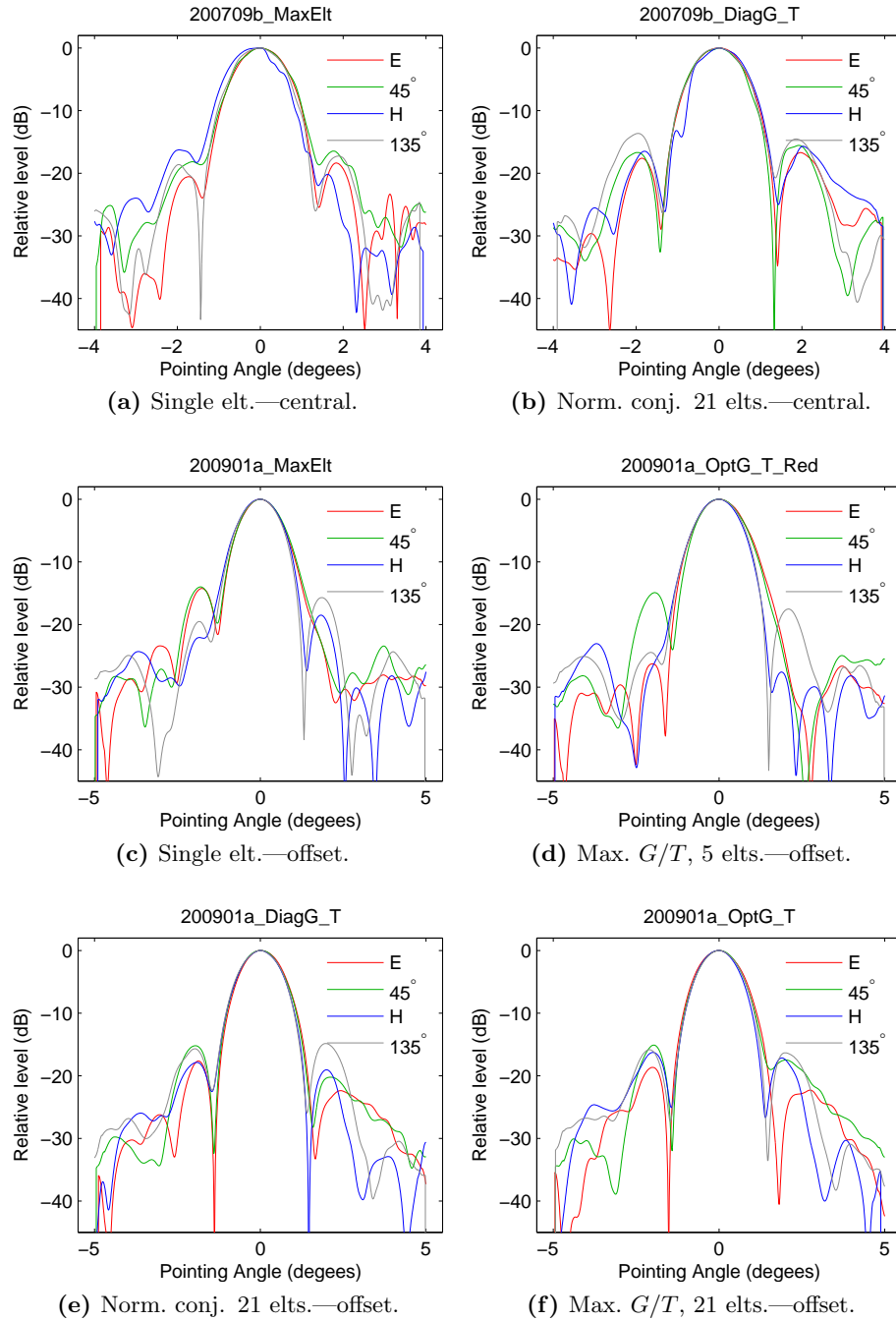


Figure 7.3 – Radiation pattern cuts at 1200 MHz for the weighting cases applied. Note the two angle ranges of 8° and 10° for the central and offset subarrays respectively.

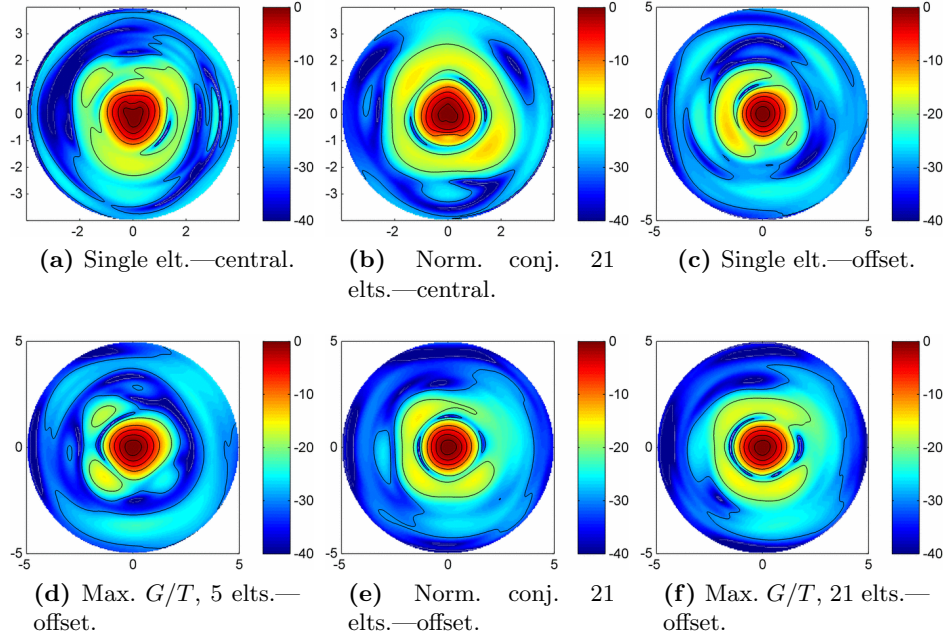


Figure 7.4 – Far field radiation patterns interpolated in azimuth and elevation at 1200 MHz for the weighting cases applied. Note that asymmetry in the main beam (a) and (b) is an artefact due to contamination of the measured data (See Section 7.4).

Time precluded the measurement of a two dimensional grid for each of the various weightings and so the four pattern cuts shown in Fig. 7.3 were used to obtain an aperture field distributions for each weighting, albeit with a low resolution. Interpolation was used to generate a two dimensional grid of far field data (Fig. 7.4). A two-dimensional-Fourier transform was applied to generate the aperture field distributions (Figs. 7.5 and 7.6). The technique and validation tests are discussed Appendix G. Note that the contamination of two of the patterns mentioned in Section 7.4 can be seen in the asymmetry of the beam in Figs. 7.4a and 7.4b.

7.6 Gain and Noise Temperature

The key figure of merit for a radiotelescope is the sensitivity or G/T (see Section 2.2). When referring to the antenna gain, G , and the equivalent system noise temperature, T_{sys} , it is important to be clear about both the reference plane and on what is included [226]. In this thesis the radiation port

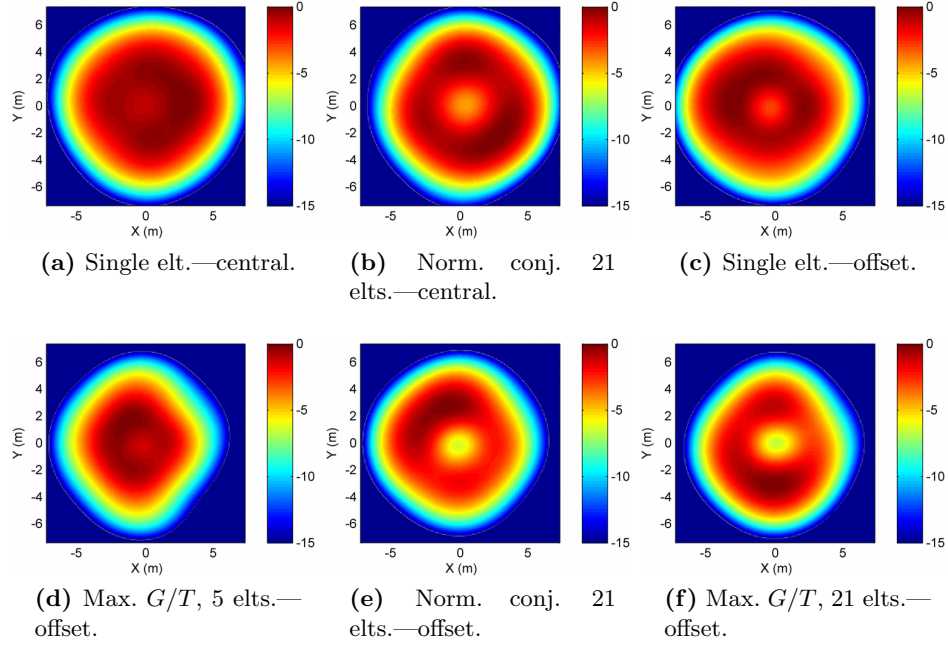


Figure 7.5 – Aperture fields from interpolated far field patterns—amplitude.

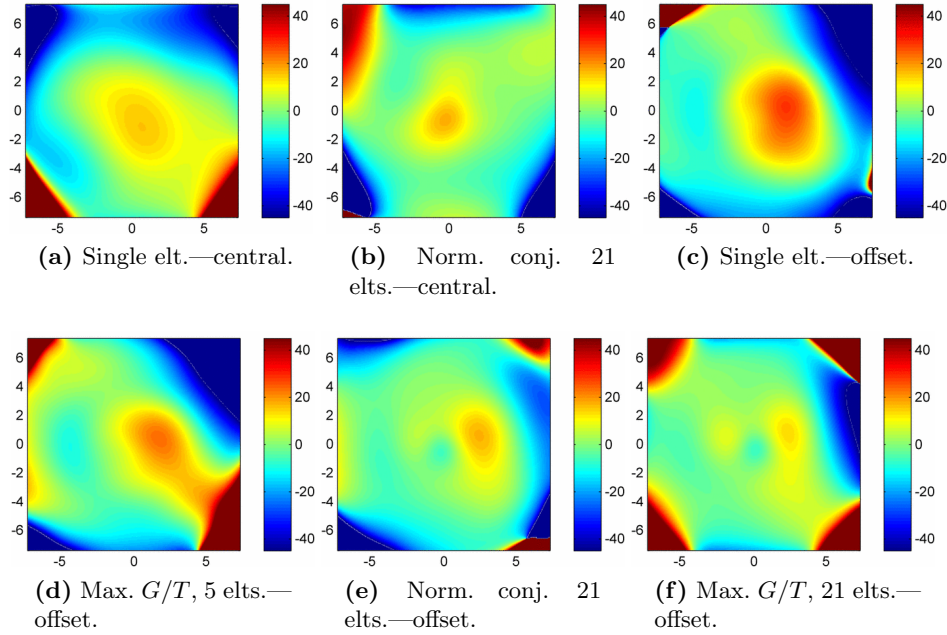


Figure 7.6 – Aperture fields from interpolated far field patterns—phase.

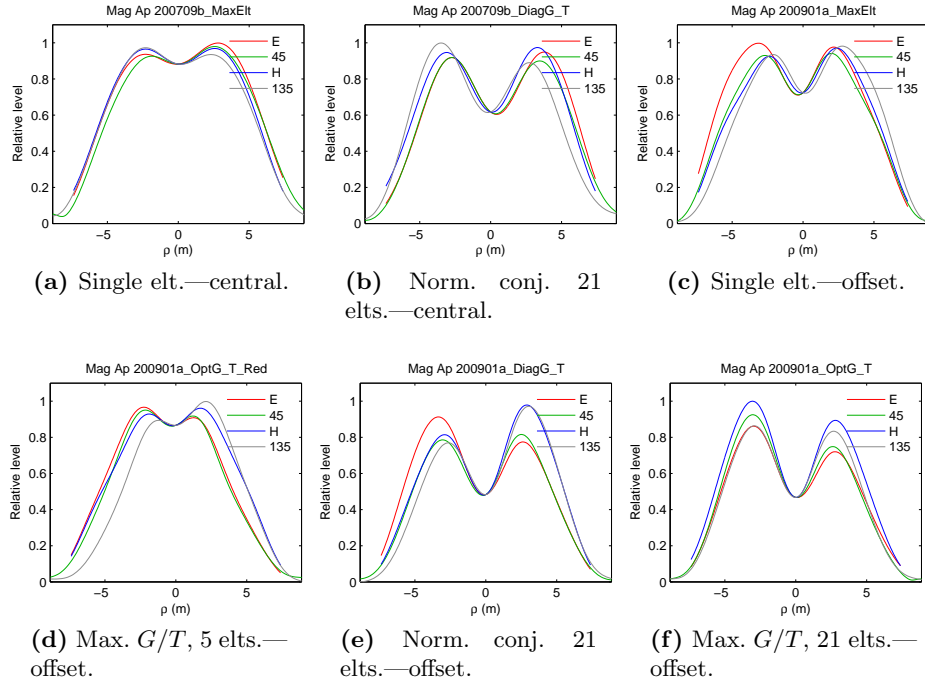


Figure 7.7 – Aperture fields from interpolated far field patterns—amplitude.

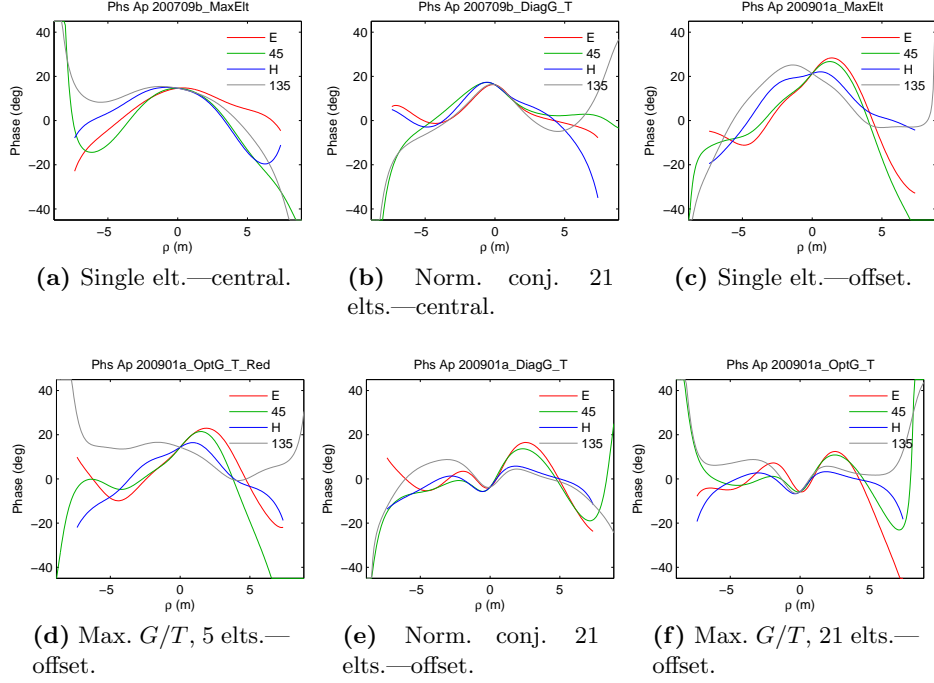


Figure 7.8 – Aperture fields from interpolated far field patterns—phase.

(see Section 4.2) has been chosen as the reference plane. For a radiotelescope the surrounding noise scene—ground and sky—is typically included in T_{sys} .

The sky component is considered to include the background radiation and thermal noise from the atmosphere under typical operating conditions. The major radio sources including the Galaxy, Sun and Moon are excluded. Antennas with very broad beams may need to take these into account as they may be present in all or most observations. Care was taken to avoid these major radio sources when measuring against the *cold sky*.

The radiation from the ground, chiefly received by the feed spillover, effectively rotates with respect to the antenna as the pointing elevation changes. Sky dip¹ measurements were made and it was found that the level changed by less than 0.05 dB for beamformed cases and 0.15 dB for a single element, indicating minimal system noise changes with elevation.

Higher accuracy relative measurements of G/T and lower accuracy absolute measurements of G/T were made for the weightings considered. These

¹A sky dip is where the noise power level is measured as the elevation is swept from zenith to the minimum, 30° in our case.

are summarized in Table 7.4 and the details described in the following sections. The uncertainties for the results are calculated and also shown in the table. The uncertainties in the ratio of the values are also considered as they are used for comparison between weighting cases.

7.6.1 FPA Losses and the Receiver Noise Temperature

The equivalent receiver noise temperature, T_{rx} , estimated in Section 6.4.4 is referred to the input of the LNAs. To refer T_{rx} to the radiation-port reference-plane (see Section 4.2) the losses in the array should be considered.

The losses have two components: reflective (or scattered) and dissipative as shown in (5.38) and (5.37). Woestenburg [303] estimates the dissipative losses as 0.5 dB for the THEA tile, as mentioned in Section 6.4.4. It is assumed not to vary greatly with the weighting applied as most of the power is taken from one element and the loss is thought to be mainly in the slot-line throat of elements.

The reflection efficiency is given by

$$\begin{aligned}\eta_{\text{reflected}} &= \frac{P_{\text{reflected}}}{P_{\text{available}}} \\ &= \frac{\mathbf{a}^H \mathbf{S}_{\text{array}}^H \mathbf{S}_{\text{array}} \mathbf{a}}{\mathbf{a}^H \mathbf{a}}.\end{aligned}\tag{7.2}$$

Using the scattering matrix (see Section 6.4.1) when port 1 of the central subarray alone is excited the $\eta_{\text{reflected}} = -1.0$ dB or 80%. Of the 20% loss, 11% is from mutual coupling, i.e. appears on other ports and 9% is reflected back into the excited port (S_{11}).

For the beamformed cases, in principle the weights could be used to calculate the scattering loss. The beamformer weight vector, \mathbf{u} , however, differs from the scattering matrix vector \mathbf{a} by two steps. Firstly the amplitudes and phases of the electronic gains need to be compensated for to convert \mathbf{u} to \mathbf{w} (see Section 5.2.1) and secondly the weights need to be converted from the black-box model to the scattering matrix model, \mathbf{w} to \mathbf{a} , (see eqn. (5.45)).

Element 1 is dominant in all weightings however, taking up 65 to 74% of the power based on the beamformer weight vector \mathbf{u} . Therefore the radiation efficiency for the single element was used for the beamformed cases as well.

Taking into account the dissipative and reflective losses, the radiation efficiency is then -1.5 dB or 71%. This resulted in a modified receiver tem-

Table 7.4 – Beamformed performance at 1200 MHz.

Subarray	Weighting	Num. elts.	Relative measures ^a			On-Off M87			Absorber ^b				
			ΔG (dB)	Δ Noise (dB)	$\Delta G/T^c$ (dB)	Y (dB)	G/T (dB(1/K))	$T_{\text{sys}}/\eta_{\text{ap}}$ (K)	Y (dB)	T_{sys} (K)	T_{ant} (K)	η_{sky} (%)	η_{ap}^d (%)
Central	Single	1	0.00	0.00	0.00	0.11	17.8	532^{+131}_{-93}	2.63	273	81	74	51
Central	Norm. conj.	21	2.14	0.09	2.05	0.15	19.4	364^{+61}_{-50}	—	Not measured			
Offset	Single	1	0.00	0.00	0.00	0.09	17.1	614^{+178}_{-119}	2.43	281	89	72	46
Offset	Max. G/T	5	0.46	-0.70	1.16	0.13	18.8	419^{+80}_{-63}	3.31	229	37	89	55
Offset	Norm. conj.	21	0.99	-0.94	1.93	0.16	19.6	350^{+56}_{-47}	3.36	227	35	90	65
Offset	Max. G/T	21	0.81	-1.19	2.00	0.16	19.5	357^{+59}_{-48}	3.57	216	24	94	60
Uncertainty low			-0.07	-0.05	-0.09	-0.02	-0.7	See ^e	-0.01	-14	-24	-5	-10
Uncertainty high			+0.07	+0.05	+0.09	+0.02	+0.7	See ^e	+0.01	+24	+13	+8	+10

^a Not true gain or noise—see Section 7.6.2.^b $T_{\text{rx}} = 192$ K was used to calculate these values.^c $\Delta G/T$ is the ratio of the G/T with the weighting and the corresponding single element G/T .^d η_{ap} is calculated from the On-Off M87 and the absorber Y -factors.^e The uncertainties are included as sub- and superscripts as they vary substantially for the different weightings.

perature of

$$T_{\text{rx}} = \frac{T'_{\text{rx}}}{\eta_{\text{rad}}} = \frac{137}{0.71} = 192(\text{K}). \quad (7.3)$$

The corresponding lower and upper uncertainties are -24 K and $+42 \text{ K}$ respectively.²

7.6.2 Relative G and T Measures

By scaling the weighting vector to a Euclidean norm of unity, the gain and noise of the weightings can be compared with each other. The gain is measured from the interferometer response to a point source. This is a much more sensitive measurement than the single dish total power response as the receiver noise is almost eliminated. The noise is measured by the single dish total power response with the dish pointed away from all strong sources.

The mutual coupling effects expressed in the denominator of (5.4) prevent this being a true comparison of directivity³ and similarly for noise (5.7). The effect is cancelled in their ratio, however, and so the G/T comparison should be accurate. The gain, noise temperature and their ratio relative to the response of the central single element is shown in Table 7.4.

The uncertainty, determined by repeatability, in the gain measure is 0.07 dB (i.e. 1.6%) and 0.05 dB (i.e. 1.2%) for the noise. Combining these as the root sum of squares, the uncertainty for their ratio, G/T , is 0.09 dB (i.e. 2.0%).

While relative G/T measures are useful in comparing weightings, the absolute G/T value is the critical figure of merit for predicting a radiotelescope's capability. The following section shows how the G/T was determined on this instrument.

7.6.3 Y-Factor From a Known Strength Source

The G/T of a radiotelescope can be determined by recording the difference in the single dish total power response pointed at a source of known flux

²Note that this increase in the effective receiver noise due to the radiation efficiency was not considered in [7] resulting in slightly different T_{ant} and η_{ap} values in Table 7.4.

³The chosen reference plane equates directivity with gain here.

and the power pointed away from it as shown in Section 4.8. From (4.45),

$$G/T = 4\pi \frac{2k_B(Y_{\text{src}} - 1)}{\lambda^2 \mathbb{S}} \quad (7.4)$$

where k_B is the Boltzmann constant, Y_{src} is the on-source/off-source power ratio and \mathbb{S} is the spectral power flux density of the source.

The galaxy M87 was used as the source and its strength was determined from published data as described in Section E.3 giving the value of $\sim 230 \pm 16$ Jy at 1200 MHz. The uncertainty in Y_{src} , 0.02 dB, dominates the combined uncertainty of $\sim \pm 0.7$ dB (i.e. $\sim 17\%$).

The system temperature T_{sys} to aperture efficiency η_{ap} ratio (2.18) was also calculated using:

$$\frac{T_{\text{sys}}}{\eta_{\text{ap}}} = \frac{A\mathbb{S}}{2k_B(Y_{\text{src}} - 1)} \quad (7.5)$$

where A is the dish area. This is a useful figure of merit for comparing feed systems because it is independent of dish size. The results are given in Table 7.4 and the uncertainty contributions are shown graphically in Fig. 7.9. For example, for the maximum G/T weighting for the offset subarray, $T_{\text{sys}}/\eta_{\text{ap}} = 357$ K, with a combined uncertainty of $-48, +59$ K.

As the dominant uncertainty, Y_{src} , does not correlate between the different weighting measurements, the uncertainty in the difference between measurements is similar to that for the individual measurements.

7.6.4 Noise Temperature from Absorber Y-Factor

A technique often used to measure the noise temperature for reflector antennas is to measure the Y-factor with and without the feed covered by radio-wave absorbing material (absorber). This approximates the hot (absorber) and cold (sky) immersion test introduced in Section 4.2. As it is impractical to immerse a large dish in a hot environment, only the feed is covered with absorber with attendant uncertainties.

The absorber covering the feed presents its physical temperature, about 300 K, to the receiver. With the absorber removed, the receiver is presented with the reflection of the sky in the dish and the ground where the feed pattern spills over the edge of the dish. The feed pattern will also ‘see’ the sky directly to a small degree. At 1200 MHz the sky brightness temperature, when the Galaxy, sun, moon and other strong sources are avoided, is

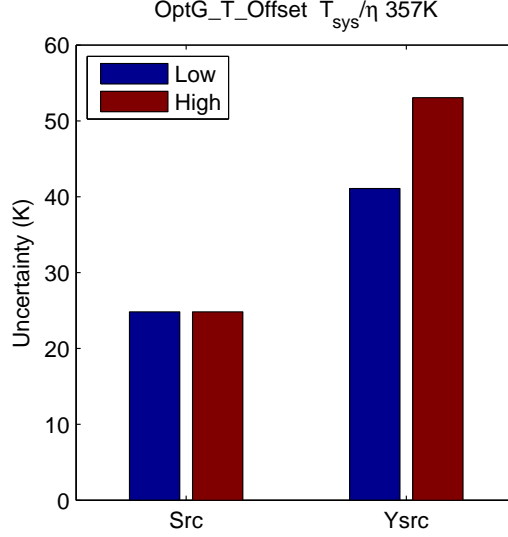


Figure 7.9 – Uncertainty contributions to the system temperature on efficiency calculation for the maximum G/T weighting on the offset subarray.

estimated to be 6 ± 1 K [306]. The ground radiates at close to its ambient temperature of about 300 K.

The formulation in (4.4) is modified to account for the choice of reference plane (see Section 4.2.1).⁴ The equivalent system temperature $T_{\text{sys}} = T_{\text{ant}} + T_{\text{rx}}$, where T_{ant} is the equivalent temperature contribution surrounding scene and T_{rx} is the equivalent noise temperature of the receiver (see (7.3)). The Y-factor, in various forms, is

$$Y_{\text{abs}} = \frac{P_{\text{abs}}}{P_{\text{sky}}} = \frac{T_{\text{abs}} + T_{\text{rx}}}{T_{\text{ant}} + T_{\text{rx}}} = \frac{T_{\text{abs}} + T_{\text{sys}} - T_{\text{ant}}}{T_{\text{sys}}} = \frac{T_{\text{abs}} + T_{\text{rx}}}{T_{\text{sys}}} \quad (7.6)$$

where Y_{abs} is the ratio of the power with the absorber covering the feed P_{abs} and the antenna looking at blank sky P_{sky} . T_{abs} is the physical temperature of the absorber.

To find the system temperature, the receiver noise performance, T_{rx} , or the noise from the surrounding scene, T_{ant} , (from (4.41)) is required. Here we use the estimated receiver temperature from Section 7.6.1. Rearranging (7.6), we obtain

$$T_{\text{sys}} = \frac{T_{\text{abs}} + T_{\text{rx}}}{Y_{\text{abs}}}. \quad (7.7)$$

⁴This issue was highlighted by Bert Woestenburger [299] during correspondence about the performance of the THEA tile.

The results obtained are shown in Table 7.4. The uncertainty⁵ in T_{abs} is ± 1 K, Y_{abs} is ± 0.01 dB and T_{rx} is $-24, +42$ K. The combined uncertainty in T_{sys} is $-14, +24$ K, dominated by the uncertainty in T_{rx} .

The uncertainty in the ratio of two T_{sys} values is dependent only on Y_{abs} and any difference in T_{rx} between weightings. The former contributes only $\pm 0.3\%$ while the latter is difficult to quantify with the available information. As an example of the sensitivity, a change in η_{rad} from 0.71 to 0.8 changes T_{rx} from 192 to 172 K and reduces the calculated value of T_{sys} by 4% or about 9 K for the values in Table 7.4.

The antenna temperature, chiefly spillover, is calculated from $T_{\text{ant}} = T_{\text{sys}} - T_{\text{rx}}$. For the single elements the values are 81 K and 89 K for the central and offset subarrays respectively. Beamforming with the maximum G/T weighting reduces this to 24 K. The combined uncertainty of T_{ant} is $-24, +13$ K, is dominated by the uncertainty in T_{rx} . An example of the contributions is shown graphically in Fig. 7.10. The relative uncertainty between the T_{ant} values is much less however. For example the uncertainties of in differences between T_{ant} values are typically less than 10%, allowing valid comparisons to be made between them.

The spillover efficiency can be estimated from T_{ant} if we assume that most of spillover strikes the ground. The validity of this assumption for a single element is less certain than for beamformed cases where the feed pattern is more directive. Firstly the radiation pattern is divided at the horizon with the sky efficiency, η_{sky} being the fraction of the power pattern received by the antenna from the sky:

$$\eta_{\text{sky}} = \frac{\iint_{\text{sky}} D(\theta, \phi) d\Omega}{\iint_{\Omega} D(\theta, \phi) d\Omega} = \frac{1}{4\pi} \iint_{\text{sky}} D(\theta, \phi) d\Omega \quad (7.8)$$

where the integral of directivity over a sphere is 4π from its definition. The antenna temperature is then:

$$T_{\text{ant}} = \eta_{\text{sky}} T_{\text{sky}} + (1 - \eta_{\text{sky}}) T_{\text{gnd}} \quad (7.9)$$

where T_{sky} and T_{gnd} are strictly weighted averages of the sky and ground physical temperatures respectively—the weighting is the radiation pattern.

⁵Two effects contribute to asymmetry in the combined uncertainty: (1) the contributing uncertainties can be asymmetric and (2) the measurand can be a non-linear function of the contributing parameters. Both of these apply in the cases evaluated here.

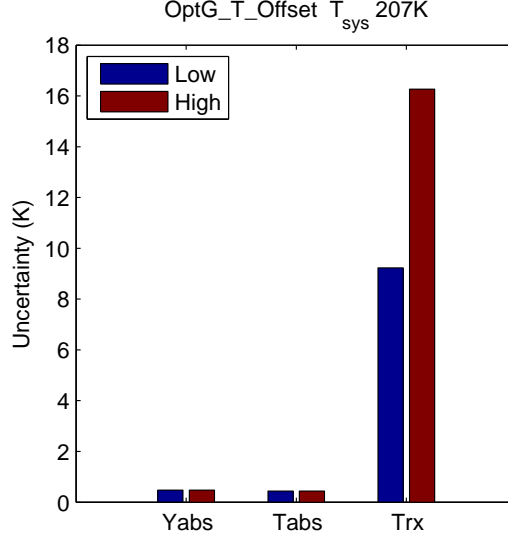


Figure 7.10 – Uncertainty contributions to the system temperature calculation for the maximum G/T weighting on the offset subarray.

Rearranging (7.9) gives:

$$\eta_{\text{sky}} = \frac{T_{\text{gnd}} - T_{\text{ant}}}{T_{\text{gnd}} - T_{\text{sky}}}. \quad (7.10)$$

$T_{\text{gnd}} 300 \pm 5$ K and $T_{\text{sky}} 6 \pm 1$ K are used for the results shown in Table 7.4. The total uncertainty, $-5, +8\%$ in absolute terms, is dominated by the uncertainty in T_{rx} .

Using the assumption that most of the spillover strikes the ground,

$$\eta_{\text{spill}} \lesssim \eta_{\text{sky}}. \quad (7.11)$$

For completeness, to find the system temperature when the estimate for T_{ant} is superior to the estimate for T_{rx} is:

$$T_{\text{sys}} = \frac{T_{\text{abs}} - T_{\text{ant}}}{Y_{\text{abs}} - 1}. \quad (7.12)$$

Incidentally, the calculations in this section are much simpler if the reference plane for the antenna is chosen to include the radiation from the ground as discussed in Section 4.2.1. In this case the reference plane is a plane between the antenna and the sky parallel to the ground. With this reference plane, both the system temperature and the directivity are di-

vided by η_{sky} : $T'_{\text{sys}} = T_{\text{sys}}/\eta_{\text{sky}}$ and $D' = D/\eta_{\text{sky}}$. If the absorber is at the same temperature as the ground, as is usually the case, then covering the feed with absorber is essentially indistinguishable from placing a black body plane over the antenna. T'_{sys} can be found from the Y-factor:

$$Y_{\text{abs}} = \frac{T_{\text{abs}} + T'_{\text{sys}} - T_{\text{sky}}}{T'_{\text{sys}}}. \quad (7.13)$$

The *on-off source* measurement provides $(G/T)_{\text{on-off src}}$ from (7.4) and so the directivity with this reference plane is given by $D' = T'_{\text{sys}}(G/T)_{\text{on-off src}}$.

7.6.5 Aperture Efficiency

The known source and absorber measurements described above can be combined to find the antenna aperture efficiency. From (7.5) and (7.7),

$$\eta_{\text{ap}} = \frac{T_{\text{sys}}}{T_{\text{sys}}/\eta} = \frac{(T_{\text{abs}} + T_{\text{rx}})}{Y_{\text{abs}}} \frac{2k_{\text{B}}(Y_{\text{src}} - 1)}{AS}. \quad (7.14)$$

These were measured for the offset subarray of elements (Table 7.4) and range from 46–65%. The combined uncertainty of $\pm 10\%$ in absolute terms is dominated by Y_{src} and with T_{rx} contributing only 2–5% to the total. An example of the contributions is shown graphically in Fig. 7.11. As the dominant contributor to the uncertainty, Y_{src} , is uncorrelated across weightings, the ratio of these efficiencies will have a similar uncertainty to the individual results.

7.6.6 Noise Temperature From Extended HI Regions

In addition to using a point celestial source for determining telescope properties, extended regions that cover all or most of the main beam of an antenna can be used [309]. The use of an extended region provides system temperature in a way related to the absorber method described above. In this case the hot load measurement is made with the antenna pointed at the extended region of known brightness temperature and the cold load measurement is made with the antenna pointed at the cold sky.

The moon is one possibility for the extended source with a well characterized brightness temperature (see Section E.2) but it subtends only half

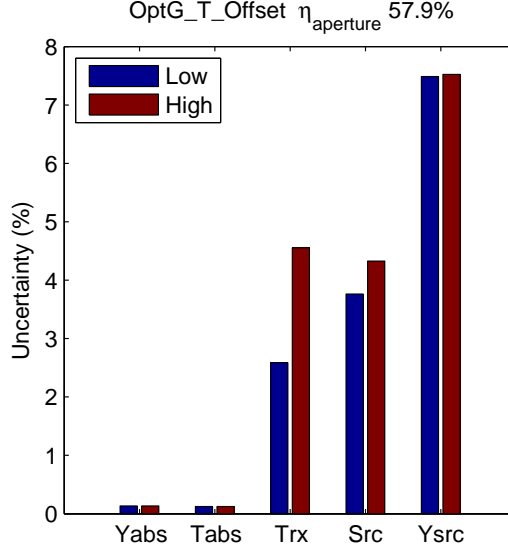


Figure 7.11 – Uncertainty contributions to the aperture efficiency calculation for the maximum G/T weighting on the offset subarray. The vertical scale is in absolute percent, e.g. the contribution of Y_{src} yields $57.8 \pm 9\%$ or 17% of η_{ap} .

the beamwidth of the telescope. Therefore its use is very sensitive to the correction factor, K , described below.

Hydrogen line (HI) regions that extend for at least 3° – 4° (cf. the HPBW of 1.2°), provide a more convenient extended source albeit only at 1420 MHz. Information on such regions is available in Section E.5. The spectra of the central element and NCM for the central subarray of elements are shown in Fig. 7.12. The region used is designated S9 with a brightness temperature T_{HI} of 85 ± 6 K [309]. The power at the HI peak is the sum of the contributions from the system temperature and the extended region. A correction factor, K , is derived from the integral of the product of the antenna radiation pattern and the brightness temperature of the HI region. This compensates for incomplete coverage of the radiation pattern. Williams [309] provides a guide to estimating K and, with the region extending about 3 times the diameter of the half power beamwidth, the value is taken as 1.2 ± 0.1 . With radiation patterns and a good map of the HI region, the uncertainty in K could be reduced.

The HI region only intercepts the forward radiation of the dish and so the power of the hot load needs to be reduced by the factor of the spillover

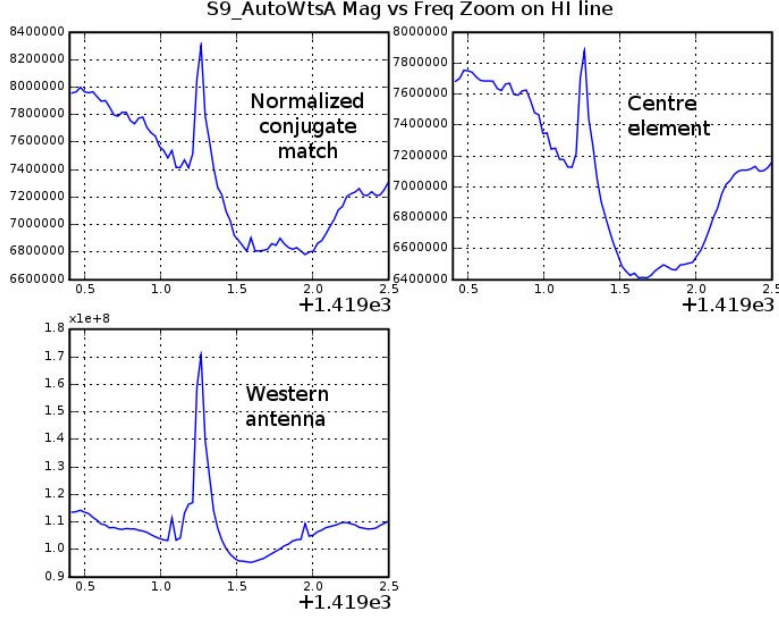


Figure 7.12 – Spectra from extended HI region S9 for different weights.

efficiency. This is particularly important for the single element case where the spillover is expected to be high. As no other estimates were available, the values in Table 7.4 that were calculated for 1200 MHz were used.

The power ratio of the HI peak to the noise floor is given by

$$Y_{\text{HI}} = \frac{T_{\text{sys}} + \eta_{\text{sky}} T_{\text{HI}} / K}{T_{\text{sys}}}. \quad (7.15)$$

Rearranging gives

$$T_{\text{sys}} = \frac{\eta_{\text{sky}} T_{\text{HI}}}{K(Y_{\text{HI}} - 1)}. \quad (7.16)$$

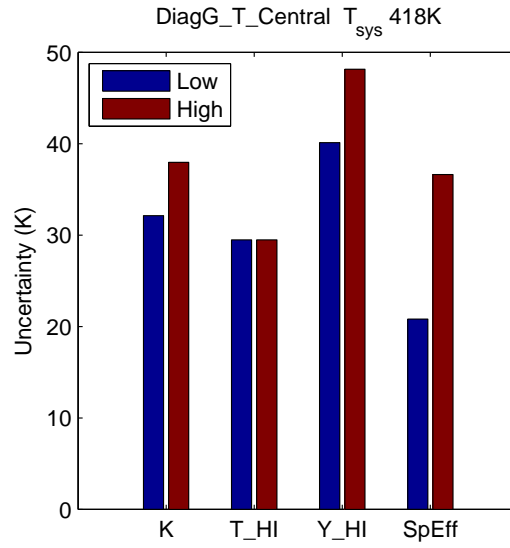
The results from the measurements shown in Fig. 7.12 are given in Table 7.5. The uncertainties are fairly symmetrical and so the root-sum-of-squares (RSS) of the high and low uncertainties is shown.

An example of the uncertainty contributions is shown graphically in Fig. 7.13.

This technique was not pursued as the performance of the array at 1420 MHz differs substantially from that of the 1200 MHz band which was chosen to focus on (see Section 6.4.3). The difference in performance is seen

Table 7.5 – Extended HI region system temperature measurement.

Case	Noise floor power	HI peak power	Y_{HI} (W/W)	T_{sys} (K)	Combined uncertainty (K)
	(arbitrary units)	(arbitrary units)			
Single element	69 ± 1	79.0	1.14	348	60
Norm. conj.	72 ± 1	83.2	1.15	417	70
Western antenna	1000 ± 30	1720	1.72	95	14

**Figure 7.13** – Uncertainty contributions to the system temperature calculation from the extended HI region. SpEff is the spillover efficiency.

in the scattering parameters in Section 6.4.1 and expected from the larger element spacing.

7.7 Summary

This chapter presented the practical implementation of real-time beamforming an FPA in a prototype radiotelescope. Single element, NCM and maximum G/T weightings were applied. Both the central and offset subarrays of FPA elements were employed in the measurements.

A range of evaluation techniques suitable for use with FPAs was demonstrated including the use of limited radiation patterns for determining aperture field distributions. Relative and absolute measures of gain and noise temperature determination were shown along with uncertainty analyses.

A larger far-field map would have been preferred to give better resolution of the aperture. Appendix G also discusses some ways in which aperture distributions generated from limited cut data may be improved.

The maximum G/T solution was demonstrated using the noise covariance matrix. While a similar approach was published by Jeffs et al. in October 2008 [9], this is believed to be the first time this was done with an interferometer.

Procedures for generating beamforming weights using only signals typically available from an interferometer radiotelescope were developed and demonstrated.

Further analysis of the data collected could provide insight into the stability of the electronic gains and the covariance matrix. The study of spillover noise variation with elevation and its control, other weighting solutions and more detailed aperture field determination is well suited to the more sensitive FPA systems such as the Apertif [86], the BYU-NRAO developments [38] and the CSIRO Parkes Testbed Facility [310].

Chapter 8

Discussion of Results

The preceding chapters have described the NTD Interferometer (Chapter 6) and the measurements conducted to evaluate its performance (Chapter 7). In this chapter these results are discussed in detail and the measurements are compared with predictions.

The radiation patterns are analysed with a discussion of beamwidth, coma aberration and sidelobe levels. The aperture field distributions are then used to further the understanding of the beamforming behaviour. To understand the contributions of various effects on the aperture efficiency, the dimensions of the antenna and feed structure are used to estimate a set of subefficiencies. An upper limit of the total aperture efficiency is found from enclosed power calculations and is compared with the measured efficiency.

The element weightings are also analysed and compared to further understand the beamforming process.

8.1 Key Antenna Parameters

The measured performance of the system is compared with predictions based on the knowledge of the physical structure. The key parameters used in the calculations are listed in Table 8.1 where dimensions are expressed in terms of their electrical length, i.e. in terms of wavelengths at 1200 MHz.

Table 8.1 – Dish and FPA physical parameters in terms of electrical length at 1200 MHz.

Parameter	Physical	Electrical
Diameter	14174 mm	56.7λ
Focal length	5661 mm	22.7λ
F/D	0.399	
RMS surface error	3 mm	0.012λ
Mesh spacing	6 mm	0.024λ
Strut diameter	140 mm	0.56λ
Focus package (square)	1444×1444 mm	$5.8 \times 5.8 \lambda$
Element Spacing	127.5 mm	0.510λ

8.2 Radiation Patterns

Characteristics of the radiation patterns can be interpreted in terms of the antenna structure and beamforming behaviour. These include the half-power beamwidth, coma aberration and sidelobe levels. The purpose here is to identify possible causes of the salient features of the NTD radiation patterns.

8.2.1 Half-Power Beamwidth

The half-power beamwidth (HPBW), θ_{HPBW} , allows some initial inferences regarding the antenna performance. Two reference values are considered for comparison with the measurement: (1) the uniform-circular-aperture where $\theta_{\text{HPBW}} = 58.4\lambda/D = 1.03^\circ$, and (2) a typical value for parabolic reflector antennas [311] where $\theta_{\text{HPBW}} = 70\lambda/D = 1.23^\circ$. The θ_{HPBW} values for the cases measured, summarized in Table 8.2, are wider than the uniform-circular-aperture beamwidth as expected. They are close to the typical value showing that the feed is reasonably close to the focus and is not severely under-illuminating the reflector.

A related observation can be made by using θ_{HPBW} to estimate the approximate directivity of the aperture. As θ_{HPBW} is a high *angular* frequency feature, it is dominated by the low *spatial* frequency features of the aperture amplitude and phase, rather than the higher spatial frequency features such as blockage. Stutzman provides a number of values for the $D\theta_{\text{HPBW}}^2$ where D is the directivity. The value for circular apertures with a parabolic-taper-

Table 8.2 – Directivity from half power beamwidth.

Subarray	Weighting	Num. elts.	θ_{HPBW} ($^{\circ}$)	From θ_{HPBW}		
				D^a (dBi)	ΔD^a (dB)	η_{ap}^b (%)
central	single	1	1.16	44.6	0.00	90
central	norm. conj.	21	1.18	44.5	−0.10	88
offset	single	1	1.17	44.6	0.00	90
offset	max. G/T	5	1.27	43.8	−0.74	75
offset	norm. conj.	21	1.22	44.2	−0.35	83
offset	max. G/T	21	1.24	44.1	−0.50	80

^a Directivity.^b Aperture efficiency. When calculated from the θ_{HPBW} , this does not include spillover or losses due to feed and strut blockage.

on-a-pedestal profile is used here [27, eqn. (7-176)] and so

$$D = 39000 \text{ deg}^2 / \theta_{\text{HPBW}}^2. \quad (8.1)$$

The aperture efficiency is calculated from this directivity value for comparison with the values from the gain and G/T measurements. The results are listed in Table 8.2. The high efficiency values suggest low edge tapers (almost uniform illumination) for the single element cases, and slightly higher tapers for the beamformed cases. The η_{ap} values from the gain and G/T measurements are much lower, unsurprisingly, as θ_{HPBW} only provides a crude indication of the aperture illumination.

8.2.2 Coma Aberration

Offsetting the feed in a paraboloid introduces a coma effect that is readily apparent, for example, in the Parkes 21-cm Multibeam Receiver [82, 312]. Correcting this aberration was demonstrated in some of the first dense FPA investigations [57] (see Chapter 2) and it is also demonstrated by the measurements in Chapter 7.

The beam peak for the offset subarray is 1.67° from the reflector axis (1.35 times the typical $\theta_{\text{HPBW}} = 70\lambda/D$). The coma is apparent in the E-plane and 45° -plane pattern cuts in the single (Fig. 7.3c) and five-element (Fig. 7.3d) cases. The radiation patterns for the full complement of 21 elements (Figs. 7.3e and 7.3f) show the beamforming reducing the coma. This

improvement in the symmetry can also be seen in the interpolated two dimensional far field patterns in Fig. 7.4.

8.2.3 Sidelobe Levels

The level of the first sidelobes for the eastern NTD antenna are given in Table 7.3. As the second and subsequent sidelobes are not well defined, only the first sidelobe level will be considered here (Fig. 7.3). We might expect them to be lower than the sidelobes of a uniform circular aperture, -17.6 dB or 13% of the main beam field [27] as some degree of aperture tapering is expected, but they range from -16.3 to -13.7 dB, or 15% to 21% of the main beam field.

The sidelobe levels in a reflector antenna are determined by a number of factors, including blockage of the aperture and reflector surface errors, as well as the underlying aperture illumination. Possible causes for these high sidelobes are discussed in the following sections and the impact of sidelobes on radiotelescope performance is discussed in Section 9.1.3.

Aperture Blockage Contribution to Sidelobes

Aperture blockage is caused by the feed package and its supporting struts. The approaches to modelling blockage can be quite complex if high accuracy is required [313–315]. In our situation, however, particularly without an accurate feed pattern, an approach providing only the approximate magnitude of the effect on sidelobes is warranted.

The model used here is to set the field to zero in the shadow of the blocking structures. The pattern of the blockage used is shown in Fig. 8.1. Physical optics is used to transform the aperture distribution to the far field using (G.1).

As the actual reflector illumination is not known, a uniform aperture is used for the blockage effect estimates.

Far-field pattern cuts for a number of apertures are shown in Fig. 8.2. As the model uses an aperture with two planes of symmetry and with a purely real field, the far field shares the planes of symmetry and is also purely real.¹ Using superposition, the far field of the blocked aperture is approximated by the difference between the far field of the unblocked aperture and the far

¹The standard proof for this property in Fourier transforms can be applied to (G.1).

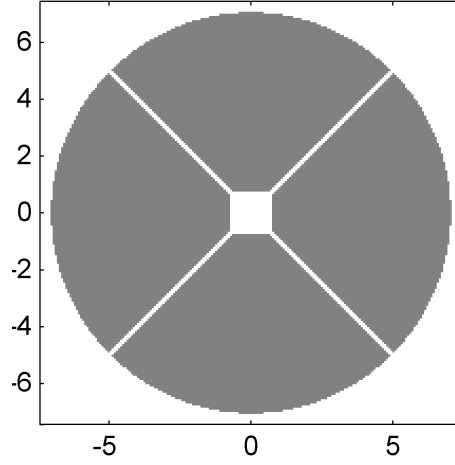


Figure 8.1 – Dish aperture showing strut and feed blockage. The scales are in metres.

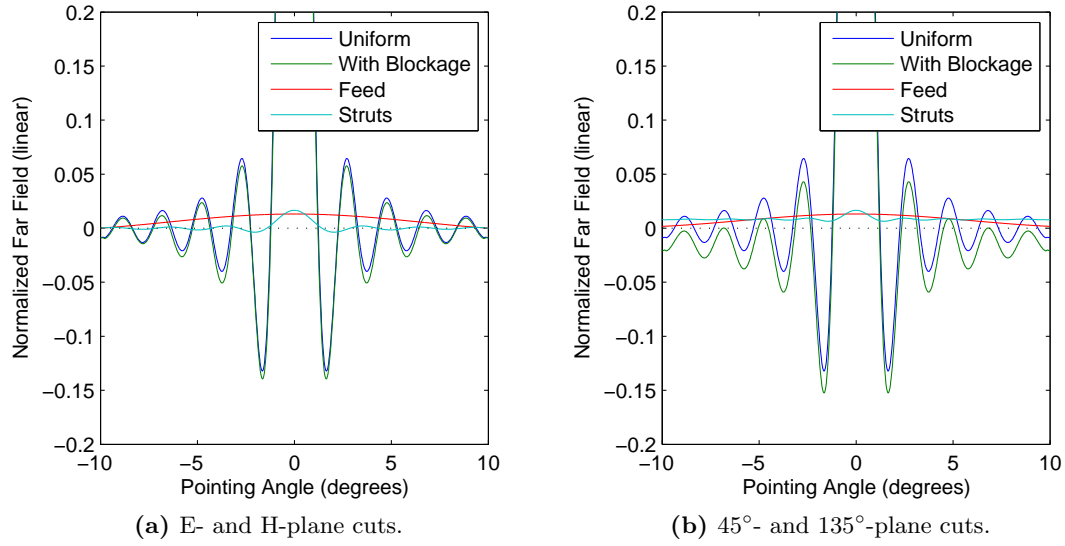


Figure 8.2 – Far-field patterns for different blockage conditions. The data is scaled so the unblocked pattern has a peak of 1.

Uniform: Uniformly illuminated circular aperture with no blockage.

With Blockage: Uniform aperture with the blockage shown in Fig. 8.1.

Feed: The field that is subtracted by the feed blockage.

Struts: The field that is subtracted by the strut blockage.

field generated by the blocked regions [313]. An effect of blockage revealed by more detailed modelling is the filling in of sidelobe nulls.

The focus package is 1444×1444 mm square, taking 1.3% of the total aperture area. The far field pattern from this is much broader than the pattern from the reflector. Therefore, the effect on the unblocked pattern is to (1) subtract from the main beam and first few even sidelobes and (2) add to the first few odd sidelobes.

The feed mounting struts cause blockage in two regions of the reflector. In the region under the struts they block incident radiation from reaching the reflector. In the region of the reflector between the strut mounting point and the edge, they block the reflected field from reaching the feed. The first region forms a simple rectangular shadow and the second region forms a more complex shape dependent on the reflector system geometry [313]. For this study, only the approximate magnitude of these effects is being considered and so the strut blockage is modelled using two crossed rectangles as shown in Fig. 8.1. These rectangles cover 2.3% of the aperture, a little more than the feed package. This explains why, in Fig. 8.2, the far field pattern from the struts is slightly greater on-axis than the pattern from the feed package. The strut blockage creates a far field pattern that is the sum of two thin apertures. In the 45° - and 135° -planes, the pattern is the sum of a very broad sinc function from the struts perpendicular to the cut and a narrow sinc function from the struts in line with the cut. This narrow sinc function has a slightly higher angular frequency than the unblocked pattern. In the E- and H-planes, the contributions of the two rectangles are the same and so the pattern is a single sinc function with an angular frequency slightly lower than the unblocked pattern. The impact of the strut blockage in these planes is much lower as can be seen in Fig. 8.2.

The far field from the aperture with both feed and strut blockage (Fig. 8.1) is also shown in Fig. 8.2. The sidelobes for this case are increased from -17.6 dB to -16.3 dB, i.e. 13.2% and 15.3% of the peak field respectively. Repeating the exercise for a tapered aperture decreases the unblocked sidelobes and slightly increases the impact of the blockage because of the reduced total efficiency. The analysis here suggests that while blockage contributes to the high sidelobes, there are likely to be other factors present.

Surface Error Contribution to Sidelobes

The NTD antenna surface survey reported an RMS error of 0.012λ . Using Ruze's formula [316], this reduces the peak power by 2.2% and correspondingly the peak field by 1.1%. If the surface errors are random, this power is scattered into a broad pattern and so the field in the first sidelobes can be assumed to be increased, by up to 1.1%. Ling et al. [317] demonstrated that sidelobes are often higher than predicted by this formula. Another factor is the regular structure in the construction of the reflectors causing periodic reflector distortions. This is clearly seen in Fig. 8.3 where the construction has inherent axial and radial periodicity. The rings supporting the mesh introduce an axial periodicity and the overlap between the mesh panels introduces a radial periodicity. The presence of periodic distortions can have a grating lobe effect and so increase sidelobes substantially more than that indicated by random surface error analysis. The magnitude of the periodic distortions in the reflector has not been determined but they could contribute substantially to the sidelobes in the NTD Interferometer.

Aperture Taper Contribution to Sidelobes

Tapering the aperture amplitude distribution toward its edge reduces the sidelobes as mentioned above. The degree of edge taper is a combination of the embedded element patterns, the increase in path length loss from the centre of the reflector to the rim and beamforming. Beamforming is expected to increase the edge taper over the single element illumination because the single elements are expected to produce too much spillover to maximize either gain or G/T . All these effects suggest the actual reflector illumination should result in lower sidelobes than the uniform circular aperture case. It would also suggest the beamformed cases should have lower sidelobes than the single element cases. In the central subarray, however, the first sidelobe levels are higher for the beamformed case (Figs. 7.3a and 7.3b). It is possible for the beamforming to produce an annular illumination pattern which can in turn increase the sidelobes. The mechanism for this increase is seen by considering the reduced field in the centre of the annulus in a similar way to the feed blockage where a broad pattern is subtracted from the narrow main pattern. The aperture illumination is discussed in detail in the following section.



Figure 8.3 – NTD reflector: the reflector was constructed by fixing radial mesh panels to pipes formed into rings.

Table 8.3 – FPA Resolution.

Number of elements	5	21
Diameter/Element Spacing	2	4
D_{FPA} (mm)	0.255	0.510
D_{FPA}/λ	1.02	2.04
Angular resolution: λ/D_{FPA} (deg)	56	28
Arc at vertex: $\lambda/D_{\text{FPA}}F$ (m)	5.5	2.8

No single cause for the high sidelobes has been identified but it is concluded that a combination of the candidates listed above is responsible. If constraints were put on the sidelobes in the beamforming algorithm, it is likely they could be reduced. For instance, compensating for periodic reflector errors was analysed by Rudge and Davies [88] and Cornwell and Napier [78].

8.3 Aperture Field Distribution

The aperture field distributions were calculated from the limited far-field radiation patterns as described in Section 7.5 and Appendix G. They are shown in Figs. 7.5 to 7.8. As noted the patterns have low spatial resolution and the inherent smoothing masks sharp transitions in the aperture expected at the reflector rim and the blocked regions. Nonetheless, away from these boundaries, the test cases in Appendix G suggest the accuracy of the aperture calculations is about 5%.

The chief motivation for calculating the aperture fields is to study the beamformed feed radiation pattern. This study is assisted by the using the FPA size to estimate the spatial resolution of the aperture illumination. An effective subarray diameter is used to determine the upper limit of the angular resolution. This is then used to find the corresponding arc length on the surface of the reflector [78]. The results of these calculations are listed in Table 8.3.

The aperture field distributions show an increase in edge taper for the beamformed cases and it is also more pronounced for the 21-element case than the 5-element case. This narrowing in the aperture corresponds to the inverse relationship in the θ_{HPBW} values.

The dip in the centre of the aperture also increases with beamforming. The angular resolution calculations suggest that beamforming may introduce a dip in the centre of the feed pattern—to reduce the blockage loss.

The phase cuts for the single element cases show the phase centre of the array elements was below the focal plane. The beamformed cases demonstrate the ability of an FPA to correct the defocussing.

It would have been preferable to use a two dimensional far-field grid covering a wider range of angles for the aperture calculations, providing a superior spatial resolution. Time, however, did not allow for this. Nonetheless, the technique developed here has proven very useful, particularly for comparing multiple beamforming weightings as demonstrated above.

8.4 G/T Performance Predictions

Some predictions can be made regarding the achievable aperture efficiency from typical reflector antenna behaviour. The total efficiency is calculated from the product of contributing subefficiencies [27, 318]. This aids in understanding the mechanisms that determine the overall efficiency. Upper bounds on the aperture efficiency can also be determined from calculating the power enclosed by the effective area of the FPA in a similar manner to that described in Chapter 3.

The effective receiver noise estimated in Section 7.6.1 is used to set an upper bound for the system noise before spillover is added.

8.4.1 Subefficiency Estimates

Estimates of some of the standard subefficiencies [27, 318] have been calculated and are presented in Table 8.4 .

In order to calculate most subefficiencies, a feed pattern needs to be assumed. Representative feed models are presented in texts such as Kildal [318] and Stutzman and Thiele [27]. The feed pattern was approximated using $\cos^q(\theta)$ for $\theta < \pi/2$ and zero for $\pi/2 \geq \theta > \pi$. Formulas chiefly from Stutzman [27, Ch. 7] are used to calculate the subefficiencies. To determine the sensitivity of the subefficiencies to the feed pattern, they were calculated for values from $q = 0.44$ to $q = 2$, corresponding to edge tapers of 6 dB to 17.25 dB. Using the similar FARADAY array as a guide (Section 6.4), the edge taper of the THEA tile is about 9 dB for a single element, corresponding

Table 8.4 – Subefficiencies for a model feed.

Edge Taper (dB)	6	9	11	14	17.25
Feed Model q	0.44	0.85	1.13	1.55	2
Mesh (%)	99.9	99.9	99.9	99.9	99.9
Surface Errors (%)	98	98	98	98	98
Strut Blockage (%)	96	96	96	96	96
Feed Blockage (%)	97	97	97	97	97
Spillover (%)	79	89	93	97	98
Ap. Taper (%)	96	92	89	83	77
Illumination (%) ^a	76	82	83	80	76
η_{total} (%)	69	74	75	73	68

^a The illumination efficiency is the product of spillover and aperture efficiencies [27].

to $q = 0.85$. As q corresponds to a specific angular resolution of the feed pattern, it also corresponds to a minimum feed size. Using the diameters of the subarrays in Table 8.3 to calculate maximum directivities corresponding to uniform circular apertures,

$$D_{\text{max}} = \frac{4\pi \text{Area}}{\lambda^2} \quad (8.2)$$

the value of q can be calculated by inverting [188, eqn. (4)]:

$$q_{\text{max}} = \frac{D/2 - 1}{2} \quad (8.3)$$

For the 5 and 21 element subarrays the maximum values of q are 2.1 and 9.8 respectively. Therefore the beamformed FPA cases can achieve flatter aperture illumination than the $\cos^q(\theta)$ feed models used here. The feed models also do not account for back radiation seen in the single element patterns for the similar FARADAY array shown in Fig. 6.5 [295]. With beamforming, however, the feed pattern is expected to narrow and the back radiation is expected to be reduced. The subefficiency calculations were made with these caveats in mind.

The loss through the mesh was calculated using Astrakhan's formula [319] and reduces the efficiency by 0.10%. The random surface error efficiency was calculated using Ruze's formula [316] and the estimated surface errors reduce the efficiency by 2.2%.

Blockage reduces the gain of an antenna in two ways, most easily described in transmit mode: firstly energy striking the blocking structures is scattered into the sidelobes, near and far, and secondly the aperture area is reduced by the blockage [27, p346]. The aperture blockage efficiency can be estimated from a reduction of the aperture area. For feed blockage this is usually weighted by taper efficiency η_{taper} to account for the concentration of power in the centre of the reflector. The blockage efficiency can then be approximated by [27, eqn. (7-236)]

$$\eta_{\text{blockage}} = \left(1 - \frac{1}{\eta_{\text{taper}}} \frac{A_{\text{blockage}}}{A_{\text{physical}}} \right)^2 \quad (8.4)$$

The reduction in the area ratio is squared to account for the two effects: scattering and reduced effective area. With an FPA, as seen in the discussion regarding the aperture illumination in Section 8.3, the scattering component from the feed can be reduced by the beamformer weighting creating a dip in the centre of the aperture. The impact of feed blockage, at $\sim 3\%$, is much smaller than the illumination efficiency and so the reduction in scattering will not make a large difference to the overall efficiency. It could have a significant effect on the sidelobe structure however. Note also that the feed blockage efficiency varies by only 0.7% over the range of feed models used here.

The strut blockage was calculated using the simple reduction of area, i.e. $\eta_{\text{taper}} = 1$ in (8.4) and reduces the efficiency by 4.5%. Detailed studies of both strut and feed blockage [313, 314, 320] may provide better estimates but the approach taken is considered adequate for this study. The important conclusions here are the estimate of the blockage efficiency and the observation that it is relatively independent of the feed pattern.

The spillover and aperture taper efficiencies are heavily dependent on the feed pattern. Their product however, the illumination efficiency, is much less dependent on the feed pattern, with a broad maximum at edge tapers of about 11 dB [27].

Traditionally, feed losses are included in the radiation subefficiency [27, 318] but this is not done as here as the directivity is used as the gain reference (see Sections 4.2 and 7.6). Other subefficiencies such as phase are not included in this analysis because there is no convenient basis available for estimating them.

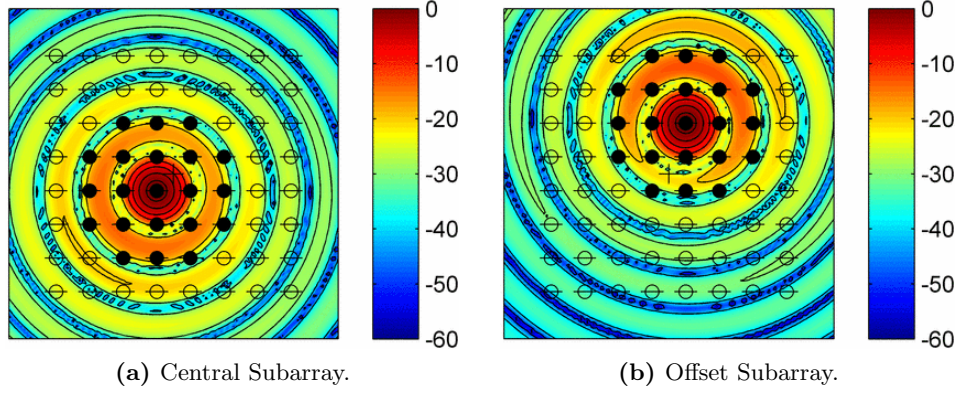


Figure 8.4 – Focal plane power flux density, S_z , for the NTD antenna. The fields are overlaid with the centres of the array elements. The filled circles are the 21 elements selected for beamforming.

The mesh, surface error and blockage subefficiencies provide an estimate of the contributions to the overall NTD antenna efficiency. As the beam-formed subarrays may be capable of producing higher illumination efficiencies than the $\cos^q(\theta)$, the calculated illumination efficiencies are less relevant. Instead, enclosed-power calculations are used in the following section to provide an upper limit on the beamformed FPA illumination efficiency.

8.4.2 Enclosed Power

The encircled power approach of Chapter 3 can be used to place an upper limit on the achievable directivity. Specifically, the directivity must be less than the enclosed power percentage corresponding to the effective area of the FPA. The focal plane fields for the NTD central and offset subarrays were calculated and are shown in Fig. 8.4. The power enclosed in the areas corresponding to the central and offset subarrays was calculated and the efficiencies are listed in Table 8.5.

Estimating the effective area of the FPA elements introduces an uncertainty, however, as the elements respond to field components beyond their physical area or cell. Equivalently, a transmitting element generates currents beyond its corresponding cell and these currents contribute to the transmitted radiation. This is particularly evident when looking at a single element radiation pattern—for instance the patterns in Fig. 6.5 show angular fre-

Table 8.5 – Enclosed power efficiency for the areas covered by the elements for the NTD FPA.

Subarray	Num. elts.	η_{encl} (%)	$\eta_{\text{encl tot}}$ (%)
Central ^a	1	45	41
Central	21	83	75
Offset ^a	1	43	39
Offset	5	68	62
Offset	21	82	74

^a The single element efficiencies are likely to be underestimated as the model does not account for contributions of fields outside the element area.

Table 8.6 – Calculated limits and measured values for η_{ap} and $T_{\text{sys}}/\eta_{\text{ap}}$.

Subarray	Weighting	Num. elts.	$T_{\text{sys}}/\eta_{\text{ap}}$		η_{ap}	
			Min. (K)	Meas. ^a (K)	Max. (%)	Meas. ^a (%)
Central	Single	1		532^{+131}_{-93}		51^{+10}_{-10}
Central	Norm. conj.	21	256	364^{+61}_{-50}	75	
Offset	Single	1		614^{+178}_{-119}		46^{+10}_{-10}
Offset	Max. G/T	5	310	419^{+80}_{-63}	62	55^{+10}_{-10}
Offset	Norm. conj.	21	259	350^{+56}_{-47}	74	65^{+10}_{-10}
Offset	Max. G/T	21	259	357^{+59}_{-48}	74	60^{+10}_{-10}

^a The 95% confidence interval is shown as sub- and superscripts.

quency components that are higher than the 127° limit indicated by the cell size alone. Nonetheless, it is unlikely these outer currents will add constructively in a beamformed case. This is particularly the case at the edge of the subarray where, in the sidelobes of the received focal plane field, the amplitude and phase is changing rapidly as can be seen in Fig. 8.4. Therefore the enclosed power values can be considered an upper limit on the aperture efficiency for the beamformed cases.

The efficiency calculated using the enclosed power, η_{encl} , does not include the mesh, surface error and blockage losses. An upper limit on the aperture efficiency can then be set at

$$\eta_{\text{encl tot}} = \eta_{\text{blockage}} \eta_{\text{mesh}} \eta_{\text{surf}} \eta_{\text{encl}}. \quad (8.5)$$

The value of $\eta_{\text{blockage}} \eta_{\text{mesh}} \eta_{\text{surf}}$ is almost constant at 91% for different q values. From these calculations, when 21 elements are beamformed the aperture efficiency can be at most 75% and for 5 elements the upper limit is 62% (Table 8.5).

Using the estimated receiver noise temperature from (7.3) the minimum $T_{\text{sys}}/\eta_{\text{ap}}$ from the a-priori knowledge of the system is about $192 \text{ K}/0.75 = 256 \text{ K}$. The values for the other cases are listed in Table 8.6 where they are compared with the measured values from Table 7.4.

The measured values for both $T_{\text{sys}}/\eta_{\text{ap}}$ and η_{ap} are well within the limits calculated above. These measurements are analysed in the following sections.

8.5 G/T Measurements

In this section each measurement technique, its uncertainties and the results are discussed and then comparisons are made with predictions. In the following section the results are combined to interpret the beamformer weightings.

8.5.1 Relative Measures

The relative measures, employing the interferometer for gain and the off-source power for noise, provide a rapid and precise method for evaluating weightings relative to each other. It is much less affected by uncertainties than the absolute G/T measurement methods used here.

While the ΔG and ΔT_{sys} measures do not fully account for coupling losses with beamforming (see Section 7.6.2), they change in the expected direction (Table 7.4) with one exception. As expected, as the number of beamformed elements increases from 1 to 5 to 21, the noise reduces and the gain increases. Both of these effects are explained by reduced spillover. The maximum G/T weighting also has less gain and less noise than the NCM weighting as expected. The differences in the ratio, G/T , also change as expected: it increases as the number of elements increase and the maximum G/T weighting has a higher G/T than the NCM weighting. The exception is the noise of the central subarray where it increases by 0.09 dB between the single element and beamformed cases. ΔG is over 2 dB compared to less than 1 dB for the offset cases. The central and offset subarrays, however, have very similar $\Delta G/T$ values. Without the ability to repeat the measurement, it is difficult to explain this result. One possibility is the element weights were not correctly normalized, increasing the apparent power measurement for both the relative gain and relative noise measures.

8.5.2 On-off Source

Determining the G/T from a known source can be rapidly and conveniently undertaken. The required data can also be acquired at the same time as the data for relative measures, as they both involve the same antenna pointing movements. The *on-off source* approach is well accepted for single dish telescopes. It is also the mode in which they are used in standard operation.

The uncertainty in the measurements in this thesis is dominated by the power ratio, Y_{src} (Fig. 7.9). This is directly dependent on the system noise and the source strength—the uncertainty reduces for a stronger source and lower system noise. The uncertainty in Y_{src} may also be reduced by repeating the measurement or increasing the integration time. The other contributor to the uncertainty is the source flux. This is dependent on the recency and accuracy of the source’s characterization. Sources used as calibrators for modern radiotelescopes are generally weaker than M87, the one used in this work. This is because they need to be more compact than is required for characterizing the relatively small dishes of the NTD Interferometer. Repeating the characterization of larger and stronger sources may be worth the required telescope time, given the interest in relatively small dishes for the SKA and its pathfinders.

The G/T values in Table 7.4 increase as expected with increasing element count. The maximum G/T weighting gives a G/T value that is 0.1 dB lower than the NCM result; however this is well within the uncertainty of ± 0.7 dB. The more sensitive relative G/T measures show the maximum G/T weighting with a higher G/T value, albeit only 0.07 dB.

8.5.3 Absorber Under the Feed

A common method used to determine a feed's noise performance is to present it alternately with microwave absorber and the sky and measure the power ratio Y_{abs} . This is often done with the feed pointing upward at the sky before it is mounted in a reflector. It can also be repeated when the feed is mounted at the focus.

In the case of the NTD Interferometer, measurements with absorber were only made after the feed was mounted in the reflector. To extract the system temperature, T_{sys} , from the focus Y-factor measurement, the receiver temperature, T_{rx} , or the antenna temperature, T_{ant} , is needed (see (7.6)). The latter, T_{ant} , can be calculated from the antenna radiation pattern using (4.41) or (7.9):

$$T_{\text{ant}} = \frac{1}{4\pi} \iint_{\Omega} T_{\text{scene}}(\theta, \phi) D(\theta, \phi) d\Omega = \eta_{\text{sky}} T_{\text{sky}} + (1 - \eta_{\text{sky}}) T_{\text{gnd}}. \quad (8.6)$$

Rather than using the full radiation pattern, the feed pattern can be used to estimate η_{sky} in most cases. η_{sky} is estimated from the parts of the feed pattern ‘seeing’ the reflection of the sky in the dish and any back lobe ‘seeing’ the sky directly. In the case of the THEA tile, the only estimates of the feed pattern are from the aperture field patterns and the pattern from the similar FARADAY array shown in Section 6.4. The aperture field patterns only show the feed pattern within bounds of the reflector and so provide no quantitative information about spillover. The FARADAY array is sufficiently different from the THEA tile to prevent using the T_{ant} value calculated from the feed pattern for finding T_{sys} for the single element NTD Interferometer measurements. The uncertainty is exacerbated by the sensitivity of T_{ant} to the radiation pattern at the wide angles beyond the dish edge. This region is particularly dependent on edge effects and the electrical size of the array.

Therefore, as T_{ant} could not be readily determined, the receiver temperature T_{rx} was used. The high uncertainty in T_{rx} is approximately halved in its

contribution to the T_{sys} uncertainty through being divided by Y_{abs} in (7.7). Note that the values of T_{ant} for the single element measurements at 81 K and 89 K are substantially higher than the value of 47 K calculated from the FARADAY radiation patterns.

The Y-factors increase as expected: as more elements are beamformed, the noise performance improves and the maximum G/T weighting has a better noise performance than the NCM weighting. It is worth noting for future comparisons that the value of T_{ant} at 24 K for the maximum G/T weighting is 11% of the total system temperature T_{sys} . For a lower noise receiver, $T_{\text{ant}}/T_{\text{sys}}$ will be higher. As the size of the beamformed array increases, however, T_{ant} should reduce as an efficient illumination pattern can be maintained with better spillover reduction.

8.5.4 Aperture Efficiency

The aperture efficiency, η_{ap} , primarily reveals how effectively the feed illuminates the dish. The on-off M87 and absorber measurements were both required for this calculation (7.14). The resulting uncertainty of $\pm 10\%$ (in absolute terms) is dominated by Y_{src} . The values of η_{ap} , shown in Table 8.6, are ordered as expected: the efficiency increases as the number of beamformed elements increases from 1 to 5 to 21. The maximum G/T weighting also, as expected, has a lower efficiency than the NCM weighting.

For the single element $\eta_{\text{ap}} = 46 \pm 10\%$ compared with the enclosed power upper bound $\eta_{\text{encl tot}} = 39\%$. While the bound is within the 95% confidence interval, a higher efficiency is likely as explained by the conjecture in Section 8.4.2 that the array elements respond to fields outside their cells.

As mentioned in Section 8.4.2, the beamformed values of η_{ap} are less than the $\eta_{\text{encl tot}}$ upper limits. The 5 and 21 element subarrays with maximum G/T weighting are expected to have lower efficiencies than the maximum as the spillover is reduced. The NCM weighting on the other hand is shown to be very similar to the maximum gain weighting. With a $\eta_{\text{encl tot}}$ that is 9% higher than η_{ap} , it is just within the confidence interval. A lower efficiency could be explained, however, by (1) T_{rx} being higher than the estimate or (2) an imperfect match presented by the array to the incident fields, particularly the cross-polarized and axial fields, as discussed in Section 3.8.1.

8.5.5 System Temperature from Extended HI Regions

Determining T_{sys} from extended HI regions has similarities to the *absorber under feed* measurement. In both cases knowing the spillover efficiency or more strictly sky efficiency, η_{sky} (see (7.8)) would allow the system temperature to be determined more accurately.

In this case the spillover efficiency, η_{spill} , from the 1200 MHz measurements was used which may be quite different from η_{spill} at 1400 MHz. The single element system temperature is less than the beamformed case when the opposite would be expected, suggesting the spillover efficiency value used may be incorrect.

8.6 Comparison of Beamforming Weightings

In this section a comparison is made between weightings to further understand the FPA behaviour.

8.6.1 The Normalized Conjugate Match and Maximum G/T

The measurements show the NCM and the maximum G/T weightings are very similar. They have very similar radiation patterns, gain, noise and G/T .

As expected the NCM weighting has a slightly higher (5%) aperture efficiency, albeit well within the 95% confidence interval of 10%. The narrower θ_{HPBW} also supports the NCM weighting aperture efficiency being slightly higher.

The maximum G/T weighting has a 5% lower noise temperature determined from the absorber measurement. This is just outside the 95% confidence interval which is 4% (see Section 7.6.4).

The relative G/T measurements have a much lower uncertainty than the absolute on-off source measurement and so they are better for comparing weightings: the maximum G/T weighting has a higher G/T than the NCM weighting—just within the 95% confidence interval.

The similarity between NCM and the maximum G/T weightings can be explained in terms of the spillover noise temperature relative to the receiver noise temperature. Recall that the maximum G/T weighting vector is given by (5.14) as

$$\mathbf{u} = \mathbf{C}_{T_{\text{sys}},u}^{-1} \mathbf{e}_p^*. \quad (8.7)$$

The $\mathbf{C}_{T_{\text{sys},u}}^{-1}$ multiplier can be interpreted as a correction to the conjugate match vector $\hat{\mathbf{e}}_p^*$. The noise covariance matrix, $\mathbf{C}_{T_{\text{sys},u}}$, contains noise data from both the receiver and the scene. The off diagonal terms represent noise coupled from other LNA elements, spillover noise and dissipative losses in the array structure.

The NCM uses only the diagonal of $\mathbf{C}_{T_{\text{sys},u}}$. This de-emphasizes noisier elements but does not reduce the spillover unless some elements receive more spillover noise than others. This is unlikely as all but the edge elements are expected to have very similar embedded patterns and the edge elements have only small weights.

The lower the receiver noise is relative to the spillover, the less the diagonal elements of $\mathbf{C}_{T_{\text{sys},u}}$ will dominate and spillover will have more effect. Therefore the NCM and the maximum G/T weightings will differ more for lower noise FPAs than the THEA tile.

The aperture distributions narrow with the increase in the number of elements from 1 to 5 to 21 showing the over illumination by the single elements being reduced by beamforming. This is also borne out in the reduction of noise shown in the absorber measurements, most of which is thought to be spillover reduction.

8.6.2 The Normalized Conjugate Match and Maximum Gain

The relationship between the NCM and the maximum gain weightings is treated in Section 5.4.5. There it is shown that a sufficient condition for these weightings to be equal is for (1) all the element radiation efficiencies, $\eta_{\text{radiated},i}$, to be identical and (2) all the element noise temperatures, $[\mathbf{C}_{T_{\text{sys}}}]_{ii}$, to be identical.

The argument for $\eta_{\text{radiated},i}$ being similar for all elements was presented in Section 5.4.5. With no direct measurement of the noise performance of each element, the differences were deduced from the ratio of the off-source power (system noise) to the power received from the vertex noise source (see Section 6.4.5).

The reduction of the maximum on-axis gain by the variation of noise performance is dependent on the applied element weights. This reduction can be approximated by the gain reduction caused by perturbing the NCM vector (Table 7.2) by the element noise variations (Fig. 6.15). When the measured values are applied, the gain reduces by only 0.03 dB. The reason

why element variability of up to 2.7 dB from the mean can have such a small impact can be understood from the following argument. The situation is greatly simplified by the errors being in amplitude only and that, for the on-axis gain, the weighting aligns the phase of the signals from the elements. The implicit normalization of the weight vector reduces apparently large differences. Consider a worst case situation, where the array weighting is dominated by the two very different elements. Modelling this with a two element array, with each element receiving the same field strength, the power gain is $|w_1 + w_2|^2 / (w_1^2 + w_2^2)$. For equal weighting the power gain is 2. Taking a weighting error of $w_1/w_2 = 1.41$ (3 dB), the power gain is 1.94, only 0.13 dB lower than the equal power case. This gain reduction diminishes with elements receiving different field strengths (the central element takes about 70% of the total energy).

The conclusion is that, for this system, the NCM results in a gain that is within the order of 0.03 dB of the maximum achievable gain. The on-axis gain of other FPA systems can be expected to be similarly insensitive to amplitude errors. Such errors may, however, have a major impact on sidelobes.

8.7 Summary

The measurements in Chapter 7 have been analysed and compared with predictions. In most cases, the results have not only been explained but insight has also been provided into the FPA system and the beamforming process.

The radiation pattern results demonstrated the ability of beamforming to reduce coma aberration and correct for defocussing. Using a point source for beamforming also naturally corrected any pointing errors. The first sidelobes were higher than expected with periodic reflector distortion and annular reflector illumination being the most likely causes. The sidelobes could be reduced by placing constraints on them in the beamforming algorithm. The aperture distributions, transformed from the far field, supported these investigations and showed increased edge taper as the number of beamformed elements was increased. The utility of these distributions would have been greatly improved had the far field patterns been more extensive—providing higher spatial resolution. This would have provided a

superior characterization of the feed radiation pattern from the FPA and allowed greater confidence in the interpretation of the aperture field distributions.

The gain and noise measurements showed reasonable consistency with predictions, particularly the relationship between weightings. The *on-off source* measurements provided G/T_{sys} and the *absorber-under-feed* measurement provided an estimate of T_{sys} . While it would have been preferred to use only external measurements to determine T_{sys} , either the receiver noise, T_{rx} , or the antenna temperature T_{ant} is needed to extract T_{sys} from the absorber measurements (see Section 7.6.4). T_{rx} was used here, introducing considerable uncertainty in the T_{sys} results. Nonetheless, the results were consistent with predictions, particularly with respect to each other. Having estimated the receiver temperature, the resulting spillover temperatures also took credible values.

The NCM and maximum G/T weightings were tested and found to perform as expected. The NCM weighting was shown to be very close to the true maximum gain weighting where the receiver noise is similar for each element, as was the case with the NTD Interferometer.

The calculated uncertainties proved very valuable in the analysis of the results. For instance the relative G/T measure was used instead of the on-off source result to show the maximum G/T weighting did indeed have a higher G/T than the NCM. Even though considerable effort is required to calculate uncertainties, doing so identifies areas of improvement and greatly enhances confidence in the conclusions drawn from the measurements.

The experimental work was limited to relatively few experiments due to the immature nature of the system and eventual equipment failure. In addition, RFI limited the tests to a single frequency. A more stable system in a low RFI environment would allow a more comprehensive evaluation of performance. Despite the limitations of the NTD Interferometer, it was a luxury to work on a dedicated FPA testbed without having to compete with astronomical observations as is the case with using the Parkes 64 m for interferometry with the 12 m FPA test-bed dish.

In both the central and offset subarrays, one of the 21 beamformed elements failed or performed intermittently. In both cases the beamformed performance demonstrated the system was capable of tolerating these failures, indicating the robustness of radiotelescopes employing FPAs.

Had the FPA been better characterized before mounting it in the reflector, the analysis of these results would have been much simpler. Measuring the noise temperature on the ground as in [181, 310] would have greatly reduced the uncertainty in the receiver noise temperature. Measuring the embedded-element radiation patterns of the FPA would have allowed the aperture illumination and spillover to be calculated from the beamformer weights. The decision was taken not to do so at the time as CSIRO's focus was on gaining experience in the entire system rather than examination of this particular array. This situation encouraged a *black-box* approach to be taken to the beamforming and measurements as described in Chapter 4. An advantage was that this fostered consideration of methods that could be applied to other situations where an installed FPA is not well characterized and to situations where the FPA performance changes after installation, such as due to element failure.

In conclusion, the experimental work described in this thesis has demonstrated successful beamforming of a dense FPA in a prototype radiotelescope. The performance of the FPA has been described and analysed.

Chapter 9

Conclusion

This chapter summarises the outcomes from the project as a whole. Additional conclusions from the various sections have been provided in the *Summary* section of each chapter. The contributions of this thesis are summarized in Section 1.3. Publications resulting from this thesis project to date are listed in Appendix H.

The objective of the project was to investigate and demonstrate beamforming of a focal plane array (FPA) in the context of radiotelescopes. The first step involved a study of focal plane fields, resulting in a rule-of-thumb formula for FPA size as a function of focal ratio and scan angle (Chapter 3). A model of the array was developed in Chapter 4 and beamforming approaches were explored in Chapter 5. The instrument used for the experimental program is described in Chapter 6 and the measurement results are presented and analysed in Chapters 7 and 8.

The theoretical treatment in this thesis is summarized in Section 9.1 and suggestions are provided. This is followed by a discussion of the experimental work of the thesis along with comments on refinements and alternative measurement techniques 9.2. Finally, the FPA system design is covered in Section 9.3.

9.1 Theoretical Treatment of FPAs

9.1.1 Enclosed Power Study of FPA Size Requirements

In Chapter 3 physical optics was used to calculate focal plane fields. The power enclosed in these fields was used to find the required FPA size for a

given field-of-view over the range of practical focal ratios for parabolic dishes. These data were reduced to closed form expressions in focal ratio and beam-width. These formulae were shown to differ substantially from more basic theoretical approximations. Studying the focal plane fields also assisted in the understanding of other aspects of this project, including the beamforming and experimental work. For instance, encircled power calculations were used to set an upper limit on the aperture efficiency to be determined from the experimental work.

The encircled power approach could be extended to cover other geometries such as cylindrical and spherical reflectors as well as dual reflector antennas. The correction of reflector imperfections and conformal feed surfaces could also be considered by this approach.

9.1.2 FPA Model

A ‘black-box’ approach to the active receiving-array model is introduced in Chapter 4. This is considered essential for situations where access to internal ports in an array is not available. This was the case with the instrument used for the experimental work in this thesis, namely the NTD Interferometer. The development of the theory was also instructive in understanding the mechanisms contributing to the FPA performance. Considering the relationship between the black-box and scattering matrix models provided the insight that the normalized conjugate match weighting is similar to the maximum gain weighting as discussed in Sections 5.4 and 8.6.2.

The relationship of the black-box model to various other array models could be explored further. For instance there have been recent developments in clarifying definitions for low noise arrays [20,33,241] and the relationship of this model with respect to these definitions should be established. Other possible extensions include separating the mutual coupling effects that have been implicit in the black-box model and further study of the relationship between array models and readily measurable parameters.

The model could also be extended to active transmitting arrays which received only cursory treatment in Chapters 4 and 5 as this was of limited interest to the main topic here. For transmitting arrays without access to internal ports, array losses are indistinguishable from the transmitter circuitry in a manner similar to active receiving arrays.

9.1.3 Beamforming Weighting Algorithms

Two beamforming weightings were used in the experimental work: (1) the maximum sensitivity (or equivalently, the maximum G/T), and (2) the conjugate match normalized by the noise of each element, referred to in this thesis as the normalized conjugate match. These were addressed in the theoretical treatment in Chapter 5.

The very weak signals involved in radio astronomy leads to a premium on sensitivity above other figures of merit. Recent work by O’Sullivan [275] has shown that, for a synthesis telescope, the maximum sensitivity weighting must be used to maximize the signal to noise ratio of the final image. This was not immediately obvious as a synthesized image over the entire field-of-view could be formed from the superposition of a variety of basis beams [321]. Therefore, while other factors are important, the beamforming weighting used in an operational telescope will, in most cases, be very close to the maximum sensitivity weighting. Nonetheless, the weighting can be perturbed to meet other objectives with only a small penalty in sensitivity [9, 274, 286].

Priorities in beamforming will undoubtedly depend on the application. Single dish and synthesis telescopes operate in quite different ways and so the issues dealt with by beamforming are likely to have differences. For instance, synthesis telescopes automatically filter out interference spatially through the imaging process in a way that single dishes do not. Therefore, interference mitigation may be a higher priority for single dishes than synthesis array telescopes.

Pattern Stability

The dynamic nature of FPA systems not only allows both the opportunity to adjust the radiation patterns and but raises the challenge of dealing with changing patterns. This is compounded by the large number of receiver chains where temporal changes in the phase and amplitude responses will cause a change to the radiation pattern. Conversely, with care, FPAs may also be able to increase pattern stability, for example compensating for gravity deformations.

Changes in the main beam can distort the production of an image in both single dish and synthesis array telescopes. For single dish radiotelescopes, celestial sources, interference and radiation from the ground can all

reduce the sensitivity of an observation by increasing the received power pattern through the sidelobes [9, 290]. Synthesis radiotelescope arrays suffer from these effects as well, although substantial protection is provided by the inherent spatial filtering provided by the imaging process. The presence of strong sources in the antenna sidelobes can, however, produce artefacts across the image. If the level received through sidelobes changes during an observation then the ability to excise the artefacts from the image through deconvolution is reduced [322].

The radiation pattern (main beam shape and sidelobes) for an FPA equipped reflector can be determined at the time of commissioning through direct measurements. This can be repeated from time to time, but such measurements are time consuming. In the interim the full pattern measurements could be used to interpolate between points determined by sources within the field-of-view. Accurate modelling of the antenna system, including blockage, may also assist in maintaining an accurate model of the radiation pattern.

Polarimetry

The field of polarization performance of FPA systems is another area of research as discussed in Section 5.1.3. The flexibility FPAs offer allows the possibility to minimize instrumental polarization across a wide field-of-view. The method for achieving this for a high sensitivity instrument is currently under investigation [284, 285].

9.2 FPA Prototyping and Evaluation

Much that has been learnt from this prototype system is being applied in the development and testing of the Australian Square Kilometre Array Pathfinder (ASKAP) prototypes. The confidence building tests in Chapter 6 proved important in identifying system faults and instabilities. The implementation of the calibration system, using the radiator on the dish surface, provided for repeatable measurement of the signal paths including relative phase. This greatly enhanced the system development and refinement.

The use of real time digital beamforming was important for CSIRO's technology development and provided rapid feedback on the system performance. For instance, it allowed checks to be made of pointing drift. Incorrect settings and failures were also immediately apparent allowing measurement

programs to be halted and the problem rectified early rather than continuing as can happen with an off-line processing approach. Another practical advantage of real-time beamforming is that it has a much lower data storage rate than a comparable off-line processing system. Achievable data storage rates can limit the bandwidth and hence sensitivity of the system—as has been the case with early development at the Parkes Testbed facility.

The ability to store raw data and perform correlations and beamforming off-line, however, as an adjunct to the real time system is highly recommended. Such an approach allows beamforming weights to be determined after the measurement and so many different weightings can be evaluated. It also reduces the impact of gain drift, as the same data used for the measurement can be used for calculating the weights. The availability of simultaneous off-line and real-time beamforming allows the operation of the real-time system to be confirmed with bit-perfect emulation. Other FPA development programs have implemented off-line processing prior to employing real-time systems [4, 6, 164, 209].

The measurement program demonstrated two weighting cases, the normalized conjugate match and the maximum sensitivity weightings. These were compared with the central element of the beamformed subarray. Two different 21 element subarrays were used, one in the centre and the other at the edge of the 64 elements of the FPA. The evaluations of the FPA included radiation pattern measurements and gain and noise measurements.

The analysis explained the measurements in terms of the reflector, an estimate of the FPA noise performance and FPA beamforming behaviour. The ability of FPAs to reduce coma aberration, correct defocussing and correct pointing errors was demonstrated. The measurement program also demonstrated the ability of the beamforming algorithm to adjust to the failure of elements.

The explicit calculation and analysis of uncertainties greatly enhanced the interpretation of the measurements and indicated the most important areas for improving measurement accuracy. For instance, while the on-off source single dish measurement was needed for the absolute G/T determination, a more accurate relative G/T measure was obtained using the interferometry results.

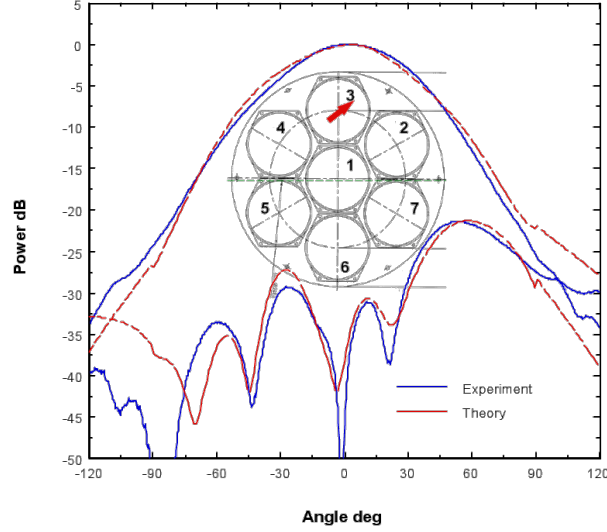


Figure 9.1 – Example of a horn feed pattern. This is the horizontal plane radiation pattern of horn 3 at 1.27 GHz of the seven element test array for the Parkes 21 cm multibeam receiver. The red arrow shows the polarization of the feed. From Bird and Hayman [96].

9.2.1 Characterization of Dense FPAs Compared with Single Feeds and Discrete FPAs

The characterization of dense FPAs is substantially more demanding than discrete FPAs or single feeds. The challenges of modelling dense FPAs, with a large number of electrically small structures and close interaction with the LNAs, have been discussed in Section 4.1. Measurements are also more difficult and time consuming.

The embedded element patterns of dense FPAs, compared to single feeds and discrete FPAs, tend to be less smooth, wider and have greater rearward radiation, i.e. for $|\theta| > 90^\circ$. For example, compare the Vivaldi element pattern, Fig. 6.5, with the element of a multibeam horn feed, Fig. 9.1. Even though these effects may be minimized by beamforming, to adequately predict and understand the final performance they should be characterized. Measuring these wide radiation patterns requires greater attention to range reflections and mounting arrangements than for the more directive patterns of horn feeds. Ideally the elements will be terminated with the LNAs they will use in service. This adds power and, in the case of the ASKAP feed package, water cooling requirements, to the measurement setup.

A single feed has one, or if dual polarized, two ports and so only two radiation patterns and two sensitivity measurements are required. A discrete FPA multiplies this effort by the number of elements. A dense FPA, on the other hand, not only has many more ports than a discrete FPA¹ (with the same aperture diameter) but there is a range of possible beamforming weightings.

Measuring the noise performance of a dense FPA is typically more difficult than for single and discrete FPA feeds. Feed noise performance is usually determined using the power ratio, or Y-factor, measured from hot and cold loads presented to the feed. With a dense FPA this requires a more elaborate setup as, if taking the elements singly, the embedded-element patterns are generally wider than horn patterns and if beamformed, the full receiver and beamformer is required.

A sheet of microwave absorber and the sky are usually used as the hot and cold loads for the Y-factor measurement as shown in Fig. 9.2. The wider radiation patterns of the dense FPA require a larger hot load and the consideration of radiation from the ground impinging on the cold load measurements. The ground radiation can be reduced by using a shield, as done by ASTRON and Brigham Young University/NRAO [135].

Beamforming is needed for the noise measurement to account for the interactions between the FPA elements. It also has the effect of narrowing the beam and so the ground radiation pattern is less of an issue. Establishing the beamforming weights, however, poses another problem. These measurements are most conveniently done before the feed is mounted in the reflector and so the weights need to be determined either from modelling or some other approximation to what they will be when in the reflector. One empirical approach is to beamform on a small antenna mounted above the feed. However, this has the disadvantage that the array weighting is substantially different from weighting it will have in the dish. Nonetheless, if the full covariance matrix is recorded for the hot and cold loads, the noise performance for any weighting can be calculated later from these data. Thus, once the weightings in the dish are determined, they can be applied retrospectively to the ground Y-factor data.

¹Note that most FPA designs have two planes of symmetry reducing the number of unique elements to about a quarter of the total or for two polarizations, an eighth of the total. This can be taken advantage of in both discrete and dense FPA measurement programs.



Figure 9.2 – Y-factor Measurement of a prototype FPA. The absorber sheet is mounted in the box above the array. The hot load can be wheeled off the array for the cold-sky measurement. The array under test is a prototype for the ASKAP project.

The increased complexity of dense FPAs has required the adaptation of established measurement techniques. These methods could be further revised, particularly as the uncertainties involved are reviewed.

9.2.2 Recommendations for FPA Characterization

In addition to the measurements demonstrated in this thesis, it is recommended that FPA characterization programs include more extensive pattern cuts and, if possible, these be taken on a two dimensional grid. The characterization of the FPA without the reflector should also be given more emphasis than it has in this project. This should include embedded element radiation patterns and noise temperature measurements.

There are also two sensitivity measurement techniques that warrant further investigation.

1. A similar approach to the single dish on-off-source Y-factor technique is to use correlation coefficients from an interferometer measured on a source compared to the single dish responses measured off the source [310, 323]. This requires either the sensitivity of the second dish to be characterized or at least three antennas to be used. The technique is particularly effective in the measurements at the Parkes Testbed Facility where the very sensitive and well characterized 64m dish is used as the reference for the 12m FPA equipped dish. Using an array such as the WSRT² or ASKAP can also provide this sensitivity.
2. The variance of correlation coefficients from an interferometer can be used as a measure of the relative sensitivity of different weightings. In this case the interferometer is set to track a source and the variance of the correlation coefficients from a number of integration samples is calculated [324]. Extracting the sensitivity of one of the arms of the interferometer requires the other arm to either be identical or characterized beforehand. The sensitivity of the antenna in question can then be determined using the analysis in Crane and Napier [29] or Thompson et al. [13, Sec. 6.2]. A similar approach is to use at the dynamic range of the fringe-rate vs. delay amplitude image for a point source (top right in Fig. 6.31) [325]. These techniques have the advantage that they provide continuous sensitivity measures. These

²Westerbork Synthesis Radio Telescope, the Netherlands.

measures are also more sensitive to some of the system artefacts such as cross talk and as such may be more representative of the sensitivity impact on the SNR of the synthesized image. The inclusion of these artefacts can also obscure the sensitivity of the antenna under study and may therefore be more suitable as an indicator for overall system performance rather than for studying the sensitivity of an individual antenna.

FPA characterization techniques will undoubtedly continue to be developed and refined with the high level of current activity in the field.

9.3 FPA Systems

With the development of two dense FPA radiotelescopes, ASKAP and Aperitif,³ well underway and others under consideration, FPA system design has progressed significantly in recent years. There are, however, a number of areas that would benefit from further research and development. The motivations for this further work are chiefly in enhancing ASKAP and Aperitif, the potential FPAs have for the SKA and for retrofitting large reflector radio telescopes.

9.3.1 Calibration

The balance between tracking and compensating element drift and recalculating weights from scratch is also an area of research [277]. The use of celestial sources in the field-of-view is another possible approach to tracking element drift. It is suggested that for most pointings of an array like ASKAP, there may be enough sources of sufficient strength to calibrate the beams and possibly individual elements [275, 326]. There is also significant overlap between the methods for FPAs and low frequency arrays such as LOFAR⁴ and MWA⁵ [327–330]. The design of systems for measuring the element drift is also an area currently being studied [276].

³Aperture tile in focus, see Section 2.6.4.

⁴The Low Frequency Array in the Netherlands.

⁵The Murchison Widefield Array in Western Australia.

9.3.2 Reflector Design

The ability of an FPA to correct for surface errors as discussed in Section 2.5.1 opens possibilities for substantially reducing reflector cost. Some of these are listed below.

- A reflector support structure is not only required to have sufficient strength to support the reflector and feed but also have sufficient rigidity to prevent deformation from gravity and wind. The cost of the structure may be reduced if the rigidity tolerance were less stringent. Deformation with gravity could be compensated with predicted perturbations or infrequently re-calculated weights. Deformation with wind, on the other hand, would require a more dynamic solution.
- A lower tolerance to random surface errors may reduce manufacturing costs for the reflector.
- A lower tolerance to systematic surface errors may simplify the construction. For instance the reflector could be made from panels curved in only one direction rather than two as is usually the case. The umbrella reflector is such an example. It is used in spacecraft antennas as it can be made deployable [331, 332] but it may also be less costly to manufacture for ground based antennas.

9.3.3 FPA Elements

As outlined in Section 2.6.2, the Vivaldi and chequerboard arrays have received the most attention as elements for dense FPAs for radiotelescopes. There is certainly scope for further development of the relatively recently developed chequerboard array. The Vivaldi array is a far more mature design but improvements will undoubtedly be made. The areas for improvement are chiefly in extending the bandwidth and the efficiency of the match to the incoming radiation. The co-optimization of the array and first low noise amplifier (LNA) design is an important feature of the design process. Other structures may be superior to both the chequerboard and Vivaldi and the process of investigating them, although difficult, is becoming more tractable with recent electromagnetic modelling improvements.

The single embedded element patterns are important even though it is the beamformed feed pattern that is required to efficiently illuminate the reflector. The embedded patterns impact the design, however, particularly

at the top of the band where only a few elements receive most of the energy and hence are highly weighted for a given pointing direction. In this situation there is less freedom to correct a poor embedded pattern. Equivalently, inefficiently illuminating elements require a closer spacing than efficiently illuminating ones. The consequence of a closer spacing is a higher element count which increases the receiver and beamformer cost. More closely spaced elements generally have higher mutual coupling leading to a higher sensitivity of the impedance and radiation patterns to the surrounding elements.

Wideband dense FPAs are generally more likely to suffer from out of band reception than the traditionally used horn feeds. Horns have an in-built high-pass filter created by the waveguide cut-off. This natural filter is absent from the wideband dense FPA elements such as the chequerboard, Vivaldi and dipole. Placing additional filters before the LNA is usually impractical because of the impact on noise. Therefore, even in a location that is radio quiet in the operational band, care also needs to be taken to ensure any out of band interference does not produce significant distortion products in the operational band.

Another factor that may make dense FPAs more susceptible to interference is the typically wider radiation embedded element patterns than single feeds and discrete FPAs. Even though the beamformed FPA feed pattern may have minimal spillover, it is the signals from each element that is typically digitized. Therefore, if the dynamic range in the signal processing is insufficient, the interference would not be cancelled by beamforming.

9.3.4 Receiver Chains

One of the issues that have been under consideration in FPA system design is the location of the key components in the signal path. Using ASKAP as an example, 188 signals need to be transported from the array to the down-converter at radio frequency. From there these signals are transported to the digitizer then to the beamformer. The current design uses coaxial cable to bring these signals the 40 m from the reflector focus to the antenna pedestal. The constraints on the cable weight and diameter result in a relatively thin cable, with its inherent loss, being used.

Options for overcoming these constraints include (1) transporting the signals on optical fibre at radio frequency (RF); (2) down converting the signal at the focus; and (3) digitising at the focus [180]. ‘RF over fibre’ is

attractive because optical fibre has much lower loss per unit length, is lighter and is less bulky than coaxial cable. Recent developments have lowered the cost of optical transmission and reception equipment and it is currently under investigation at CSIRO. A 40 element prototype for ASKAP used down conversion at the focus [310]. This allowed the signal to be transported at a much lower frequency and hence lower loss. The challenges of doing this with an FPA the size of the full ASKAP array include cooling and the physical constraints, particularly weight, of the focus package. The third option of digitizing at the focus and transporting the digital signals on optical fibres requires very compact receivers such as the ‘receiver on a chip’ development by Jackson et al. [333, 334]. Digitizing at RF without down conversion has also been considered and may become more amenable as semiconductor device speeds increase.

The digital signal processing requirements for beamforming and correlation for dense FPA based telescopes is substantial—for ASKAP it is over 10^{15} arithmetic operations per second [180]. Four mainstream technologies present themselves as possible solutions [335]. These are central processor units (CPUs), graphical processor units (GPUs), field-programmable gate arrays (FPGAs) and application specific integrated circuits (ASICs). These options are in rough order of increasing non-recurring engineering design costs, decreasing per unit costs in high volumes and decreasing power consumption. A confounding factor in making a choice is the continual improvement in the technology available. By the time a solution is engineered in a less flexible option, new technology in one of the more flexible options will possibly be superior. Examples of choices taken are LOFAR⁶ which uses a cluster of CPU based machines [336, 337] and ASKAP which uses FPGAs [180]. ASICs are a serious consideration for the SKA with its far larger scale.

9.4 Summary

At the time of writing, dense FPAs designs are maturing. They are currently showing system temperatures of less than 70 K and instantaneous bandwidths of 300 MHz, with the capability for instantaneous fields of view of

⁶The *LOW Frequency ARray*, a phased-array radio telescope located in the Netherlands, operating at 20–240 MHz. Although this is not an FPA based telescope the signal processing is not dissimilar.

30 beam-areas or more. As these systems are refined and deployed, they are expected to demonstrate a technology capable of revolutionizing centimetre-band radio astronomy.

The NTD Interferometer was an important step on the way, demonstrating real time digital beamforming for the first time on an FPA equipped radiotelescope. The author's work described in this thesis refined and stabilized the performance of the instrument allowing the demonstration of the maximum sensitivity weighting. The performance of the FPA system was comprehensively analysed and the theory behind the beamforming was fully explained. The FPA size calculations provide a design tool for future FPA based radiotelescopes such as that proposed for the SKA.

Appendix A

Focal Plane Array Size Results

Results from the calculations in Chapter 3 are displayed and listed in this appendix. All of the focal plane radii, R , are shown in terms of wavelength.

A.1 Focal Plane Power Plots

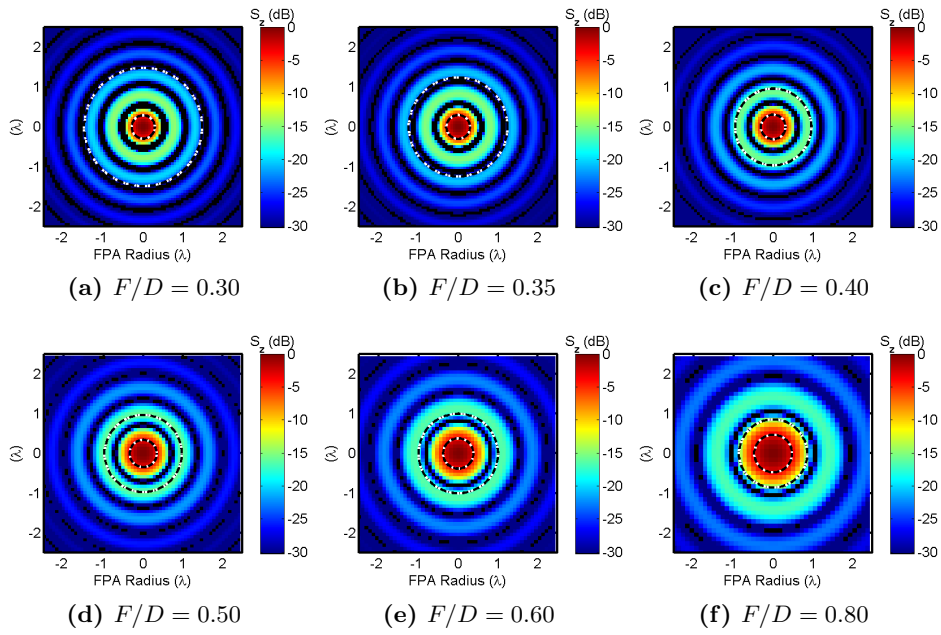


Figure A.1 – Focal plane power, $D = 70.0$, $F/D = 0.3$ to 0.8 , $\theta_s = 00.00^\circ$.

A. Focal Plane Array Size Results

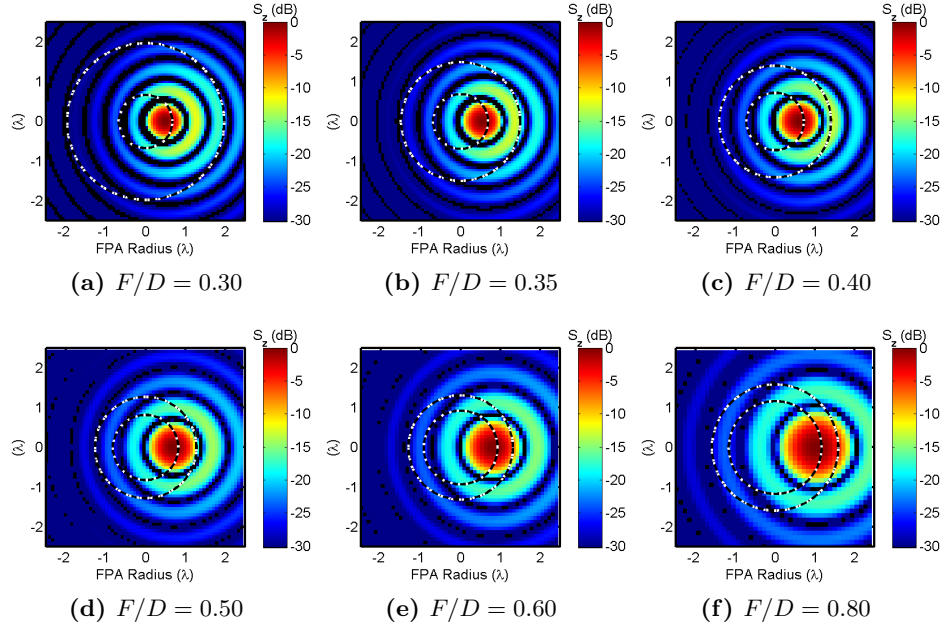


Figure A.2 – Focal plane power, $D = 70.0$, $F/D = 0.3$ to 0.8 , $\theta_s = 01.00^\circ$.

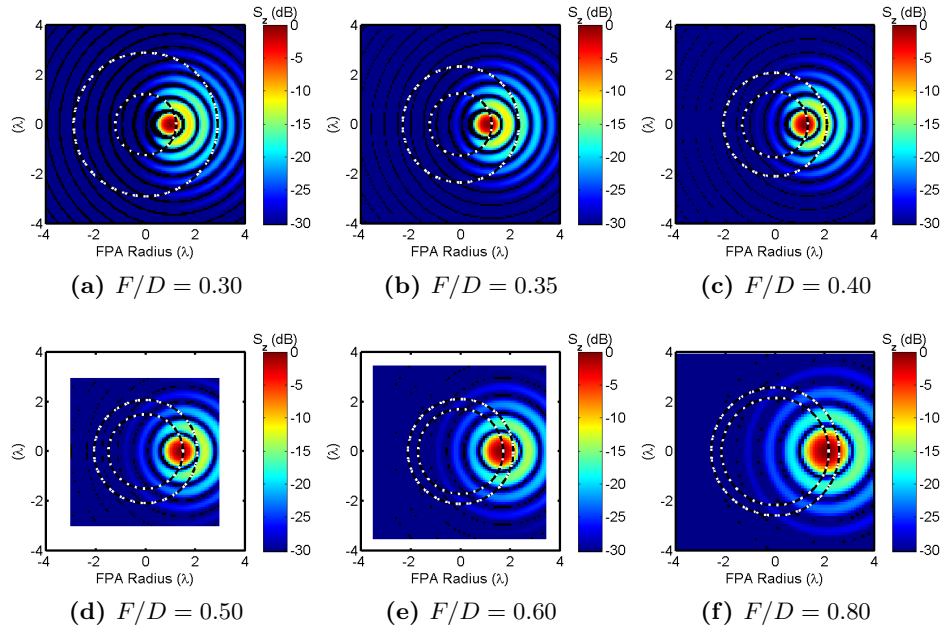


Figure A.3 – Focal plane power, $D = 70.0$, $F/D = 0.3$ to 0.8 , $\theta_s = 02.00^\circ$.

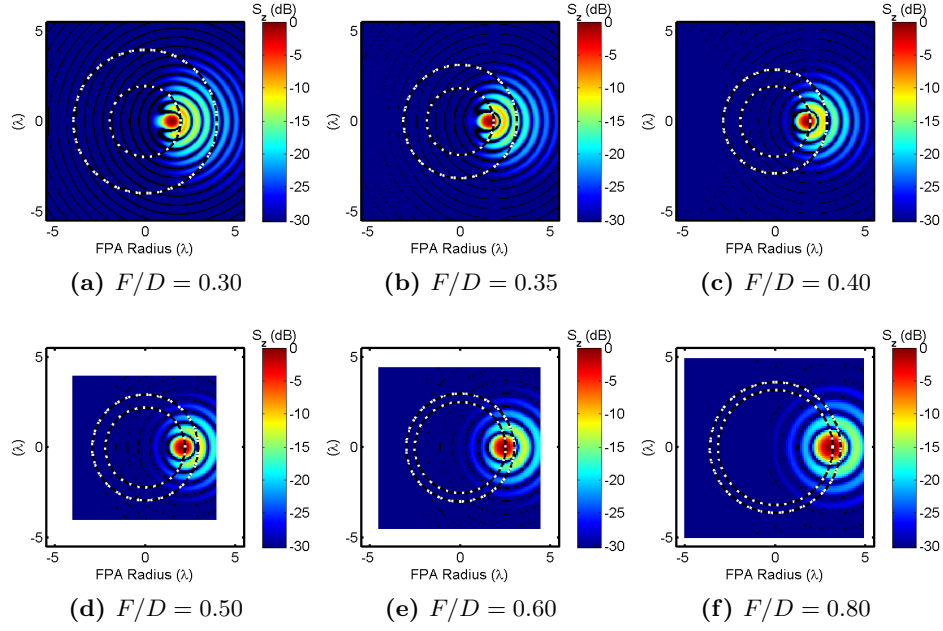


Figure A.4 – Focal plane power, $D = 70.0$, $F/D = 0.3$ to 0.8 , $\theta_s = 03.00^\circ$.

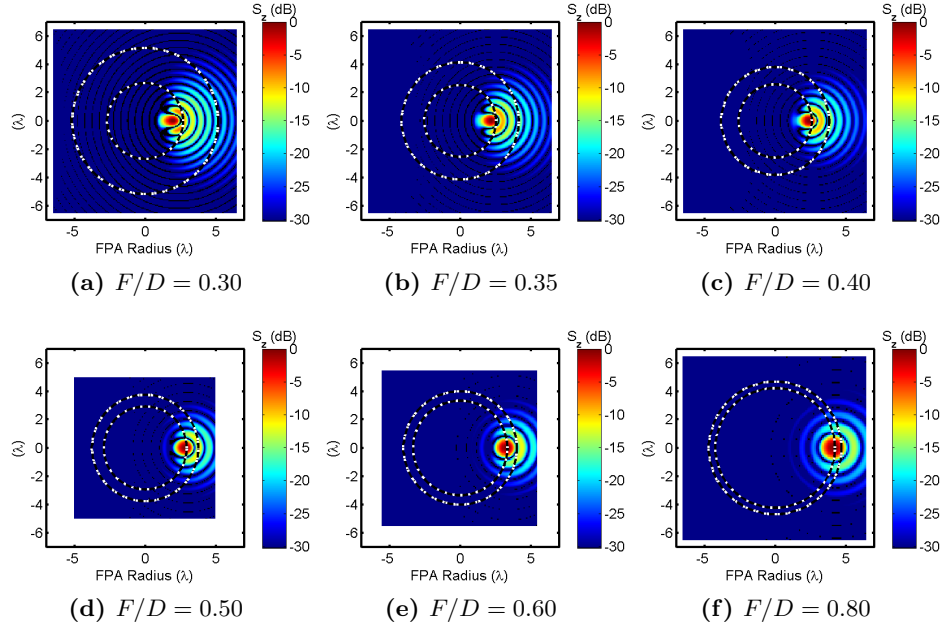


Figure A.5 – Focal plane power, $D = 70.0$, $F/D = 0.3$ to 0.8 , $\theta_s = 04.00^\circ$.

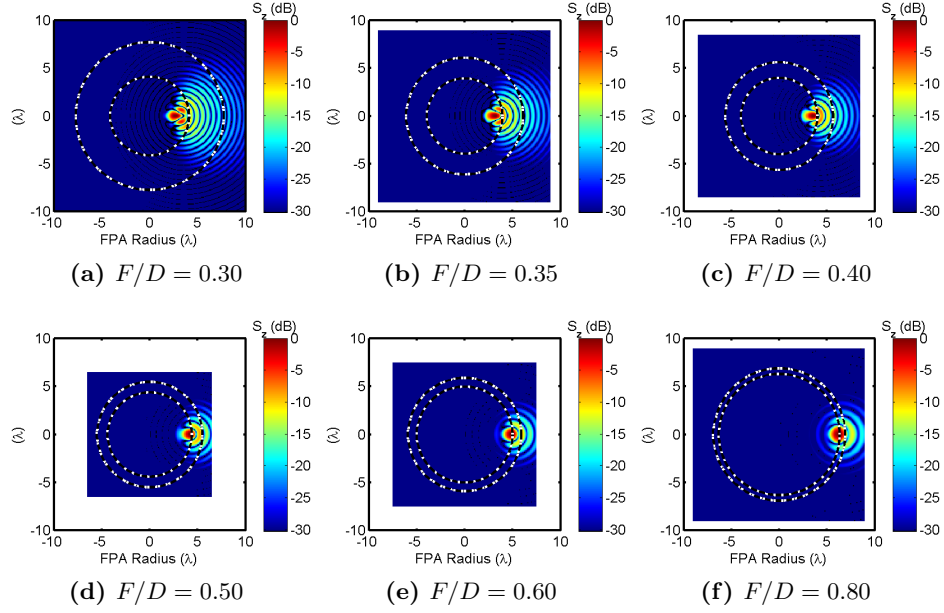


Figure A.6 – Focal plane power, $D = 70.0$, $F/D = 0.3$ to 0.8 , $\theta_s = 06.00^\circ$.

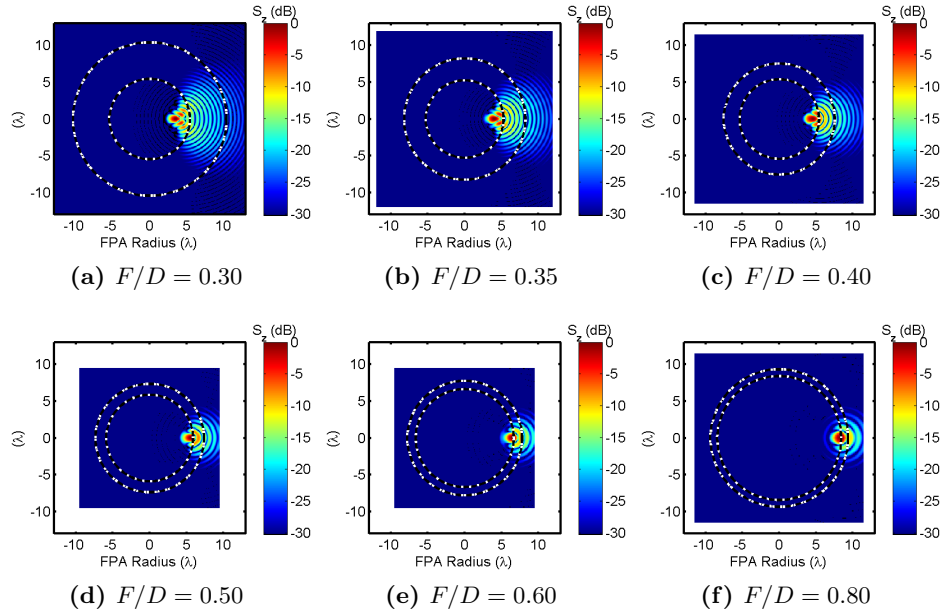


Figure A.7 – Focal plane power, $D = 70.0$, $F/D = 0.3$ to 0.8 , $\theta_s = 08.00^\circ$.

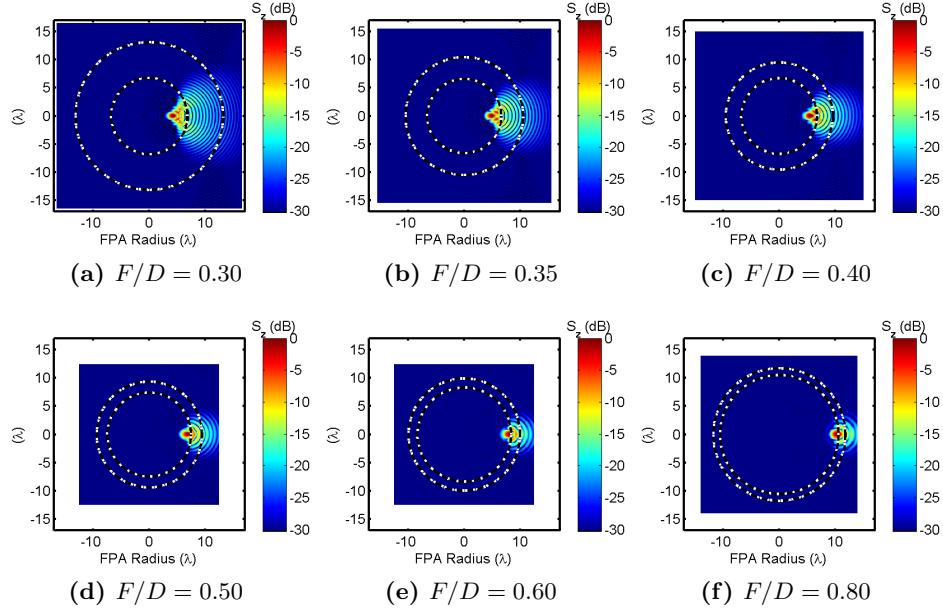


Figure A.8 – Focal plane power, $D = 70.0$, $F/D = 0.3$ to 0.8 , $\theta_s = 10.00^\circ$.

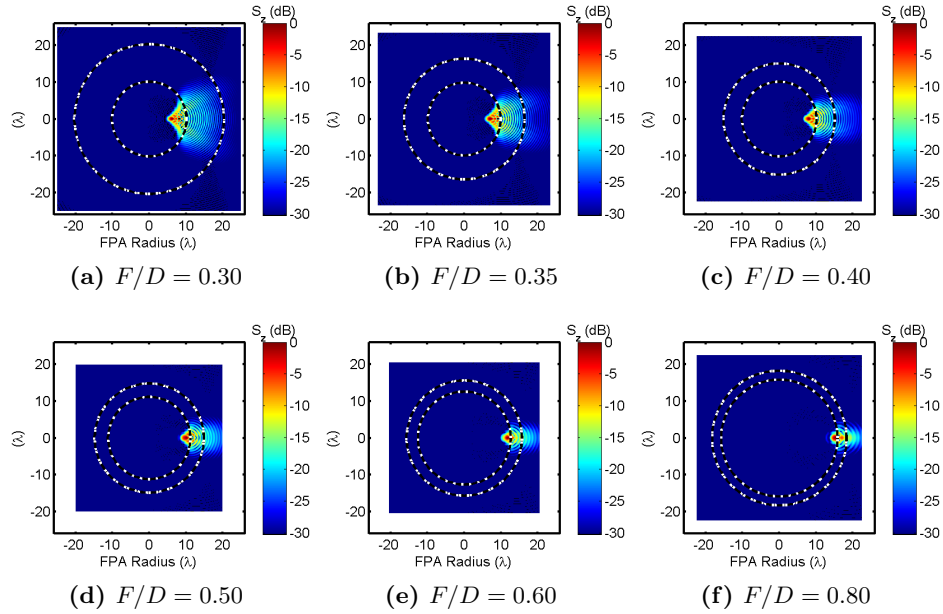


Figure A.9 – Focal plane power, $D = 70.0$, $F/D = 0.3$ to 0.8 , $\theta_s = 15.00^\circ$.

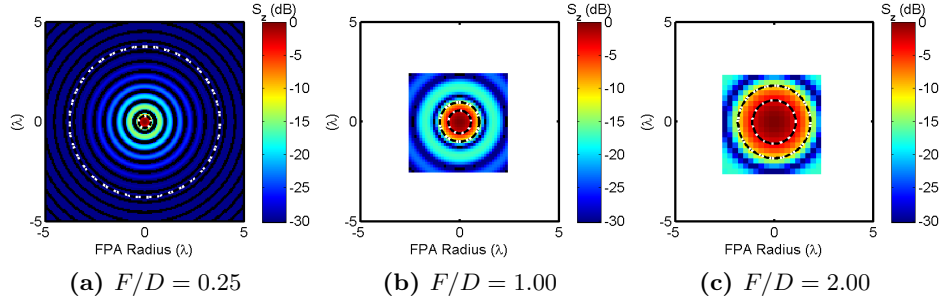


Figure A.10 – Focal plane power, $D = 70.0$, $F/D = 0.25, 1, 2$, $\theta_s = 00.00^\circ$.

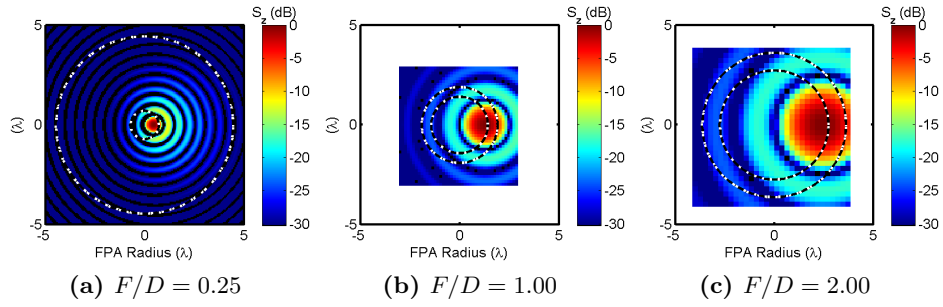


Figure A.11 – Focal plane power, $D = 70.0$, $F/D = 0.25, 1, 2$, $\theta_s = 01.00^\circ$.

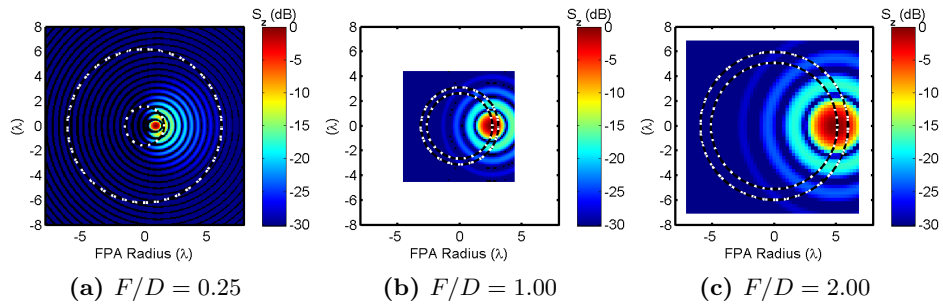


Figure A.12 – Focal plane power, $D = 70.0$, $F/D = 0.25, 1, 2$, $\theta_s = 02.00^\circ$.

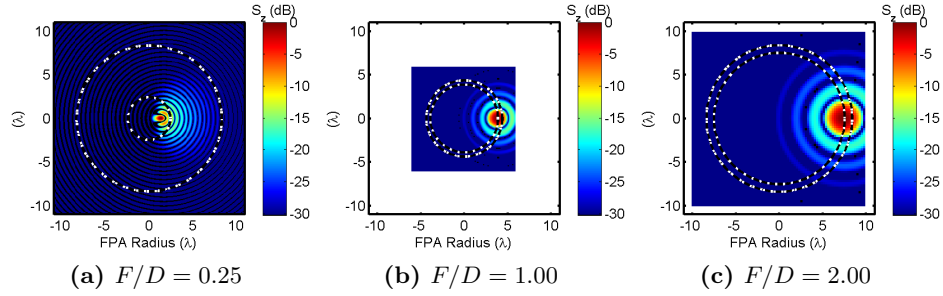


Figure A.13 – Focal plane power, $D = 70.0$, $F/D = 0.25, 1, 2$, $\theta_s = 03.00^\circ$.

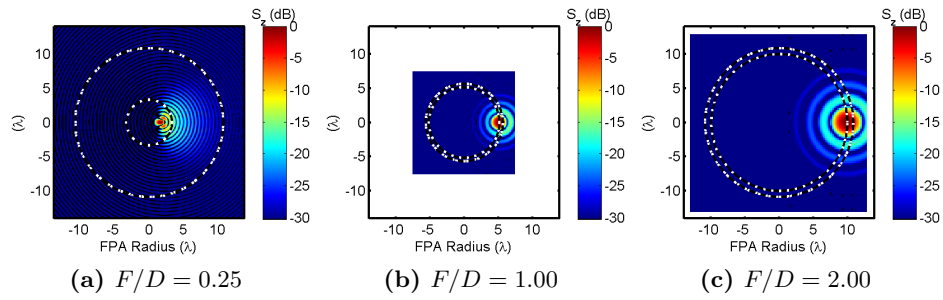


Figure A.14 – Focal plane power, $D = 70.0$, $F/D = 0.25, 1, 2$, $\theta_s = 04.00^\circ$.

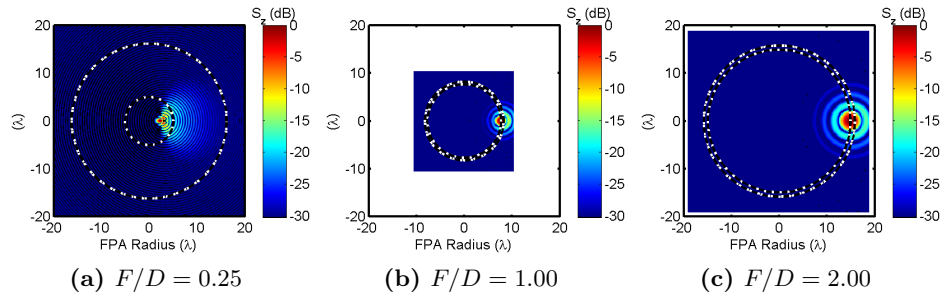


Figure A.15 – Focal plane power, $D = 70.0$, $F/D = 0.25, 1, 2$, $\theta_s = 06.00^\circ$.

A. Focal Plane Array Size Results

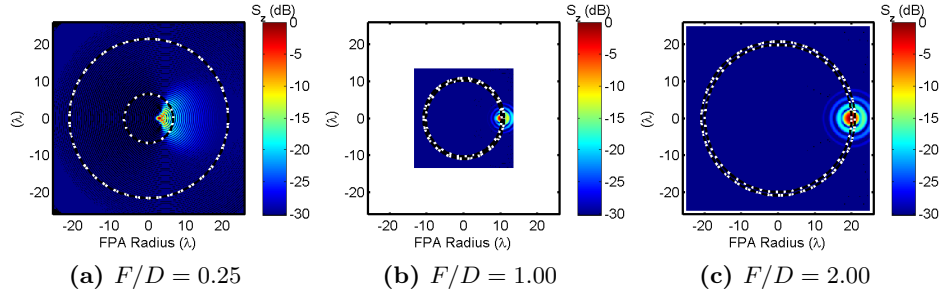


Figure A.16 – Focal plane power, $D = 70.0$, $F/D = 0.25, 1, 2$, $\theta_s = 08.00^\circ$.

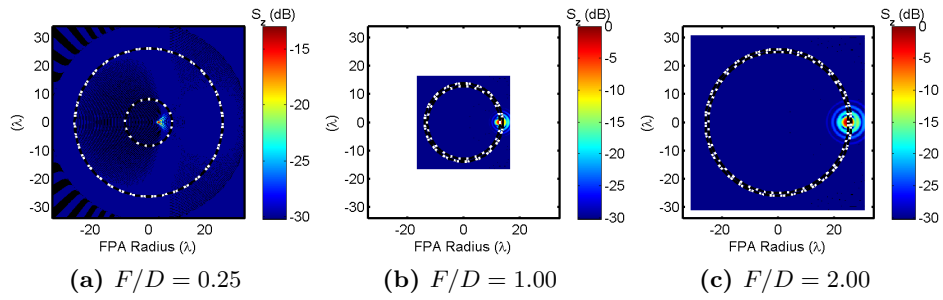


Figure A.17 – Focal plane power, $D = 70.0$, $F/D = 0.25, 1, 2$, $\theta_s = 10.00^\circ$.

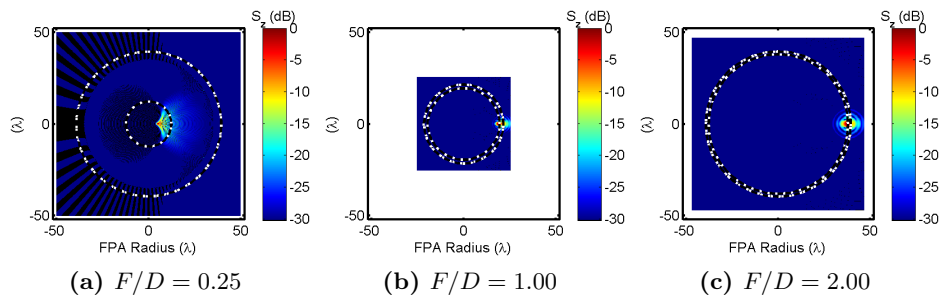


Figure A.18 – Focal plane power, $D = 70.0$, $F/D = 0.25, 1, 2$, $\theta_s = 15.00^\circ$.

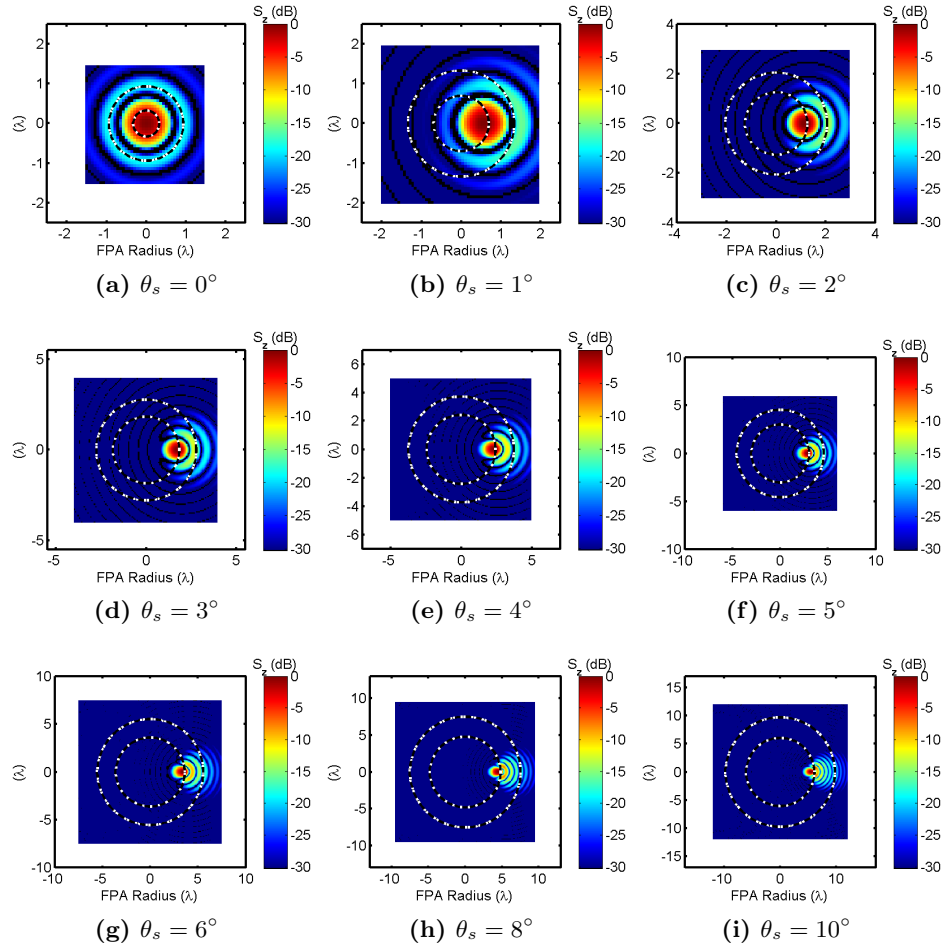


Figure A.19 – Focal plane power, tapered aperture, $D = 70.0$, $F/D = 0.4$.

A.2 FPA Size

The radii, R , in terms of wavelength, calculated from the integration of the focal plane power are listed in Table A.1 for a dish diameter $D = 70\lambda$ and Table A.2 for other diameters. For $D = 70\lambda$, the scan angle, θ_s , is equivalent to the nominal half power beamwidth θ_{HPBW} from (3.1). For the other dish diameters the scan angle in terms of half power beamwidths has been shown (Table A.2) for comparison between dish sizes. In a few cases the area of the focal plane evaluated was too small to capture enough of the power to reach $\eta_{\text{enc}} = 79\%$ of the total—they are represented as *not a number* (NaN).

Table A.1 – FPA radii for $D = 70\lambda$.

D	F/D	$\theta_s(^{\circ})$	$R_{\eta=79\%}$	$R_{\eta=50\%}$	D	F/D	$\theta_s(^{\circ})$	$R_{\eta=79\%}$	$R_{\eta=50\%}$
70	0.25	0.00	3.79	0.31	70	0.50	3.57	3.41	2.63
70	0.25	1.00	4.47	0.72	70	0.50	4.00	3.76	2.94
70	0.25	2.00	6.21	1.57	70	0.50	6.00	5.50	4.40
70	0.25	3.00	8.37	2.46	70	0.50	8.00	7.39	5.90
70	0.25	3.57	9.76	2.94	70	0.50	10.00	9.40	7.46
70	0.25	4.00	10.88	3.35	70	0.50	15.00	14.89	11.22
70	0.25	6.00	16.23	5.06	70	0.50	20.00	17.18	14.02
70	0.25	8.00	21.58	6.66	70	0.60	0.00	1.01	0.39
70	0.25	10.00	26.27	8.32	70	0.60	1.00	1.32	0.93
70	0.25	15.00	39.41	12.31	70	0.60	2.00	2.12	1.72
70	0.30	0.00	1.49	0.30	70	0.60	3.00	3.01	2.53
70	0.30	1.00	1.98	0.67	70	0.60	3.57	3.57	3.00
70	0.30	2.00	2.91	1.24	70	0.60	4.00	4.02	3.35
70	0.30	3.00	3.99	1.98	70	0.60	6.00	5.92	5.01
70	0.30	3.57	4.70	2.40	70	0.60	8.00	7.80	6.67
70	0.30	4.00	5.17	2.69	70	0.60	10.00	9.96	8.35
70	0.30	5.00	6.47	3.38	70	0.60	15.00	15.71	12.66
70	0.30	6.00	7.74	4.13	70	0.60	20.00	18.56	16.10
70	0.30	8.00	10.44	5.47	70	0.80	0.00	0.86	0.48
70	0.30	10.00	13.16	6.80	70	0.80	1.00	1.60	1.17
70	0.30	12.00	15.89	8.19	70	0.80	2.00	2.59	2.17
70	0.30	15.00	20.38	10.19	70	0.80	3.00	3.63	3.20
70	0.30	20.00	34.58	13.52	70	0.80	3.57	4.24	3.79
70	0.35	0.00	1.25	0.30	70	0.80	4.00	4.70	4.24
70	0.35	1.00	1.50	0.69	70	0.80	6.00	6.91	6.33
70	0.35	2.00	2.35	1.26	70	0.80	8.00	9.38	8.44
70	0.35	3.00	3.15	1.87	70	0.80	10.00	11.77	10.57
70	0.35	3.57	3.75	2.24	70	0.80	15.00	18.34	15.90
70	0.35	4.00	4.15	2.54	70	1.00	0.00	1.00	0.58
70	0.35	6.00	6.11	3.96	70	1.00	1.00	1.92	1.43
70	0.35	8.00	8.26	5.28	70	1.00	2.00	3.13	2.65
70	0.35	10.00	10.49	6.63	70	1.00	3.00	4.39	3.90
70	0.35	15.00	16.46	9.93	70	1.00	3.57	5.12	4.62
70	0.40	0.00	0.97	0.31	70	1.00	4.00	5.67	5.17
70	0.40	1.00	1.41	0.73	70	1.00	6.00	8.27	7.73
70	0.40	2.00	2.09	1.33	70	1.00	8.00	10.97	10.31
70	0.40	3.00	2.89	1.96	70	1.00	10.00	13.90	12.91
70	0.40	3.57	3.46	2.32	70	1.00	15.00	21.53	19.49
70	0.40	4.00	3.82	2.60	70	1.00	20.00	26.25	25.07
70	0.40	5.00	4.65	3.28	70	2.00	0.00	1.83	1.10
70	0.40	6.00	5.65	4.01	70	2.00	1.00	3.64	2.75
70	0.40	8.00	7.56	5.42	70	2.00	2.00	5.98	5.11
70	0.40	10.00	9.56	6.74	70	2.00	3.00	8.41	7.54
70	0.40	15.00	15.17	10.18	70	2.00	3.57	9.81	8.94
70	0.40	20.00	23.20	13.59	70	2.00	4.00	10.87	10.00
70	0.50	0.00	0.98	0.35	70	2.00	6.00	15.84	14.95
70	0.50	1.00	1.28	0.82	70	2.00	8.00	20.89	19.96
70	0.50	2.00	2.09	1.51	70	2.00	10.00	26.02	25.02
70	0.50	3.00	2.94	2.22	70	2.00	15.00	39.51	37.98
					70	2.00	20.00	54.70	51.56

Table A.2 – FPA radii for $D = 10, 20, 30, 140\lambda$.

D	F/D	$\theta_s(^{\circ})$	θ_{BW}	$R_{\eta=79\%}$	$R_{\eta=50\%}$
10	0.25	0.00	0.00	3.28	0.31
10	0.25	28.00	4.00	NaN	3.06
10	0.40	0.00	0.00	0.97	0.31
10	1.00	0.00	0.00	1.00	0.58
20	0.25	0.00	0.00	3.73	0.31
20	0.40	0.00	0.00	0.97	0.31
20	1.00	0.00	0.00	1.00	0.58
30	0.30	0.00	0.00	1.49	0.30
30	0.30	4.67	2.00	2.92	1.24
30	0.30	9.33	4.00	5.34	2.68
30	0.30	14.00	6.00	8.30	4.08
30	0.30	18.67	8.00	12.92	5.37
30	0.30	23.33	10.00	26.30	6.71
30	0.30	28.00	12.00	NaN	8.00
30	0.30	35.00	15.00	NaN	9.82
30	0.40	16.33	7.00	7.31	4.72
35	0.25	0.00	0.00	3.78	0.31
35	0.25	8.00	4.00	10.71	3.33
35	0.40	0.00	0.00	0.97	0.31
35	0.40	8.00	4.00	3.87	2.60
35	1.00	0.00	0.00	1.00	0.58
35	1.00	8.00	4.00	5.72	5.19
140	0.25	0.00	0.00	3.80	0.31
140	0.25	2.00	4.00	10.92	3.37
140	0.40	0.00	0.00	0.97	0.31
140	0.40	2.00	4.00	3.81	2.60
140	1.00	0.00	0.00	1.00	0.58
140	1.00	2.00	4.00	5.65	5.16

Table A.3 – Focal plane array radii for the tapered aperture and comparison with the uniform aperture. See Sections 3.6.1 and 3.8.4. $D = 70\lambda$ and $F/D = 0.4$.

D/λ	$\theta_s(^{\circ})$	R_{taper} ($\eta_{\text{enc}} = 79\%$)	R_{taper} ($\eta_{\text{enc}} = 50\%$)	$R_{\text{taper}} - R_{\text{uniform}}$ ($\eta_{\text{enc}} = 79\%$)	$R_{\text{taper}} - R_{\text{uniform}}$ ($\eta_{\text{enc}} = 50\%$)
70	0.00	0.94	0.33	−0.03	0.02
70	1.00	1.34	0.70	0.06	−0.01
70	2.00	2.06	1.27	0.26	−0.02
70	3.00	2.79	1.85	−0.10	−0.11
70	3.57	3.28	2.18	0.42	−0.03
70	4.00	3.74	2.44	−0.08	−0.17
70	5.00	4.57	3.03		
70	6.00	5.55	3.62	0.98	−0.06
70	8.00	7.55	4.82	−0.02	−0.60
70	10.00	9.76	6.08	0.21	−0.66
70	15.00	17.80	9.24	2.62	−0.94

Appendix B

Mathematical Relationships

This appendix contains mathematical relationships and proofs used in the thesis. Matrices are represented by upper case bold characters **A** and vectors by lower case bold characters **a**.

B.1 Matrix Formulation of the Overlap Integral

Let **x** and **u** be column vectors with **u** a function of t . Consider the following expression:

$$\int \left| \sum_i x_i u_i \right|^2 dt.$$

By reversing the order of summation and integration, we can express this in matrix form:

$$\begin{aligned} \int \left| \sum_i x_i u_i \right|^2 dt &= \int \left(\sum_i x_i u_i \right)^* \left(\sum_i x_i u_i \right) dt \\ &= \int \left(\sum_i x_i^* u_i^* \right) \left(\sum_i x_i u_i \right) dt \\ &= \int \mathbf{x}^H \mathbf{u}^* \mathbf{u}^T \mathbf{x} dt \\ &= \mathbf{x}^H \int \mathbf{u}^* \mathbf{u}^T dt \mathbf{x} \\ &= \mathbf{x}^H \mathbf{U} \mathbf{x} \end{aligned} \tag{B.1}$$

where

$$[\mathbf{U}]_{mn} = \int u_i^* u_n dt. \tag{B.2}$$

When no integration is involved this simplifies to:

$$\left| \sum_i x_i u_i \right|^2 = \mathbf{x}^H \mathbf{u}^* \mathbf{u}^T \mathbf{x} = \mathbf{x}^H \mathbf{U} \mathbf{x} \quad (\text{B.3})$$

where

$$[\mathbf{U}]_{ij} = u_i^* u_j.$$

B.2 Spectral Decomposition Theorem

We use the spectral decomposition theorem in this work and it is stated here for convenience:

For any normal matrix \mathbf{A} (i.e. $\mathbf{A}^H \mathbf{A} = \mathbf{A} \mathbf{A}^H$) there exists a matrix $\mathbf{\Gamma}$ that is unitary (i.e. $\mathbf{\Gamma}^H = \mathbf{\Gamma}^{-1}$), whose columns contain the eigenvalues of \mathbf{A} , and a diagonal matrix $\mathbf{\Lambda}$ of eigenvalues where

$$\mathbf{A} = \mathbf{\Gamma} \mathbf{\Lambda} \mathbf{\Gamma}^H.$$

B.3 Square Root of a Normal Matrix

Given a normal matrix \mathbf{A} we can define a matrix \mathbf{B} such that $\mathbf{B} \mathbf{B} = \mathbf{A}$. The spectral decomposition theorem can be used to show this matrix exists:

Proof: As \mathbf{A} is normal, we can perform a spectral decomposition on it: $\mathbf{A} = \mathbf{\Gamma} \mathbf{\Lambda}_A \mathbf{\Gamma}^H$ where $\mathbf{\Gamma}$ is unitary and $\mathbf{\Lambda}_B$ is a diagonal matrix of eigenvalues:

$$\mathbf{\Lambda}_A = \begin{bmatrix} \lambda_{A1} & \cdots & 0 \\ \vdots & \ddots & \vdots \\ 0 & \cdots & \lambda_{AN} \end{bmatrix}.$$

Let $\lambda_{Bn} = \sqrt{\lambda_{An}}$, $n = 1 \dots N$ and define

$$\mathbf{\Lambda}_B = \begin{bmatrix} \lambda_{B1} & \cdots & 0 \\ \vdots & \ddots & \vdots \\ 0 & \cdots & \lambda_{BN} \end{bmatrix}.$$

Let $\mathbf{B} = \mathbf{\Gamma}\mathbf{\Lambda}_B\mathbf{\Gamma}^H$. Then

$$\begin{aligned}\mathbf{B}\mathbf{B} &= \mathbf{\Gamma}\mathbf{\Lambda}_B\mathbf{\Gamma}^H\mathbf{\Gamma}\mathbf{\Lambda}_B\mathbf{\Gamma}^H \\ &= \mathbf{\Gamma}\mathbf{\Lambda}_B\mathbf{\Lambda}_B\mathbf{\Gamma}^H \\ &= \mathbf{\Gamma}\mathbf{\Lambda}_A\mathbf{\Gamma}^H \\ &= \mathbf{A}\end{aligned}$$

\mathbf{B} is written as $\mathbf{A}^{1/2}$. ■

This can be extended to $\mathbf{A}^{1/k}$ by changing $\lambda_{Bn} = \sqrt{\lambda_{An}}$ to $\lambda_{Bn} = \sqrt[k]{\lambda_{An}}$. In multiplying out \mathbf{B}^k , the same cancellation occurs to arrive at \mathbf{A} .

If \mathbf{A} is positive semidefinite, the eigenvalues are real and zero or greater and so $\mathbf{A}^{1/n}$ is unique.

B.4 Hermitian Form Maximum

Theorem 1 (Hermitian Form Maximum)

The minimum and maximum values of

$$\alpha = \frac{\mathbf{x}^H \mathbf{A} \mathbf{x}}{\mathbf{x}^H \mathbf{x}} \tag{B.4}$$

are the minimum and maximum eigenvalues of \mathbf{A} where \mathbf{A} is normal. Here we allow our definition of eigenvalues to include zero.

Proof: Using the spectral decomposition theorem, let

$$\mathbf{\Gamma}\mathbf{\Lambda}\mathbf{\Gamma}^H = \mathbf{A}$$

Without loss of generality, order the eigenvalues in $\mathbf{\Lambda}$ in decreasing order so $\lambda_{\max} = \lambda_1 \geq \lambda_2 \geq \dots \geq \lambda_{\min} = \lambda_N$ and

$$\mathbf{\Lambda} = \begin{bmatrix} \lambda_1 & \cdots & 0 \\ \vdots & \ddots & \vdots \\ 0 & \cdots & \lambda_N \end{bmatrix}.$$

Let $\mathbf{y} = \mathbf{\Gamma}^H \mathbf{x}$ and so $\mathbf{x} = \mathbf{\Gamma} \mathbf{y}$, $\mathbf{x}^H = \mathbf{y}^H \mathbf{\Gamma}^H$ and $\mathbf{y}^H \mathbf{y} = \mathbf{x}^H \mathbf{\Gamma} \mathbf{\Gamma}^H \mathbf{x} = \mathbf{x}^H \mathbf{x}$. Substituting \mathbf{y} for \mathbf{x} in (B.4):

$$\begin{aligned} \alpha &= \frac{\mathbf{y}^H \mathbf{\Lambda} \mathbf{y}}{\mathbf{y}^H \mathbf{y}} \\ &= \frac{\sum \lambda_n y_n^* y_n}{\sum y_n^* y_n} \\ &\leq \frac{\lambda_{\max} \sum y_n^* y_n}{\sum y_n^* y_n}. \end{aligned}$$

But $\alpha = \lambda_{\max}$ for $\mathbf{y} = (1, 0, \dots, 0)^T$ and so the maximum value of α is λ_{\max} , the maximum eigenvalue of \mathbf{A} . Similarly the minimum value is the minimum eigenvalue:

$$\alpha \leq \frac{\lambda_{\min} \sum y_n^* y_n}{\sum y_n^* y_n}.$$

But $\alpha = \lambda_{\min}$ for $\mathbf{y} = (0, \dots, 0, 1)^T$ and so the minimum value of α is λ_{\min} . ■

Corollary 2 (Conjugate match condition)

The maximum value of

$$\alpha = \frac{\mathbf{x}^H \mathbf{a}^* \mathbf{a}^T \mathbf{x}}{\mathbf{x}^H \mathbf{x}} \tag{B.5}$$

is $\alpha = \mathbf{a}^T \mathbf{a}^* = \mathbf{a}^T \mathbf{a}$ and holds for $\mathbf{x} = k \mathbf{a}^*$ where $k \neq 0$ and $k \in \mathbb{C}$. The minimum value is zero and holds for any vector orthogonal to \mathbf{a}^* .

Proof: Let $\mathbf{a}^* \mathbf{a}^T = \mathbf{A}$ in (B.4). By inspection, \mathbf{A} is rank one and so has only one non-zero eigenvalue and corresponding eigenvector. Try \mathbf{a}^* :

$$\begin{aligned} \mathbf{A} \mathbf{a}^* &= (\mathbf{a}^* \mathbf{a}^T) \mathbf{a}^* \\ &= \mathbf{a}^* (\mathbf{a}^T \mathbf{a}^*) \\ &= (\mathbf{a}^T \mathbf{a}^*) \mathbf{a}^*. \end{aligned}$$

Therefore $\mathbf{a}^T \mathbf{a}^*$ and \mathbf{a}^* satisfy the eigenvalue and eigenvector definition.

If \mathbf{x} is orthogonal to \mathbf{a}^* (i.e. $\mathbf{x}^H \mathbf{a}^* = 0$) then and by inspection of (B.5), $\alpha = 0$. ■

The conjugate match can be understood in geometric terms as follows: from the numerator of (B.5) note that

$$(\mathbf{x}^H \mathbf{a}^*)^* = \mathbf{a}^T \mathbf{x} = \sum_i a_i \times x_i = \mathbf{a} \cdot \mathbf{x}.$$

The denominator of (B.5) makes the result independent of the amplitude of \mathbf{x} . Therefore maximizing α is equivalent to maximizing $\|\mathbf{a}^T \mathbf{x}\|$ for $\|\mathbf{x}\| = k$, k an arbitrary constant. In other words the problem is to maximize the weighted sum of a set of complex numbers whilst the norm of the weights is constrained.

First choose the phase of the weights x_i to bring each element to have the same phase, say φ_k , thus defining $\arg(x_i) = -\arg(a_i) + \varphi_k$. Considering the case where $\varphi_k = 0$, $\mathbf{a}^T \mathbf{x}$ will now be real. The problem is now reduced to finding the normalized weight amplitudes that maximize a set of real numbers. Let $b_i = |a_i|$ and $y_i = |x_i|$ and so

$$\mathbf{a}^T \mathbf{x} = \mathbf{b}^T \mathbf{y} = \mathbf{b} \cdot \mathbf{y}$$

the projection of \mathbf{y} onto \mathbf{b} . This projection will be maximized when \mathbf{y} and \mathbf{b} are aligned and so the amplitude of each element in \mathbf{x} must be proportional to \mathbf{a} . Considering the amplitude and phase arguments together produces the conjugate match.

B.5 Rational Hermitian Form Maximum

Theorem 3 (Rational Hermitian Form Maximum)

The minimum and maximum values of

$$\alpha = \frac{\mathbf{x}^H \mathbf{A} \mathbf{x}}{\mathbf{x}^H \mathbf{B} \mathbf{x}} \tag{B.6}$$

are the minimum and maximum eigenvalues of $\mathbf{B}^{-1} \mathbf{A}$ where \mathbf{A} is normal and \mathbf{B} is a positive definite Hermitian matrix. Again we allow our definition of eigenvalues to include zero.

Proof: As \mathbf{B} is Hermitian and therefore normal, we can find $\mathbf{B}^{1/2}$. Also as \mathbf{B} is positive definite, so is $\mathbf{B}^{1/2}$ and \mathbf{B} is invertible as is $\mathbf{B}^{1/2}$ and \mathbf{B}^{-1} and $\mathbf{B}^{-1/2}$ are also positive definite Hermitian matrices.

Let $\mathbf{y} = \mathbf{B}^{1/2}\mathbf{x}$ and so $\mathbf{x} = \mathbf{B}^{-1/2}\mathbf{y}$. Substituting into the denominator of (B.6):

$$\mathbf{x}^H \mathbf{B} \mathbf{x} = \mathbf{x}^H \mathbf{B}^{1/2H} \mathbf{B}^{1/2} \mathbf{x} = \mathbf{y}^H \mathbf{y}$$

and so

$$\alpha = \frac{\mathbf{y}^H \mathbf{B}^{-1/2} \mathbf{A} \mathbf{B}^{-1/2} \mathbf{y}}{\mathbf{y}^H \mathbf{y}}. \quad (\text{B.7})$$

From Appendix B.4 the maximum and minimum values of α are the maximum and minimum eigenvalues of $\mathbf{B}^{-1/2} \mathbf{A} \mathbf{B}^{-1/2}$. Now we show that the eigenvalues of $\mathbf{B}^{-1/2} \mathbf{A} \mathbf{B}^{-1/2}$ are the same as the eigenvalues of $\mathbf{B}^{-1} \mathbf{A}$:

Let λ be an eigenvalue of $\mathbf{B}^{-1/2} \mathbf{A} \mathbf{B}^{-1/2}$:

$$\mathbf{B}^{-1/2} \mathbf{A} \mathbf{B}^{-1/2} \mathbf{y} = \lambda \mathbf{y}$$

Substituting $\mathbf{y} = \mathbf{B}^{1/2} \mathbf{x}$:

$$\begin{aligned} \mathbf{B}^{-1/2} \mathbf{A} \mathbf{B}^{-1/2} \mathbf{B}^{1/2} \mathbf{x} &= \lambda \mathbf{B}^{1/2} \mathbf{x} \\ \Leftrightarrow \mathbf{B}^{-1/2} \mathbf{B}^{-1/2} \mathbf{A} \mathbf{B}^{-1/2} \mathbf{B}^{1/2} \mathbf{x} &= \lambda \mathbf{B}^{-1/2} \mathbf{B}^{1/2} \mathbf{x} \\ \Leftrightarrow \mathbf{B}^{-1} \mathbf{A} \mathbf{x} &= \lambda \mathbf{x} \end{aligned}$$

and so $\mathbf{B}^{-1/2} \mathbf{A} \mathbf{B}^{-1/2}$ and $\mathbf{B}^{-1} \mathbf{A} \mathbf{x}$ share eigenvalues. ■

Corollary 4 (Rational hermitian form with rank 1 numerator)

The maximum value of

$$\alpha = \frac{\mathbf{x}^H \mathbf{a}^* \mathbf{a}^T \mathbf{x}}{\mathbf{x}^H \mathbf{B} \mathbf{x}} \quad (\text{B.8})$$

is $\alpha = \mathbf{a}^T \mathbf{B}^{-1} \mathbf{a}^*$ and holds for $\mathbf{x} = \mathbf{B}^{-1} \mathbf{a}^*$, where \mathbf{B} a positive definite Hermitian matrix.

Proof: Let $\mathbf{y} = \mathbf{B}^{1/2} \mathbf{x}$ and $\mathbf{d} = \mathbf{B}^{-1/2} \mathbf{a}$. Then $\mathbf{d}^* \mathbf{d}^T = \mathbf{B}^{-1/2} \mathbf{a}^* \mathbf{a}^T \mathbf{B}^{-1/2}$ and (B.7) becomes

$$\alpha = \frac{\mathbf{y}^H \mathbf{d}^* \mathbf{d}^T \mathbf{y}}{\mathbf{y}^H \mathbf{y}}.$$

This is the same form as (B.5) and so Corollary 2 tells us α is maximized for $\mathbf{y} = \mathbf{d}^*$:

$$\begin{aligned}\mathbf{x} &= \mathbf{B}^{-1/2}\mathbf{y} \\ &= \mathbf{B}^{-1/2}\mathbf{d}^* \\ &= \mathbf{B}^{-1/2}\mathbf{B}^{-1/2}\mathbf{a}^* \\ &= \mathbf{B}^{-1}\mathbf{a}^*.\end{aligned}$$

Substituting into (B.8):

$$\begin{aligned}\alpha &= \frac{\mathbf{a}^T\mathbf{B}^{-1H}\mathbf{a}^*\mathbf{a}^T\mathbf{B}^{-1}\mathbf{a}^*}{\mathbf{a}^T\mathbf{B}^{-1H}\mathbf{B}\mathbf{B}^{-1}\mathbf{a}^*} \\ &= \frac{(\mathbf{a}^T\mathbf{B}^{-1H}\mathbf{a}^*)\mathbf{a}^T\mathbf{B}^{-1}\mathbf{a}^*}{\mathbf{a}^T\mathbf{B}^{-1H}\mathbf{a}^*} \\ &= \mathbf{a}^T\mathbf{B}^{-1}\mathbf{a}^*.\end{aligned}$$

■

B.6 Hermitian Form Maximum With Null Constraints

Theorem 5 (Hermitian Form Maximum With Null Constraints)

The maximum value of

$$\alpha = \frac{\mathbf{x}^H\mathbf{a}^*\mathbf{a}^T\mathbf{x}}{\mathbf{x}^H\mathbf{x}} \tag{B.9}$$

with the constraint of \mathbf{x} orthogonal to the vectors $\mathbf{b}_1 \dots \mathbf{b}_M$ is $\alpha = \mathbf{a}^T\mathbf{P}\mathbf{a}^$ and holds for $\mathbf{x} = \mathbf{P}\mathbf{a}^*$. \mathbf{P} is the projection*

$$\mathbf{P} = \mathbf{I} - \sum_{l=1}^L \mathbf{e}_l\mathbf{e}_l^H \tag{B.10}$$

and $\mathbf{e}_1 \dots \mathbf{e}_L$ is an orthonormal basis spanning the same subspace as $\mathbf{b}_1 \dots \mathbf{b}_M$.

Note that $L \leq M$ with the inequality holding for $\{\mathbf{b}_m\}$ not being linearly independent.

Proof: As $\{\mathbf{b}_m\}$ and $\{\mathbf{e}_l\}$ span the same subspace, requiring \mathbf{x} to be orthogonal to each \mathbf{b}_m is the same as being orthogonal to all of \mathbf{e}_l . Note

that from inspection $\mathbf{P}^H = \mathbf{P}$ and using the orthogonality of the \mathbf{e}_l vectors $\mathbf{P}^2 = \mathbf{P}$.

Let $\mathbf{a}_\perp = \mathbf{P}^* \mathbf{a}$. Then $\mathbf{a}_\perp^* = \mathbf{P} \mathbf{a}^*$ and

$$\mathbf{a}^* = \mathbf{a}_\perp^* + \sum_{l=1}^L \mathbf{e}_l \mathbf{e}_l^H \mathbf{a}^*$$

and so using $\mathbf{x}^H \mathbf{e}_l = \mathbf{e}_l^H \mathbf{x} = 0$

$$\begin{aligned} \mathbf{x}^H \mathbf{a}^* \mathbf{a}^T \mathbf{x} &= \left(\mathbf{x}^H \mathbf{a}_\perp^* + \mathbf{x}^H \sum_{l=1}^L \mathbf{e}_l \mathbf{e}_l^H \mathbf{a}^* \right) \left(\mathbf{a}_\perp^T \mathbf{x} + \sum_{l=1}^L \mathbf{a}^T \mathbf{e}_l \mathbf{e}_l^H \mathbf{x} \right) \\ &= \left(\mathbf{x}^H \mathbf{a}_\perp^* + \sum_{l=1}^L \underbrace{\mathbf{x}^H \mathbf{e}_l}_{0} \mathbf{e}_l^H \mathbf{a}^* \right) \left(\mathbf{a}_\perp^T \mathbf{x} + \sum_{l=1}^L \mathbf{a}^T \mathbf{e}_l \underbrace{\mathbf{e}_l^H \mathbf{x}}_0 \right) \\ &= \mathbf{x}^H \mathbf{a}_\perp^* \mathbf{a}_\perp^T \mathbf{x}. \end{aligned}$$

Therefore applying the constraints gives

$$\alpha = \frac{\mathbf{x}^H \mathbf{a}_\perp^* \mathbf{a}_\perp^T \mathbf{x}}{\mathbf{x}^H \mathbf{x}}.$$

Using Corollary 2 gives the maximum as

$$\begin{aligned} \alpha &= \mathbf{a}_\perp^T \mathbf{a}_\perp^* \\ &= \mathbf{a}^T \mathbf{P}^H \mathbf{P} \mathbf{a}^* \\ &= \mathbf{a}^T \mathbf{P} \mathbf{a}^* \\ &= \|\mathbf{P} \mathbf{a}^*\|^2. \end{aligned}$$

This holds for $\mathbf{x} = \mathbf{a}_\perp^* = \mathbf{P} \mathbf{a}^*$. ■

The orthonormal basis $\{\mathbf{e}_l\}$ can be found using the Gram-Schmidt process and in fact the expression for \mathbf{a}_\perp^* is the final step in this process.

Where there is only one orthogonality constraint $\mathbf{e}_1 = \mathbf{b} / \|\mathbf{b}\|$ so

$$\begin{aligned} \mathbf{x} = \mathbf{a}_\perp^* &= \left(\mathbf{I} - \frac{\mathbf{b} \mathbf{b}^H}{\mathbf{b}^H \mathbf{b}} \right) \mathbf{a}^* \\ &= \mathbf{a}^* - \frac{\mathbf{b}^H \mathbf{a}^*}{\mathbf{b}^H \mathbf{b}} \mathbf{b}. \end{aligned} \tag{B.11}$$

This is the result quoted by Bird [77, 96].

B.6.1 Gram–Schmidt Process

The Gram–Schmidt process involves finding the component of each vector that is orthogonal to all of its predecessors [338]. If $\mathbf{b}_1 \dots \mathbf{b}_M$ are linearly independent the process can be written as:

$$\begin{aligned}
 \mathbf{e}_1 &= \mathbf{b}_1 / \|\mathbf{b}_1\| \\
 \mathbf{c}_2 &= (\mathbf{I} - \mathbf{e}_1 \mathbf{e}_1^H) \mathbf{b}_2 \\
 \mathbf{e}_2 &= \mathbf{c}_2 / \|\mathbf{c}_2\| \\
 \mathbf{c}_3 &= (\mathbf{I} - \mathbf{e}_1 \mathbf{e}_1^H - \mathbf{e}_2 \mathbf{e}_2^H) \mathbf{b}_3 \\
 \mathbf{e}_3 &= \mathbf{c}_3 / \|\mathbf{c}_3\| \\
 &\vdots \\
 \mathbf{c}_l &= \left(\mathbf{I} - \sum_k^{l-1} \mathbf{e}_k \mathbf{e}_k^H \right) \mathbf{b}_l \\
 \mathbf{e}_l &= \mathbf{c}_l / \|\mathbf{c}_l\|.
 \end{aligned}$$

B.6.2 Stabilized Gram–Schmidt Process

If $\{\mathbf{b}_m\}$ are not all linearly independent, at least some of the \mathbf{c}_l values will be zero. The process can be modified to cope with this by ignoring these constraints. The algorithm below does this and performs the projections incrementally to improve the stability of the process [338].

```

 $\mathbf{e}_1 = \mathbf{b}_1 / \|\mathbf{b}_1\|$ 
 $l = 2$ 
for  $m = 2$  to  $M$ 
     $\mathbf{e}_l = \mathbf{b}_m$ 
    for  $k = 1$  to  $l - 1$ 
         $\mathbf{e}_l = \mathbf{e}_l - \mathbf{e}_k^H \mathbf{e}_l \mathbf{e}_k$       (remove component of  $\mathbf{e}_l$  in the direction  $\mathbf{e}_k$ )
    end for
    if  $\|\mathbf{e}_l\| > 0$                       (check  $\mathbf{b}_m$  is linearly independent of  $\mathbf{e}_1 \dots \mathbf{e}_{l-1}$ )
         $\mathbf{e}_l = \mathbf{e}_l / \|\mathbf{e}_l\|$ 
         $l = l + 1$ 
    end if
end for.

```

B.6.3 Rational Hermitian Form with Null Constraints

Theorem 6 (Rational Herm. Form Max. with Null Constraints)

The maximum value of

$$\alpha = \frac{\mathbf{x}^H \mathbf{a}^* \mathbf{a}^T \mathbf{x}}{\mathbf{x}^H \mathbf{B} \mathbf{x}} \quad (\text{B.12})$$

where \mathbf{B} is a positive definite Hermitian matrix, \mathbf{x} is orthogonal to the vectors $\mathbf{b}_1 \dots \mathbf{b}_M$ is $\alpha = \mathbf{a}^T \mathbf{B}^{-1/2} \mathbf{P} \mathbf{B}^{-1/2} \mathbf{a}^*$ and holds for $\mathbf{x} = \mathbf{B}^{-1/2} \mathbf{P} \mathbf{B}^{-1/2} \mathbf{a}^*$. \mathbf{P} is the projection

$$\mathbf{P} = \mathbf{I} - \sum_{l=1}^L \mathbf{e}_l \mathbf{e}_l^H \quad (\text{B.13})$$

where $\mathbf{e}_1 \dots \mathbf{e}_L$ is an orthonormal basis spanning the same subspace as $\mathbf{B}^{-1/2} \mathbf{b}_1 \dots \mathbf{B}^{-1/2} \mathbf{b}_M$.

Proof: Let $\mathbf{d} = \mathbf{B}^{-1/2} \mathbf{a}$ and $\mathbf{y} = \mathbf{B}^{1/2} \mathbf{x}$. Substituting, we have the same form as Corollary 4:

$$\alpha = \frac{\mathbf{y}^H \mathbf{d}^* \mathbf{d}^T \mathbf{y}}{\mathbf{y}^H \mathbf{y}}$$

with the constraints now being \mathbf{y} orthogonal to the set of vectors $\{\mathbf{B}^{-1/2} \mathbf{b}_m\}$. Let $\{\mathbf{e}_l\}$ be an orthonormal basis built from $\{\mathbf{B}^{-1/2} \mathbf{b}_m\}$. So substituting into (B.10) gives α maximum for

$$\begin{aligned} \mathbf{y} &= \mathbf{P} \mathbf{d}^* \\ \Rightarrow \mathbf{B}^{1/2} \mathbf{x} &= \mathbf{P} \mathbf{B}^{-1/2} \mathbf{a}^* \\ \Rightarrow \mathbf{x} &= \mathbf{B}^{-1/2} \mathbf{P} \mathbf{B}^{-1/2} \mathbf{a}^* \end{aligned} \quad (\text{B.14})$$

$$= \left(\mathbf{B}^{-1} - \mathbf{B}^{-1/2} \sum_{l=1}^L \mathbf{e}_l \mathbf{e}_l^H \mathbf{B}^{-1/2} \right) \mathbf{a}^*. \quad (\text{B.15})$$

■

Where there is only one orthogonality constraint, $\mathbf{e} = \mathbf{B}^{-1/2} \mathbf{b} / \|\mathbf{B}^{-1/2} \mathbf{b}\|$ so

$$\mathbf{x} = \mathbf{B}^{-1} \mathbf{a}^* - \frac{\mathbf{B}^{-1/2} \mathbf{B}^{-1/2} \mathbf{b} \mathbf{b}^H \mathbf{B}^{-1/2} \mathbf{B}^{-1/2} \mathbf{a}^*}{\mathbf{b}^H \mathbf{B}^{-1/2} \mathbf{B}^{-1/2} \mathbf{b}}.$$

$\mathbf{B}^{-1/2}$ is Hermitian as \mathbf{B} is Hermitian and so

$$\mathbf{x} = \mathbf{B}^{-1} \left(\mathbf{I} - \frac{\mathbf{b}\mathbf{b}^H \mathbf{B}^{-1}}{\mathbf{b}^H \mathbf{B}^{-1} \mathbf{b}} \right) \mathbf{a}^* \quad (\text{B.16})$$

$$= \mathbf{B}^{-1} \left(\mathbf{a}^* - \frac{\mathbf{b}^H \mathbf{B}^{-1} \mathbf{a}^*}{\mathbf{b}^H \mathbf{B}^{-1} \mathbf{b}} \mathbf{b} \right). \quad (\text{B.17})$$

B.6.4 Hermitian Inner Product Equality

Theorem 7

Given two complex matrices, \mathbf{A} and \mathbf{B} , if

$$\mathbf{a}^H \mathbf{A} \mathbf{a} = \mathbf{a}^H \mathbf{B} \mathbf{a} \quad (\text{B.18})$$

for all \mathbf{a} , then $\mathbf{A} = \mathbf{B}$.

Proof: For each pair m, n construct these four test vectors with zero entries in all positions except for those indicated:

$$[\mathbf{a}_1]_m = 1 \quad (\text{B.19})$$

$$[\mathbf{a}_2]_n = 1 \quad (\text{B.20})$$

$$[\mathbf{a}_3]_m = j \text{ and } [\mathbf{a}_3]_n = j \quad (\text{B.21})$$

$$[\mathbf{a}_4]_m = 1 + j \text{ and } [\mathbf{a}_4]_n = 1 - j \quad (\text{B.22})$$

where $j = \sqrt{-1}$. Observing

$$\mathbf{a}^H \mathbf{A} \mathbf{a} = \sum_m \sum_n a_m^* [\mathbf{A}]_{mn} a_n \quad (\text{B.23})$$

the four equations from the test vectors become

$$[\mathbf{A}]_{mm} = [\mathbf{B}]_{mm} \quad (\text{B.24})$$

$$[\mathbf{A}]_{nn} = [\mathbf{B}]_{nn} \quad (\text{B.25})$$

$$\begin{aligned} & [\mathbf{A}]_{mm} + [\mathbf{A}]_{mn} + [\mathbf{A}]_{nm} + [\mathbf{A}]_{nn} \\ &= [\mathbf{B}]_{mm} + [\mathbf{B}]_{mn} + [\mathbf{B}]_{nm} + [\mathbf{B}]_{nn} \end{aligned} \quad (\text{B.26})$$

$$\begin{aligned} & 2[\mathbf{A}]_{mm} - j2[\mathbf{A}]_{mn} + j2[\mathbf{A}]_{nm} + 2[\mathbf{A}]_{nn} \\ &= 2[\mathbf{B}]_{mm} - j2[\mathbf{B}]_{mn} + j2[\mathbf{B}]_{nm} + 2[\mathbf{B}]_{nn}. \end{aligned} \quad (\text{B.27})$$

Applying (B.24) and (B.25) to remove the first and last terms of each side of (B.26) and (B.27), the remaining terms give

$$[\mathbf{A}]_{mn} + [\mathbf{A}]_{nm} = [\mathbf{B}]_{mn} + [\mathbf{B}]_{nm} \quad (\text{B.28})$$

$$-j2[\mathbf{A}]_{mn} + j2[\mathbf{A}]_{nm} = -j2[\mathbf{B}]_{mn} + j2[\mathbf{B}]_{nm}. \quad (\text{B.29})$$

As can be seen, the four equations formed by applying \mathbf{a}_1 to \mathbf{a}_4 are independent and lead to $\mathbf{A} = \mathbf{B}$. ■

Appendix C

Element Numbering Scheme

The elements are numbered in the order of increasing radii from the central point. Elements equidistant from the centre are ordered from left to right then bottom to top. Consequently, for on-axis beams, elements with the same excitations have adjacent numbers. Offset beams will have less symmetry.

The numbering scheme leads to an n element symmetrical subset being the first n elements in the scheme. In this system, the beam is centred on a single element leading to the symmetrical subsets being 1, 5, 9 and 13 elements. This allowed for convenient selection of smaller active arrays for faster debugging and for comparison with the larger 21 element active array.

The scheme has similar properties for other array grids such as hexagonal grids. The centre could also be between elements—for instance, for the centre beam of an array with an even number of elements across it. The steps are:

- generate a list of the array element coordinates in any order,
- define a reference point slightly to the left and below the chosen centre to avoid equalities,
- calculate the distance from each element to the reference point, and
- sort the list according to ascending distance from the reference point.

Appendix D

Pointing for offset beams

To obtain pointing directions, pattern cuts and holography grids from the offset beams formed from FPAs, the pointing directions need to be corrected. In the NTD interferometer, the equatorial mount determines the way in which these corrections should be made. The beam offset can be estimated from the location of the centre of the beam in the focal plane and using the beam deviation factor (see Section 3.5.2). In the experimental set up this was refined by finding the peak power level from pattern cuts. The pointing of the reflector is then calculated from the desired direction of the point source target with respect to the beam.

The problem is approached through rotational conversions between a series of coordinate frames [339], listed below.

- **M**: the mount coordinate frame. This is fixed to the earth and oriented with respect to the equatorial mount axes. \mathbf{M}_x aligns with the hour angle axis and points away from the south celestial pole. \mathbf{M}_y aligns with the declination axis when the hour angle is 12 hrs and points toward the west. \mathbf{M}_z points upward on the reflector boresight when mount is in the neutral position.¹
- **R**: the reflector coordinate frame. This is fixed to the reflector and aligns with the mount coordinate system when the mount is in the neutral position.
- **B**: beam direction frame. \mathbf{B}_z is the beam maximum direction. Ideally \mathbf{B}_x and \mathbf{B}_y would be chosen to de-rotate the sky. In this case the trans-

¹The equatorial mount neutral position: The hour angle is 12 hours and the declination is zero

formation for the equatorial mount was applied. This was considered acceptable as, for small offsets; the polarization error is very small.

Now define three direction vectors:

- **r**: mount or boresight of reflector,
- **b**: beam maximum, and
- **p**: pointing.

Using subscripts to denote the frame of reference used we define Euler matrices \mathbf{A}_{BR} and \mathbf{A}_{RM} to transform from between them:

$$\mathbf{p}_R = \mathbf{A}_{BR}\mathbf{p}_B \quad (\text{D.1})$$

$$\mathbf{p}_M = \mathbf{A}_{RM}\mathbf{p}_R \quad (\text{D.2})$$

$$\mathbf{A} = \begin{bmatrix} cd & 0 & sd \\ sh.sd & ch & -sh.cd \\ -ch.sd & sh & ch.cd \end{bmatrix} \quad (\text{D.3})$$

where:

$$\begin{aligned} cd &= \cos(dec) & ch &= \cos(ha) \\ sd &= \sin(dec) & sh &= \sin(ha) \end{aligned}$$

The inverse of these matrices is equal to their transpose.

D.1 Finding the Correct Offset

To find the offset to apply to the mount setting:

- find the beam centre by scanning \mathbf{r}_M on a given target \mathbf{p}_M . These will be in radec coordinates,
- calculate the Euler matrix \mathbf{A}_{RM} from the mount setting \mathbf{r}_M , and
- calculate the beam offset with respect to the reflector: $\mathbf{b}_R = \mathbf{p}_R = \mathbf{A}_{RM}^T \mathbf{p}_m$.

D.2 Mount Setting

We are seeking the mount setting given the target point source direction \mathbf{p}_M , the offset of the beam from the reflector \mathbf{b}_R and the offset we desire from the beam (for pattern measurement) \mathbf{p}_B .

- Calculate the Euler matrix \mathbf{A}_{BR} from the beam offset \mathbf{b}_R using D.3.
- Calculate the target with respect to the reflector $\mathbf{p}_R = \mathbf{A}_{BR}\mathbf{p}_B$.
- Use an iterative solver to find \mathbf{r}_M using D.3 and $\mathbf{p}_M = \mathbf{A}_{RM}\mathbf{p}_R$.

Appendix E

Choice of Radio Sources for Antenna Measurements

Distant radio sources such as man-made satellites and naturally occurring celestial sources are often used for large antenna characterization [260, 340, 341]. The characteristics of celestial sources are comprehensively covered in Kuz'min and Salomonovich [14]. Man-made satellites are often used, particularly for holography [342, 343]. The considerations that went into the choice of suitable sources for making measurements with the NTD Interferometer are outlined in this appendix.

E.1 Satellites

Geostationary satellites can provide convenient sources for characterizing antennas. The advantages are listed below.

- The power flux densities are much higher than celestial sources.
- If the satellite has not been allowed to drift too much, no tracking is required.
- The frequency band they use will be protected and so there should be no local interference.
- They appear as a point source.

The disadvantages are listed below.

- Power flux density is difficult to determine in absolute terms. Sometimes the satellite operator is willing to generate a signal of relatively well known strength but this will typically only be available for a short

time. There may also be a narrow-band beacon available on the satellite.

- The signal is usually modulated and so the power flux density can have short term power fluctuations.
- The power flux density may be so much higher than that expected in the normal operation of the radiotelescope that the receiver chain is saturated and may need to be put into a different mode of operation.
- The frequency may not be suitable for the measurement campaign.
- If the satellite has been allowed drift more than a small fraction of the beamwidth, tracking is complicated by the need to obtain ephemeris information and for the antenna pointing system to follow this tracking. Any antenna patterns need to be taken with offsets relative to the actual position of the satellite adding to the complexity of the operation (see D).

Non-geostationary satellites have similar advantages and disadvantages with the main difference being the tracking is much faster.

The Optus MobileSat transponder, on one of their B-series satellites, was used for some of the earlier work on the NTD interferometer.¹ The frequency was 1.5–1.6 GHz. The spectrum consisted of fluctuating narrow peaks above a noise floor pedestal, probably a single channel per carrier system. The peaks were mainly in the upper half of the pedestal and so the received band can be limited to avoid these and use only the pedestal.

The use of MobileSat was eventually rejected as at this frequency, the radiation pattern from a single feed (close to the centre of the array) was found to be highly asymmetrical. The array spacing was also getting quite large at this frequency: 0.66λ .

Satellites from the Global Positioning System (GPS) were considered primarily in preparation commissioning tests for the Parkes Test-bed Facility (PTF) [164] (see Section 2.6.3). In the commissioning stage the Parkes 64 m radiotelescope was not available for interferometry and so a strong signal source was desirable. The GPS satellites provided this strong signal. Another feature was their rate motion was convenient for drift tests.

A drift scan was used to measure the G/T . In this case the dish being measured is pointed in the path of the satellite and the power level is recorded as the satellite passes through the beam. This worked but suffered

¹Primarily by Tim Cornwell and Maxim Voronkov

from what appeared to be additional satellites being detected, adding to the uncertainty of the measurement.

The signal was sufficiently strong that a low gain horn (designed as a feed for the NTD dishes) could be used as the reference arm of an interferometer, providing a way of testing the interferometry set up prior to using the 64 m telescope.

The characteristics of the GPS satellites are as follows [344]:

Orbits The orbits are in a number of intersecting planes, 12 hour duration (leading to an angular rate as seen from the ground of $0.5^\circ/\text{min}$). In some of the measurements taken, other satellites appeared to come into the sidelobes of the antenna under test. In interferometer mode, the spatial resolution provided by increasing the integration time and/or the baseline could ameliorate this problem. Data for calculating the location of the satellites is available from [345, 346].

Frequency 1227.60 MHz (known as the L2 band). There are a number of other frequencies in use.

Bandwidth 20 MHz for the L2 P(Y) signal used.

Power flux density The power flux density for each code transmitted is of the order of -166 dBW [347] into a 0 dBi antenna. This translates to $26\,000\text{ Jy}$ for the 20 MHz signal used. As found by Wang [348] the absolute value of the power flux density is difficult to determine accurately and it varies as the satellite passes due the radiation pattern of the satellite's antenna. None the less, it appeared to be sufficiently stable over angular ranges of $\sim 10^\circ$ for antenna patterns.

E.2 Moon

The moon was considered for G/T measurements as it is strong source at $\sim 215\text{ K}$ [349], $\sim 7000\text{ Jy}$ [350]. It has been shown that with care, accurate measurements can be made in spite of its angular extent ($\sim 0.5^\circ$) and the variation in its radiation [349–352]. This was not pursued in this project due to additional effort required but it may be useful for future G/T measurements.

E.3 Stars and Galaxies

Celestial sources move slowly across the sky and can be readily tracked.

The advantages are listed below.

- The power flux densities are often well known if they are used calibrators for radiotelescopes.
- Their positions are well known and radiotelescopes will be equipped to track them.
- They generally emit broad noise leaving a great deal of choice in the frequency of observation.

The disadvantages are listed below.

- The power flux densities are much lower than most satellites.
- The power flux densities can change with time.
- Larger sources are often not in current use as calibrators and so the knowledge of their power flux density may not be well characterized.
- They are usually available for only part of the day or night.

A list of possible celestial sources shown in Table E.1 was maintained for this work. Even weaker sources provided enough of a response allowing the system development to continue when the stronger sources were not available.

The strength of M87 was investigated in some detail as it was deemed the most useful “known flux” calibrator [354]. There were three sources of spectral flux density versus frequency data: Kuz'min and Salomonovich (1966) [14], Baars et al. (1977) [355] and Ott et al. (1994) [356]. The data are shown in Figure E.1a with log-log linear fit to the Baars data and a log-log quadratic fit to the Ott data. Ott provides the most recent data with the tightest tolerances but the frequency range does not cover our main frequency of interest, 1200 MHz. Kuz'min and Baars show the general behaviour beyond the range covered in Ott, including the frequency of interest. The slight flattening of the spectrum over time seen in Fig. E.1a is also noted in Ott. Considering the data and uncertainties presented in these references, it is reasonable to extrapolate the data from Ott to 1200 MHz, giving 230 Jy. The uncertainty of the 1408 MHz point is 3% and so considering the extrapolation and possible changes with time, a value of 7% or ± 16 Jy is used for G/T calculations.

Table E.1 – Celestial point sources.

Identifiers	RA (J2000)	DEC (J2000)	Flux (Jy) ^a
3C161	0407 −658	04:08:20.380	15.5
	0521 −365	05:22:57.984651	12.09
	0624 −058	06:27:10.0960	16.42
	1226 +023	12:29:06.699729	47.14
M87, Virgo A	1228 +126	12:30:49.423381	214.61
	1253 −055	12:56:11.166560	10.13
	1717 −358	17:20:21.8042	20.04
SGRA*	1742 −289	17:45:40.0383	65.86
	1814 −637	18:19:35.002381	13.36
	1830 −210	18:33:39.9150	12.22
	1934 −638	19:39:25.026	14.95
M17, Omega Nebula	18:20:26	−16:10:36	650.

^a Flux at 20 cm.

The data are from the ATNF Compact Array calibrator database [353] with the exception of M17 which is from Kuz'min and Salomonovich [14].

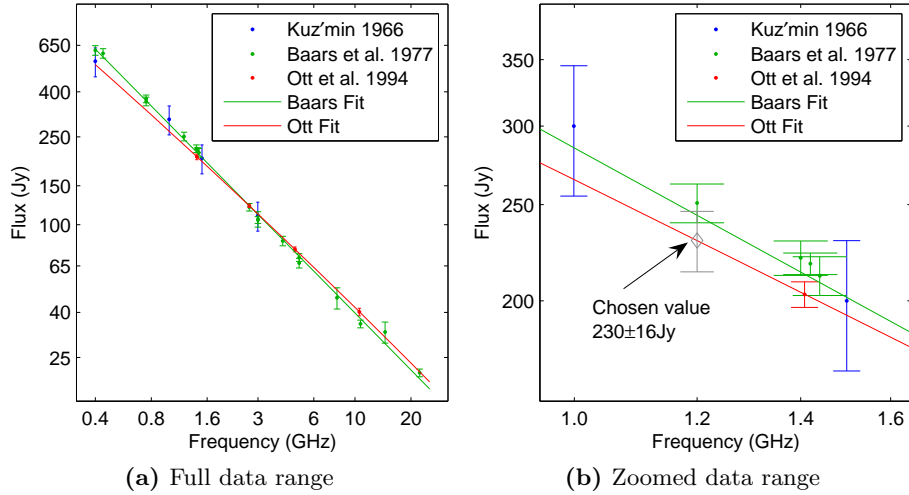


Figure E.1 – Spectral flux density of M87 from Kuz'min and Salomonovich (1966) [14], Baars et al. (1977) [355] and Ott et al. (1994) [356]. The best-fit lines are $\log_{10}(S) = 5.023 - 0.856 \log_{10}(\nu)$ for Baars and $\log_{10}(S) = 4.484 - 0.603 \log_{10}(\nu) - 0.0280 \log_{10}^2(\nu)$ for Ott where ν is the frequency in MHz.

Table E.2 – Extended HI regions.

Name	Designation	RA J2000	Dec J2000	T_{eq} (K)	Ref.
S6	1531 –024	15:28:58	–2.25.00	45	[309]
S8		05:47:21.3	–01.40.18	63	[309]
S9	1752 –344	17:52:05.4	–34.25.45	74	[309]
	1714 –397	17:17:38.6	–39.48.51	100	[357]

E.4 Source Availability

A critical part of planning measurements was the times various sources were within the range of the antenna system—preferably high in the sky. To assist in determining this, code was written to show the rise and set times and coordinates of the sources for any day: the times the key sources were available on Saturday, October 25, 2008 are shown in Fig. E.2.

E.5 Extended HI Regions

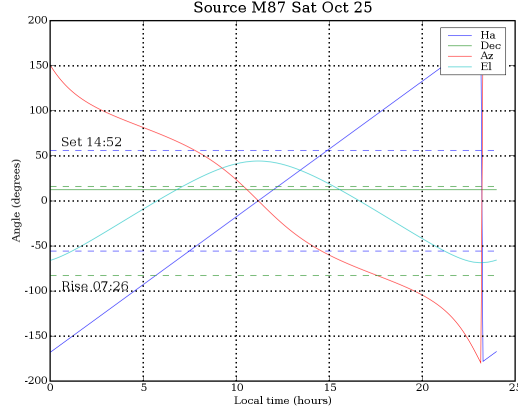
Extended regions of HI can be used for system temperature calculations as described in Section 7.6.6. Source details are provided in Table E.2.

E.6 Summary

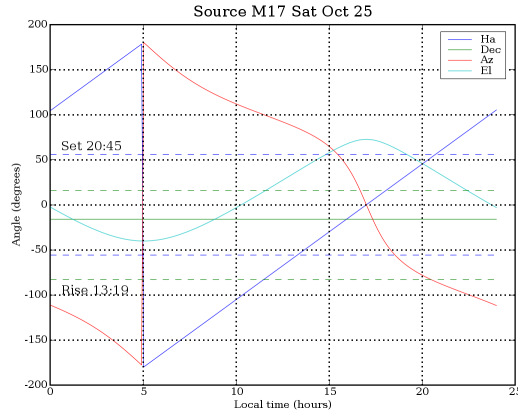
Whichever radio source is used, care needs to be taken of other sources in the sky that are comparable or stronger than the source being used. For instance with GPS satellites, other satellites in the constellation proved an issue and with M87, the sun comes close to its position during November.

The elevation of the source is also important. With the NTD Interferometer, interference from trees became an issue for the western antenna as sources set in the west. Pattern cuts can also be limited by the source’s elevation.

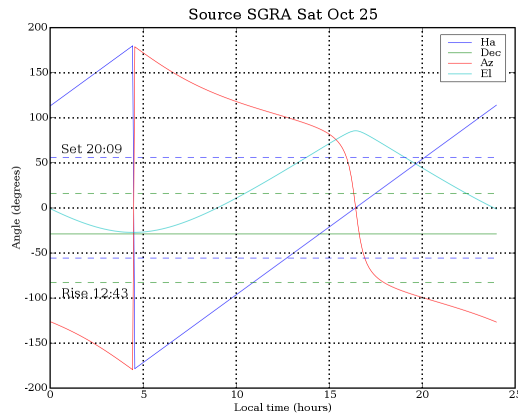
E. Choice of Radio Sources for Antenna Measurements



(a) M87



(b) M17



(c) SGR A*

Figure E.2 – Radio source availability plots for the NTD Interferometer. The hour angle and declination limits are plotted as dashed blue and green lines respectively. The source is available while the hour angle is between the dashed blue lines.

Appendix F

Combining Uncertainties

Every value produced from a measurement or calculation in engineering or science will have a (possibly zero) uncertainty or error bars attached to it. Frequently this is not expressed explicitly as finding the uncertainties in all of the input parameters to a calculation or in a measurement can be very difficult and combining these uncertainties rigorously is also complicated. Nonetheless, when an engineer or scientist quotes a value they will usually have some idea of the uncertainty involved.

The method described below is a pragmatic approach where the resultant value is the result of a calculation from a number of input parameters with known or estimated uncertainties. The uncertainties in the input parameters are assumed to be uncorrelated and the output value varies monotonically with respect to each input. When there is a correlation, the calculation can sometimes be reformulated to reduce the number of inputs or separate them so they are uncorrelated.

This method is based on the method in [358] with the main difference being the number of degrees of freedom calculation is not included and this method does not assume the output is linear with respect to the input. It has not been thoroughly evaluated for statistical validity but is thought to be sufficiently accurate for most purposes. A superior approach where non-linearity is involved and or where the uncertainty distributions are asymmetrical would be to use a Monte Carlo simulation method [358].

The uncertainty for each variable needs to be expressed in terms of a common coverage factor. The 95% estimate (2σ for a Gaussian distribution) is used in this work and in terms of the GUM [359] it is twice the *standard*

uncertainty. Most quoted uncertainties can be assumed to be Gaussian. A minor correction can be made for rectangular distributions, appropriate for some manufacturer's specifications: the conversion is [358]

$$U_{95\%} = (\sqrt{3}/1.96)U_{\text{spec}} = 0.884U_{\text{spec}}. \quad (\text{F.1})$$

For a mismatch in a transmission line, the distribution can be U shaped and more care is needed [360].

For an output value f with input parameters $\mathbf{x} = (x_1, \dots, x_n)$, the steps involved are as follows: Calculate the expected value

$$f_0 = f(\mathbf{x}).$$

For each input variable x_i with lower and upper bounds $x_{\Delta L,i}$ and $x_{\Delta U,i}$ calculate

$$\begin{aligned} f_{xb,i} &= f(\mathbf{x}_{\Delta L,i}) \\ f_{xt,i} &= f(\mathbf{x}_{\Delta U,i}) \end{aligned}$$

where $\mathbf{x}_{\Delta L,i} = (x_1, \dots, x_{\Delta L,i}, \dots, x_n)$ and $\mathbf{x}_{\Delta U,i} = (x_1, \dots, x_{\Delta U,i}, \dots, x_n)$. Find the minimum and maximum values of these ranges for each variable

$$\begin{aligned} f_{\Delta L,i} &= \min(f_{xL,i}, f_{xU,i}) \\ f_{\Delta U,i} &= \max(f_{xL,i}, f_{xU,i}). \end{aligned}$$

The lower and upper combined uncertainties are then

$$f_{\Delta L} = \left(\sum_{i=1}^n (f_0 - f_{\Delta L,i})^2 \right)^{1/2} \quad (\text{F.2})$$

$$f_{\Delta U} = \left(\sum_{i=1}^n (f_{\Delta U,i} - f_0)^2 \right)^{1/2}. \quad (\text{F.3})$$

The uncertainty distribution is usually at least roughly Gaussian as due the central limit theorem. An exception to this is where the combined uncertainty is dominated by one non-Gaussian input uncertainty. In this case the distribution will be similar to the input if the relationship is linear with respect to the variable concerned.

Appendix G

Pattern Interpolation and Aperture Distribution

G.1 Pattern Cut Interpolation

The interpolation of antenna radiation patterns is common where a near continuous data is desired and it is less time consuming to interpolate on a smaller data set than collect all the data. In this work a step, track and measure approach was used rather than collecting data as the antenna was moving relative to the source, avoiding the need to compensate for smearing with movement. Other reasons for interpolating rather than collecting all the desired data are time limitations due to source availability if an astronomical source is used and minimizing the impact of gain drift in the system.

Interpolation can be confidently applied to antenna patterns due to their quasi band limited nature. After trialling options including Whittaker [361] and Fourier interpolation, the method described by Bucci [362] was chosen. With Nyquist sampling of $\sim 1^\circ$, the pattern was four times over-sampled at the 0.25° spacing that was employed.

The pattern cuts were interpolated to 15 times the original data spacing and 13 points (3.35°) were used as the kernel for the interpolation function with appropriate truncation at the ends of the cut.

Further enhancements could involve using the band limited nature of the data to remove outliers (e.g. from momentary RFI) and improve the signal to noise ratio by smoothing the data.

G.2 Aperture Distribution from Far Field Pattern Cuts

The motivation for developing a method to extract the low spatial-frequency behaviour of an aperture field distribution from a limited number of pattern cuts is outlined in Section 7.5.

The technique involves the following steps listed below.

- Interpolating the pattern cuts (in the θ coordinate as described in Section G.1)
- Centring the patterns on peak and resample. This is to compensate for small drift (fraction of a degree) in the source tracking between cuts.
- Normalizing the phase and magnitude to the central common point of the cuts ($\theta = 0$)
- Interpolating the axial (ϕ) coordinate using a cubic spline. Augment the data at each end by wrapping around the circle to make the result smooth where it joins.
- Resampling the now two dimensional θ - ϕ radiation pattern on a u - v grid using simple linear interpolation.
- Applying a Hamming window to reduce truncation artefacts on transformation.
- Zero padding to obtain better resolution in the aperture.
- Shifting to put the zero spatial frequency at $[0,0]$ for 2D Fourier transform.
- Applying the 2D Fourier transform to aperture.
- Truncating the data to the dish size.
- Scaling the aperture field to central point in phase and maximum in magnitude.

This approach was applied to models of aperture distributions to test its validity and limitations. The trial aperture distribution was a parabolic taper on a pedestal with differing profiles and 6 dB edge illumination ($C = 0.5$): $E(\rho) = C + (1 - C)[1 - (\rho/a)^2]^n$. a is the radius of the dish. Strut and feed blockage was added and quadratic and cubic phase distortions of the form $\arg(E(\rho)) = 20^\circ (\rho/a)^n$ were tried. The quadratic case was chosen to match the phase seen in the single element plots. The aperture was transformed to the far field, $E_{\text{ff}}(\theta, \phi)$, using the formulation given by Stutzman and Thiele

[27, pp281–283].

$$E_{\text{ff}}(\theta, \phi) = \frac{1 + \cos \theta}{2} \iint E_{\text{ap}}(x, y) \exp(j2\pi/\lambda(x \sin \theta \cos \phi + y \sin \theta \sin \phi)) dx dy \quad (\text{G.1})$$

where $E_{\text{ap}}(x, y)$ is the aperture field. The interpolation process was then applied to the four far-field cuts. The process is illustrated graphically in Fig. G.1.

Comparing the initial and regenerated aperture field distributions, it can be seen the spatial filtering effect introduces large errors around the dish edges and central blocked region. In the annular range $\rho = 2$ to 6 m however, the RMS phase error was 0.24° for the quadratic distortion case and much less for the flat phase cases. The RMS amplitude error was 2% and 5% for the $n = 1$ and $n = 2$ cases respectively.

As long as care is used in the interpretation of the aperture distributions, techniques such as this can show some features of an antenna system with minimal data. For instance, even a single cut can show the degree and direction of defocussing.

G.3 Further work

Fourier or Bucci's interpolation may be superior for the axial interpolation due to the natural periodic nature of the data. These approaches were not pursued because initial investigations in Fourier interpolation showed it appeared to be more susceptible to outliers, propagating the error throughout the pattern.

The aperture distribution technique suffers from the intrinsic low frequency filtering corrupting the edges and blockage. This led to the consideration of other possible approaches which are listed below.

- Extend the interpolated far field in an iterative manner as shown by Rahmat-Sammii [363].
- As above but add a transform to the focal plane [364]: far field \Rightarrow aperture \rightarrow truncate \Rightarrow focal plane \rightarrow truncate \Rightarrow aperture \rightarrow truncate and add blockage \Rightarrow far field. Repeat until the aperture stabilizes.
- Fit a set of orthonormal functions to the data:

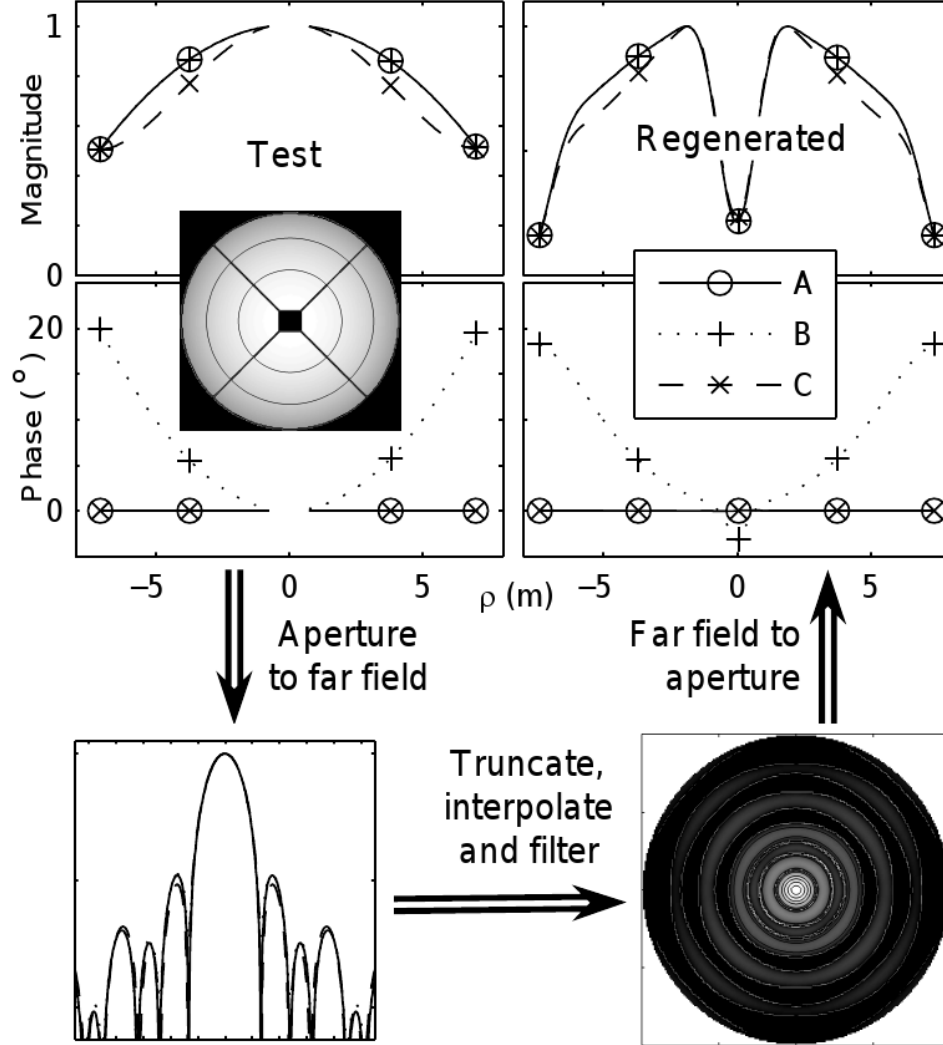


Figure G.1 – E-plane cuts of test and regenerated apertures. The 2D insert shows the FPA and strut blockage used in the model. The parameters for the apertures are: A : $n = 1$, flat phase; B : $n = 1$ quadratic phase; C : $n = 2$, flat phase, all with 6 dB edge taper. ©IEEE from [7].

1. Create a set of aperture basis functions including known effects such as blockage.
 2. Use the Gram-Schmidt process to orthonormalize these on the domain of the collected data.
 3. Calculate the far field from each basis function.
 4. Find the coefficients of each basis function that reproduce the measured data using the integral of the product of the measured and calculated far fields.
 5. Regenerate the aperture as the weighted sum of aperture basis functions.
- Fit a model to the data using a standard optimization technique.
 1. Create a model of the aperture that contains the anticipated aberrations, such as

$$E_a(x, y) = e^{j\Phi(x,y)} \left\{ C + (1 - C) \left[1 - \frac{x^2 + y^2}{R^2} \right]^n \right\} \quad (\text{G.2})$$

where $\Phi(x, y)$ contains defocussing d and beam scanning b terms.

2. Overlay blockage on E_a
3. Minimize the difference between the far field generated from E_a and the measured data. This leads to four parameters c , n , d and b optimize.

The first of these techniques was tried but, with a limited investigation, it proved less satisfactory than the one adopted.

Appendix H

Publications Related to this Thesis

During the candidature for this degree, the author produced or contributed to a number of related publications. Two of the publications have been appended for convenience.

H.1 Publications with Content from this Thesis

D. B. Hayman, T. S. Bird, P. Hall, and K. Esselle, “Beamforming for focal plane arrays,” in *9th Australian Symposium on Antennas*, Sydney, Australia. Sydney, Australia: CSIRO, 2005, p. 41.

D. B. Hayman, T. S. Bird, K. P. Esselle, and P. J. Hall, “Encircled power study of focal plane field for estimating focal plane array size,” in *IEEE AP-S Int. Symp. Digest*, vol. 3A, Jul. 3–8, 2005, pp. 371–374.

D. B. Hayman, T. S. Bird, P. J. Hall, and K. Esselle, “How big is that focal plane array?” in *SKA 2005*. Pune, India, 2005.

D. B. Hayman and T. Cornwell, “NTD THEA tile measurements,” in *Third International Focal Plane Array Workshop*, March 2007.

D. B. Hayman, “Phased array feed development with the Marsfield interferometer,” in *Australia Telescope National Facility Annual Student Symposium*, June 2007.

D. B. Hayman, “Focal plane array beamforming with the NTD interferometer,” in *CSIRO ICT Centre Conference*, 2008. Runner up in best student poster competition.

D. B. Hayman, T. S. Bird, P. Hall, and K. Esselle, “Evaluation of beamforming radioastronomy focal plane arrays,” in *UNSC/URSI National Radio Science Meeting*, 2009.

D. B. Hayman, “Focal plane arrays for radio astronomy,” in *Macquarie University Faculty of Science Research Conference*, Sep. 2009. Runner up in best poster competition.

D. B. Hayman, T. S. Bird, K. P. Esselle, and P. J. Hall, “Evaluation of radioastronomy focal plane arrays,” in *CSIRO ICT Centre Conference*, 2009.

D. B. Hayman, T. S. Bird, K. P. Esselle, and P. J. Hall, “Experimental demonstration of focal plane array beamforming in a prototype Radiotelescope,” *IEEE Trans. Antennas Propag.*, vol. 58, no. 6, pp. 1922–1934, Jun. 2010.

D. Hayman, T. S. Bird, K. P. Esselle, and P. J. Hall, “Focal plane array evaluation on a prototype radiotelescope,” in *Workshop on Applications of Radio Science (WARS10)*, 2010.

D. B. Hayman, T. S. Bird, K. P. Esselle, and P. J. Hall, “Practical aspects of focal plane array testing,” in *International Workshop on Phased Array Antenna Systems for Radio Astronomy*. Brigham Young University, Provo, Utah, USA, May 3–5 2010. [Online]. Available: <http://csas.ee.byu.edu/docs/Workshop/ByuHayman.pdf>

H.2 Supporting FPA Measurements

D. B. Hayman, “Radiation pattern and scattering matrix measurement of the NTD five by one linear connected array,” CSIRO ICT Centre, Tech. Rep. 06/385, December 2006.

D. B. Hayman, “Experimental verification of array modelling,” in *Tenth Australian Symposium on Antennas, Sydney Feb. 14-15, 2007*, p. 68.

Reprinted in Section H.5.

H.3 NTD Interferometer development

D. Hayman, R. Beresford, J. Bunton, C. Cantrall, T. Cornwell, A. Grancea, C. Granet, J. Joseph, M. Kesteven, J. O’Sullivan, J. Pathikulangara, T. Sweetnam, and M. Voronkov, “The NTD interferometer: A phased array feed test bed,” in *Workshop on Applications of Radio Science (WARS08)*, 2008.

Reprinted in Section H.6.

C. Granet, I. M. Davis, C. Cantrall, A. Grancea, D. B. Hayman, and A. R. Forsyth, “NTD prime-focus horns,” CSIRO ICT Centre, Tech. Rep. 07/019, Nov 2007.

H.4 CSIRO’s FPA work

These publications report on the state of CSIRO’s FPA work which include parts of this work:

D. B. Hayman, D. Ferris, S. Jackson, L. Li, K. Smart, P. Hall, T. Bird, and A. Parfitt, “Digital focal plane arrays,” in *Focal Plane Arrays: Towards instant imaging systems: 1st Faraday Focal Plane Array Workshop.*, ASTRON, Dwingeloo, The Netherlands, May 2004.

T. S. Bird, D. B. Hayman, S. Jackson, and R. H. Ferris, “Focal plane array related activities at CSIRO,” in *Focal Plane Arrays: Towards Instant Imaging Systems : 1st Faraday Focal Plane Array Workshop.* ASTRON, Dwingeloo, The Netherlands, May 2004.

J. S. Kot, J. Bunton, D. B. Hayman, and S. Jackson, “Large array with focal plane array feeds for the SKA,” in *IEEE/MTT-S International Microwave Symposium.* Long Beach, CA, USA, 2005.

J. O’Sullivan, R. Gough, D. B. Hayman, A. Grancea, C. Granet, S. Hay, and J. Kot, “Recent focal plane array developments for the Australian SKA Pathfinder,” in *International Symposium on Microwave and Optical Technology*, Dec 2007.

S. G. Hay, J. D. O’Sullivan, J. S. Kot, C. Granet, A. Grancea, A. R. Forsyth, and D. B. Hayman, “Focal plane array development for ASKAP (Australian SKA Pathfinder),” in *EuCAP*, Edinburgh, Nov. 2007, pp. 1–5.

H. Publications Related to this Thesis

J. D. O’Sullivan, F. Cooray, C. Granet, R. Gough, S. Hay, D. B. Hayman, M. Kesteven, J. Kot, A. Grancea, and R. Shaw, “Phased array feed development for the Australian SKA Pathfinder,” presented at the URSI General Assembly, Sep. 2008.

D. B. Hayman, A. P. Chippendale, R.-Y. Qiao, J. D. Bunton, R. J. Beresford, P. Roberts, and P. Axtens, “Gain calibration of phased array feeds,” in *Int. Conf. on Electromagnetics in Advanced Applications (ICEAA)*, Sep. 23 2010, pp. 418–421.

H.5 Tenth Australian Symposium on Antennas, 2007

D. B. Hayman, “Experimental verification of array modelling,” in *Tenth Australian Symposium on Antennas, Sydney Feb. 14-15, 2007*, p. 68.

Pages 286-290 of this thesis have been removed as they contain copyright material.

H.6 Workshop on Applications of Radio Science, 2008

D. Hayman, R. Beresford, J. Bunton, C. Cantrall, T. Cornwell, A. Grancea, C. Granet, J. Joseph, M. Kesteven, J. O’Sullivan, J. Pathikulangara, T. Sweetnam, and M. Voronkov, “The NTD interferometer: A phased array feed test bed,” in *Workshop on Applications of Radio Science (WARS08)*, 2008.

Pages 292-298 of this thesis have been removed as they contain copyright material.

References

- [1] W. N. Christiansen and J. A. Högbom, *Radiotelescopes*, 2nd ed. Cambridge University Press, 1985.
- [2] J. R. Fisher and R. F. Bradley, “Full-sampling focal plane arrays,” in *Imaging at Radio through Submillimeter Wavelengths*, ser. Astron. Soc. Pac. Conf., J. G. Mangum and S. J. E. Radford, Eds., vol. 217, 2000, pp. 11–18. [Online]. Available: <http://adsabs.harvard.edu/abs/2000ASPC..217...11F>
- [3] M. V. Ivashina, “Holographic performance verification of a focal plane array prototype,” in *Focal Plane Array Workshop*. Dwingeloo, Netherlands: ASTRON, 2005.
- [4] W. van Cappellen, “Initial tests with the DIGESTIF system,” in *SKADS MCCT Workshop*, 26–30 Nov. 2007. [Online]. Available: <http://www.astron.nl/other/workshop/MCCT/ThursdayCappellen.pdf>
- [5] K. F. Warnick, J. Waldron, J. Landon, M. Lilrose, B. D. Jeffs, J. R. Fisher, and R. Bradley, “Experimental results on interference mitigation with a 19 element array feed,” in *Eu. Conf. on Antennas and Propagation (EuCAP)*, Edinburgh, Nov. 11–16, 2007, pp. 1–5.
- [6] B. Veidt, T. Burgess, R. Messing, G. Hovey, and R. Smegal, “The DRAO phased array feed demonstrator: Recent results,” in *ANTEM Symposium*, Banff, AB, Feb. 15–18 2009, pp. 1–4.
- [7] D. B. Hayman, T. S. Bird, K. P. Esselle, and P. J. Hall, “Experimental demonstration of focal plane array beamforming in a prototype radiotelescope,” *IEEE Trans. Antennas Propag.*, vol. 58, no. 6, pp. 1922–1934, Jun. 2010.
- [8] D. B. Hayman and T. Cornwell, “NTD THEA tile measurements,” in *Third International Focal Plane Array Workshop*. Sydney Australia: CSIRO ATNF, Mar. 2007.

REFERENCES

- [9] B. D. Jeffs, K. F. Warnick, J. Landon, J. Waldron, D. Jones, J. R. Fisher, and R. D. Norrod, "Signal processing for phased array feeds in radio astronomical telescopes," *IEEE J. Sel. Topics Signal Process.*, vol. 2, no. 5, pp. 635–646, Oct. 2008.
- [10] D. B. Hayman, T. S. Bird, P. Hall, and K. Esselle, "Evaluation of beamforming radioastronomy focal plane arrays," in *USNC-URSI National Radio Science Meeting*, Jun. 1–5 2009.
- [11] M. V. Ivashina, O. A. Iupikov, R. Maaskant, W. A. van Cappellen, L. Bakker, and T. Oosterloo, "Off-axis beam performance of focal plane arrays for the Westerbork Synthesis Radio Telescope—initial results of a prototype system," in *IEEE AP-S Int. Symp. Digest*, Charleston, SC, Jun. 1–5, 2009, pp. 1–4.
- [12] D. Hayman, R. Beresford, J. Bunton, C. Cantrall, T. Cornwell, A. Grancea, C. Granet, J. Joseph, M. Kesteven, J. O'Sullivan, J. Pathikulangara, T. Sweetnam, and M. Voronkov, "The NTD interferometer: A phased array feed test bed," in *URSI Workshop on Applications of Radio Science*, 2008.
- [13] A. R. Thompson, J. M. Moran, and G. W. Swenson, Jr, *Interferometry and Synthesis in Radio Astronomy*, 2nd ed. John Wiley and Sons, Inc., 2001.
- [14] A. D. Kuz'min and A. E. Salomonovich, *Radioastronomical methods of antenna measurements*. Academic Press, New York, 1966.
- [15] An introduction to pulsars. Accessed June 2011. [Online]. Available: <http://outreach.atnf.csiro.au/education/everyone/pulsars/>
- [16] S. Johnston, M. Bailes, N. Bartel, C. Baugh, M. Bietenholz, C. Blake, R. Braun, J. Brown, S. Chatterjee, J. Darling, A. Deller, R. Dodson, P. G. Edwards, R. Ekers, S. Ellingsen, I. Feain, B. M. Gaensler, M. Haverkorn, G. Hobbs, A. Hopkins, C. Jackson, C. James, G. Joncas, V. Kaspi, V. Kilborn, B. Koribalski, R. Kothes, T. L. Landecker, E. Lenc, J. Lovell, J.-P. Macquart, R. Manchester, D. Matthews, N. M. McClure-Griffiths, R. Norris, U.-L. Pen, C. Phillips, C. Power, R. Protheroe, E. Sadler, B. Schmidt, I. Stairs, L. Staveley-Smith, J. Stil, R. Taylor, S. Tingay, A. Tzioumis, M. Walker, J. Wall, and M. Wolleben, "Science with the Australian Square Kilometre Array Pathfinder," *Publ. Astron. Soc. Aust.*, vol. 24, no. 4, pp. 174–188, 2007. [Online]. Available: <http://www.publish.csiro.au/paper/AS07033>
- [17] J.-P. Macquart, M. Bailes, N. D. R. Bhat, G. C. Bower, J. D. Bunton, S. Chatterjee, T. Colegate, J. M. Cordes, L. D'Addario,

- A. Deller, R. Dodson, R. Fender, K. Haines, P. Hall, C. Harris, A. Hotan, S. Jonston, D. L. Jones, M. Keith, J. Y. Koay, T. J. W. Lazio, W. Majid, T. Murphy, R. Navarro, C. Phillips, P. Quinn, R. A. Preston, B. Stansby, I. Stairs, B. Stappers, L. Staveley-Smith, S. Tingay, D. Thompson, W. van Straten, K. Wagstaff, M. Warren, R. Wayth, and L. Wen (the CRAFT Collaboration), “The commensal real-time ASKAP fast-transients (CRAFT) survey,” *Publ. Astron. Soc. Aust.*, vol. 27, no. 3, pp. 272–282, 2010. [Online]. Available: <http://www.publish.csiro.au/paper/AS09082>
- [18] J. D. Romney, “Cross correlators,” in *Synthesis Imaging in Radio Astronomy II*, ser. Astron. Soc. Pac. Conf., G. B. Taylor, C. L. Carilli, and R. A. Perley, Eds., vol. 180, 1999, pp. 57–78. [Online]. Available: <http://adsabs.harvard.edu/abs/1999ASPC..180...57R>
- [19] *Standard definitions of terms for radio wave propagation*, IEEE Std. 211-1997, May 1998.
- [20] K. F. Warnick and B. D. Jeffs, “Efficiencies and system temperature for a beamforming array,” *IEEE Antennas Wireless Propag. Lett.*, vol. 7, pp. 565–568, 2008.
- [21] R. E. Collin, “The receiving antenna,” in *Antenna Theory*, ser. Inter-University Electronics Series, Vol. 7, R. E. Collin and F. J. Zucker, Eds. New York: McGraw-Hill, 1969, vol. 1, ch. 4, pp. 93–137.
- [22] W. D. Cotton, “Calibration and imaging of polarization sensitive Very Long Baseline Interferometer observations,” *Astronomical Journal*, vol. 106, pp. 1241–1248, Sep. 1993. [Online]. Available: <http://adsabs.harvard.edu/abs/1993AJ....106.1241C>
- [23] G. Stokes, “On the composition and resolution of streams of polarized light from different sources,” *Trans. Cambridge Philos. Soc.*, vol. 9, pp. 399–416, 1852.
- [24] J. S. Hollis, T. J. Lyon, and L. Clayton, Eds., *Microwave antenna measurements*, 2nd ed. Scientific-Atlanta, 1971.
- [25] B. Veidt, G. Hovey, T. Burgess, R. Smegal, R. Messing, A. Willis, A. Gray, and P. Dewdney, “Demonstration of a dual-polarized phased-array feed,” *IEEE Trans. Antennas Propag.*, vol. 59, no. 6, pp. 2047–2057, Jun. 2011.
- [26] A. Ludwig, “The definition of cross polarization,” *IEEE Trans. Antennas Propag.*, vol. 21, no. 1, pp. 116–119, 1973.
- [27] W. L. Stutzman and G. A. Thiel, *Antenna theory and design*, 2nd ed. USA: John Wiley and Sons, Inc., 1998.

REFERENCES

- [28] P. J. Napier, “The primary antenna elements,” in *Synthesis Imaging in Radio Astronomy II*, ser. Astron. Soc. Pac. Conf., G. B. Taylor, C. L. Carill, and R. A. Perley, Eds., vol. 180, 1999, pp. 37–56. [Online]. Available: <http://adsabs.harvard.edu/abs/1999ASPC..180...37N>
- [29] P. C. Crane and P. J. Napier, “Sensitivity,” in *Synthesis Imaging in Radio Astronomy*, ser. Astron. Soc. Pac. Conf., R. A. Perley, F. R. Schwab, and A. H. Bridle, Eds., vol. 6, Jun. 1989, pp. 139–165. [Online]. Available: <http://adsabs.harvard.edu/abs/1989ASPC...6..139C>
- [30] S. Johnston and A. Gray, “Surveys with the xNTD and CLAR,” SKA Telescope Memo, SKA Memo 72, Mar. 1 2006. [Online]. Available: http://www.skatelescope.org/uploaded/24448_72_Johnston.pdf
- [31] K. F. Warnick and B. D. Jeffs, “Gain and aperture efficiency for a reflector antenna with an array feed,” *IEEE Antennas Wireless Propag. Lett.*, vol. 5, no. 1, pp. 499–502, Dec. 2006.
- [32] M. V. Ivashina, M. N. M. Kehn, P. S. Kildal, and R. Maaskant, “Decoupling efficiency of a wideband Vivaldi focal plane array feeding a reflector antenna,” *IEEE Trans. Antennas Propag.*, vol. 57, no. 2, pp. 373–382, Feb. 2009.
- [33] K. F. Warnick, M. V. Ivashina, R. Maaskant, and B. Woestenburger, “Unified definitions of efficiencies and system noise temperature for receiving antenna arrays,” *IEEE Trans. Antennas Propag.*, vol. 58, no. 6, pp. 2121–2125, Jun. 2010.
- [34] *Standard definitions of terms for antennas*, IEEE Std. 145-1993, Mar. 1993.
- [35] P. J. Hall, R. T. Schilizzi, P. E. F. Dewdney, and T. J. W. Lazio, “The Square Kilometer Array (SKA) radio telescope: Progress and technical directions,” *Radio Sci. Bull.*, vol. 326, pp. 4–19, Sep. 2008. [Online]. Available: http://astronomy.curtin.edu.au/local/docs/PHall_RSB_reprint.pdf
- [36] P. J. Hall, “Phased array feed and multi-feed cluster naming,” Personal Communication, 2005.
- [37] B. Veidt and P. Dewdney, “Development of a phased-array feed demonstrator for radio telescopes,” in *ANTEM Symposium*. Saint-Malo, France, Jun. 2005.
- [38] K. F. Warnick, B. D. Jeffs, J. Landon, J. Waldron, D. Jones, J. R. Fisher, and R. Norrod, “Beamforming and imaging with the

- BYU/NRAO L-band 19-element phased array feed,” in *ANTEM Symposium*, Banff, AB, Feb. 15–18, 2009, pp. 1–4.
- [39] W. A. van Cappellen, L. Bakker, and T. A. Oosterloo, “Experimental results of a 112 element phased array feed for the Westerbork Synthesis Radio Telescope,” in *IEEE AP-S Int. Symp. Digest*, Charleston, SC, Jun. 1–5, 2009, pp. 1–4.
- [40] M. V. Ivashina and J. D. B. A. van Ardenne, “A way to improve the field of view of the radiotelescope with a dense focal plane array,” in *Proc. 12th International Conference Microwave and Telecommunication Technology*. Weber Publishing, 2002, pp. 278–281.
- [41] S. G. Hay, J. D. O’Sullivan, J. S. Kot, C. Granet, A. Grancea, A. R. Forsyth, and D. B. Hayman, “Focal plane array development for ASKAP (Australian SKA Pathfinder),” in *Eu. Conf. on Antennas and Propagation (EuCAP)*, Edinburgh, Nov. 2007, pp. 1–5.
- [42] N.-T. Huang, R. Mittra, M. Ivashina, and R. Maaskant, “Numerical study of a dual-polarized focal plane array (FPA) with Vivaldi elements placed in the vicinity of a large feed box using the parallelized FDTD code GEMS,” in *IEEE AP-S Int. Symp. Digest*, Charleston, SC, Jun. 1–5, 2009, pp. 1–4.
- [43] M. Ng Mou Kehn, M. V. Ivashina, P.-S. Kildal, and R. Maaskant, “Definition of unifying decoupling efficiency of different array antennas—case study of dense focal plane array feed for parabolic reflector,” *AEU - International Journal of Electronics and Communications*, vol. 64, no. 5, pp. 403–412, 2010. [Online]. Available: <http://www.sciencedirect.com/science/article/B7GWW-4WFGJWT-1/2/9f5cbd6cd6d15fea6c8977b09eb3cf1f>
- [44] S. J. Blank and W. A. Imbriale, “Array feed synthesis for correction of reflector distortion and vernier beamsteering,” *IEEE Trans. Antennas Propag.*, vol. 36, no. 10, pp. 1351–1358, 1988.
- [45] A. R. Cherrette, R. J. Acosta, P. T. Lam, and S. W. Lee, “Compensation of reflector antenna surface distortion using an array,” *IEEE Trans. Antennas Propag.*, vol. 37, no. 8, pp. 966–978, 1989.
- [46] T. S. Bird, “Antenna feeds,” in *Encyclopedia of RF and microwave engineering*, K. Chang, Ed. John Wiley, 2005, vol. 1, pp. 185–217.
- [47] J. G. Bij de Vaate and M. V. Ivashina, “Focal plane arrays: Radio astronomy enters the CCD area,” in *URSI General Assembly*, 2005. [Online]. Available: [http://www.ursi.org/Proceedings/ProcGA05/pdf/J04.7\(0632\).pdf](http://www.ursi.org/Proceedings/ProcGA05/pdf/J04.7(0632).pdf)

REFERENCES

- [48] K. F. Warnick, B. D. Jeffs, J. Landon, J. Waldron, D. Jones, J. R. Fisher, and R. Norrod, "Phased array antenna design and characterization for next-generation radio telescopes," in *IEEE Int. Workshop on Antenna Technology (iWAT)*, Santa Monica, CA, Mar. 2–4, 2009, pp. 1–4.
- [49] M. Born and E. Wolf, *Principles of Optics: Electromagnetic theory of propagation, interference and diffraction of light*, 7th ed. Cambridge University Press, 1999.
- [50] R. C. Spencer, C. J. Sletten, and J. E. Walsh, "Correction of spherical aberration by a phased line source," in *Proc. National Electronics Conference*, vol. 5. National Engineering Conference, inc., 1949, pp. 320–333.
- [51] A. Love, "Spherical reflecting antennas with corrected line sources," *Proc. IRE*, vol. 10, no. 5, pp. 529–537, Sep. 1962.
- [52] W. E. Gordon, "Arecibo Ionospheric Observatory," *Science*, vol. 146, pp. 26–30, 1964.
- [53] C. Sletten, R. Mack, W. Mavroides, and H. Johanson, "Corrective line sources for paraboloids," *Antennas and Propagation, IRE Transactions on*, vol. 6, no. 3, pp. 239–251, Jul. 1958.
- [54] R. J. Mailloux, "Hybrid antennas," in *The Handbook of Antenna Design*, ser. IEE electromagnetic waves series (vol. 15), A. W. Rudge, Ed. Peter Peregrinus, 1982, vol. 1, ch. 5, pp. 415–465.
- [55] L. J. Ricardi, R. N. Assaly, and W. C. Danforth, Jr., "A mechanically fixed radar antenna with scanning capability," Massachusetts Inst. of Tech. Lexington Lincoln Lab., Tech. Rep. 315G-2, Oct. 16 1961, AS-TIA No. 266048.
- [56] H. Ward, C. Fowler, and H. Lipson, "Gca radars: Their history and state of development," *Proc. IEEE*, vol. 62, no. 6, pp. 705–716, Jun. 1974.
- [57] P. Loux and R. Martin, "Efficient aberration correction with a transverse focal plane array technique," in *Proc. IRE International Convention Record*, vol. 12. IEEE, 1964, pp. 125–131.
- [58] A. W. Rudge and M. J. Withers, "Beam-scanning primary feed for parabolic reflectors," *Electronics Letters*, vol. 5, pp. 39–41, Feb. 6, 1969.
- [59] P. Shelton, "Multiple-feed systems for objectives," *IEEE Trans. Antennas Propag.*, vol. 13, no. 6, pp. 992–994, Nov. 1965.

-
- [60] E. A. Ohm, "A proposed multiple-beam microwave antenna for earth stations and satellites," *Bell Systems Technical Journal*, vol. 53, pp. 1657–1665, 1974. [Online]. Available: <http://www.alcatel-lucent.com/bstj/vol53-1974/articles/bstj53-8-1657.pdf>
- [61] V. Galindo-Israel, S.-W. Lee, and R. Mittra, "Synthesis of a laterally displaced cluster feed for a reflector antenna with application to multiple beams and contoured patterns," *IEEE Trans. Antennas Propag.*, vol. 26, no. 2, pp. 220–228, 1978.
- [62] E. Ohm, "Multifixed-beam satellite antenna with full area coverage and a rain-tolerant polarization distribution," *IEEE Trans. Antennas Propag.*, vol. 29, no. 6, pp. 937–943, Nov. 1981.
- [63] G. T. Poulton, T. S. Bird, S. G. Hay, and Y. K. Choi, "Rigorous design of an antenna for AUSSAT-B," in *IEEE AP-S Int. Symp. Digest*, vol. 4, 1990, pp. 1900–1903.
- [64] G. T. Poulton and S. G. Hay, "Efficient design of shaped reflectors using successive projections," *Electronics Letters*, vol. 27, no. 23, pp. 2156–2158, 1991.
- [65] K. Tokunaga, H. Tsunoda, Y. Matsumoto, and T. Ohira, "Electric design and prototype development of phased array feed for onboard reflector antennas," *Electronics and Communications in Japan (Part I: Communications)*, vol. 84, no. 6, pp. 22–31, 2001. [Online]. Available: [http://dx.doi.org/10.1002/1520-6424\(200106\)84:6<22::AID-ECJA3>3.0.CO;2-0](http://dx.doi.org/10.1002/1520-6424(200106)84:6<22::AID-ECJA3>3.0.CO;2-0)
- [66] W. L. Williams and J. M. Howell, "Communications satellite antennas with on-orbit pattern flexibility," *Microwave Journal*, vol. 8, pp. 22–43, Aug. 2004.
- [67] R. Sorbello, P. Karmel, and R. Gruner, "Feed array and beam forming network design for a reconfigurable satellite antenna," in *IEEE AP-S Int. Symp. Digest*, vol. 18, 1980, pp. 78–81.
- [68] P. Balling, "Digital beamforming antenna RF design and analysis—impact of amplifier errors," in *8th COST 260 Meeting on Smart Antenna Computer Aided Design & Technology*. Université de Rennes I, Rennes, France, Oct. 2000. [Online]. Available: <http://www.emi.dtu.dk/research/afg/cost260/rennes/balling.pdf>
- [69] T. S. Bird, "Mode coupling in a planar circular waveguide array," *Microwaves, Optics and Acoustics*, vol. 3, no. 5, pp. 172–180, Sep. 1979.

REFERENCES

- [70] —, “Analysis of mutual coupling in finite arrays of different-sized,” *IEEE Trans. Antennas Propag.*, vol. 38, no. 2, pp. 166–172, 1990.
- [71] T. S. Bird and D. G. Bateman, “Mutual coupling between rotated horns in a ground plane,” *IEEE Trans. Antennas Propag.*, vol. 42, no. 7, pp. 1000–1006, 1994.
- [72] T. S. Bird, “Improved solution for mode coupling in different-sized circular apertures and its application,” *IEE Proc. H: Microwaves Antenn. Propag.*, vol. 143, no. 6, pp. 457–464, 1996.
- [73] —, “Mutual coupling in arrays of coaxial waveguides and horns,” *IEEE Trans. Antennas Propag.*, vol. 52, no. 3, pp. 821–829, 2004.
- [74] B. Minnett, H.; Thomas, “A method of synthesizing radiation patterns with axial symmetry,” *IEEE Trans. Antennas Propag.*, vol. 14, no. 5, pp. 654–656, Sep. 1966.
- [75] B. Thomas, “Matching focal-region fields with hybrid modes,” *IEEE Trans. Antennas Propag.*, vol. 18, no. 3, pp. 404–405, 1970.
- [76] T. Bird, J. Boomars, and P. Clarricoats, “Multiple-beam dual-offset reflector antenna with an array feed,” *Electronics Letters*, vol. 14, no. 14, pp. 439–441, 6 1978.
- [77] T. S. Bird, “Contoured-beam synthesis for array-fed reflector antennas by field correlation,” *Proc. Inst. Elect. Eng. Microwaves, Opt. Antennas*, vol. 129, pp. 293–298, Dec. 1982.
- [78] T. J. Cornwell and P. J. Napier, “The focal plane coherence function of an imaging antenna and its use in measuring and correcting aberrations,” *Radio Sci.*, vol. 23, pp. 739–748, 1988.
- [79] R. Padman, “Optical fundamentals for array feeds,” in *Multi-feed systems for radio telescopes*, ser. Astron. Soc. Pac. Conf., vol. 75, Tucson, AZ, May 16–18, 1994. [Online]. Available: <http://adsabs.harvard.edu/abs/1995ASPC...75....3P>
- [80] K. Bahadori and Y. Rahmat-Samii, “An array-compensated spherical reflector antenna for a very large number of scanned beams,” *IEEE Trans. Antennas Propag.*, vol. 53, no. 11, pp. 3547–3555, 2005.
- [81] D. T. Emerson and J. M. Payne, Eds., *Multi-feed systems for radio telescopes*, ser. Astron. Soc. Pac. Conf., vol. 75, Tucson, AZ, May 16–18, 1994.
- [82] L. Staveley-Smith, W. E. Wilson, T. S. Bird, M. J. Disney, R. D. Ekers, K. C. Freeman, R. F. Haynes, M. W. Sinclair, R. A. Vaile, R. L.

- Webster, and A. E. Wright, "The Parkes 21 cm multibeam receiver," *Publ. Astron. Soc. Aust.*, vol. 13, pp. 243–248, Nov. 1996.
- [83] J. F. Johansson, "Fundamental limits for focal-plane array efficiency," in *Multi-feed systems for radio telescopes*, ser. Astron. Soc. Pac. Conf., vol. 75, Tucson, AZ, May 16–18, 1994, pp. 34–41. [Online]. Available: <http://adsabs.harvard.edu/abs/1995ASPC...75...34J>
- [84] B. Veidt, "Focal-plane array architectures: horn clusters vs. phase-array techniques," International Square Kilometre Array Steering Committee, SKA Memo 71, 2006. [Online]. Available: http://www.skatelescope.org/PDF/memos/71_Veidt.pdf
- [85] S. G. Hay, "Comparison of single-ended and differential beamforming on the efficiency of a checkerboard phased array feed in offset- and front-fed reflectors," in *Eu. Conf. on Antennas and Propagation (EuCAP)*, Apr. 2010, pp. 1–5.
- [86] T. Oosterloo, M. Verheijen, W. van Cappellen, L. Bakker, G. Heald, and M. Ivashina, "Apertif—the focal-plane array system for the WSRT," in *Widefield Science and Technology for the SKA, SKADS Conference, Chateau de Limelette, Belgium*, Nov. 4–6 2009. [Online]. Available: <http://www.citebase.org/abstract?id=oai:arXiv.org:0912.0093>
- [87] J. Bunton and S. Hay, "Achievable field of view of chequerboard phased array feed," in *Int. Conf. on Electromagnetics in Advanced Applications (ICEAA)*, Sep. 2010, pp. 728–730.
- [88] A. W. Rudge and D. E. N. Davies, "Electronically controllable primary feed for profile-error compensation of large parabolic reflectors," *Proc. IEE*, vol. 117, no. 2, pp. 351–358, Feb. 1970.
- [89] W. L. Smith, W. T. Stutzman, "A pattern synthesis technique for array feeds to improve radiation performance of large distorted reflector antennas," *IEEE Trans. Antennas Propag.*, vol. 40, pp. 57–62, Jan. 1992.
- [90] L. L. Porras and A. G. Pino, "Synthesis of array feeds for optimum illumination of reflector antennas and low spillover," *Microwave Opt Technol Lett*, vol. 15, no. 5, pp. 334–338, 1997.
- [91] G. T. Poulton, "Minimisation of spectrometer ripple in prime focus radiotelescope," CSIRO Div. Radiophysics, Tech. Rep. RPP 2170(L), 1974.

REFERENCES

- [92] D. R. Williams, “A harmonic analysis solution to the Parkes spectrometer baseline ripple,” *Publ. Astron. Soc. Aust.*, vol. 4, pp. 264–266, 1981.
- [93] C. K. Hansen, K. F. Warnick, B. D. Jeffs, J. R. Fisher, and R. Bradley, “Interference mitigation using a focal plane array,” *Radio Sci.*, vol. 40, p. RS5S16, Jun. 2005.
- [94] B. D. Jeffs, K. F. Warnick, R. Fisher, R. Norrod, J. Landon, D. Jones, J. Waldron, M. Elmer, and A. Stemmons, “Interference cancellation with a focal plane array,” Nov. 5 2007, Presentation at NROA, Green Bank. [Online]. Available: http://wiki.gb.nrao.edu/pub/Electronics/ResultPresentations/JeffsNov5_07.pdf
- [95] T. Gunaratne, L. Bruton, and P. Agathoklis, “Broadband beam-forming of focal plane array (FPA) signals using real-time spatio-temporal 3D FIR frustum digital filters,” *IEEE Trans. Antennas Propag.*, vol. 59, no. 6, pp. 2029–2040, Jun. 2011.
- [96] T. S. Bird and D. B. Hayman, “Focal-plane array concepts for the Parkes radio telescope,” in *URSI General Assembly*. Lille, France, Sep. 1996.
- [97] K. F. Warnick and P. Russer, “Quantifying the noise penalty for a mutually coupled array,” in *IEEE AP-S Int. Symp. Digest*, San Diego, CA, Jul. 5–11, 2008, pp. 1–4.
- [98] M. Roy and D. George, “Estimation of coupled noise in low noise phased array antennas,” *IEEE Trans. Antennas Propag.*, vol. 59, no. 6, pp. 1846–1854, Jun. 2011.
- [99] S. G. Hay and J. D. O’Sullivan, “Analysis of common-mode effects in a dual-polarized planar connected-array antenna,” *Radio Sci.*, vol. 43, pp. 1–9, Dec. 2008.
- [100] J. Simons, J. Bij de Vaate, M. Ivashina, M. Zuliani, V. Natale, and N. Roddis, “Design of a focal plane array system at cryogenic temperatures,” in *Eu. Conf. on Antennas and Propagation (EuCAP)*, Nov. 2006, pp. 1–5.
- [101] R. Norrod, J. Fisher, B. Jeffs, and K. Warnick, “Development of cryogenic phased array feeds for radio astronomy antennas,” in *IEEE Int. Symp. on Phased Array Systems and Technology*, Oct. 2010, pp. 629–631.
- [102] R. T. Schilizzi, P. Alexander, J. M. Cordes, P. E. Dewdney, R. D. Ekers, A. J. Faulkner, B. M. Gaensler, P. J. Hall, J. L. Jonas,

- and K. I. Kellermann, "Preliminary specifications for the Square Kilometre Array," SKA Telescope Memo, Tech. Rep. 100, Dec. 10 2007. [Online]. Available: http://www.skatelescope.org/uploaded/5110_100_Memo_Schilizzi.pdf
- [103] S. Weinreb, "Noise temperature estimates for a next generation very large microwave array [HEMT LNAs]," in *IEEE MTT-S Int. Microwave Symp. Digest*, vol. 2, Jun. 1998, pp. 673–676.
- [104] L. Bakker, "Progress on FPA LNA developments and LNA characterisation," in *1st RadioNet-FP7 Engineering Forum Workshop*, Jun. 2009.
- [105] CSIRO. Australian Square Kilometre Array Pathfinder (ASKAP). Accessed 2011-03-01. [Online]. Available: <http://www.atnf.csiro.au/projects/askap/index.html>
- [106] A. O. Boryssenko, D. H. Schaubert, and C. Craeye, "A wave-based model for mutual coupling and truncation in finite tapered-slot phased arrays," in *IEEE AP-S Int. Symp. Digest*, vol. 4, 2003, pp. 11–14.
- [107] D. H. Schaubert, A. O. Boryssenko, and T.-H. Chio, "Analysis of finite arrays of wideband tapered slot antennas," in *URSI General Assembly*, 2002.
- [108] C. Craeye, A. O. Boryssenko, and D. H. Schaubert, "Computation of truncation effects in broadband tapered-slot phased arrays using efficient frequency-domain and time-domain approaches," in *IEE Int. Conf. on Antennas and Propagation (ICAP)*, vol. 2, 2003, pp. 445–448.
- [109] D. Ferris, "A baseband receiver architecture for medium-N SKA," in *International SKA Meeting*. Groningen, 2002. [Online]. Available: http://www.atnf.csiro.au/projects/ska/techdocs/Ferris_BBRxArcchi.pdf
- [110] D. H. Schaubert, A. O. Boryssenko, A. van Ardenne, J. Bij de Vaate, and C. Craeye, "The Square Kilometer Array (SKA) antenna," in *IEEE Int. Symp. on Phased Array Systems and Technology*, 2003, pp. 351–358.
- [111] J. D. Bunton, J. Pathikulangara, J. Joseph, T. Bateman, and L. de Souza, "ASKAP beamformer development," in *URSI Workshop on Applications of Radio Science*, 2008.
- [112] G. Cortes-Medellin, K. F. Warnick, and B. Jeffs, "Obtaining the simulated response of a 19 element focal phased array for the feasibility study for the Arecibo radio telescope," in

REFERENCES

- Int. Workshop on Phased Array Antenna Systems for Radio Astronomy*. Brigham Young University, Provo, Utah, USA, May 3–5 2010. [Online]. Available: http://csas.ee.byu.edu/docs/Workshop/BYU_GCortes_PAF_Workshop_fin.pdf
- [113] H. Q. Gan, C. J. Jin, H. Y. Zhang, and Y. Su, “A way to improve the field of view of large aperture radio telescopes,” *Chinese Astronomy and Astrophysics*, vol. 29, no. 3, pp. 343–352, 2005.
 - [114] C. Jin, K. Zhu, H. Gan, and R. Nan, “PAF for the FAST telescope,” in *Int. Workshop on Phased Array Antenna Systems for Radio Astronomy*. Brigham Young University, Provo, Utah, USA, May 3–5 2010. [Online]. Available: <http://csas.ee.byu.edu/docs/Workshop/BYU-FAST-2010-0503-PAF-workshop-Utah.pdf>
 - [115] P. J. Hall, “An SKA engineering overview,” International Square Kilometre Array Steering Committee, SKA Memo 91, 2007.
 - [116] P. E. Dewdney, P. J. Hall, R. T. Schilizzi, and T. J. L. W. Lazio, “The Square Kilometre Array,” *Proc. IEEE*, vol. 97, no. 8, pp. 1482–1496, Aug. 2009.
 - [117] C. Carilli and S. Rawlings, Eds., *Science with the Square Kilometre Array*, ser. New Astronomy Reviews. Elsevier, 2004, vol. 48. [Online]. Available: <http://www.aoc.nrao.edu/~ccarilli/CHAPS.shtml>
 - [118] P. Hall, “The Square Kilometre Array: An international engineering perspective,” in *The Square Kilometre Array: An International Engineering Perspective*, P. J. Hall, Ed. Springer Netherlands, 2005, pp. 5–16.
 - [119] B. Veidt, E. Reid, and P. Dewdney, “FPA developments for the LAR,” in *Focal Plane Array Workshop*. Dwingeloo, The Netherlands: AS-TRON, May 2004.
 - [120] B. Veidt and P. Dewdney, “A phased-array feed demonstrator for radio telescopes,” in *URSI General Assembly*, 2005.
 - [121] J. D. Bunton, “Cylindrical reflectors,” *Experimental Astron.*, vol. 17, no. 1–3, pp. 185–189, 2004.
 - [122] D. Deboer, R. Ackermann, L. Blitz, D. Bock, G. Bower, M. Davis, J. Dreher, G. Engargiola, M. Fleming, Girmay-Keleta, G. Harp, J. Lugten, J. Tarter, D. Thornton, N. Wadefalk, S. Weinreb, and W. J. Welch, “The allen telescope array,” in *The Square Kilometre Array: An Engineering Perspective*, P. J. Hall, Ed. Springer Netherlands, 2005, pp. 19–34.

-
- [123] J. Kot, R. Donelson, N. Nikolic, D. Hayman, M. O'Shea, and G. Peeters, "A spherical lens for the SKA," *Experimental Astron.*, vol. 17, no. 1–3, pp. 141–148, 2004.
 - [124] A. Ardenne, P. Wilkinson, P. Patel, and J. Vaate, "Electronic multi-beam radio astronomy concept: Embrace a demonstrator for the european ska program," in *The Square Kilometre Array: An Engineering Perspective*, P. J. Hall, Ed. Springer Netherlands, 2005, pp. 65–77.
 - [125] E. Woestenburg and J. Kuenen, "Low noise performance perspectives of wideband aperture phased arrays," in *The Square Kilometre Array: An Engineering Perspective*, P. J. Hall, Ed. Springer Netherlands, 2005, pp. 89–99.
 - [126] W. A. Cappellen, J. D. Bregman, and M. J. Arts, "Effective sensitivity of a non-uniform phased array of short dipoles," in *The Square Kilometre Array: An Engineering Perspective*, P. J. Hall, Ed. Springer Netherlands, 2005, pp. 101–109.
 - [127] R. Norris, "The Australian SKA New Technology Demonstrator program," *Experimental Astron.*, vol. 17, pp. 79–85, 2004.
 - [128] D. B. Hayman and L. Li, "Measurement of a prototype CSIRO Lunenburg lens," CSIRO ICT Centre, Tech. Rep. 04/1819, Apr. 2004.
 - [129] T. S. Bird, D. B. Hayman, A. R. Forsyth, K. J. Greene, I. W. Chu, and D. G. Bateman, "A close-packed dielectric-loaded horn array for 60 GHz," in *Asia-Pacific Microwave Conf. Proc. (APMC)*, vol. 3, Taipei, Dec.3–6 2001, pp. 1362–1365.
 - [130] K. A. S. Qassim and N. J. McEwan, "Focal plane dielectric rod arrays with printed launchers," in *IEE Int. Conf. on Antennas and Propagation (ICAP)*, vol. 2, Edinburgh, UK, 1993, pp. 792–795.
 - [131] S. Hanham and T. Bird, "A focal-plane array of dielectric rod antennas for THz imaging," in *Eu. Conf. on Antennas and Propagation (EuCAP)*, Apr. 2011, pp. 3173–3175.
 - [132] T. S. Bird, "Coaxial feed array for a short focal-length reflector," in *IEEE AP-S Int. Symp. Digest*, vol. 3, 1997, pp. 1618–1621.
 - [133] K. Warnick, D. Carter, T. Webb, J. Landon, M. Elmer, and B. Jeffs, "Design and characterization of an active impedance matched low-noise phased array feed," *IEEE Trans. Antennas Propag.*, vol. 59, no. 6, pp. 1876–1885, Jun. 2011.
 - [134] K. F. Warnick, "Optimal noise matching for a phased array feed," in *IEEE AP-S Int. Symp. Digest*, Charleston, SC, Jun. 1–5, 2009, pp. 1–4.

REFERENCES

- [135] J. Landon, M. Elmer, J. Waldron, D. Jones, A. Stemmons, B. D. Jeffs, K. F. Warnick, J. R. Fisher, and R. D. Norrod, "Phased array feed calibration, beamforming, and imaging," *The Astronomical Journal*, vol. 139, no. 3, pp. 1154–1167, 2010. [Online]. Available: <http://stacks.iop.org/1538-3881/139/i=3/a=1154>
- [136] K. Warnick, B. Jeffs, D. Carter, T. Webb, J. Landon, M. Elmer, R. Norrod, and J. Fisher, "Active impedance matching, calibration, and interference mitigation for the BYU/NRAO L-band phased array feed," in *IEEE Int. Symp. on Phased Array Systems and Technology*, Oct. 2010, pp. 624–628.
- [137] D. H. Schaubert, "Wide-band phased arrays of Vivaldi notch antennas," in *IEE Int. Conf. on Antennas and Propagation (ICAP)*, vol. 1, 1997, pp. 6–12.
- [138] D. H. Schaubert and T.-H. Chio, "Wideband Vivaldi arrays for large aperture antennas," in *Perspectives on Radio Astronomy—Technologies for Large Antenna Arrays*, A. B. Smolders and M. P. van Haarlem, Eds. Netherlands Foundation for Research in Astronomy, 1999.
- [139] J. P. Weem, B. M. Notaros, and Z. Popovic, "Broadband element array considerations for SKA," in *Perspectives on Radio Astronomy—Technology for Large Antenna Arrays*. Netherlands Foundation for Research on Astronomy, 1999.
- [140] P. J. Gibson, "The Vivaldi aerial," in *Proc. 9th European Microwave Conference*, 1979.
- [141] Y. H. Choung and C. C. Chen, "44 GHz slotline phased array antenna," in *IEEE AP-S Int. Symp. Digest*, vol. 3, 1989, pp. 1730–1733.
- [142] E. Gazit, "Improved design of the Vivaldi antenna," *IEE Proc. H: Microwaves Antenn. Propag.*, vol. 135, no. 2, pp. 89–92, 1988.
- [143] N. Fourikis, N. Lioutas, and N. V. Shuley, "Parametric study of the co- and crosspolarisation characteristics of tapered planar and antipodal slotline antennas," *IEE Proc. H: Microwaves Antenn. Propag.*, vol. 140, no. 1, pp. 17–22, 1993.
- [144] J. D. S. Langley, P. S. Hall, and P. Newham, "Novel ultrawide-bandwidth Vivaldi antenna with low crosspolarisation," *Electronics Letters*, vol. 29, pp. 23, 24, Nov. 1993.
- [145] —, "Balanced antipodal Vivaldi antenna for wide bandwidth phased arrays," *IEE Proc. H: Microwaves Antenn. Propag.*, vol. 143, no. 2, pp. 97–102, 1996.

-
- [146] S. Kasturi, A. O. Boryssenko, and S. D. H., "Infinite arrays of tapered slot antennas with and without dielectric substrate," in *Antenna Applications Symposium*. Robert Allerton Park, 2002.
 - [147] A. O. Boryssenko and D. H. Schaubert, "Single-polarized, dielectric-free, Vivaldi tapered slot phased array: performance prediction," in *IEEE AP-S Int. Symp. Digest*, vol. 2, 2001, pp. 436–439.
 - [148] —, "A design approach for small arrays of dielectric-free Vivaldi antennas to minimize truncation effects," in *IEEE Int. Symp. on Phased Array Systems and Technology*, 2003, pp. 399–404.
 - [149] J. Bij de Vaate, L. Bakker, E. Woestenburger, R. Witvers, G. Kant, and W. van Cappellen, "Low cost low noise phased-array feeding systems for SKA pathfinders," in *ANTEM conference, Banff, Canada*, 2009.
 - [150] E. Thiele and A. Taflov, "FD-TD analysis of Vivaldi flared horn antennas and arrays," *IEEE Trans. Antennas Propag.*, vol. 42, no. 5, pp. 633–641, 1994.
 - [151] T. A. Axness, R. V. Coffman, B. A. Kopp, and K. W. O'Haver, "Shared aperture technology development," *Johns Hopkins APL Technical Digest*, vol. 17, no. 3, pp. 285–294, 1996. [Online]. Available: <http://techdigest.jhuapl.edu/td1703/axness.pdf>
 - [152] H. Loui, J. P. Weem, and Z. Popovic, "A dual-band dual-polarized nested Vivaldi slot array with multilevel ground plane," *IEEE Trans. Antennas Propag.*, vol. 51, no. 9, pp. 2168–2175, 2003.
 - [153] H. Holter, "A new type of antenna element for wide-band wide-angle dual polarized phased array antennas," in *IEEE Int. Symp. on Phased Array Systems and Technology*, 2003, pp. 393–398.
 - [154] G. Virone, R. Sarkis, C. Craeye, G. Addamo, and O. Peverini, "Gridded vivaldi antenna feed system for the northern cross radio telescope," *IEEE Trans. Antennas Propag.*, vol. 59, no. 6, pp. 1963–1971, Jun. 2011.
 - [155] Y. Mushiake, "The input impedance of slit antennas," *J. IEE Japan*, vol. 69, no. 3, pp. 87–88, Mar. 1949.
 - [156] —, "Self-complementary antennas," *IEEE Antennas Propag. Mag.*, vol. 34, no. 6, pp. 23–29, 1992.
 - [157] X. Dardenne and C. Craeye, "Simulation of the effects of a ground plane on the radiation characteristics of self-complementary arrays," in *IEEE AP-S Int. Symp. Digest*, vol. 1, 2003, pp. 383–386.

REFERENCES

- [158] D. B. Hayman, "Experimental verification of array modelling," in *Tenth Australian Symposium on Antennas*. Sydney, Australia: CSIRO ICT Centre, Feb. 14–15 2007, p. 68.
- [159] R. C. Hansen, "Dipole arrays with non-Foster circuits," in *IEEE Int. Symp. on Phased Array Systems and Technology*, 2003, pp. 40–44.
- [160] S. G. Hay, "FPA modelling concepts at CSIRO," in *Focal Plane Array Workshop*, ASTRON, Dwingeloo, the Netherlands, Jun. 2005. [Online]. Available: <http://www.astron.nl/fpaworkshop2005/>
- [161] S. Hay, J. O'Sullivan, and R. Mittra, "Connected patch array analysis using the characteristic basis function method," *IEEE Trans. Antennas Propag.*, vol. 59, no. 6, pp. 1828–1837, Jun. 2011.
- [162] M. V. Ivashina and J. D. Bregman, "Vivaldi array feed for radio telescope with small F/D ratio," in *Focal Plane Array Workshop*. Dwingeloo, The Netherlands: ASTRON, May 2004.
- [163] J. R. Nagel, K. F. Warnick, B. D. Jeffs, J. R. Fisher, and R. Bradley, "Experimental verification of radio frequency interference mitigation with a focal plane array feed," *Radio Sci.*, vol. 42, p. RS6013, 2007.
- [164] J. D. O'Sullivan, F. Cooray, C. Granet, R. Gough, S. Hay, D. B. Hayman, M. Kesteven, J. Kot, A. Grancea, and R. Shaw, "Phased array feed development for the Australian SKA Pathfinder," presented at the URSI General Assembly, Sep. 2008.
- [165] P.-S. Kildal, L. Baker, and T. Hagfors, "The arecibo upgrading: electrical design and expected performance of the dual-reflector feed system," *Proc. IEEE*, vol. 82, no. 5, pp. 714–724, May 1994.
- [166] C. Craeye, A. B. Smolders, A. G. Tijhuis, and D. H. Schaubert, "Computation of finite array effects in the framework of the Square Kilometer Array project," in *IEE Int. Conf. on Antennas and Propagation (ICAP)*, vol. 1, Manchester, Apr. 17–20, 2001, pp. 298–301.
- [167] J. Simons, J. Bij de Vaate, M. V. Ivashina, M. Zuliani, V. Natale, and N. Roddis, "Design of a focal plane array system at cryogenic temperatures," in *Eu. Conf. on Antennas and Propagation (EuCAP)*, Nice, Nov. 6–10, 2006, pp. 1–6.
- [168] M. V. Ivashina, J. Simons, and J. Bij de Vaate, "Efficiency analysis of focal plane arrays in deep dishes," *Experimental Astron.*, vol. 17, no. 1-3, pp. 149–162, Jun. 2004.
- [169] M. V. Ivashina, J. D. Bregman, J.-G. Bij de Vaate, L. Li, and A. J. Parfitt, "Experimental results for a focal plane array, synthesized with conjugate field method," in *IEEE AP-S Int. Symp. Digest*, 2004.

-
- [170] H. van der Marel, "Measurements of Faraday at the WSRT," in *Focal Plane Array Workshop*. Dwingeloo, The Netherlands: ASTRON, May 2004.
- [171] W. A. van Cappellen, J. Bij de Vaate, M. V. Ivashina, L. Bakker, and T. Oosterloo, "Focal plane arrays evolve," in *URSI General Assembly*, 2008, pp. 7–16.
- [172] A. van Ardenne, J. D. Bregman, W. A. van Cappellen, G. W. Kant, and J. Bij de Vaate, "Extending the field of view with phased array techniques: Results of european ska research," *Proc. IEEE*, vol. 97, no. 8, pp. 1531–1542, Aug. 2009.
- [173] D. Glynn, R. Nesti, N. Bij de Vaate, J.G. and Roddis, and E. Limiti, "Realization of a focal plane array receiver system for radio astronomy applications," in *Microwave Conference, 2009. EuMC 2009. European*, Sep. 9 – Oct. 1 2009, pp. 922–925.
- [174] M. A. W. Verheijen, T. A. Oosterloo, W. A. van Cappellen, L. Bakker, M. V. Ivashina, and J. M. van der Hulst, "Apertif, a focal plane array for the WSRT," in *The Evolution of Galaxies Through the Neutral Hydrogen Window*, ser. Am Inst Phys Conf Proc, vol. 1035, Aug. 2008, pp. 265–271.
- [175] R. Braun, "Prospects for a WSRT FPA system: synthesis enters the radio 'CCD era'," in *Focal Plane Array Workshop*. Dwingeloo, May 2004.
- [176] M. Arts, M. Ivashina, O. Iupikov, L. Bakker, and R. van den Brink, "Design of a low-loss low-noise tapered slot phased array feed for reflector antennas," in *Eu. Conf. on Antennas and Propagation (EuCAP)*, Apr. 2010, pp. 1–5.
- [177] K. F. Warnick, B. D. Jeffs, J. Landon, J. Waldron, D. Jones, A. Stemmons, J. R. Fisher, R. Norrod, and R. Bradley, "BYU/NRAO 19 element L-band focal plane array feed sensitivity, efficiency, and RFI mitigation," in *Eu. Conf. on Antennas and Propagation (EuCAP)*, Edinburgh, UK, Nov. 2007. [Online]. Available: http://wiki.gb.nrao.edu/pub/Electronics/ResultPresentations/ArrayFeed.EuCAP_Nov07.pdf
- [178] D. Baker, J. Jonas, A. Loots, D. de Haaij, and R. Booysen, "The Karoo array telescope (KAT) & FPA effort in South Africa," in *Focal Plane Array Workshop*, Dwingeloo, The Netherlands. Dwingeloo, The Netherlands: ASTRON, Jun. 2005. [Online]. Available: http://www.astron.nl/fpaworkshop2005/Monday/Baker_FPA2005.pdf

REFERENCES

- [179] T. S. Bird, D. B. Hayman, S. Jackson, and R. H. Ferris, "Focal plane array related activities at CSIRO," in *Focal Plane Array Workshop*. Dwingeloo, The Netherlands, May 2004.
- [180] D. R. DeBoer, R. G. Gough, J. D. Bunton, T. J. Cornwell, R. J. Beresford, S. Johnston, I. J. Feain, A. E. Schinckel, C. A. Jackson, M. J. Kesteven, A. Chippendale, G. A. Hampson, J. D. O'Sullivan, S. G. Hay, C. E. Jacka, T. W. Sweetnam, M. C. Storey, L. Ball, and B. J. Boyle, "Australian SKA pathfinder: A high-dynamic range wide-field of view survey telescope," *Proc. IEEE*, vol. 97, no. 8, pp. 1507–1521, Aug. 2009.
- [181] A. Chippendale, J. O'Sullivan, J. Reynolds, R. Gough, D. Hayman, S. Hay, R. Shaw, and R.-Y. Qiao, "Testing a 5x4 chequerboard phased array feed," in *Int. Workshop on Phased Array Antenna Systems for Radio Astronomy*. Brigham Young University, Provo, Utah, USA, May 3–5 2010. [Online]. Available: http://csas.ee.byu.edu/docs/Workshop/BYU_Chippendale_2010_05_03_fullres.pdf
- [182] T. Westmeier and S. Johnston, "The Australian Square Kilometre Array Pathfinder," in *International SKA Forum*, 2010. [Online]. Available: http://pos.sissa.it/archive/conferences/112/056/ISKAF2010_056.pdf
- [183] J. Yang, M. Pantaleev, P.-S. Kildal, B. Klein, Y. Karandikar, L. Helldner, N. Wadefalk, and C. Beaudoin, "Cryogenic 2-13 GHz Eleven feed for reflector antennas in future wideband radio telescopes," *IEEE Trans. Antennas Propag.*, vol. 59, no. 6, pp. 1918–1934, Jun. 2011.
- [184] T. Cornwell and J. O'Sullivan, "A plan for NTD initial observations," ATNF, Tech. Rep., May 2005.
- [185] T. Cornwell, "LNSD reconsidered—the Big Gulp option," ATNF, Tech. Rep., Jul. 2005.
- [186] J. Bunton, "SKA signal processing costs," International Square Kilometre Array Steering Committee, SKA Memo 65, 2005.
- [187] S.-W. Lee and Y. Rahmat-Samii, "Simple formulas for designing an offset multibeam parabolic reflector," *IEEE Trans. Antennas Propag.*, vol. 29, no. 3, pp. 472–478, 1981.
- [188] Y. Rahmat-Samii, J. Cramer, P., K. Woo, and S. Lee, "Realizable feed-element patterns for multibeam reflector antenna analysis," *IEEE Trans. Antennas Propag.*, vol. 29, no. 6, pp. 961–963, Nov. 1981.

-
- [189] K. S. Yngvesson, J. F. Johansson, Y. Rahmat-Samii, and Y. S. Kim, "Realizable feed-element patterns and optimum aperture efficiency in," *IEEE Trans. Antennas Propag.*, vol. 36, no. 11, pp. 1637–1641, 1988.
- [190] W. Imbriale, P. Ingerson, and W. Wong, "Large lateral feed displacements in a parabolic reflector," *IEEE Trans. Antennas Propag.*, vol. 22, no. 6, pp. 742–745, 1974.
- [191] P. Lam, S.-W. Lee, D. Chang, and K. Lang, "Directivity optimization of a reflector antenna with cluster feeds: a closed-form solution," *IEEE Trans. Antennas Propag.*, vol. 33, no. 11, pp. 1163–1174, 1985.
- [192] B. Veidt and P. Dewdney, "Bandwidth limits of beamforming networks for low-noise focal-plane arrays," *IEEE Trans. Antennas Propag.*, vol. 53, no. 1, pp. 450–454, 2005.
- [193] J. D. Bunton and S. G. Hay, "SKA cost model for wide field-of-view options," *Experimental Astron.*, vol. 17, no. 1–3, pp. 381–405, 2004.
- [194] J. D. Bregman, "Cost effective frequency ranges for multi-beam dishes, cylinders, aperture arrays, and hybrids," *Experimental Astron.*, vol. 17, pp. 407–416, 2004.
- [195] M. V. Ivashina, M. N. M. Kehn, and P. S. Kildal, "Optimal number of elements and element spacing of wide-band focal plane arrays for a new generation radio telescope," in *Eu. Conf. on Antennas and Propagation (EuCAP)*, Edinburgh, Nov. 11–16, 2007, pp. 1–7.
- [196] D. B. Hayman, T. S. Bird, K. P. Esselle, and P. J. Hall, "Encircled power study of focal plane field for estimating focal plane array size," in *IEEE AP-S Int. Symp. Digest*, vol. 3A, Jul. 3–8, 2005, pp. 371–374.
- [197] W. H. Watson, "The field distribution in the focal plane of a paraboloidal reflector," *IEEE Trans. Antennas Propag.*, vol. 12, no. 5, pp. 561–569, Sep. 1964.
- [198] H. C. Minnett and M. Thomas, B, "Fields in the image space of symmetrical focussing reflectors," *Proc. IEE*, vol. 115, no. 10, pp. 1419–1430, Oct. 1968.
- [199] B. Thomas, H. Minnett, and V. Bao, "Fields in the focal region of a spherical reflector," *IEEE Trans. Antennas Propag.*, vol. 17, no. 2, pp. 229–232, 1969.
- [200] J. J. Stamnes, *Waves in focal regions*. Bristol, England: Adam Hilger, 1986.

REFERENCES

- [201] Y. T. Lo and S. W. Lee, Eds., *The antenna handbook*. Van Nostrand Reinhold (ITP), 1993.
- [202] J. Ruze, "Lateral-feed displacement in a paraboloid," *IEEE Trans. Antennas Propag.*, vol. 13, no. 5, pp. 660–665, Sep. 1965.
- [203] P. Ingerson and W. Wong, "Focal region characteristics of offset fed reflectors," in *IEEE AP-S Int. Symp. Digest*, vol. 12, jun 1974, pp. 121–123.
- [204] A. W. Rudge, "Multiple-beam antennas: Offset reflectors with offset feeds," *IEEE Trans. Antennas Propag.*, vol. 23, no. 3, pp. 317–322, may 1975.
- [205] N. Amitay and H. Zucker, "Compensation of spherical reflector aberrations by planar array feeds," *IEEE Trans. Antennas Propag.*, vol. 20, no. 1, pp. 49–56, 1972.
- [206] C. Granet, I. M. Davis, C. Cantrall, A. Grancea, D. B. Hayman, and A. R. Forsyth, "NTD prime-focus horns," CSIRO ICT Centre, Tech. Rep. 07/019, Nov. 2007.
- [207] C. Granet, J. S. Kot, A. R. Forsyth, M. J. Kesteven, S. G. Hay, and J. D. O'Sullivan, "Reflector options for MIRANdA (Australian SKA Pathfinder)," in *Eu. Conf. on Antennas and Propagation (EuCAP)*, Nov. 2007, Edinburgh, UK, CD-Digest.
- [208] A. W. Rudge and M. J. Withers, "New technique for beam steering with fixed parabolic reflectors (wide angle microwave antenna radiation beam steering with fixed parabolic reflectors, using adaptive primary feed for intercepted field spatial fourier transformation)." *IEE Proc.*, vol. 118, pp. 857–863, Jul. 1971.
- [209] J. R. Fisher and R. F. Bradley, "Full sampling array feeds for radio telescopes," in *Proc. SPIE, Radio Telescopes*, H. R. Butcher, Ed., vol. 4015. SPIE, Jul. 2000, pp. 308–318.
- [210] R. Chantalat, P. Dumon, B. Jecko, M. Thevenot, and T. Monediere, "Interlaced feeds design for a multibeam reflector antenna using a 1-d dielectric pbg resonator," in *IEEE AP-S Int. Symp. Digest*, vol. 4, 2003, pp. 867–870.
- [211] S. Stein, "On cross coupling in multiple-beam antennas," *IEEE Trans. Antennas Propag.*, vol. AP-10, no. 5, pp. 548–557, Sep. 1962.
- [212] J. Allen, "A theoretical limitation on the formation of lossless multiple beams in linear arrays," *Antennas and Propagation, IRE Trans. on*, vol. 9, no. 4, pp. 350–352, Jul. 1961.

-
- [213] A. Ludwig, "Mutual coupling, gain and directivity of an array of two identical antennas," *IEEE Trans. Antennas Propag.*, vol. 24, no. 6, pp. 837–841, 1976.
- [214] J. F. Johansson, "A comparison of some feed types," in *Multi-feed systems for radio telescopes*, ser. Astron. Soc. Pac. Conf., vol. 75, Tucson, AZ, May 16–18, 1994, pp. 34–41. [Online]. Available: <http://adsabs.harvard.edu/abs/1995ASPC...75...82J>
- [215] Y. Lo, "On the beam deviation factor of a parabolic reflector," *Antennas and Propagation, IRE Trans. on*, vol. 8, no. 3, pp. 347–349, may 1960.
- [216] M. V. Ivashina and C. G. M. van't Klooster, "Focal field analyses for front-fed and offset reflector antenna," in *IEEE AP-S Int. Symp. Digest*, vol. 2, 2003, pp. 750–753.
- [217] G. T. Poulton and T. S. Bird, "Earth-station antennas for multiple satellite access," *Journal of Electrical and Electronics Engineering, Australia - IE Aust. and IREE Aust.*, vol. 8, no. 3, pp. 168–176, Sep. 1988.
- [218] C. Granet, J. S. Kot, S. G. Hay, and J. D. OSullivan, "A study of optimized dual-reflector systems with phased array feeds for 'ASKAP'," in *URSI Workshop on Applications of Radio Science*, 2008. [Online]. Available: <http://www.ncrs.org.au/wars/wars2008/Granet%20et%20al%20WARS%202008.pdf>
- [219] P. Hannan, "Microwave antennas derived from the cassegrain telescope," *Antennas and Propagation, IRE Trans. on*, vol. 9, no. 2, pp. 140–153, Mar. 1961.
- [220] C. Granet, "Designing axially symmetric Cassegrain or Gregorian dual-reflector antennas from combinations of prescribed geometric parameters," *IEEE Antennas Propag. Mag.*, vol. 40, no. 2, pp. 76–82, Apr. 1998.
- [221] W. Wong, "On the equivalent parabola technique to predict the performance characteristics of a cassegrainian system with an offset feed," *IEEE Trans. Antennas Propag.*, vol. 21, no. 3, pp. 335–339, May 1973.
- [222] W. Rusch and A. Ludwig, "Determination of the maximum scan-gain contours of a beam-scanning paraboloid and their relation to the petzval surface," *IEEE Trans. Antennas Propag.*, vol. 21, no. 2, pp. 141–147, Mar. 1973.

REFERENCES

- [223] R. Mizzoni, "The cassini high gain antenna (HGA): a survey on electrical requirements, design and performance," in *Spacecraft Antennas, IEE/SEE Seminar on*, may 1994, pp. 6/1–6/10.
- [224] J. S. Waldron, "Nineteen-element phased-array feed development and analysis on effects of focal plane offset and beam steering on sensitivity," Master's thesis, Brigham Young University, 2008. [Online]. Available: <http://contentdm.lib.byu.edu/u?/ETD,1536>
- [225] J. S. Waldron, D. B. Jones, K. F. Warnick, and B. D. Jeffs, "Effects of focal plane array offset and beam steering on sensitivity," in *IEEE AP-S Int. Symp. Digest*, San Diego, CA, Jul. 5–11 2008, pp. 1–4.
- [226] W. van Cappellen, "Efficiencies and sensitivity definitions for reflector antennas in radio-astronomy," in *SKADS MCCT Workshop*, Nov., 26–30 2007. [Online]. Available: <http://www.astron.nl/other/workshop/MCCT/TuesdayCappellen.pdf>
- [227] W. A. Imbriale, *Large Antennas of the Deep Space Network*. Jet Propulsion Laboratory, 2002. [Online]. Available: <http://descanso.jpl.nasa.gov/Monograph/mono.cfm>
- [228] G. L. James, *Geometrical theory of diffraction for electromagnetic waves*, ser. IEE electromagnetic waves series. Peter Peregrinus, 1986.
- [229] K. Pontoppidan, *Technical description of GRASP8*. TICRA, 2002. [Online]. Available: <http://www.ticra.com>
- [230] V. V. S. Prakash and R. Mittra, "Characteristic basis function method: A new technique for efficient solution of method of moments matrix equations," *Microwave and Optical Technology Letters*, vol. 36, no. 2, pp. 95–100, Jan. 2003.
- [231] R. Maaskant, A. G. Tijhuis, R. Mittra, M. V. Ivashina, W. A. van Cappellen, and M. J. Arts, "Hybridization of efficient modeling techniques for fast analysis of large-scale antenna structures in the context of the Square Kilometre Array project," in *European Microwave Conference (EuMC)*, Oct. 27–31, 2008, pp. 837–840.
- [232] S. Hay, F. Cooray, J. O'Sullivan, N.-T. Huang, and R. Mittra, "Numerical and experimental studies of a dual-polarized planar connected-array antenna for the Australian Square Kilometer Array Pathfinder," in *IEEE AP-S Int. Symp. Digest*, Charleston, SC, Jun. 1–5, 2009, pp. 1–4.
- [233] R. Maaskant, M. Ivashina, O. Iupikov, E. Redkina, S. Kasturi, and D. Schaubert, "Analysis of large microstrip-fed tapered slot antenna

- arrays by combining electrodynamic and quasi-static field models,” *IEEE Trans. Antennas Propag.*, vol. 59, no. 6, pp. 1798–1807, Jun. 2011.
- [234] K. F. Warnick and M. A. Jensen, “Effects of mutual coupling on interference mitigation with a focal plane array,” *IEEE Trans. Antennas Propag.*, vol. 53, no. 8, pp. 2490–2498, Aug. 2005.
- [235] R. Maaskant and E. E. M. Woestenburger, “Applying the active antenna impedance to achieve noise match in receiving array antennas,” in *IEEE AP-S Int. Symp. Digest*, Honolulu, HI, Jun. 9–15, 2007, pp. 5889–5892.
- [236] G. T. Poulton, S. H. Lim, and P. H. Masterman, “Calculation of input-voltage standing-wave ratio for a reflector antenna,” *Electronics Letters*, vol. 8, pp. 610–611, Dec. 14 1972.
- [237] G. T. Poulton, “Minimisation of spectrometer ripple in prime focus radiotelescopes,” CSIRO Division of Radiophysics, Tech. Rep. RPP 2170(L), 1974.
- [238] R. Padman, “Reduction of the baseline ripple on spectra recorded with the Parkes radio telescope,” *Publ. Astron. Soc. Aust.*, vol. 3, pp. 111–113, Sep. 1977.
- [239] M. Bandinelli, F. Milani, G. Guida, M. Bercigli, P. Frandsen, S. Sorensen, B. Bencivenga, and M. Sabbadini, “Feed-array design in presence of strong scattering from reflectors,” in *Eu. Conf. on Antennas and Propagation (EuCAP)*, Apr. 2011, pp. 3844–3848.
- [240] L. Belostotski and J. Haslett, “Sub-0.2 db noise figure wideband room-temperature cmos lna with non-50 ohm signal-source impedance,” *IEEE J. Solid-State Circuits*, vol. 42, no. 11, pp. 2492–2502, nov. 2007.
- [241] M. V. Ivashina, R. Maaskant, and B. Woestenburger, “Equivalent system representation to model the beam sensitivity of receiving antenna arrays,” *IEEE Antennas Wireless Propag. Lett.*, vol. 7, pp. 733–737, 2008.
- [242] K. F. Warnick, B. Woestenburger, L. Belostotski, and P. Russer, “Minimizing the noise penalty due to mutual coupling for a receiving array,” *IEEE Trans. Antennas Propag.*, vol. 57, no. 6, pp. 1634–1644, Jun. 2009.
- [243] S. G. Hay, “Maximum-sensitivity matching of connected-array antennas subject to Lange noise constants,” *International Journal of Microwave and Optical Technology*, vol. 5, no. 6, pp. 375–383, Nov.

REFERENCES

2010. [Online]. Available: <http://www.ijmot.com/ijmot/uploaded/trmzswogu.pdf>
- [244] M. L. Morris and M. A. Jensen, "Network model for MIMO systems with coupled antennas and noisy amplifiers," *IEEE Trans. Antennas Propag.*, vol. 53, no. 1, pp. 545–552, 2005.
- [245] K. F. Warnick and M. A. Jensen, "Optimal noise matching for mutually coupled arrays," *IEEE Trans. Antennas Propag.*, vol. 55, no. 6, pp. 1726–1731, Jun. 2007.
- [246] D. A. Jones, "Characterization of a phased array feed model," Master's thesis, Brigham Young University, 2008. [Online]. Available: <http://contentdm.byu.edu/u?/ETD,1494>
- [247] R. Maaskant, "Noise budget analysis of the FPA," in *Focal Plane Array Workshop*. Dwingeloo, Netherlands: ASTRON, 2005.
- [248] R. Maaskant, E. E. M. Woestenburg, and M. J. Arts, "A generalized method of modeling the sensitivity of array antennas at system level," in *European Microwave Conference (EuMC)*, vol. 3, 2004, pp. 1541–1544.
- [249] C. T. Stelzried, A. J. Freiley, and M. S. Reid, "System noise concepts with DSN applications," in *Low-Noise Systems in the Deep Space Network*, M. S. Reid, Ed. Jet Propulsion Laboratory, 2008, ch. 2, pp. 13–94. [Online]. Available: <http://descanso.jpl.nasa.gov/Monograph/mono.cfm>
- [250] A. A. Ksienski, "Signal-processing antennas," in *Antenna Theory*, ser. Inter-University Electronics Series, Vol. 7, R. E. Collin and F. J. Zucker, Eds. New York: McGraw-Hill, 1969, vol. 2, ch. 27, pp. 580–654.
- [251] E. Jacobs, "A figure of merit for signal processing reflector antennas," *IEEE Trans. Antennas Propag.*, vol. 33, no. 1, pp. 100–101, Jan. 1985.
- [252] A. Waldman and G. J. Wooley, "Noise temperature of a phased array receiver," *Microwave Journal*, vol. Sept., pp. 89–96, 1966.
- [253] J. J. Lee, "G/T and noise figure of active array antennas," *IEEE Trans. Antennas Propag.*, vol. 41, no. 2, pp. 241–244, Feb. 1993.
- [254] D. B. Hayman, K. W. Smart, and K. J. Greene, "Measurement of domestic pay TV satellite dishes," in *AMTA Symposium*. Denver, Co., Oct. 2001.

-
- [255] J. Ashkenazy, E. Levine, and D. Treves, "Radiometric measurement of antenna efficiency," *Electronics Letters*, vol. 21, no. 3, pp. 111–112, Jan. 1985.
- [256] D. M. Pozar and B. Kaufman, "Comparison of three methods for the measurement of printed antenna," *IEEE Trans. Antennas Propag.*, vol. 36, no. 1, pp. 136–139, 1988.
- [257] *Standard definitions of terms for antennas*, IEEE Std. 145-1983, Jun. 1983.
- [258] G. Sinclair, "The transmission and reception of elliptically polarized waves," *Proc. IRE*, vol. 38, no. 2, pp. 148–151, Feb. 1950.
- [259] G. Cortes-Medellin, "Antenna noise temperature calculations," Cornell University, Tech. Rep., Oct. 2004.
- [260] D. F. Wait, "Precision measurement of antenna system noise using radio stars," *IEEE Trans. Instrum. Meas.*, vol. 32, no. 1, pp. 110–116, Mar. 1983.
- [261] W. D. Cotton, "Polarization in interferometry," in *Synthesis Imaging in Radio Astronomy II*, ser. Astron. Soc. Pac. Conf., G. B. Taylor, C. L. Carilli, and R. A. Perley, Eds., vol. 180, 1999, pp. 111–126. [Online]. Available: <http://adsabs.harvard.edu/abs/1999ASPC..180..111C>
- [262] B. Van Veen and K. Buckley, "Beamforming: a versatile approach to spatial filtering," *ASSP Magazine, IEEE*, vol. 5, no. 2, pp. 4–24, Apr. 1988.
- [263] J. E. Hudson, *Adaptive Array Principles*. Peter Peregrinus, 1981.
- [264] T. S. Bird, "Feed antennas," in *Modern Antenna Handbook*, S. A. Balanis, Ed. John Wiley, 2008, ch. 18.
- [265] V. Rumsey, "Horn antennas with uniform power patterns around their axes," *IEEE Trans. Antennas Propag.*, vol. 14, no. 5, pp. 656–658, Sep. 1966.
- [266] J. M. Howell, "Radar principles," in *Electronics Handbook*, 2nd ed., J. C. Whitaker, Ed. CRC Press, 2005, ch. 17, p. 1818.
- [267] M. V. Ivashina, J. Bij de Vaate, R. Braun, and J. D. Bregman, "Focal plane arrays for large reflector antennas: first results of a demonstrator project," in *SPIE Astronomical Telescopes and Instrumentation*. Glasgow, Scotland United Kingdom, 2004.

REFERENCES

- [268] D. K. Cheng and F. I. Tseng, "Gain optimization for arbitrary antenna arrays," *IEEE Trans. Antennas Propag. (Commun.)*, vol. AP-13, pp. 973–974, Nov. 1965.
- [269] F. Bryn, "Optimum signal processing of three-dimensional arrays operating on gaussian signals and noise," *The Journal of the Acoustical Society of America*, vol. 34, no. 3, pp. 289–297, 1962.
- [270] S. P. Applebaum, "Adaptive arrays," *IEEE Trans. Antennas Propag.*, vol. 24, no. 5, pp. 585–598, Sep. 1976.
- [271] H. Back and J. E. Hansen, "Uniformly spaced arrays," in *Antenna Theory*, ser. Inter-University Electronics Series, Vol. 7, R. E. Collin and F. J. Zucker, Eds. New York: McGraw-Hill, 1969, vol. 1, ch. 5, pp. 138–206.
- [272] W. Briskin, "A Vivaldi focal plane array for EVLA," National Radio Astronomy Observatory, EVLA Memo 53, Mar. 2003. [Online]. Available: <http://www.aoc.nrao.edu/evla/geninfo/memoseries/evlamemo53.pdf>
- [273] W. Briskin and C. Craeye, "Focal plane array beam-forming and spill-over cancellation using Vivaldi antennas," National Radio Astronomy Observatory, EVLA Memo 69, Jan. 2004. [Online]. Available: <http://www.aoc.nrao.edu/evla/geninfo/memoseries/evlamemo69.pdf>
- [274] O. Iupikov, M. Ivashina, and O. Smirnov, "Reducing the complexity of the beam calibration models of phased-array radio telescopes," in *Eu. Conf. on Antennas and Propagation (EuCAP)*, Apr. 2011, pp. 930–933.
- [275] J. O'Sullivan, "Phased Array Feeds—beamformers, beams and flat field of view calibration," The Australia Telescope National Facility Colloquium, Jul., 18 2011.
- [276] D. B. Hayman, A. P. Chippendale, R.-Y. Qiao, J. D. Bunton, R. J. Beresford, P. Roberts, and P. Axtens, "Gain calibration of phased array feeds," in *Int. Conf. on Electromagnetics in Advanced Applications (ICEAA)*, Sep. 23 2010, pp. 418–421.
- [277] W. van Cappellen and M. Ivashina, "Temporal beam pattern stability of a radio astronomy phased array feed," in *Eu. Conf. on Antennas and Propagation (EuCAP)*, Apr. 2011, pp. 926–929.
- [278] S. Applebaum and D. Chapman, "Adaptive arrays with main beam constraints," *IEEE Trans. Antennas Propag.*, vol. 24, no. 5, pp. 650–662, 1976.

-
- [279] Y. T. Lo, S. W. Lee, and Q. H. Lee, "Optimization of directivity and signal-to-noise ratio of an arbitrary antenna array," *Proc. IEEE*, vol. 54, no. 8, pp. 1033–1045, 1966.
- [280] W. Briskin, "Focal plane arrays for the VLA?" in *Focal Plane Array Workshop*. Dwingeloo, May 2004.
- [281] M. Kesteven, G. Hobbs, R. Clement, B. Dawson, R. Manchester, and T. Uppal, "Adaptive filters revisited: Radio frequency interference mitigation in pulsar observations," *Radio Sci.*, vol. 40, pp. 1–10, May 2005.
- [282] B. D. Jeffs, L. Li, and K. F. Warnick, "Auxiliary antenna-assisted interference mitigation for radio astronomy arrays," *IEEE Trans. Signal Process.*, vol. 53, pp. 439–451, Feb. 2005.
- [283] J. Andersen and H. Rasmussen, "Decoupling and descattering networks for antennas," *IEEE Trans. Antennas Propag.*, vol. 24, no. 6, pp. 841–846, 1976.
- [284] B. Veidt, "Polarimetry with phased-array feeds," in *Int. Workshop on Phased Array Antenna Systems for Radio Astronomy*. Brigham Young University, Provo, Utah, USA, May 3–5 2010. [Online]. Available: http://csas.ee.byu.edu/docs/Workshop/Veidt_polarization.pdf
- [285] K. F. Warnick, B. Jeffs, M. Ivashina, R. Maaskant, and S. Wijnholds, "Polarimetric phased array beamforming and calibration," in *Int. Workshop on Phased Array Antenna Systems for Radio Astronomy*, May 3–5 2010. [Online]. Available: <http://csas.ee.byu.edu/docs/Workshop/Polarimetric%20Beamforming%20April2010.pdf>
- [286] M. Ivashina, O. Iupikov, R. Maaskant, W. van Cappellen, and T. Oosterloo, "An optimal beamforming strategy for wide-field surveys with phased-array-fed reflector antennas," *IEEE Trans. Antennas Propag.*, vol. 59, no. 6, pp. 1864–1875, Jun. 2011.
- [287] J. W. Wallace and M. A. Jensen, "Mutual coupling in MIMO wireless systems: a rigorous network theory analysis," *Wireless Communications, IEEE Transactions on*, vol. 3, no. 4, pp. 1317–1325, 2004.
- [288] W. Wasylkiwskyj and W. Kahn, "An explicit relation between mutual coupling and the pattern of an antenna array," in *IRE International Convention Record*, vol. 14, 1966, pp. 167–171.
- [289] D. M. Pozar, *Microwave Engineering*. Wiley, 2004.
- [290] B. D. Jeffs and K. F. Warnick, "Bias corrected PSD estimation for an adaptive array with moving interference," *IEEE Trans. Signal Process.*, vol. 56, pp. 3108–3121, Jul. 2008.

REFERENCES

- [291] M. Elmer and B. Jeffs, "Beamformer design for radio astronomical phased array feeds," in *Acoustics Speech and Signal Processing (ICASSP), 2010 IEEE International Conference on*, Mar. 2010, pp. 2790–2793.
- [292] J. D. Bunton, I. G. Jones, and D. R. Brown, "High resolution mapping with the FST," *Publ. Astron. Soc. Aust.*, vol. 6, pp. 93–100, 1985. [Online]. Available: <http://adsabs.harvard.edu/abs/1985PASAu...6...93B>
- [293] G. W. Kant, A. B. Kokkeler, A. B. Smolders, and A. W. Gunst, "Receiver architecture of the thousand-element array (THEA)," in *Proc. SPIE, Radio Telescopes*, ser. Presented at the Society of Photo-Optical Instrumentation Engineers (SPIE) Conference, H. R. Butcher, Ed., vol. 4015, Jul. 2000, pp. 287–298.
- [294] S. J. Wijnholds, A. G. Bruyn, J. D. Bregman, and J. Bij de Vaate, "Hemispheric imaging of galactic neutral hydrogen with a phased array antenna system," *Experimental Astron.*, vol. 17, no. 1-3, pp. 59–64, Jun. 2004.
- [295] M. Ivashina, "THEA tile radiation patterns," personal communication, 17 Nov. 2008.
- [296] M. Arts, "S-parameter measurements of the THEA Vivaldi array," ASTRON, Tech. Rep. Report SKA - 00460, Jan. 2002.
- [297] (2010) Register of radiocommunication licences. Australian Communications and Media Authority. Accessed 2010-07-03. [Online]. Available: http://web.acma.gov.au/pls/radcom/register_search.main_page
- [298] Australian Communications and Media Authority, "Australian radiofrequency spectrum plan," 2009. [Online]. Available: <http://www.acma.gov.au/>
- [299] E. E. M. Woestenburg, personal communication, 2007.
- [300] "CGY2106TS dual LNA data sheet," Philips Semiconductors, 2000.
- [301] A. Grancea, personal communication, 2006.
- [302] E. E. M. Woestenburg, "Influence of antenna efficiencies on noise temperature measurement," ASTRON, P.O. Box 2, 7990 AA Dwingeloo, The Netherlands, Tech. Rep., Aug. 2007.
- [303] E. E. M. Woestenburg and K. F. Dijkstra, "Noise characterization of a phased array tile," in *European Microwave Conference (EuMC)*, vol. 1, 2003, pp. 363–366.

-
- [304] E. B. Fomalont and R. A. Perley, “Calibration and editing,” in *Synthesis Imaging in Radio Astronomy II*, ser. Astron. Soc. Pac. Conf., G. B. Taylor, C. L. Carilli, and R. A. Perley, Eds., vol. 180, 1999, pp. 79–110. [Online]. Available: <http://adsabs.harvard.edu/abs/1999ASPC..180...79F>
- [305] A. J. Kemball and M. H. Wieringa. (2000, Jan.) MeasurementSet definition version 2.0. ATNF. [Online]. Available: <http://www.atnf.csiro.au/computing/software/casacore/casacore-0.4.0/doc/notes/229.html>
- [306] B. M. Oliver, “The rationale for a preferred frequency band: The water hole,” in *SP-419 SETI: The Search for Extraterrestrial Intelligence*, P. Morrison, J. Billingham, and J. Wolfe, Eds., no. SP-419. NASA, 1977. [Online]. Available: <http://history.nasa.gov/SP-419/sp419.htm>
- [307] R. C. Hansen, *Phased Array Antennas*, K. Chang, Ed. Wiley, 1998.
- [308] J. Bennett, A. Anderson, P. McInnes, and A. Whitaker, “Microwave holographic metrology of large reflector antennas,” *IEEE Trans. Antennas Propag.*, vol. 24, no. 3, pp. 295–303, May 1976.
- [309] D. R. W. Williams, “Studies of four regions for use as standards in 21cm observations,” *Astronomy and Astrophysics Supplement*, vol. 8, pp. 505–516, 1973.
- [310] A. Chippendale, J. O’Sullivan, J. Reynolds, R. Gough, D. Hayman, and S. Hay, “Phased array feed testing for astronomy with ASKAP,” in *IEEE Int. Symp. on Phased Array Systems and Technology*, Oct. 12–15 2010, pp. 648–652.
- [311] T. A. Milligan, *Modern antenna design*. Wiley, 2005.
- [312] L. Staveley-Smith, W. E. Wilson, T. S. Bird, M. W. Sinclair, R. D. Ekers, and R. L. Webster, “The Parkes 21 cm multibeam receiver,” in *Multi-Feed Systems for Radio Telescopes*, ser. Astron. Soc. Pac. Conf., vol. 75, Tucson, AZ, May 16–18, 1994, pp. 34–41. [Online]. Available: <http://adsabs.harvard.edu/abs/1995ASPC...75..136S>
- [313] W. V. T. Rusch and P. D. Potter, *Analysis of Reflector Antennas*. Academic Press, 1970.
- [314] J. Dijk, J. M. Berends, and E. J. Maanders, “Aperture blockage in dual reflector antenna systems: A review (effects of two reflector antenna aperture blockage on directive gain pattern and near sidelobes),” Eindhoven University of Technology, Tech. Rep., 1971. [Online]. Available: <http://alexandria.tue.nl/extra1/erap/publichtml/7302606.pdf>

REFERENCES

- [315] A. Toccafondi, B. Romani, R. Mizzoni, M. Maci, and R. Tiberio, "Spherical wave blockage in reflector antennas," *IEEE Trans. Antennas Propag.*, vol. 45, no. 5, pp. 851–857, May 1997.
- [316] J. Ruze, "Antenna tolerance theory: A review," *Proc. IEEE*, vol. 54, no. 4, pp. 633–640, Apr. 1966.
- [317] H. Ling, Y. Lo, and Y. Rahmat-Samii, "Reflector sidelobe degradation due to random surface errors," *IEEE Trans. Antennas Propag.*, vol. 34, no. 2, pp. 164–172, feb 1986.
- [318] P.-S. Kildal, *Foundations of antennas : a unified approach*. Studentlitteratur, 2000.
- [319] Y. Rahmat-Samii and S.-W. Lee, "Vector diffraction analysis of reflector antennas with mesh surfaces," *IEEE Trans. Antennas Propag.*, vol. 33, no. 1, pp. 76–90, Jan. 1985.
- [320] W. V. T. Rusch, T. S. Chu, A. R. Dion, P. A. Jensen, and A. W. Rudge, "Quasi-optical antenna design and applications," in *The Handbook of Antenna Design*, ser. IEE Electromagnetic Waves, A. W. Rudge, K. Milne, A. D. Olver, and P. Knight, Eds. London, UK: Peter Peregrinus, 1982, vol. 1, ch. 3, pp. 128–337.
- [321] M. Voronkov and T. Cornwell, "On the calibration and imaging with eigenbeams," CSIRO, ANTF SKA Memo 12, 2007. [Online]. Available: <http://www.atnf.csiro.au/SKA/newdocs/eigenbeams.pdf>
- [322] —, "Notes on the calibration and simulation strategy," CSIRO, ANTF SKA Memo 11, Oct. 18 2006. [Online]. Available: http://www.atnf.csiro.au/projects/askap/newdocs/calsim_strategy.pdf
- [323] R. Perley, "On the use of correlation coefficients for determining antenna sensitivity," EVLA, Memo 127, Aug. 21 2008.
- [324] M. J. Kesteven, "G/T from visibility statistics," personal communication, 2007.
- [325] T. Cornwell, "G/T from visibility statistics from fringe rate vs. delay image," personal communication, 2007.
- [326] —, "ASKAP calibration," Internal presentation, May 29 2009.
- [327] S. J. Wijnholds and A. J. Boonstra, "A multisource calibration method for phased array radio telescopes," in *Sensor Array and Multichannel Processing, 2006. Fourth IEEE Workshop on*, Waltham, MA, Jul. 12–14, 2006, pp. 200–204.

-
- [328] D. Mitchell, L. Greenhill, R. Wayth, R. Sault, C. Lonsdale, R. Cappallo, M. Morales, and S. Ord, "Real-time calibration of the murchison widefield array," *IEEE J. Sel. Topics Signal Process.*, vol. 2, no. 5, pp. 707–717, oct. 2008.
- [329] S. J. Wijnholds and A. van der Veen, "Self-calibration of radio astronomical arrays with non-diagonal noise covariance matrix," in *17th European Signal Processing Conference (EuSiPCo)*, Aug. 24–28 2009. [Online]. Available: <http://adsabs.harvard.edu/abs/2010arXiv1003.2497W>
- [330] S. Wijnholds and W. van Cappellen, "In situ antenna performance evaluation of the lofar phased array radio telescope," *IEEE Trans. Antennas Propag.*, vol. 59, no. 6, pp. 1981–1989, Jun. 2011.
- [331] W. Rusch and R. Wanselow, "Boresight-gain loss and gore-related sidelobes of an umbrella reflector," *IEEE Trans. Antennas Propag.*, vol. 30, no. 1, pp. 153–157, jan 1982.
- [332] R. Lenormand, E. El-Shirbini, J. Neron, J. Marre, B. Saint Andre, R. Coirault, and E. Rammos, "A versatile array fed reflector antenna-part a: reception," in *IEEE AP-S Int. Symp. Digest*, vol. 2, Jun. 1988, pp. 502–505.
- [333] S. A. Jackson, "RF design of a wideband CMOS integrated receiver for phased array applications," *Experimental Astron.*, vol. 17, no. 1, pp. 201–210, Jun. 2004.
- [334] S. Jackson, R. Gough, and Y. Moghe, "Receiver integration for mid-band Square Kilometer Array demonstrator applications," in *Compound Semiconductor Integrated Circuit Symposium (CSICS), 2010 IEEE*, Oct. 2010, pp. 1–3.
- [335] W. Turner, "Technology roadmap document for SKA signal processing," SKA Program Development Office, Tech. Rep. WP2?040.030.011?TD?001, 2011.
- [336] K. van der Schaaf, C. Broekema, G. van Diepen, and E. van Meijeren, "The LOFAR central processing facility architecture," *Experimental Astron.*, vol. 17, pp. 43–58, 2004.
- [337] M. de Vos, A. Gunst, and R. Nijboer, "The LOFAR telescope: System architecture and signal processing," *Proc. IEEE*, vol. 97, no. 8, pp. 1431–1437, Aug. 2009.
- [338] J. R. Rice, "Experiments on Gram-Schmidt orthogonalization," *Mathematics of Computation*, vol. 20, no. 94, pp. 325–328, Apr. 1966. [Online]. Available: <http://www.jstor.org/stable/2003512>

REFERENCES

- [339] Y. Rahmat-Samii, "Useful coordinate transformations for antenna applications," *IEEE Trans. Antennas Propag.*, vol. 27, no. 4, pp. 571–574, 1979.
- [340] P. Smith, "Measurement of the complete far-field pattern of large antennas by radio-star sources," *IEEE Trans. Antennas Propag.*, vol. 14, no. 1, pp. 6–16, 1966.
- [341] J. Baars, "The measurement of large antennas with cosmic radio sources," *IEEE Trans. Antennas Propag.*, vol. 21, no. 4, pp. 461–474, 1973.
- [342] A. N. Lasenby, "Surface measurements of the NRAO 12m antenna," in *European Southern Observatory Conference and Workshop Proceedings*, ser. European Southern Observatory Conference and Workshop Proceedings, P. A. Shaver & K. Kjar, Ed., vol. 22, 1985, pp. 77–83. [Online]. Available: <http://adsabs.harvard.edu/abs/1985ESOC...22...77L>
- [343] D. Rochblatt and Y. Rahmat-Samii, "Effects of measurement errors on microwave antenna holography," *IEEE Trans. Antennas Propag.*, vol. 39, no. 7, pp. 933–942, Jul. 1991.
- [344] ARINC Engineering Services LLC, "Navstar GPS space segment/navigation user interfaces," GPS Joint Program Office, Tech. Rep., 2004. [Online]. Available: <http://www.navcen.uscg.gov/gps/geninfo/IS-GPS-200D.pdf>
- [345] N. G. Survey. (2008) National Geodetic Survey precise GPS orbits. [Online]. Available: <http://www.ngs.noaa.gov/orbits>
- [346] T. S. Kelso. (2008) Celestrak. Center for Space Standards and Innovation. Accessed 2009-03-03. [Online]. Available: <http://www.celestrak.com>
- [347] NAVCEN, "NAVSTAR GPS user equipment introduction," U.S. Coast Guard Navigation Center, Tech. Rep., 1996. [Online]. Available: <http://www.navcen.uscg.gov/pubs/gps/gpsuser/gpsuser.pdf>
- [348] C. Wang, R. A. Walker, and M. P. Moody, "An improved single antenna attitude system based on GPS signal strength," in *Proc. American Institute of Aeronautics and Astronautics—Guidance, Navigation, and Control Conference*, 2005. [Online]. Available: <http://eprints.qut.edu.au/archive/00002938/>
- [349] K. G. Johannsen and L. Titus, "Determination of Ku-band earth station antenna G/T using the moon as RF source," *IEEE Trans. Instrum. Meas.*, vol. 35, pp. 344–348, Sep. 1986.

-
- [350] R. P. Corkish, "Use of the moon in figure-of-merit measurements of satellite earth stations," *Journal of Electrical and Electronics Engineering, Australia—IE Aust. and IREE Aust.*, vol. 9, pp. 92–101, Sep. 1989.
- [351] K. G. Johannsen and A. Koury, "The moon as source for G/T measurements," *IEEE Trans. Aerosp. Electron. Syst.*, vol. AES-10, no. 5, pp. 718–727, 1974.
- [352] S. Doclo and M. Moonen, "Design of far-field and near-field broadband beamformers using eigenfilters," *Signal Processing*, vol. 83, no. 12, pp. 2641–2673, 2003.
- [353] Australia telescope compact array calibrator search tool. CSIRO. Accessed 2008. [Online]. Available: <http://www.narrabri.atnf.csiro.au/calibrators/>
- [354] J. Caswell, personal communication, 2008.
- [355] J. W. M. Baars, R. Genzel, I. I. K. Pauliny-Toth, and A. Witzel, "The absolute spectrum of CAS A—an accurate flux density scale and a set of secondary calibrators," *Astronomy and Astrophysics*, vol. 61, pp. 99–106, Oct. 1977.
- [356] M. Ott, A. Witzel, A. Quirrenbach, T. P. Krichbaum, K. J. Standke, C. J. Schalinski, and C. A. Hummel, "An updated list of radio flux density calibrators," *Astronomy and Astrophysics*, vol. 284, pp. 331–339, Apr. 1994.
- [357] J. M. Dickey, S. R. Kulkarni, C. E. Heiles, and J. H. van Gorkom, "A survey of HI absorption at low latitudes," *Astrophysical Journal Supplement Series*, vol. 53, pp. 591–621, Nov. 1983.
- [358] R. E. Bentley, *Uncertainty in measurement: the ISO guide*, ser. NML technology transfer series. CSIRO Telecommunications and Industrial Physics, 2001.
- [359] *ISO/IEC GUIDE 98-3:2008(E): Uncertainty of measurement Part 3: Guide to the expression of uncertainty in measurement (GUM:1995)*, ISO Std., 2008.
- [360] Agilent, "Fundamentals of RF and microwave power measurements (part 3): Power measurement uncertainty per international guides," Application Note 1449-3, Jun. 2009. [Online]. Available: <http://www.home.agilent.com/agilent/editorial.jsp?id=272209&ckey=272209&nid=-34816.0.02&lc=eng&cc=AU>
- [361] L. N. Trefethen, *Spectral Methods in MATLAB*. SIAM, 2000.

REFERENCES

- [362] O. M. Bucci, C. Gennarelli, and C. Savarese, “Optimal interpolation of radiated fields over a sphere,” *IEEE Trans. Antennas Propag.*, vol. 39, no. 11, pp. 1633–1643, Nov. 1991.
- [363] Y. Rahmat-Samii, “Surface diagnosis of large reflector antennas using microwave holographic metrology: An iterative approach,” *Radio Sci.*, vol. 19, pp. 1205–1217, 1984.
- [364] S. Hay, personal communication, 2009.